Production and Characterization of Micro-Tubular Solid Oxide Fuel Cells

Michele Casarin

PRODUCTION AND CHARACTERIZATION OF MICRO-TUBULAR SOLID OXIDE FUEL CELLS

Michele Casarin
E-mail: michele.casarin@ing.unitn.it

Approved by:
Prof. Sglavo, V.M., Advisor
Department of Industrial Engineering
University of Trento, Italy.

Ph.D. Commission:
Prof. Sglavo, V.M.,
Department of Industrial Engineering
University of Trento, Italy.

Prof. Smeacetto F.,
Department of Applied Science
and Technology
University of Torino, Italy.

Prof. Bermejo R.,
Department of Structural
and Functional Ceramics
University of Leoben, Austria.

University of Trento,
Department of Industrial Engineering

December 2013

"Do not go where the path may lead;
go instead where there is no path
and leave a trail."
R.W. Emerson

Abstract

In the present work, micro-tubular solid oxide fuel cells (μt-SOFCs) constituted by NiO/YSZ anode with an embedded current collector, YSZ as electrolyte, YSZ/LSM as functional cathode layer and pure LSM as cathode current collector layer were fabricated by dip-coating technique. The fuel cell was designed according to the anode-supported configuration with a metallic coil introduced within the anode during the cell fabrication. The production of the devices through wet colloidal process required the optimization of suspensions employed for the dip-coating. Then, investigation on rheological properties for the anode and electrolyte water-base slurries was carried out with particular emphasis to the solid loading and the concentration of slurry additives as well as temperature. In addition, thermal analyses elucidated the response of anode, electrolyte and cathode layers during drying, binder burn-out and sintering processes. The thermal behaviour of pyrolisable materials and oxidation of the metal components used as current collector was performed using conditions identical to cell fabrication like temperatures as high as 1400°C in oxidative atmosphere. After sintering, the complete μt-SOFCs with embedded current collector were produced with outer diameter as low as 1.0 mm and length of 30 mm with an effective active cathode length of 20 mm resulting in an active area of 0.63 cm^2. The cell performance was analyzed by V-j plots in the temperature range of 700-800°C where the effect of the cell diameter and current collector characteristics on power density was pointed out. The efficiency of current collector was examined by comparing coils with different configurations (turns per unit length) as well as nature of the metal. The cell performance was demonstrated to be related to the current collector configuration. In particular, as twice the turns per unit length are as double the current density is thus making the power density 4-fold. An additional improvement of the cell performance was found for the palladium current collector where the power density was increased by a factor more than 4 in comparison with the cell made with nickel collector due to the higher catalytic activity of palladium for electrochemical reactions. On the basis of these findings, a further development of μt-SOFCs with embedded collector was suggested with an alternative design of palladium current collector for which an estimate of power density of micro-tubular cell provided values higher than 0.7 W/cm^2 at temperature of 800°C.

Table of contents

Preface

This thesis concerns the development of micro-tubular SOFCs undertaken by the ceramics research group at the Department of Industrial Engineering of the University of Trento since Marco Cologna realized a first prototype whose development was carried out by Ricardo De la Torre García who produced a micro-tubular cell with well-defined geometry and characteristics with an embedded current collector introduced during the cell fabrication. The present work on micro-tubular SOFCs is based on the cell design by Ricardo De la Torre García who demonstrated the efficiency of the embedded current collector as effective connection for the anode in comparison with the conventional connection with a straight wire along the fuel channel, usually adopted for the anode-supported configuration of tubular SOFCs (Ricardo De la Torre García, 2011). The benefit of this innovative design is an improvement of cell performance resulting from a reduction of cell resistance due to the better contact of current collector with the anode electrode and homogeneous current distribution throughout the anode electrode. On the other hand, the current collector introduced during cell fabrication offers an effective strategy for the electrical connections which is particularly challenging for devices with small size like micro-tubular SOFCs. On the basis of these results, the present work involves the achievement of reliable ceramic processing for the production and development of micro-tubular SOFCs with embedded current collector whose properties, first during cell fabrication and subsequently during electrochemical testing, are crucial for the performance and reliability of micro-tubular SOFCs. The thesis consists of a brief introduction on fuel cells and particularly SOFCs (chapter 1), followed by the description of experimental procedure (chapter 2) which is outlined according to the procedure of cell fabrication similarly to the results presented in chapter 3. Lastly, in chapter 4 the most relevant results are summarized where suggestions for the improvement of ceramic processing and design for the micro-tubular cells are also given.

Chapter I

Introduction

1.1 Fuel Cells

1.1.1 General aspects

Fuel cells (FCs) are electrochemical devices that convert chemical energy of fuel and oxidant gases directly to electricity with high efficiency as no intermediate steps are involved differently from the conventional chemical-to-electrical conversions whose efficiency is 40% at most, as a result of Carnot limitation. A higher energy-conversion efficiency implies lower emissions of greenhouse gases NO_x, SO_x, CO and CO_2, making FCs a technology of low environment impact. However, most of FCs work exclusively with hydrogen and those characterized by fuel flexibility work better with hydrogen than other hydrocarbons. Consequently, the "hydrogen economy" is usually connected with FC technology and until the production of hydrogen from renewable energy sources will not be established (figure 1.1), the environment compatibility of FC technology is severely restricted by the hydrogen production from hydrocarbons (Atkinson, 2004).
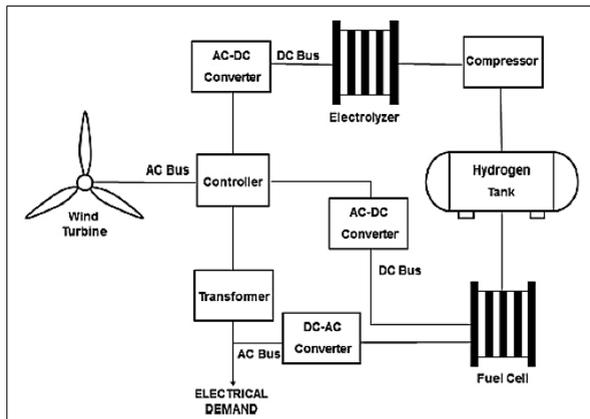
Figure 1.1. Schematic of hydrogen production from clean source, i.e. wind, for a wind turbine-electrolyzer-fuel cell system (Genç, 2012).

To date, although the hydrogen production from clean sources is far to be an affirmed reality, the worldwide interest on fuel cells is being increasing as a result of

3

their high efficiency, low production of greenhouse gases and wide flexibility for power generation applications. Indeed, FCs when are integrated to traditional power generation plants, support an increment of the overall system efficiency, especially when high grade heat is produced by FCs, generally ceramic fuel cells. In this case, combined heat and power (cogeneration) as well as combined gas-turbine and fuel cell applications are possible, with efficiency of the system usually above 60%, as proved by some demonstration plants (Hassmann, 2001; Bakalis, 2013). The efficiency of different power plants technology depends also on scaling effect (power plant output) as outlined in figure 1.2.
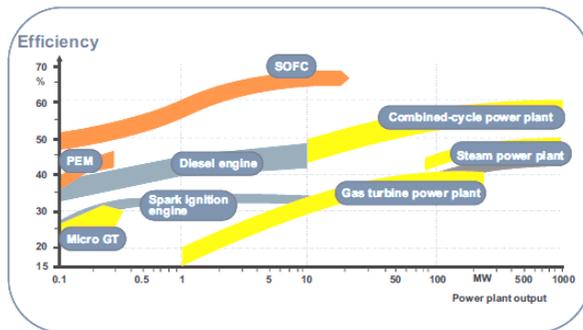
Figure 1.2. Efficiency of different power plants technology; GT stands for gas turbines while PEM and SOFC stand respectively for polymer electrolyte membrane fuel cell and solid oxide fuel cell (Hassmann, 2001).

Moreover, some type of FCs have a dual role on the hydrogen economy because they can work as electrolyzers, then storing the excess of grid energy as hydrogen and subsequently use the fuel for producing electricity (Yang, 2010; Laguna-Bercero, 2011); in this condition, the fuel cell acts similarly to a secondary battery. Differently from batteries, fuel cells do not need recharging and work as long as reactants are supplied, yet produce DC electricity at low voltage, usually < 1 V, similarly to most of single batteries. In order to fulfill the demanding power, single fuel cells can be arranged in series and parallel to produce stacks where also DC/AC converters, fuel supply and system controller among the main ancillary components form the fuel cell systems for stationary power generation applications as shown in figure 1.1. In addition to stationary applications, FCs interest the transport sector where they are adopted as auxiliary power unit (APU) in trucks, as power generators in ships but also in hybrid electrical vehicles (HEV) as city buses for meeting the demanding restrictions on pollution and noise in some metropolitan cities (Andújar, 2009). A growing concern in FCs regards portable and mobile applications where miniaturization of fuel cell devices is necessary in powering laptops and mobile phones as the increasing power demands of mobile devices is expected to be only partially fulfilled by Li-ion batteries in future (Tasa, 2006; Dyer, 2002). Fuel cells are

widely used in the military sector (US army) for transport, power generation and mobile applications (Singhal, 2002; Fuel Cells Bulletin, 2005). Conversely, civil applications of FCs are controlled by long-term durability and costs which are not the first issues for military applications. Indeed, the greatest hurdle to commercialization of fuel cells relies on the costs principally related to the operative lifetime and manufacturing. Consequently, technological advances for fuel cells are driven to increase their long-term durability and power output per unit cost while the production of clean hydrogen is seen as a parallel breakthrough rather an essential issue for the FC development as established by the possibility of some fuel cells (solid oxide FCs) to work as electrolyzers and to be integrated in conventional power generation plants increasing significantly the overall system efficiency and therefore better utilize the current energy sources.

1.1.2   Type of fuel cells

Several types of fuel cells have been developed and characterized by common underlying electrochemical principles as well as different materials, operative conditions, performance and applications. Fuel cells are usually distinguished by the electrolyte as it controls the operative conditions and performance and therefore the application of the device as shown in table 1.1.

Table 1.1. Types of fuel cells with usual operating temperature range, mobile ion across the electrolyte and applications (Larminie, 2003).

Fuel cell type	Mobile ion	Operating temperature	Applications and notes
Alkaline (AFC)	OH^-	50–200°C	Used in space vehicles, e.g. Apollo, Shuttle.
Proton exchange membrane (PEMFC)	H^+	30–100°C	Vehicles and mobile applications, and for lower power CHP systems
Direct methanol (DMFC)	H^+	20–90°C	Suitable for portable electronic systems of low power, running for long times
Phosphoric acid (PAFC)	H^+	~220°C	Large numbers of 200-kW CHP systems in use.
Molten carbonate (MCFC)	CO_3^{2-}	~650°C	Suitable for medium- to large-scale CHP systems, up to MW capacity
Solid oxide (SOFC)	O^{2-}	500–1000°C	Suitable for all sizes of CHP systems, 2 kW to multi-MW.

The operating temperature range (RT-220°C) for low temperature FCs, i.e. proton exchange membrane or polymer electrolyte membrane (PEM), direct methanol (DM), alkaline (A) and phosphoric acid (PA) fuel cells, is controlled by the evaporation of the electrolyte impregnated within a solid matrix as for DMFC and PAFC devices, otherwise wholly liquid in AFCs, as well as the degradation of polymer electrolyte membrane in PEMFCs. The low temperatures of these fuel cells allow a fast startup but at the same time catalysts are necessary to increase the kinetics of reactions

and thus the device performance. In addition to catalysts, usually Pt-base materials, also the fuel covers a relevant part of the costs for low temperature FCs; high-grade purity hydrogen is exclusively used as well as high purity oxygen as CO (even 50 ppm in PEMFCs) and sulphur particles must be strictly limited in order to avoid the poisoning of catalyst and impair the cell functionality. Alternatively to the electrolytic pure hydrogen, the less expensive methanol can be employed as fuel in DMFCs exploiting the polymer-electrolyte-membrane technology, even if the electro-oxidation of methanol is particularly slow than hydrogen due to the complex oxidation reactions where also undesirable byproducts like CO can be produced and damage the catalyst. Another drawback of DMFCs is the crossover of fuel that lowers the cell performance. An improvement of these primary drawbacks of PEM, DM and alkaline fuel cells, is partially solved by PAFCs since the higher operating temperature, necessary to maintain liquid the electrolyte (phosphoric acid), acts positively on electrochemical reactions where also a tolerance of 1% for CO is admitted and thus the fuelling with reformed hydrogen, less costly, is possible as long as H_2S does not exceed 50 ppm. Another advantage of PAFCs is the increment of efficiency, from 40% typically of low temperature FCs, up to ~70% in combined heat and power unit of 200 KW where good performance with relatively little maintenance is achieved for long run of one year and more (Larminie, 2003). Fuel cells working at high temperatures, like molten carbonate and solid oxide FCs, are characterized by fast electrochemical reactions and expensive catalyst as Pt-base ones are not needed with the benefit to rule out the catalyst poisoning by carbon monoxide. Indeed, CO acts as a fuel with hydrogen for MCFCs while SOFCs show wide fuel flexibility as the oxygen ions of the solid electrolyte can electro-oxidize, in principle, several hydrocarbons as well as the carbon monoxide. Nonetheless, the performance of these high temperature fuel cells is better when hydrogen is used and therefore fuel reforming units usually accompany SOFCs and MCFCs whose high temperature of exhaust gases can be employed for hydrocarbon reforming to hydrogen, cogeneration and gas turbine-fuel cell systems with high efficiency as shown in figure 1.2. A further advantage of SOFCs is the solid electrolyte which avoid the issues connected to liquid electrolyte, corrosion and safety, as molten carbonates in MCFCs. Nonetheless, the severe operating conditions of these fuel cells require the use of relatively expensive materials resistant to high temperatures and degradation of fuel cell components is of main concern as well as sealing issues which lower the cell performance on long-term runs. Then, advances in materials and components are necessary to enhance the performance for long-term stability as well as to reduce the high manufacturing costs of these devices. The potential commercial FC applications spans from portable devices as battery charges involving PEM and DM fuel cells and power generation and cogeneration applications for phosphoric acid, molten carbonate and solid oxide fuel cells though recently, an increasing interest for the miniaturization of tubular SOFCs may encompass the sector of portable applications. Lastly, SOFC technology receives particular interest also for the

hydrogen production from clean sources as a result of reversible working mode as electrolyzer. All these characteristics make SOFCs object of ongoing worldwide reasearch and development aimed to realize a market penetration in power generation systems and concerning applications.

1.2 Solid Oxide Fuel Cells

1.2.1 Principles of operation

A solid oxide fuel cell (SOFC) is a ceramic energy conversion device characterized by two porous electrodes, anode and cathode, separated by a solid electrolyte; all of these components are at solid state. The two electrodes are connected by the interconnect where electrons are attracted by the positive voltage of cathode and they combine with oxygen of air producing oxygen ions by electrochemical reduction. Then, the oxygen ions pass from the high oxygen partial pressure at cathode to the low oxygen partial pressure at anode across the solid electrolyte which is an ion conductor. At anode, oxygen ions electro-oxidize the fuel, typically hydrogen, with release of electrons which flow toward the cathode through the interconnect as the electrolyte is an electric insulator and DC electricity is produced while the electrical circuit is complete as shown in figure 1.3 (Lawlor, 2009).
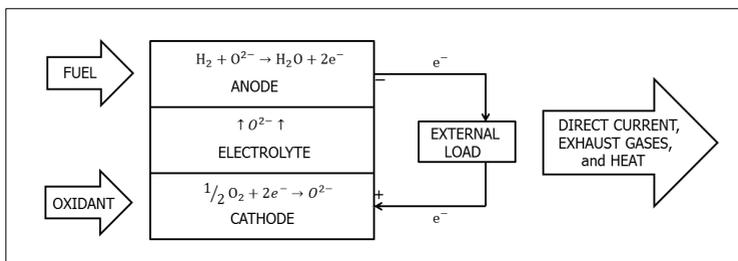
Figure 1.3. Schematic diagram of operation for SOFC working with hydrogen and oxygen as fuel and oxidant, respectively.

The electrochemical reactions for a SOFC using oxygen as oxidant and hydrogen as fuel, are described respectively by the oxygen reduction at cathode and the hydrogen oxidation at anode as shown in equation 1.1 with the overall reaction, whose products are the steam (exhaust gas) and heat, other than the electrons flowing through the electrical circuit:

$$\frac{1}{2} O_2 + 2e^- \rightarrow O^{2-} \qquad (1.1)$$

$$\frac{H_2 + O^{2-} \rightarrow H_2O + 2e^-}{H_2 + \frac{1}{2} O_2 \rightarrow H_2O + heat}$$

7
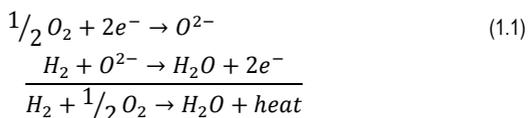
The generation of electricity involves water steam as exhaust gas with release of high grade heat due to the high operating temperatures, usually in the range 600-1000°C, without any adverse pollutants or greenhouse gases. The voltage established across the two electrodes depends on the free energy of the overall reaction of Eq. 1.1. Nernst observed that the reversible voltage of an electrochemical cell is proportional to the free energy of the overall reaction; on the basis of Van't Hoff equation, Nernst attains the reversible voltage V_{rev}, as a function of the activity of reaction species and temperature:

$$V_{rev} = E_0 - \frac{RT}{nF} ln \frac{\prod a_{products}^{v_i}}{\prod a_{reactants}^{v_i}} \qquad (1.2)$$

where E_o is the reversible voltage at standard condition of temperature and pressure (STP), R the gas constant, F the Faraday constant, n is the number of electrons involved in the reaction (more precisely the moles of electrons transferred for one mole of hydrogen molecule), a_i and v_i the activity and coefficient of reaction species. The voltage E_o is also a thermodynamic property depending on temperature and it can be expressed at conditions different from STP, after some rearrangements of the Gibbs free energy expression, as E_T (O'Hayre, 2006):

$$E_T = E_0 + \frac{\Delta S}{nF}(T - T_0) \qquad (1.3)$$

where E_T is the reversible cell voltage (at constant pressure), function of the temperature T and standard temperature T_o, the molar entropy change ΔS of the overall reaction $H_2 + 1/2O_2 \rightarrow H_2O$ (equation 1.1). Replacing the activity of reaction species of Eq. 1.2 with the partial pressure of steam (P_{H2O}), hydrogen (P_{H2}) and oxygen (P_{O2}) after the assumption of unitary activity coefficients according to ideal gas behaviour, and on the basis of equation 1.3, the Nernst voltage of the overall reaction 1.1, becomes:

$$V_{rev} = E_T - \frac{RT}{nF} ln \frac{P_{H_2O}}{P_{H_2} P_{O_2}^{1/2}} \qquad (1.4)$$

Equation 1.4 describes the thermodynamic cell voltage, and thus the maximum voltage feasible from the electrochemical reaction of hydrogen and oxygen as a function of temperature and pressure of reaction species. The cell voltage decreases with temperature by both terms of Eq. 1.4. In fact, the entropy change of the overall reaction 1.1 is negative, and therefore E_T diminishes with temperature as indicated by Eq. 1.3. On the other hand, the free energy change ΔG of the overall reaction $H_2 + 1/2O_2 \rightarrow H_2O$, is proportional to the reversible voltage ($\Delta G \propto V_{rev}$) and decreases with temperature as shown in table 1.2. The negative value of ΔG implies a

spontaneous reaction between hydrogen and oxygen to form water, although the decreasing values indicate a reduction of thermodynamic driving force, due to the exothermic nature of the electrochemical reaction, that reflects the decrease of Nernst (thermodynamic) voltage with temperature as pointed out by equation 1.3 and 1.4.

Table 1.2. Molar free Gibbs energy (Δg_f) as a function of temperature for the reaction: $H_2 + 1/2O_2 \rightarrow H_2O$ (Larminie, 2003).

Form of water product	Temperature (°C)	$\Delta \overline{g}_f$ (kJ mol^{-1})
Liquid	25	−237.2
Liquid	80	−228.2
Gas	80	−226.1
Gas	100	−225.2
Gas	200	−220.4
Gas	400	−210.3
Gas	600	−199.6
Gas	800	−188.6
Gas	1000	−177.4

From a thermodynamic point of view, the operating temperature of SOFC between 600 and 1000°C is not reasonable, as pointed out by the thermodynamic efficiency coefficient ($\Delta G/\Delta H$ with ΔH the molar enthalpy change of reaction) which changes from 83% at RT to 62% at 1000°C, on the basis of high heating value (HHV) as enthalpy of reaction (Lamirnie, 2003). On the other hand, the cell voltage of Eq. 1.4 is obtained under equilibrium state where reversible processes occur in conditions of open circuit. In this case, no net current is developed and the reversible voltage of Eq. 1.4 reflects the maximum possible voltage, usually referred as open circuit voltage (OCV). Indeed, during operating conditions of the fuel cell, net current is drawn and corresponds to a shift from equilibrium condition, which involves irreversible losses, shown up by voltage drops. From this point of view, the voltage drops reflect the irreversible losses accompanied by the net current flux, and therefore the trend of cell voltage during operating condition can be seen as a measure of the cell efficiency. As far the operating voltage from the reversible voltage (OCV), as much the irreversible losses and as low the cell efficiency. When the fuel cell works at high temperatures, the irreversible losses are reduced and therefore the cell voltage and efficiency increase along with the performance and this accounts for the high operating temperatures of SOFCs.

1.2.2   Fuel cell efficiency

Thermodynamics defines the underlying operation principles and sets the maximum voltage obtainable from the electrochemical reaction that is essential to evaluate the overall cell efficiency. The cell efficiency is given by the product of several contributions basically involving thermodynamics, kinetics and operation terms as fuel utilization. The cell efficiency is here outlined with regards to the main losses arising during normal operation conditions when no leakages and fuel starvation occurs; a more detailed description can be found in (Minh, 1995; Larminie, 2003). Figure 1.4 illustrates the typical trend of voltage curve during operative cell condition where the voltage losses, depending on irreversible processes, increase as much as higher the current (or current density) produced. When the current density is close to zero, the cell is near the equilibrium condition and the operating voltage approaches the reversible (thermodynamic) voltage.
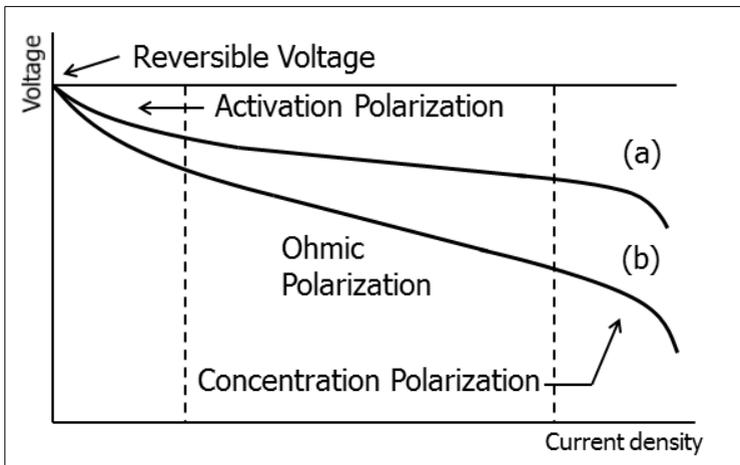
Figure 1.4. Schematic of a typical polarization curve (voltage versus current density) of a fuel cell with high efficiency (a) and low efficiency (b).

A first distinct voltage loss occurs at low current density and is dependent on the (charge) transfer of electrons between reactants and electrode surfaces during the electrochemical reactions of oxidation and reduction. The mechanism of charge transfer involves several reaction steps characterized by activation energies; in that an overpotential is spent to overcome the activation barrier of charge transfer, from which the definition of activation polarization (or activation overpotential), and permit a net current flux to occur. In the middle region of polarization curve, the voltage decreases linearly with current density and therefore the voltage loss is controlled by ohmic resistance. The principal resistances of SOFCs are mainly due to the electrical conductivity of materials/components and contact resistance at interfaces between

10

electrodes/electrolyte and electrodes/interconnect (current collector). The last portion of the polarization curves is controlled by the concentration polarization related to the gas migration whose resistance is connected to electrode microstructures and cell design. At this point, the contribution of different voltage losses on cell efficiency is investigated in more details in order to identify the causes of different cell performance in figure 1.4, where the polarization curve (a) corresponds to a SOFC with higher efficiency (lower voltage losses) than the cell characterized by the polarization curve (b). The cell voltage V_{cell} as a function of voltage losses V_{loss} is given by:

$$V_{cell} = V_{rev} - V_{loss} = V_{rev} - (\eta_{act} + \eta_{ohm} + \eta_{conc}) \tag{1.5}$$

where η_{act} is the activation polarization, η_{ohm} the ohmic polarization and η_{conc} the concentration polarization. First, the activation polarization is related to the current density through the well-known Butler-Volmer equation, which is indeed an exponential implicit form of current density as a function of activation polarization, for which numerical methods are needed to solve it. Nevertheless, during operating conditions when current is drawn, large overpotential is established and the Butler-Volmer equation simplifies to:

$$\eta_{act} = -\frac{RT}{\alpha nF} ln j_0 + \frac{RT}{\alpha nF} ln j \tag{1.6}$$

where j is the current density produced by the cell, j_0 the exchange current density and α the charge transfer coefficient. Equation 1.6 is known as Tafel equation and provides information on the kinetics of electrochemical reactions through the parameters j_0 and α. The exchange current density j_0 is proportional to the reaction rate while the charge transfer coefficient α indicates the prevailing mechanism of multistep reactions; as high j_0, as low the overpotential η_{act} to produce the current density j, and as high the cell voltage and therefore the cell performance. The exchanged current density is also expressed as:

$$j_0 \propto c_R e^{-\frac{E_a}{RT}} \tag{1.7}$$

Equation 1.7 relates the exchange current density with the concentration of reactants c_R, the activation energy E_a and temperature, and provides how to improve the reaction kinetics and thus the cell performance. For instance, an increment of reactant concentration by increasing the pressure has a positive effect on reaction kinetics, while a significant improvement of cell performance is achieved at high temperatures through the exponential dependence; this explicitly accounts for the high operating temperature of SOFCs. Similarly, an increment of performance is obtained through the reduction of activation barrier E_a of electron transfer, i.e. by using a catalyst. In figure 1.5, the effect of metal surface as catalyst on the kinetics of

hydrogen oxidation is reported in term of exchange current density whose effect on the activation polarization is shown as well. The palladium and platinum are effective catalysts for hydrogen oxidation as well as for the reduction of oxygen whose exchange current density is usually 5-6 order lower than that for hydrogen oxidation; in fact, the kinetics of reactions at cathode is much more sluggish, as a result of more complex reaction of oxygen which involves different steps in comparison with the relative simple oxidation of hydrogen.
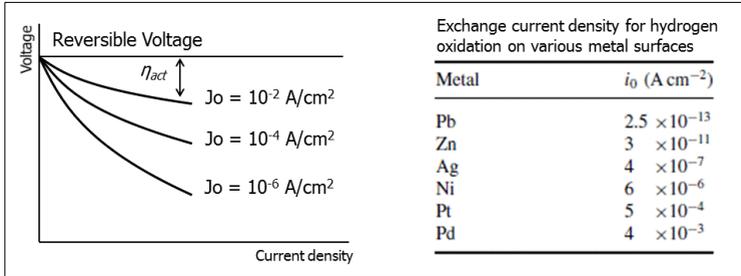
Figure 1.5. Representative behaviour of polarization curve as a function of exchange current density and table of exchange current density for different metal surface as catalyst for hydrogen oxidation at 25°C (Larminie, 2003).

Finally, the enhancement of j_o can be achieved by increasing the reaction surface corresponding to an increment of reactant concentration. In this term the reaction surface is increased for electrodes with rough surfaces, resulting in an extensive triple phase boundaries (TPB, reaction surface where gas reactants, electrolyte and electrode materials meet). For tubular SOFCs, an increment of reaction area and thus performance can be also achieved by increasing the surface per unit volume which corresponds to the miniaturization of the device, as attempted by micro-tubular SOFCs. Then, on the basis of aforementioned indications, the lower activation polarization of voltage curve (a) than curve (b) of figure 1.4 is related to a better performance of cell (a) than cell (b). For fuel cells of identical reaction surface and electrode materials, a lower operating temperature is responsible for the higher activation polarization of cell (b) than cell (a). On the other hand, for the same temperature and electrode materials, the lower voltage loss (and higher efficiency) of cell (a) can be attributed to the use of a catalyst. The ohmic polarization follows the Ohm's law and is given by:

$$\eta_{ohm} = j(ASR) \qquad (1.8)$$

where *ASR* is the area-specific resistance [Ωcm^2], that is the ohmic resistance multiplied by the area, thus *ASR* in an area-independent resistance term that allows a comparison of resistance properties among cells of different size. The area-specific resistance is therefore:

$$ASR = \frac{L}{\sigma} \tag{1.9}$$

where L is the thickness where current flows and σ the conductivity [$1/\Omega$cm] or [S/cm], a material property. For SOFCs, the main contribution to ASR is provided by the electrolyte which indeed fixes the operating temperature necessary to assure an adequate conductivity of the electrolyte, in most cases around 800°C. On the other hand, the contact resistance between the electrode/electrolyte and especially electrode/interconnect (current collector) can yield significant resistive contribution, especially for tubular-SOFCs characterized by longer current paths than planar SOFCs. Then, the lower slope of polarization curve (a) in figure 1.4, suggests a lower ASR and therefore a cell constituted by an electrolyte with higher ionic conductivity, or for the same material, a lower thickness of electrolyte; in both cases, the higher ohmic resistance of the cell with either thicker electrolyte or lower electrolyte conductivity (characterized by the polarization curve (b)) implies a lower cell efficiency and performance. These indications are well represented by figure 1.6, where the ionic conductivity for different electrolyte materials is shown along with a fixed value of 0.15 Ωcm^2 for ASR whose identifies, in this case, a performance parameter for the design of SOFCs. In fact, the maximum cell resistance, fixed as 0.15 Ωcm^2, is assured by the conventional $(ZrO_2)_{0.9}(Y_2O_3)_{0.1}$ electrolyte at 700°C, while for gadolinia-doped ceria $(Ce_{0.9}Gd_{0.1}O_{1.95})$ by much lower temperature, i.e. 500°C, for the same electrolyte thickness. Conversely, the same cell resistance at 500°C is achieved when $(ZrO_2)_{0.9}(Y_2O_3)_{0.1}$ electrolyte is ~1 μm thick, therefore one order lower than the thickness of $(Ce_{0.9}Gd_{0.1}O_{1.95})$ electrolyte. Nevertheless, several other considerations must be considered throughout the cell design; specifically about the electrolyte, the chemical and thermal stability with the electrode materials, as some of the many.
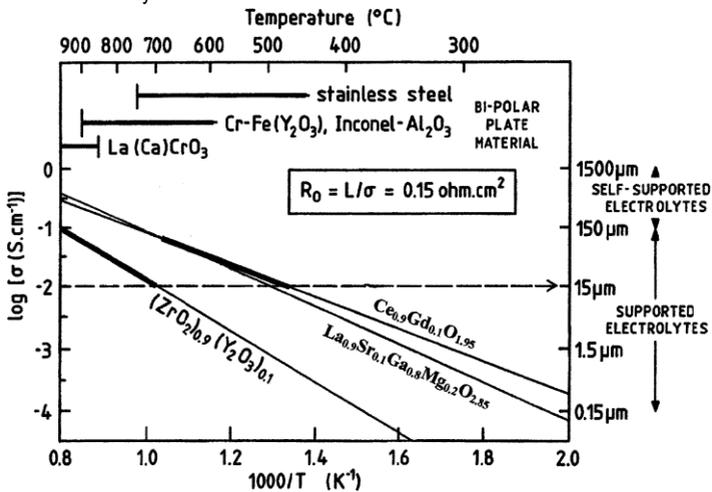
Figure 1.6. Ionic conductivity as a function of temperature for different electrolyte materials (Steele, 2001).

The concentration polarization arises at high current density as a result of depletion of reactants due to their high consume rate in comparison with their supply rate. In this condition, the low concentration of reactants causes a drop of performance which is controlled by the diffusion of reactants to the reaction surface (TPB). Then, the concentration polarization depends on the gas transport properties and therefore on the microstructure of the porous electrode. On the other hand, the design of fuel channel is also important, especially for tubular cells characterized by small diameter which can be characterized by significant pressure drop along the fuel channel with the effect of depletion of reactants. In fact, the pressure drop ΔP along fuel channel of length L is proportional to the fourth inverse power of the channel radius a, for a laminar flow of a Newtonian fluid according to Poiseuille equation (Barnes, 1989):

$$\Delta P = L \frac{8Q\eta}{\pi a^4} \tag{1.10}$$

where Q is the volume flow rate and η the gas viscosity which increases with temperature differently from the viscosity of a liquid. Nonetheless, the main contribution to the pressure drop is the length and especially the radius of fuel channel. Then, the concentration polarization can arise for those tubular cells characterized by either narrow and/or long fuel channel with the result of reduction of reactant concentration along the cell length, corresponding to a loss of active reaction surface and thus performance; micro-tubular SOFCs characterized by diameter lower than 1 mm can potentially be affected by concentration polarization. Consequently, the cell design, materials and microstructures of cell components have a significant effect on efficiency and performance of the fuel cell as here demonstrated by the contributions of main polarization losses.

1.2.3   Materials

The cell performance is influenced by the materials as well as cell design and manufacturing process which determine most of macro- and microstructural properties of the device and cell components (Othman, 2010; Li, 2014). In turn, the application and the environment where the cell operates, set limits on the selection of materials for the electrolyte, electrodes, interconnects and sealants. For instance, in combined gas turbine and fuel cell systems, the operating temperature is usually higher than 800°C, and demanding properties for sealants and interconnects are needed, where Cr- and Ni-alloys or doped $LaCrO_3$ perovskites are the only choice possible (figure 1.6) and generally result as the most expensive components throughout the fabrication of fuel cell stacks (Brett, 2008). Then, interest on lowering the operating temperature is actually conceived for residential cogeneration

applications, where the temperature range of 600-800°C supports the long-term stability of cell components and on the other hand, allows a less stringent selection for the sealants and interconnects. At the same time, lower temperatures implies a reduction of reaction kinetics and therefore high-performance materials for electrodes and especially electrolyte is needed in order to not compromise the cell performance; for instance at given temperature, the polarization curve (a) in figure 1.4 can reflect the behaviour of a fuel cell with electrolyte of higher ionic conductivity (lower ohmic polarization loss) than the cell characterized by the polarization curve (b). It is important to remark that, the choice of electrolyte material mainly determines the operating temperature of the fuel cell appointed for a given application. On the other hand, the materials control several aspects of manufacturing process due to the several interactions between cell components along the realization of a functional ceramic composite, like a SOFC. For instance, when co-sintering of the anode and electrolyte is adopted, the subsequent sintering of cathode must be carried out at temperatures lower than those of previous co-sintering, in order to maintain the integrity and stability of the composite; in this case, the sintering temperature of cathode must not exceed that of anode and electrolyte materials. As a result of this complex interplay between materials, application and fabrication, the following outline on SOFC materials will concern only the functional requirements and manufacturing constraints of NiO, YSZ (Y_2O_3-doped ZrO_2) and LSM ($La_{0.8}Sr_{0.2}MnO_{3-\delta}$) which are used here for the realization of (µt-SOFCs) and are also the current state of art materials for most of SOFCs due to their functionality, stability and cost issues with respect to the following general criteria (Ivers-Tiffée, 2001; Singhal, 2000):

- Adequate electrical conductivity; ionic conductivity for the electrolyte while ionic and electric (or mixed) conductivity for electrodes;
- Chemical and structural stability at high temperatures during cell fabrication and operation;
- Minimal reactivity and interaction between different cell components during cell fabrication and operation;
- Minimal differential thermal expansion between cell components during service (thermal cycling) and cell fabrication.

Intensive research on SOFCs is striving on the development of more competitive and high performance materials although, NiO, YSZ and LSM are the most preferred since forty years of experimental investigations, alternative materials were produced and outlined in comprehensive reviews (and references therein) for the anode (Jiang, 2004; Zhu, 2003; Goodenough, 2007), electrolyte (Kharton, 2004; Kharton, 1999 (1)) and cathodes (Kharton, 1999 (2); Sun, 2010; Jiang, 2008).

1.2.3.1 Anode

The principal function of anode is to provide the reaction sites for the electro-oxidation of the fuel and therefore it must be stable in reducing atmospheres at high temperatures, have sufficient catalytic activity and electrical conductivity. Then, it must have sufficient porosity to allow gas transport of fuel and reaction products while assure adequate mechanical strength, especially for the anode-supported SOFC configuration. During fabrication, structural compatibility of anode with other cell components, i.e. electrolyte and current collector, must be fulfilled in order to avoid cracking and delamination resulting from thermal expansion mismatch. Similarly, chemical compatibility with electrolyte prevents the formation of reaction products and phase transformations which can impair the structural integrity and the catalytic function of anode. The anode is commonly fabricated as NiO/YSZ composite which is converted into a Ni/YSZ cermet during the first service under reducing atmosphere. During service Ni/YSZ anode is stable under low oxygen partial pressure unless water concentration, either carried by humidified fuel or as reaction product of hydrogen oxidation, is maintained low at high temperatures, i.e. 950°C, in order to prevent the formation of volatile $Ni(OH)_2$ which can reduce the long-term stability of electrode (Primdhal, 1999; Zhu, 2003). The catalyst for the fuel oxidation is the metallic nickel, while the YSZ acts as supporting framework and also inhibits the coarsening of nickel particles which otherwise would reduce the reaction sites (TPB) and therefore the cell performance. The structural integrity of electrode is related to YSZ which assures an appropriate thermal expansion coefficient with the electrolyte layer; the thermal expansion coefficient is 13.3 and 10.5×10^{-6} K^{-1}, respectively for nickel and 8 mol%-YSZ, whereas for Ni/YSZ cermet (with 30 vol% Ni, 30 vol% porosity and 40 vol% YSZ) is $\sim 12.5 \times 10^{-6}$ K^{-1} (Goodenough, 2007; Minh, 1995). The YSZ has also the function to extend the reaction area from the electrolyte/anode interface throughout the electrode, where electrons and oxygen ions, provided by the percolating YSZ network, react with fuel realizing the electrochemical oxidation. The main drawback of Ni/YSZ is the low resistance to carbon deposition, derived from the oxidation of methane or other low hydrocarbons, which impair the structural integrity of electrode while eventual sulphur contamination has a detrimental but reversible effect (with temperature) on cell performance. Another limitation of Ni/YSZ cermet is the redox behaviour which can cause failure of anode due to the physical change (volume variation) accompanied by Ni to NiO transformation. A proper reduction cycle and tailoring of microstructure can improve the resistance to redox cycling and alleviate the probability of anode failure (Pihlatie, 2009). Improvement of carbon deposition and redox cycling resistance is partially achieved with modification of Ni/YSZ compositions where most of alternative anodes are nickel-based ones. This is related to the good structural and chemical compatibility with the YSZ electrolyte, the most widespread SOFC electrolyte, as well

as the good electrochemical performance and stability in reducing environment, which assure a firm technological paradigm for the development of SOFC anodes.

1.2.3.2   *Electrolyte*

The function of the electrolyte is to conduct the ions produced at one electrode to the other electrode so that the charge balance with electron flow and the electrical circuit of the fuel cell are realized (Minh, 1995). The electrolyte keeps the fuel and oxidant physically separated in order to realize the electrochemical reduction of oxygen at cathode and the electrochemical oxidation of fuel at anode and thus avoids the direct oxidation of fuel from which no current flow is possible to attain. Consequently, the electrolyte must have not only high ionic conductivity but also be gas tight and stable in both oxidant (cathode side) and reducing (anode side) atmospheres. The electrical conductivity increases with the material density and therefore as much dense the electrolyte as better the impermeable properties to gases and the ionic conductivity of the electrolyte with positive effect on cell performance (Chen, 2002). The degradation of cell performance can be also caused by electron flow across the electrolyte which must behave as pure ionic conductor with no electronic conductivity. This characteristic is demanding as several ceramic oxides show more or less partially electronic conductivity in either oxidant or reducing atmospheres at operating temperature of cell (Kharton, 2004). Concurrently, the phase stability of electrolyte in different atmosphere conditions is important as variation of conductivity properties is usually associated with phase transformations which are indeed, usually accompanied by dimensional change and hence particularly detrimental for the structural and interfacial stability of electrolyte with electrode(s). Similarly, formation of secondary phase due to solid state reactions between electrolyte and electrodes usually degrade the conductivity and long-term stability of electrolyte. Then, structural and chemical stability of electrolyte with both electrodes is required during cell fabrication and operation. The electrolyte most widely selected for SOFC applications is zirconia-based type and among these the 8 mol% Y_2O_3-doped ZrO_2 (8YSZ), which is thermodynamic stable in a wide range of temperatures and oxygen partial pressure, where its ionic-character conductivity remains stable in both electrode interfaces (Kharton, 2004). Indeed, the 8 mol% dopant concentration is realized to make stable the cubic phase of zirconia which is the most conductive among the tetragonal and monoclinic phases (Badwal, 1992). In particular, the highest conductivity is achieved at minimum concentration of dopants necessary to stabilize the cubic structure (Dixon, 1963). On the other hand during operation, degradation of ionic conductivity is observed as a result of structural modification due to one side to defect association (oxygen vacancies-cations) and in the other side to the phase transformation from cubic to tetragonal phase ((Kondoh, 1998 (2))). This phenomenon is known as aging and causes a reduction of ionic conductivity with time up to a plateau along cell operation (Linderoth, 2001; Hattori, 2004). The

degradation behaviour (aging) is reduced by a higher dopant concentration; 10 mol% YSZ does not show any variation of the initial conductivity value in 1000 h of operation, although this value at 1000°C, 0.125 S/cm, is lower than the conductivity 0.155 S/cm of as sintered 8 mol% YSZ (Hattori, 2004). On the other hand, diffusion of elements from electrodes is usually observed either during cell fabrication and operation; for instance nickel from the anode migrates to the electrolyte where it forms a solid solution up to ~1.5 mol% at high temperatures (Kuzjukevics, 1997 (2)). In this case, although the nickel enhances the stability of cubic structure of 8YSZ, the ionic conductivity is usually lower than that of pure 8YSZ (Park, 1999). In addition, the presence of Ni(O) into YSZ electrolyte seems to accelerate the aging phenomenon (Coors, 2009; Linderoth, 2001). Therefore, a protective interlayer between electrolyte and anode (as well as cathode) is sometimes adopted in order to reduce the diffusion of transition metals from electrodes and avoid or reduce eventual detrimental phase transformation, precipitation of secondary phases and segregation of impurities along grain boundary which reduce the cell performance and long-term stability (Zhu, 2003). The interlayer at electrolyte/anode interface can significantly improve the cell performance. For instance, an interlayer containing a catalytic material for hydrogen oxidation causes an increment of the power density by even a factor 4 in comparison with the same cell without interlayer (Gross, 2007; Jiang, 2004). In addition, the sintering conditions as temperature and atmosphere influence the segregation of impurities along grain boundary of YSZ electrolytes and therefore the ionic conductivity (Badwal, 1995). Then, control of sintering conditions as well as the availability of different sintering techniques are able to reduce the detrimental effects of segregation and phase partitioning of electrolyte, as well as to control the microstructure (grain size and density) with the result of high ionic conductivity at lower temperatures; typical values of ionic conductivity of 8YSZ fired with conventional sintering is in the range 0.13-0.18 S/cm at 1000°C, while ionic conductivity of 0.134 S/cm was achieved at 800°C for commercial 8YSZ powder sintered via spark plasma sintering (Rajeswari, 2011; Chen, 2002; Badwal, 1992). Alternative sintering strategy was applied during cell fabrication where the increment of cell performance was obtained through the optimization of co-sintering of electrolyte and anode (Ding, 2008; Dong, 2007). Further, a planar SOFC, constituted by Ni/YSZ anode cermet, 8YSZ electrolyte and LSM cathode, achieved 1.9 W/cm^2 at 800°C as a result of very thin electrolyte layer, i.e. 4-10 μm, produced by colloidal dispersion of commercial 8YSZ powder where stable performance was also observed throughout 700 h of operation without any aging or degradation phenomena (de Souza, 1997). These examples outline the possibility to obtain relevant ionic conductivity of electrolyte and cell performances in term not only of power density but also of long-term stability through the optimization of powder processing and sintering techniques where the aforementioned aging and degradation phenomena of 8YSZ can be relieved. Then, the relative high stability of ionic conduction over a wide range of oxygen partial pressure and temperature

makes YSZ material one of the most widespread electrolytes for SOFCs working at temperature ≥ 750°C, in addition to a relative low cost and large commercial availability of high-purity grade YSZ powders (Minh, 1995; Gibson, 1998).

1.2.3.3 Cathode

The cathode electrode provides the reaction sites for the electrochemical reduction of oxygen and therefore it must be stable in oxidizing atmospheres at high temperatures, have adequate catalytic activity and electrical conductivity. An appropriate porosity must provide gas transport of oxygen while the upper limit is set by electrical conductivity requirement rather mechanical strength one, for anode-supported SOFC configuration (Sun, 2010; Jiang, 2003). During cell fabrication and operation, structural and chemical compatibility with the electrolyte and interconnect must be fulfilled. The most commonly cathode used with YSZ electrolyte is LSM ($La_{0.8}Sr_{0.2}MnO_{3-\delta}$) whose thermal coefficient is 12.0-12.4 x 10^{-6} K^{-1}, close to 10.5 x 10^{-6} K^{-1} of 8YSZ (Jiang, 2008; Minh, 1993). A mixture of LSM and YSZ provides a better matching of thermal coefficient with the electrolyte but also an extended reaction area (TPB) for the multistep reactions of oxygen reduction (Sun, 2010). The YSZ framework of LSM/YSZ cathode extends the reaction zone from the electrolyte/electrode interface throughout the bulk of electrode with the effect of reducing the polarization losses, but also offers conduction path for oxygen ions toward the electrolyte, as LSM is predominantly an electronic conductor at operating conditions (Jiang, 2008); the best performance is found for LSM:YSZ in weight ratio 1:1, as here adopted for the functional cathode layer (Kenjo, 1992). Solid state reactions between LSM and YSZ occur at temperatures as high as 1200°C, where the formation of insulating phases, i.e. $La_2Zr_2O_7$ and $SrZrO_3$, at electrode/electrolyte interface is particularly detrimental for the cell performance. For this reason, the microstructure of LSM-based cathodes is adjusted to maximize TPB and the contact area with electrolyte through sintering processes whose temperature is between 1100 and 1180°C, at which the best cell performance can be achieved without the occurrence of insulating phases (Cronin, 2012; Soderberg, 2009; Ivers-Tiffée, 2001; Kenjo, 1992). An interesting strategy to improve the electrochemical performance of cathode is based on the "activation effect" which consists to set a cathodic polarization either to LSM or LMS/YSZ electrodes (Sun, 2010; McIntosh, 2004). Basically, the cathodic polarization promotes the formation and migration of oxygen vacancies within LSM and hence the electro-activity to oxygen reduction is enhanced. The formation of oxygen vacancies is accompanied by irreversible modifications of electrode microstructure; specifically, a broadening of active reaction area (TPB) is observed as a result of refinement of particles under cathodic polarization of LSM (Wang, 2004). Then, sintering of different LSM cathodes was carried out by using cathodic polarization with the result of microstructural refinement due to the removal of cation vacancy at A-sites, responsible for the grain growth and sintering behaviour of LSM; in this condition, cathodic polarization during sintering

suppresses grain growth with the consequence of enlargement of TPB in LSM/YSZ cathodes and thus improving the electrochemical reduction of oxygen (Jiang, 2005). An improvement of cathode performance can be also obtained by low additions of noble metals, i.e. Pd, Pt and Co, as effective catalysts for the oxygen reduction and therefore polarization losses are lowered with positive effect on cell performance (Erning, 1996; Yamahara, 2005). Then, the intrinsic properties of LSM and the possibility to improve the performance of LSM and LSM/YSZ through tailoring of structure (defect concentration) and microstructure, make of LSM an attractive cathode material even for operating temperature lower than 800°C when catalysts are employed (Babaei, 2011). Consequently, LSM-based electrodes can be an effective cathode for low temperature SOFCs, as alternative to higher performing but expensive perovskites as LSFC (($La_{0.8}Sr_{0.2})_{0.95}CoO_{3-\delta}$) cathodes.

1.2.4   Cell design

Solid oxide fuel cells are all solid-state devices which can be designed in different architectures, principally: tubular, planar and monolithic (Minh, 2004). The most promising architectures are the tubular and planar one which are characterized by the following features. The distinctive characteristic of the tubular design is that, practically no sealants are necessary, yet as secondary sealing with function exclusively of keeping the oxidant out from the fuel region (Minh, 1995). One of the principal challenges for SOFCs is the development of adequate sealant materials which is strictly indispensable for the planar design where the sealant functions not only as separator between oxidant and fuel but also as structural component which must assure mechanical integrity at high temperatures (Fergus, 2005). On the other hand, the current paths through the electrodes of the tubular cell are much longer of the "cross-plane" current paths characterizing the planar cell design. For this reason, the planar cells usually provide much higher power density (1-2 W/cm^2) than the tubular cells (0.1-1 W/cm^2), although these latter show incomparable thermal stability to rapid and repeating heating/cooling cycles without degradation of mechanical and electrochemical properties when tubular cells are in the millimeter scale (Bujalski, 2007; Du, 2008). The tubular and planar cells can be designed in different configuration: electrolyte-, cathode- and anode-supported configuration as shown in figure 1.7 (Minh, 2004).
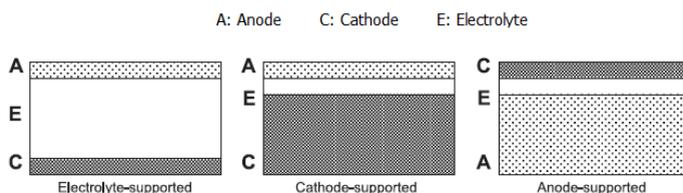

Figure 1.7. Cell configurations for tubular and planar design (Minh, 2004).

The cell configurations in figure 1.7 are based on the concept of "self-supporting support" where either the electrolyte, cathode or anode can also act as mechanical support and therefore must be sufficiently thick to assure structural integrity of the cell. A thick electrolyte and cathode layer causes respectively large ohmic and polarization resistances and in turn low cell performance. Instead, the anode-supported configuration offers higher performance due to the reduced thickness of cathode and especially electrolyte. Then, most of tubular and planar SOFCs are designed in the anode-supported configuration, although potential reoxidation must be controlled in order to avoid anode failures (Minh, 2004). An alternative strategy to overcome the use of sealant in planar cell design involves the development of single-chamber SOFCs for which a mixture of fuel and oxidant is used, precluding the need of fuel and oxidant manifolds as well as sealants. The performance of planar single-chamber SOFCs constituted by usual materials, i.e. NiO, YSZ and LSM, powered by a mixture of methane and air was lower than 10 mW/cm^2 at 700°C. This low power density is essentially related to the low concentration of gas mixture, in order to avoid the direct combustion, and to the low selectivity of electrodes for the reduction and oxidation reactions (Kuhn, 2008). These issues were tackled through the production of a planar cell with selective materials for the oxidation of methane where also catalyst, i.e. palladium, and an integrated Pt-current collector were adopted and very high gas flow was used in order to increase the kinetics of electrochemical reactions (see Eq. 1.7). Although significant performance improvement was achieved with comparable power density with most of micro-tubular SOFCS, the study was principally aimed to demonstrate the underlying mechanisms of selectivity and catalytic properties of electrodes materials (Buergler, 2005). Then, the development of single-chamber cell is mainly driven by theoretical research purposes while the research on high-temperature sealants for planar cells and strategy for improving the performance of tubular cells are of main concerns for the development and commercialization of SOFC systems.

1.2.5   Miniaturization of tubular SOFCs

The tubular architecture offers the significant advantage of a seal-less design for the realization of fuel cell stacks with concurrent benefit of avoiding adverse potential contaminations from sealant and its reactions with other cell components (Fergus, 2005). Moreover, the tubular design is characterized by thermal resistance especially for cells characterized by thin electrode (wall) thickness which result particularly resistant to high thermal shocks and rapid thermal cycling due to the low thermal mass. This entails the capacity of rapid start-up/turn off which is an essential feature to compete with batteries and fulfill the requirements for portable applications (Traversa, 2009). In fact, the miniaturization of tubular cells offers a compact design with potential rapid start-up and high power density as it increases with the inverse of

cell diameter (Kendall, 2010). On the other hand, the growing power demand of portable electronic devices, for which the current Li-ion battery technology is intrinsically limited by an opposite dependence of power density with size in comparison with tubular cells, pushes several research groups for the development of µt-SOFCs. The main hurdle of miniaturization to tackle is the realization of effective current collector for the inner diameter, i.e. fuel electrode for the anode-supported cells, in order to reduce the cell resistance derived from longer current paths along the tube and the contact resistance between anode and current collector (De la Torre García, 2013). Under this perspective, as the miniaturization of tubular cells present attractive as well as essential characteristics for the sector of mobile applications, the improvement of power density through an effective current collector is a fundamental issue to be addressed.

1.2.6   Fabrication techniques

Several techniques are available for the production of tubular and planar fuel cells from wet ceramic processing, i.e. slip casting, extrusion, EPD (electrophoretic deposition), to the more modern methods like PVD (physical vapour deposition) and EVD (electrochemical vapour deposition); a comparison of different methods is found in (Will, 2000; Minh, 1995). The planar cells are usually produced by tape-casting technique from which thin layer can be easily obtained and assembled to form the cell. Alternatively, thin electrolyte and cathode layers can be realized by spray coating on anode substrate fabricated by slip-casting. Screen-printing and brush painting are also alternative and economical techniques for producing thin electrolyte and cathode layer for anode-supported planar cells. Tubular cells are mainly produced by extrusion and also µt-SOFCs with diameters as low as 0.4 mm were realized (Suzuki, 2008). The subsequent layers can be deposited by spray deposition or dip coating technique. This latter deposition technique is commonly used for the fabrication of functional layered ceramics and it is characterized by simple equipment and easy processing (Zhang, 2009). In the present work, the µt-SOFCs are produced by dip coating technique which assures an effective route for the fabrication of micro-tubular cell with embedded current collector while other methods as extrusion and slip casting present hurdle to introduce the current collector during the cell fabrication. A possible alternative for the realization of anode-supported µt-SOFCs with integrated current collector can involve the electrophoretic deposition technique.

1.2.7   Aim of the thesis

The present work is mainly focused on the achievement and control of reliable ceramic process for the production of the µt-SOFCs with embedded current collector. Once, the micro-tubular cell was produced with well-defined geometry and

characteristics, the electrochemical performance of µt-SOFCs was analyzed by voltage versus current density plots with the aim to identify the effect of the embedded current collector on cell performance. Specifically, analytic relation of power density with configuration of current collector (turns per unit length) was established and provided indications for the improvement of cell performance. On the basis of these findings an alternative design of current collector was conceived with the aim to obtain µt-SOFCs with power density in the range of 1-2 W/cm^2 and therefore approaching the performance of the anode-supported planar cells.

Chapter II

Experimental Procedure

The experimental procedure and characterization of μt-SOFCs is outlined according to the processing steps concerned the fabrication of micro-tubular cells and finally the electrochemical testing as resumed by the scheme of figure 2.3.

2.1 Cell Supports

The μt-SOFCs with an embedded metallic coil are produced through dip coating technique. For this purpose, a support is necessary for producing the device in tubular shape as well for bearing the metallic coil. Specifically, the cell supports are constituted by a metallic coil wound around a rod, which is subsequently eliminated during heat treatment in order to create the fuel channel. The rod requires a careful choice for the demand of being pyrolisable during heat treatment releasing the minimum ash and impurities in unison with flexibility for the easy winding of metallic coil. For this peculiar feature, the rod is appointed here and forward as sacrificial inner core. In addition, the sacrificial inner core must be wetted by anode suspensions and avoids any adverse reaction with the metallic coil or any other cell components during its thermal elimination.

2.1.1   Current collector

The metallic coil acts as current collector for the anode electrode. For this aim, it should fulfill the requirements of high electrical conductivity, high melting point and high thermal oxidation resistance in order to withstand to severe sintering conditions like temperatures as high as 1400°C in air. In addition, the winding of the coil requires a malleable and mechanical resistant material as metals characterised by fcc structure. As a result, the first choice concerned a nickel wire (99.994%, Alfa Aesar, Germany) but the limited diameter (0.1 mm) along with the harshest sintering conditions, i.e. 1400°C, restricts its use due to the significant oxidation at higher temperatures. Then, the realization of electrical connections for the electrochemical testing was particular critical due to the brittleness of oxidized metallic coil. Therefore, an alternative material belonging to the same group of nickel was chosen; specifically palladium wire with diameter of 0.1 mm (99.99%, Alfa Aesar, Germany). In fact, palladium offers higher thermal resistance to oxidation and remained

malleable even after harsh heat treatment. The major drawback of palladium is the higher electrical resistivity compared to nickel one. The main properties of pure nickel and palladium are sum up in the table 2.1 (Sheckelford, 2001).

Table 2.1. Principal properties of pure nickel and palladium.

	Crystal structure	Magnetic order§	Density§ [g/cm³]	Electrical resistivity§ [μΩ·cm]	Melting point [°C]	Thermal expansion [μm/m·°C]
Ni	Fcc	Ferromagnetic	8.90	7.98	1453	13.3 *
Pd	Fcc	Paramagnetic	12.02	10.8	1552	11.8 **

§ Room temperature, * Temperature range: 20-100°C, ** Temperature: 20°C

2.1.2   Sacrificial inner core

The sacrificial inner core has the function to bear the coil. After this, it is dipped in the water-base suspensions and finally it is eliminated during heat treatment in order to leave the fuel channel. Therefore, the characteristics of the sacrificial inner core concern good mechanical strength, good wettability to polar liquids and being pyrolisable releasing the minimum ash and impurities as well as avoid any adverse reaction with other components of the cell. The material in point is a carbon-base composite similar that used in the previous work (De la Torre García, 2011). In particular, a flexible rod composed by epoxy resin and carbon fibers (PAN-derived) with a fiber volume fraction of 65% (Goodwinds, Washington, USA) with diameter of 0.5 and 0.7 mm were used. Thermal analysis of carbon-composite rod and current collector was performed according to heat treatment process.

2.1.3   Fabrication of cell supports

The fabrication of cell supports involved an in-house built electrical engine as described in (De la Torre García, 2011). Fundamentally, the metal wire was wound around a core (carbon-base rod) driven in motion by an electrical engine. The number of turns of the coil is regulated by the length of the wire between the rotating carbon-base rod and the metal wire reel. In addition, the coil was pulled along a carbon-base rod of 0.5 or 0.7 mm in diameter in order to obtain the exact number of turns per unit length. The cell supports have been produced with different diameter (0.5 and 0.7 mm) and with 5-6 as well as 11 turns per centimetre. The higher number of turns per centimetre allows a larger number of contact points within the anode whereas the coil with lower number of turns is a warrant for a higher permeability of the anode electrode. The performance of the cell scales with the fuel channel diameter and it is expected to be also influenced by the characteristics of the current collectors, as metal nature and turns per unit length. As a result, the features of cell

supports have the purpose to highlight the effect of the current collector and the inner diameter on the cell performance.

2.1.4 Thermal analysis

Thermal behaviour of the cell support components, i.e. current collector and sacrificial inner core, was analysed by thermogravimetric analysis (TGA) and differential thermal analysis (DTA). The green half-cells are subjected to co-sintering of anode and electrolyte layers and are composed by the cell support components but also organic compounds such as dispersant, binder and plasticer as well as carbon-base one, i.e. sacrificial inner core and graphite flakes (pore former). The organic compounds are eliminated in a temperature range between 200 and 400°C whereas the carbon-base ones between 600 and 800°C in oxidative atmosphere. All these coumpounds must be eliminated during the heat treatment before the sintering step. According to the thermal degradation of several compounds, in addition to TGA, heat treatments of half-cells in muffle furnace were performed in order to set properly the best conditions for a mild elimination of such components. In particular, the thermal degradation of sacrificial inner core resulted fundamental and crucial for obtaining crack-free half-cells after co-sintering.

2.1.4.1 Current collector

Nickel and palladium wires were analysed by TGA in static air up to 1300°C with 5°C/min as heating rate. Additionaly nickel and palladium coils were treated in muffle furnace at 5°C/min up to 1400°C with a dwell of 4 hours. Table 2.2 reports thermal analysis conditions for TGA and furnace treatments. Optical micrographs were also taken in order to clarify the different response on the thermal oxidation of pure nickel and palladium.

Table 2.2. Thermal analysis conditions for the current collector.

	Temperature range [°C]	Heating rate [°C/min]	Dwell (T x holding time)	Atmosphere
TGA	RT-1300	5	-	Static air
Muffle furnace	RT-1400	5	1400x4h	Static air

2.1.4.2 Sacrificial inner core

The elimination of the sacrificial inner core results crucial for obtaining crack-free samples after co-sintering. TGA along with DTA and muffle furnace treatment were carried out and their conditions are reported in table 2.3. In both cases, the composite rod was dried in oven at 110°C for a few hours before thermal analysis.

The composite rod subjected to TGA was cutted in tiny parts whereas muffle treatment concerned rods 5 cm long. The muffle treatment was devised as preliminary treatment of composite rod before cell support fabrication and dip coating step. In fact, after co-sintering all half-cells fabricated with "as-received" composite rod exhibited cracks and irregular shape. Thermal degration of the matrix component of the sacrificial inner core produced large volume of gases that caused cracks and bending of half-cells. Therefore, the muffle treatment was set in order to eliminate a proper amount of matrix, i.e. epoxy resin, to avoid cracking of half-cells. On the other hand, an excessive burn-out of epoxy resin caused frayed parts of composite rod adversely affecting the anode dip coating process. In this case, the surface of cell supports was irregular and the hydrophobic component, i.e. carbon fibers, lowers the wettability of cell supports to anode suspensions. Therefore, the proper amount of epoxy component eliminated during the preliminary treatment in muffle was fixed between 16 to 18 wt% for the rod with 0.5 mm diameter. This removed amount of epoxy resin prevents any cracking problems of sintered half-cells without compromising the integrity and wettability of cell supports. In fact, 20 wt% mass loss of the sacrificial inner core was deleterious for the dip coating process whereas 14 wt% mass loss was insufficient to avoid any cracking and warp of samples.

Table 2.3. Thermal analysis conditions for the sacrificial inner core.

	Temperature range [°C]	Heating rate [°C/min]	Dwell (T x holding time)	Atmosphere
TGA-DTA	RT-1000	2.5	-	Static air
TGA-DTA	RT-1000	5	-	Static air
TGA-DTA	RT-770	5	400x1h	Static air
Muffle furnace	RT-375	2.5	375x45'	Static air

2.1.4.3   Pore former

The role of pore former is to assure a minimum volume of porosity for the transport properties of anode. Here, the pore former is graphite powder in form of flakes (Flake, 7-10 µm, Alfa Aesar, Germany). Differently from the sacrificial inner core, the elimination of graphite is not damaging under correct conditions of burn-out although some attentions are necessary. Carbon impurities reacting with oxygen form CO and CO_2 gases, which are insoluble in most of ceramics (Rahaman, 2003). These gases when generated at high rates can produce high pressure build-up and then voids and cracks, which are detrimental for the fabrication of final product. In the current analysis, heat treatment conditions are investigated in order to ascertain the complete burn-out of graphite under oxidative atmosphere avoiding any adverse effects on the fired body. The conditions of graphite burn-out are reported in table 2.4.

Table 2.4. Thermal analysis conditions for the pore former.

	Temperature range [°C]	Heating rate [°C/min]	Dwell (T x holding time)	Atmosphere
TGA	RT-1000	5	-	Static air
TGA	RT-800	5	800x2h	Static air

It is also important to note that all carbon-base materials so far investigated as well as the next processing aids, i.e. dispersant, binder and plasticizer, are removed at high temperatures in oxidative atmosphere during the fabrication of μt-SOFCs. In these conditions, it is prevented the reaction between metallic nickel (of current collector) and CO gas at 150°C forming the $NiCO_4$ compound which is very volatile at room temperature due to its high vapour tension and whose vapours are toxic and lethal for humans (Armit, 1907; Voegtlin, 1947).

2.2 Ceramic Processing

In the processing of ceramic powders, the characteristics of powders along with the forming process establish the properties of the final product. In fact, chemical composition of starting materials identifies the intrinsic properties of the system such as melting point, elastic modulus, magnetic order and so on which are governed by the structure of material at atomic scale. The intrinsic properties are weakly affected by the modification of the microstructure (Rahaman, 2003). On the other hand, relevant properties from an engineering point of view are dependent on the microstructure like mechanical properties, electrical and thermal conductivity, etc. and are determined by the ceramic processing as illustrated in figure 2.1.
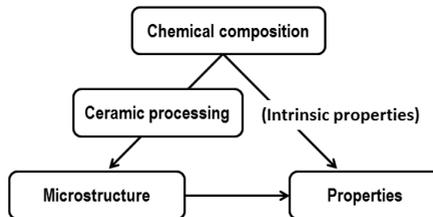
Figure 2.1. Properties of the ceramic product as a fuction of chemical composition of the starting materials, ceramic processing and microstructure.

The control and reliability of the ceramic process has the objective to pursue a specific microstructure and thus demanding properties of the final product but also allows adjusting the conditions at each step of fabrication process in order to achieve a reliable process (Boschi, 1990). In particular, the powder characteristics affect its

consolidation behaviour during the forming process and the resulting microstructure of green compact, which in turn influences the sintering response as shown in figure 2.2.
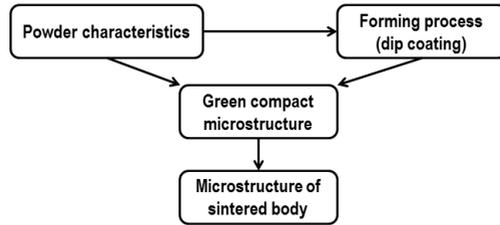
Figure 2.2. Relantionship between powder characteristics, forming process and microstructure of green and sintered body.

It is desirable a sintered product with homogeneous microstructure at a certain scale and small grain size. Certainly, a homogeneous and fine grain microstructure implies a homogeneous microstructure of green compact but the opposite is not always guaranteed. In fact, even a good green compact microstructure after forming can decline to a coarse and inhomogeneous microstructure due to abnormal grain growth resulting for instance from either improper forming process or sintering schedule. For this reason, the control of each single stage of ceramic processing from the starting materials to the sintering step is important and fundamental to obtain a final product with specific microstructure and properties. Under this perspective, the fabrication process of the μt-SOFCs has been analysed according to the scheme of figure 2.2. The study points out the features of the green compact as well as sintered body along with the conditions of each processing step with the objective to achieve high reliability of the fabrication process.

2.2.1 Processing of micro-tubular solid oxide fuel cells

The production of the μt-SOFCs is illustrated in figure 2.3. Anode slurries were prepared and deposed by dip coating on the cell supports previously fabricated and heat treated. This step requires from 4 to 5 coatings or dips and each one is followed by a drying step before the following dip. The electrolyte coating covers the anode substrate and after drying, the green half-cell is ready for the co-sintering of anode and electrolyte coatings on the cell support. Cathode layers composed by the functional layers of LSM/YSZ and current collector layer LSM, are deposed by inks. Even in this case, the drying of solvent is required before the sintering of cathode layers. From this last step, μt-SOFCs are produced and available for the electrochemical testing. The wet colloidal coating as dip coating requires the

preparation of stable suspensions for the anode and electrolyte layers. For this purpose, the optimization of anode and electrolyte slurries has been performed by rheological analysis with particular emphasis on the concentration of different slurry
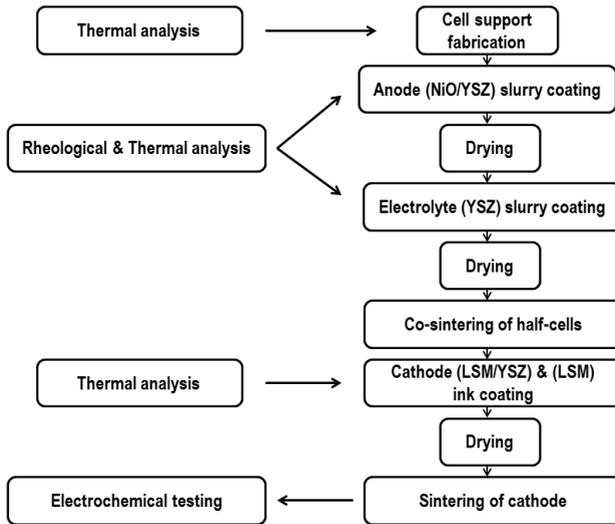
Figure 2.3. Flow chart of the ceramic processing of µt-SOFCs.

additives, solid loading as well as external variables such as temperature and humidity in order to obtain coating layers with specific microstructure and properties. Cathode layers derived from organic solvent, i.e. terpineol, did not required rheological investigation but only thermal analysis in order to highlight the response of coating upon different sintering conditions as for the anode and electrolyte layers. The experimental procedure involves the analysis of each processing step according to the flow chart of figure 2.3. The results of different analyses, i.e. rheological and thermal one, of each component as anode, electrolyte and cathode will be dealt in the same component section following the procedure of cell fabrication.

2.2.1.1   *Powders*

The anode electrode is composed by a mixture of oxide powder, i.e. NiO and YSZ which converts into Ni/YSZ cermet when fuel is introduced during service. Specifically, NiO (J.T. Baker Inc., USA) and 8 mol% Y_2O_3-ZrO_2 (TZ-8YS, Tosoh, Japan) powders were used for the anode substrate and the porosity was increased by adding graphite powder (Flake, 7-10 µm, Alfa Aesar, Germany) as pore former.

31

The electrolyte is constituted by a single phase of YSZ (TZ-8YS, Tosoh, Japan) whereas the cathode involves LSM, i.e. $La_{0.8}Sr_{0.2}MnO_{3-\delta}$ (LSM, Fuel Cell Materials, USA), for the current collector layer and a mixture of LSM and YSZ for the functional cathode layer. The specific surface area values for NiO, YSZ, graphite and LMS powders are 3.5, 6, 12 and 5.6 m^2/g respectively determined by means of nitrogen adsorption (BET) method and supplier specifications (De la Torre García, 2011). The powders as-received were also investigated by scanning electron microscope (JEOL, JSM 5500, Japan) after dispersion without any additives. Specifically, powder suspensions were prepared in deionized water covering 4 wt% and underwent ball mixing in 250 ml bottle for 2 h with zirconia balls as thumbling media for 30% in volume in a high energy rotatory mill (Turbula T2F, Bachofen, Switzerland). After milling step, suspensions were placed in a ultrasonic bath for 15' and some drops of them deposited over sample holder and drying overnight before ion sputtering for SEM investigation. Particular attention involves the pore former powder and therefore a comparison between graphite after milling and as-received is also supplied.

2.2.1.2   *Additives and preparation of suspensions and inks*

The preparation of suspensions requires additives such as dispersant, binder and plasticizer along with powders and solvent. The function of these additives is to achieve good dispersion and stability of suspensions as well as to guarantee green strength to compacts and in this specific case, also good adhesion of electrolyte coating on anode substrate. In fact, anode and electrolyte slurries are water-base suspensions and therefore characterized by high surface tension. The addition of binder and plasticizer lowers the surface tension of the slurry and in turn, the wettability of water-base suspensions on substrate is improved (Moreno, 1992). In contrast, the wettability of cathode inks based on organic solvent, i.e. terpineol, is good even upon sintered ceramics like half-cells due to lower values of surface tension typically of organic solvents (Reed, 1995). The order of additive addition is very important and respects the following two steps. In the first one, powder, solvent and dispersant are mixed obtaining a homogeneous mixture. After this, binder and plasticizer are added to the mixture and a further mixing is need for the complete preparation of suspension. These steps are very important and particular care is necessary for avoiding any adverse effects as foaming, flocculation, creaming or sedimentation of suspension constituents. The preparation of anode and electrolyte suspensions follows the methodology reported in (De la Torre García, 2006). This procedure involves the filling of the jar, i.e. polypropylene bottle of 250 ml, with thumbling media (zirconia balls with 0.5 cm in diameter) for 30% of jar volume followed by the addition of powders, deionized water and finally the dispersant. The jar is directly put in a high energy rotatory mill (Turbula T2F, Bachofen, Switzerland)

for 2 hours. The suspension after milling is mixed for 15 to 30' by magnetic stirrer. The subsequent addition of organic additives involves the binder that is dropwise added and maintained under gently stirring for 30'. Similarly, the plasticizer is added to the slurry that is further stirred for 1 h before use it. Additional information about suspension preparation are reported in table 2.5 for seek of completeness as well as to supply basic hints for further improvement of milling step here not subjected to investigation; interesting insigths on alternative routes for the preparation of suspensions are described in (Rödel, 2012; Wang, 2006).

Table 2.5. Information for the preparation of the anode and electrolyte suspensions.

Slurry system	Solid loading [wt%]	Pwd wt [g] / jar vol [ml]	Slurry wt [g] / jar vol [ml]	Pwd wt [g] / thumbling media wt [g]
	80	0.46	0.58	0.35
Anode	83	0.48	0.58	0.36
	85	0.49	0.58	0.38
Electrolyte/Anode	70	0.40	0.57	0.30

The dispersant adopted here is an anionic polyelectrolyte, i.e. ammonium polyacrylate, in water solution with pale yellow appearance (Darvan 821A, R.T. Vanderbilt Company Inc., USA). The adsorption mechanism of dispersant molecules on particle surface is far complex due to a multitudine of interactions among slurry components even in the easiest systems. Moreover, parameter as pH, ionic strength, solid loading as well as temperature can strongly affect the adsorption other than the concentration and molecular weight of dispersant itself (Cesarano III and Aksay, 1988; Guo 1998; Wang 2007). Here, just a concise outline of adsorption of anionic polyacrylate is given with reference to water-base slurries of oxide powders so as to highltight the section on rheological analysis which is correlated. In fact, the optimum amount of dispersant is correlated to the minimum viscosity of suspension (Shojai, 2000). The adsorption of dispersant depends on the net charge of surface particles and on the fraction and charge of dissociated groups of polyelectrolyte that in this case are carboxylic groups COO^- (balanced by NH_4^+ ions). Both charge of particle surfaces and dissociated groups of polyelectrolyte are determined by solvent conditions as pH and ionic strength. At low pH, lower than the isoelectric point (IEP) of powders, the net surface charge of oxide powders is positive and in this case COO^- groups experience strong affinity to those positive charges sites due to electrostatic interactions. At high pH, greater than IEP, the net surface charge of particles is negative as well as COO^- groups. Even in this condition, dispersant molecules adsorb onto particle surface as demonstrated in several studies (Cesarano III, 1988; Somasundaran 1997; Tang 1999). In fact, at every pH, the surface of oxide powders is characterized by negative, neutral and positive charges

with a predominant net charge for a specific pH (Cesarano III and Aksay, 1988). Nonetheless, the adsorption of polyelectrolyte onto particle surfaces changes from acid to basic pH through the conformation of dispersant molecules that is related to their dissociation degree of COO⁻ groups. At low pH, the conformation of dispersant molecules is compact due to low dissociation degree whereas at high pH the molecules are expanded and more rigid as a consequence of the increasing fraction of charge COO⁻ groups. This ensues different adsorption saturation limits and in turn diverse coverage of particle surface on the part of polyectrolyte molecules corresponding to different stability mechanisms of suspensions (Cesarano III, 1988). Under this scenario, the stability of suspensions seems an arduous task especially considering the different nature of powders such as NiO and YSZ (IEP nearly 10 and 7 for NiO and YSZ respectively) constituting the anode slurry along with graphite particles (Lewis, 2000). For this reason, the methodology here adopted for the preparation of suspensions has the objective to limit preferential adsorption of dispersant on different powders by adding the polyelectrolyte after powders and solvent. Moreover, conditions in table 2.5 assure repeatability of suspensions preparation which is crucial for the constancy of rheological analysis that is intended for the determination of the optimum dispersant concentration for obtaining stable suspensions. The identification of the optimum dispersant concentration is also essential for the addition of other additves such as binder and plasticizer because of the possible interaction between dispersant and these additives. The effect of this interaction does change the rheology of suspensions. It was observed at given binder concentration, an increase on suspension viscosity when the dispersant concentration exceeds the optimum value (Khan, 2000). In this condition, higher and higher concentration of dispersant corresponds to higher and higher viscosity of suspension because of the excess of dispersant and/or binder enhances the flocculation of particles due to compression of double layer (screening effect) or by depletation mechanism. The addition of such additives must be careful and it will be described and investigated in the section regarding rheological analysis. Above the effect of binder addition on suspension viscosity, other aspects of additives like insensitivity to moisture variation and clean burn-out must be considered. In table 2.6, physical and chemical properties of additives used for anode and electrolyte slurries.

Table 2.6. Physical and chemical properties of suspensions additives.

	Chemical nature	Function	Solid [wt%]	Density [g/cm³]‡	GTT [°C]#	pH‡	Ash§ [wt%]
Darvan 821A	Ammonium polyacylate solution	Dispersant	40	1.16-1.19	-	7.0-7.5	-
B-1014	Acrylic polymer	Binder	45	1.05	22	9.0-9.8	0.45

| | emulsion | | | | | | |
| B-1000 | Acrylic polymer emulsion | Plasticizer | 55 | 1.03 | -26 | 2.6-3.4 | 0.40 |

‡ at 25°, § Residue after firing in air, # Glass transition temperature

Both binder (Duramax B-1014, Rohm and Haas Co., France) and plasticizer (Duramax B-1000, Rohm and Haas Co., France) are in the form of emulsions and appear as milky liquid. The emulsion or latex is a dispersion of polymer in water and results in an ease of use compared with other binders as PVA (polyvinylalcohols) that need dissolution in water before use. In addition, the intrinsic nature of polymers to be insoluble to water and not plasticized by it, render emulsions insentitive to moisture (Carlström, 1994). For this reason, a plasticizer is usually introduced to the suspension in order to decrease the glass transition temperature of additive system in order to obtain more flexible and handy green compacts. In addition, latex with acrylic polymer added to alumina suspensions seems to maintain its pH regardless the suspension pH (Carlström, 1994). It was also observed a very low foaming of acrylic emulsions when used in analogous alumina suspensions (Tang, 1996). Another significant benefit for the processing of advanced ceramics is the low residue of acrylic additives and in particular of the ammonium derived ones which limits any adverse sodium residue of similar commercial products as sodium polyacrylic emulsions. The preparation of iks involves an organic solvent differently from water-base slurries. The solvent in point is α-terpineol (Fuel Cell Materials, USA) that is also named as terpene alcohol due to its hydroxyl functional group. A part of its chemical definition, terpineol behaves like an organic solvent and it is characterized by negligilble solubility in water, low dieletric constant and surface tension as well as flash point as reported in table 2.7.

Table 2.7. Properties of α-Terpineol and water solvent.

	Function	Density [g/cm³]‡	Surface tension [mN/m] ‡	Dielectric constant	Flash point [°C]
α-Terpineol	Solvent, dispersant and binder	~0.93* (>1)#	33*	2.8**	88#
Water	Solvent	1.0§	73§	80§	-

‡ at 20°C, * from: www.lookchem.com, ** from: www.rafoeg.de, # fuel cell materials MSDS, § (Reed, 1995)

Terpineol is used as dispersant in slurries based on organic solvents for the preparation of green ceramic tapes as well as solvent for dispersing nickel powders (Maiti, 2002; Tseng 2003). In the present work, terpineol is used as dispersant, solvent and binder component for the preparation of cathode inks. For this purpose a polypropylene jar with zirconia balls is fill with terpineol and LSM or LSM/YSZ

powders were gradually poured until achieving 20 wt% of solid loading for both cathode inks and milled for 2 hours. Differently from water-base suspensions, inks are stable for long time if solvent evaporation is prevented. Another difference arises from the mechanisms of stabilization. In particular, water-base slurries dispersed with polyectrolyte are stabilized by electrostatic repulsion or a combination of electrostatic and steric (electrosteric) stabilization. In this latter case, the steric stabilization is related to the conformation of dispersant molecules adsorbed onto particle surface and depends on pH. For instance, at low pH ammonium polyacylate polyelectrolyte is characterized by compact conformation of polymer chains which adsorb in a dense and thin layer. At high pH, fewer chains are necessary to form the adsorbed layer due to much charged part of polymer chains stretched out towards the solvent (Rahaman, 2003). In this latter case, stabilization is most electrosteric. Instead, when an organic solvent is used the stabilization is believed to be mainly steric type. In fact, low dielectric constant of solvent is associated to low dissociation degree of ionic species and consequently electrostatic repulsion should be absent. On the other hand, charged species can be produced by alternative mechanisms than dissociation, i.e. acid-base interactions. In this case, it was observed positive zeta potentials for inorganic particles with basic sites in acidic organic solvents whereas negative zeta potentials are experienced by particles with acidic sites in basic organic solvents (Pugh, 1994). Terpineol has a very low solubility in water and whether acid-base interactions can occur throughout their hydroxyl groups, electrostatic repulsion is expected to be minimal. For this reason, anode and electrolyte slurries are stabilized by electrostatic or electrosteric mechanism while cathodes ink are stabilized by steric one.

2.3 Anode

Accurate rheological analysis has concerned the realization of stable suspensions with optimal amount of dispersant. Then, the effect of solid loading, additives and temperature is studied for the stabilized slurries in order to optimize the wet colloidal process of dip coating. Rheological models were used to describe the flow behaviour of anode slurries elucidating the underlying mechanisms of particle interactions and on the other hand, to estimate flow properties of slurries as a function of solid loading and temperature. Thermal analysis on green compacts prepared from stabilized slurries has identified the effects of drying, binder burn-out and sintering conditions on fired microstructures. The role of pore former on the porosity of sintered compacts is investigated where the pore evolution throughout sintering process is accompanied by models which provide porosity values in agreement with experimental results. Finally, the reduction process of anode has pointed out the function of pore structure where an interconned porosity has assured effective gas

36

permeation during reduction of NiO/YSZ electrode even for porosity of 12-13% due to a uniform distribution of pores with appropriate size, shape and interconnectivity. A porosity of 30-33% was estimated for the Ni/YSZ cermet.

2.3.1 Rheological analysis

Rheological investigation is performed by cone and plate rheometer (Anton Paar, MCR-301, Austria). The flow of the cone and plate configuration assures constant shear rate throughout the sample along with the control of temperature, i.e. ± 0.01°C, ensuring consistency of measurements. In addition, variation of solid loading of high concentrated suspensions was controlled by accurate weighing of powders, additives and solvent throughout the preparation of slurries in order to attain reliable results (Barnes, 1989). Rheological measurements were performed by hysteresis technique consisting in increasing and decreasing shear ramps between zero and a maximum value (Mewis, 2009). This method consents to investigate time effects such as thixotropy and involves an ascending ramp from 0.85 to 70 s^{-1}, a dwell at maximum shear rate for 50 s followed by a descending ramp from 70 to 0.85 s^{-1} at temperature of 23°C unless specificated otherwise.

2.3.1.1 Screening analysis

The effect of dispersant involves screening suspensions characterized by 70 wt% solid loading. The dispersant is added on dry weight of powders (dwb%) and its optimum concentration was selected to correspond to the lowest viscosity value evaluated at 0.85 s^{-1} shear rate.

Table 2.8. Procedure for the preparation of screening suspension.

		Graphite [g]	NiO [g]	YSZ [g]	H2O [g] 1.00 (g/cm3)	Darvan [g] 1.16 (g/cm3)	Darvan [g] 1.19 (g/cm3)	Darvan [g] average
					Screening anode suspension (70 wt%)			
Theoretical values		6,307	69,505	50,331	54,055	0,88299	0,90582	0,894404
Actual values		6,31	69,59	50,34	54,20	Darvan 1st weighing		0,9992-
						Darvan 2st weighing		0,1285
						Darvan, actual weight		0,8707

	Theor. values	Actual values	Rel. err. [%]
Powder [g]	126,14	126,24	0,08
Suspension [g]	180,20	180,44	0,13
Solid loading [wt%]	70,00	69,96	-0,06

Darvan	Actual [dwb%]	0,6897
	Pristine [dwb%]	0,6150
	Actual/pristine [%]	12,15

37

The preparation of screening suspensions follows the procedure described in section 2.2.1.2 and table 2.8 where the pore former covers with 5 wt% the total solid loading while the remaining solid content interests NiO and YSZ in 58:42 weight ratio. The same procedure and powder blend ratio involve the preparation of the following anode slurries where only the solid loading varies. The costituents, i.e. powders as well as solvent and dispersant, are added by weigth and the actual values were annotated in order to calculate the relative errors in relation to theoretical values. The weighing of powders involves a scale with a sensitivity of $\pm$ 0.01 g, whereas a precision balance (Gibertini, Italy) with sensitivity of $\pm$ 0.0001 g was used for the weigth of dispersant. This is justified by the experimental evidence of significant influence on the rheological behaviour of slurries by the solid loading and particularly by the dispersant amount. Moreover, viscosity measurements are much more sensitive to small changes in the dispersant concentration than electrokinetic measurements (Pagnoux, 1998). Under this perspective, dispersant was weighed before and after its pouring to the jar in order to account for the residual dispersant onto the surfaces of graduated cylinder used for pouring. In the example reported in table 2.8, just 0.8707 g of dispersant was effectively poured to the mixture rather the 0.9992 g corresponding to a residue of dispersant of around 13%. For this reason, viscosity results are based on the actual dispersant value on dry powder base, i.e. 0.6897 dwb%, derived from the actual dispersant amount, i.e. 0.8707 g and the actual value of powder weigth corresponding to 126.24 g. The ratio between the actual concentration of dispersant and the pristine one is reported in table 2.9 for the screening suspensions where the example of table 2.8 corresponds to nearly +12% compared to 0.6150 dwb% estimated by sedimentation test (De la Torre García, 2011).

Table 2.9. Dispersant concentration and taxonomy of screening suspensions.

Dispersant conc. [dwb%]	0.615	0.63	0.69	0.76	0.91	0.96	1.02	1.04	1.20
Taxonomy	pristine	+2.3	+12	+23	+45	+57	+66	+69	+95

As last observation, the solid loading error reported in table 2.8 is lower than 0.1% corresponding to very slight variation in solid loading, i.e. 69.96 wt%. The weighing of powders was carefully carried out keeping relative errors lower than 0.1% in order to achieve solid loading of screening suspensions between 69.96 and 69.99 wt%. The meticulousness of suspension preparation is aimed to obtain reliable results for the analysis of the effect of dispersant on rhelogical and stability behaviour of suspensions as well as to limit the replica of measurements. In addition, hysteresis effect of the flow curves and the solvent evaporation of screening slurries have

supplied some interesting insights on the role of dispersant on the stability of suspensions.

2.3.1.2   Anode suspensions

The preparation and rheological characterization of the current suspensions follows the previous procedure for screening suspensions with particular care on the dispersant addition, which is strictly close to the optimal value. Here, the anode slurries were prepared at solid loading of 80, 83 and 85 wt% and the optimal dispersant concentration, i.e. 1.04 dwb% within ± 1.3% of error. The effect of solid loading on the slurry flow was investigated according to Casson, power-law, Krieger-Dougherty and Flatt models in order to characterize the rheological behaviour in term of yield stress, power-law index, viscosity, intrinsic viscosity and maximum solid concentration A. This latter parameter represents the maximum solid concentration at which the system ceases to flow and it is calculated from the following equation when the relative viscosity is first experimentally determined (Liu, 1999):

$$\eta_r = \left(1 - \frac{\phi}{A}\right)^{-2}$$ (2.1)

Where η_r is the relative viscosity and ø the volume fraction of particles. In order to remove possible effects of particle-particle interactions on the slurry viscosity, the relative viscosity is estimated extrapolating the shear rate to infinity through the plot log(η_r) versus (shear rate)$^{-1/2}$ according to Doroszkowski method (Liu, 1999; Doroszkowski, 1968). It is observed for the current anode slurries, A varying with solid loading in contrast to monodisperse and polydisperse systems characterized by constant A (Liu, 2000; Servais, 2002). The maximum solid concentration depends on particle-size distribution (PSD) of powders and then the variation of A is related to PSD change of anode slurries (Barnes, 1989). A size reduction of the as-received graphite powder is expected due to its brittle nature; specifically, higher extent of particle-particle interactions with solid loading is expected, i.e. during milling, resulting in a change of the PSD of graphite. Then, the size variation of graphite allows different particle arrangements characterized by variable A value with solid loading. This particular behaviour of A is related to the variation of PSD of anode system and provides interesting effects on the packing density ø/A, and in turn on the flow behaviour of slurries. For instance, it is observed constant relative viscosity in spite of the increment of solid concentration between 0.399 and 0.430 v/v (80 and 82 wt%), supporting that an appropriate mixture of well dispersed small and large particles ensures high packing density which controls the slurry viscosity according to the Farris effect (Barnes, 1989; Larson, 1999). In addition, experimental yield stress values are well fitted by Flatt model within experimental error of ± 1.5%. The

main inputs of Flatt model is the percolation threshold Φ_0 and A. The percolation threshold describes a critical solid concentration, Φ_0, where a percolating network of undispersed particles is formed and a certain shear stress, τ_Y, breaks down this continuos structure and induces the flow of slurry; in other words, it defines the changeover from Newtonian to shear thinning behaviour of a slurry system by identifying the setting of yield stress. Here, the predicted yield stress values by Flatt model are consistent with the experimental ones in condition far from isoelectric point (IEP) where Φ_0 is different from zero. This confirms the validity of Flatt model even for systems far from IEP condition for which the model was first and exclusively verified. On the other hand, Flatt model confirms the variable value of A for the anode slurries composed by graphite particles. Moreover, the assumption of binary hard-sphere system conceives aggregation processes extending the understanding of rheological behaviour to slurry structure. In fact, aggregation processes as the clustering of larger particles, i.e. graphite ones, is predicted on the basis of binary hard-sphere system and also supported by rheological analysis. Finally, the effect of slurry structure i.e. dispersed or flocculated, and solid loading on the sintered microstructures are highlighted by micrographs of fired samples derived from 80, 83 and 85 wt% slurries. The fired sample prepared from 80 wt% slurry shows fine microstructure with uniform open porosity resulting as good candidate for the anode electrode since ensures good mechanical, electrical and transport properties.

2.3.1.3   *Anode suspensions for dip coating*

The anode suspensions for dip coating differ from the previous anode suspensions for the addition of additives, i.e. binder and plasticizer, after the dispersant addition. The function of these additives is to achieve good dispersion and stability of suspensions as well as to guarantee green strength to compacts and also good adhesion of electrolyte coating on anode substrate necessary for dip coating process. Table 2.10 sums up the experimental procedure and its goals for the anode slurries so far seen.

Table 2.10. Description of experimental procedure of rheological analysis for anode slurries.

	Experimental Procedure	**Description**
Screening suspensions	Fixed solid loading, i.e. 70 wt%; variable dispersant conc.	Optimization of slurry viscosity and stability
Anode suspensions	Fixed dispersant conc., 1.04 dwb% (optimum value); Solid loading: 80, 83 and 85 wt%	Effect of solid loading on slurry flow and fired microstructures; Modeling of yield stress

Anode suspensions for dip coating	Fixed conc. of dispersant and binder and plasticizer (*); Temperature: 18, 23 and 30°C	Effect of temperature and solid loading on slurry flow and fired microstructures

(*) 2% of binder B-1014 and 10% of plasticizer B-1000 on the basis of slurry weigth

For the current suspensions for dip coating, the addition of additives is fixed at 2 and 10% respectively for binder and plasticizer on the basis of slurry weigth; the ratio of emulsions over powders varies from 14.1 to 15.0 wt%, respectively for 85 and 80 wt% slurry. It is observed that suspensions with additives are less viscous in comparison with those with only dispersant as a result of dilution coming from the water of emulsions. In this analysis, differently from the previous anode suspensions, the determination of the effective solid concentration Φ is not accomplished. Firstly, it is not essential for the preparation of slurry for dip coating process and secondly because the account of solid fraction of additives (acrylic polymers) into suspensions is not straightforward due to unknown partial properties of emulsion constituents and adsorption isotherms. Nevertheless, a simple estimation of solid loading for these slurries (based on ideal solution of emulsions) provides 75.3, 77.8 and 79.4 wt% respectively for the 80, 83 and 85 wt% anode slurries (§ 2.3.1.2) from which derived and keep the same designation. Conversely, for the previous anode slurries, the partial properties of polyelectrolyte solution were estimated from properties of polyacrylic acid salts available in literature (Hiraoka, 1982). Specifically, even for the less diluited slurry, i.e. 85 wt%, the water of dispersant solution behaves as free water (with density 0.99754 g/cm^3 at 23°C) and the acrylic polyelectrolyte is characterized by molar volume of 53.04 cm^3/mol, corresponding to 1.67 g/cm^3 for the same condition in water. Then, the obtained density of dispersant solution is 1.19 g/cm^3 in good agreement with that of manufacture specifications, i.e. 1.16-1.19 g/cm^3. In addition, the low amount of polyelectrolyte and its effect of dilution allow to determine the solid concentration of anode slurries as "bare" particles (the adsorbed layer of polyectrolyte is not accounted). This approximation is also vindicated by the low thickness of layer compared to the particle size as reported from literature data. Secondly, as the solid loading increases, the adsorbed layer decreases as experimentally shown by (Greenwood, 1995). Finally, experimental values of relative viscosity are well described by Krieger-Dougherty model proving that the solid fraction based on "bare" particles provides a good approximation for the anode slurries. In addition, experimental values of yield stress for highly concentrated slurries are in good agreement with those predicted by Flatt model based on hard-sphere interaction. Unfortunately, the same approach for modelling the rheological behaviour can not be applied for anode suspensions with additives because the assumption of hard-sphere interaction fades away and the determination of the effective solid concentrations is not accessible. Nonetheless, useful and practical indications were obtained as the effect of temperature on the rheological behaviour

simulating the conditions along thelwe-month period, i.e. 18-30°C. In addition, the fired microstructure is investigated by SEM micrographs providing useful connections between the properties of the slurry and final product.

2.3.2   Thermal analysis

2.3.2.1   *Drying and binder burn-out*

After forming process, the drying and removal of processing additives, i.e. dispersant, binder and plasticizer (here referred broadly as binders) from the green body, are essential steps prior the sintering. Microstructural defects present in the green body cannot be generally removed during sintering process. For this reason, the control of drying and binder removal is fundamental in order to avoid the introduction of defects as well as to control the green body microstructure for obtaining the final product with specific properties. Under this point of view, the thermal response of green body to sintering process is investigated for different drying and binder burn-out conditions as shown in table 2.11.

Table 2.11. Drying and sintering conditions for the anode green body.

	Drying	Sintering °		
	Dwell (T x holding time)	Temperature range [°C]	Heating rate [°C/min]	Dwell (T x holding time)
A	RTx4days	RT-1380	5	400x1h-800x1h # 1380x3h
B	RTx12h-60°Cx12h-120°Cx12h	RT-1380	5	400x1h-800x1h # 1380x3h
C	RTx12h-60°Cx12h-120°Cx12h	RT-800 800-1380	2.5 5	300x1h-400x1h-800x1h # 1380x3h

Binder burn-out step, ° Static air

Specifically, the effect of drying is pointed out by the comparison of sample A and B which are fired with the same heat treatment whereas the effect of binder removal regards sample B and C dried at same condition with different burn-out schedule; sample C shows milder condition of binder burn-out, i.e. low heating rate along the temperature range of RT-800°C and additional dwell at 300°C. The effects of different heat treatments are evaluated by porosity measurements and dilatometric curves (horizontal dilatometer, Linseis L75, Germany) of sintered bodies prepared from 80 wt% slurry for dip coating (75.3 wt% effective solid loading with dispersant, binder and plasticizer). Dilatometric analysis uses samples 20 mm long and nearly 10 mm^2 as section obtained from the casting of slurry into aluminium moulds and cut down to the proper size after drying. These samples sintered in the dilatometry were subsequent used for porosity measurements based on Archimede's method in

according to ASTM standard C20; averaged values of three measurements for sample are determined with standard deviation derived from the theory of error propagation. It was emphasized the influence of green microstructure on the sintering response; the higher the green density, the higher the sintered density as expected. The green microstructure of sample A, B and C is influenced by the conditions of drying and binder burn-out. Capillary forces developed during drying in oven and mild binder burn-out conditions supports particle arrangements with the result of green microstructure with higher density and narrower pore-size distribution, which promotes the achievement of high sintered density. Therefore, it is possible to tailor the fired microstructure by controlling the conditions of drying and binder burn-out for a fixed powder composition and sintering schedule. Specifically, sintered compacts were produced with total porosity (TP) extending from nearly 13 to 23%, most of it retained as open porosity (OP), i.e. 90 to 100% of OP/TP. In order to describe the porosity evolution of anode composite, the relative density RD[+] and RD[#] are defined as follows:

$$RD^+ \equiv \frac{Bulk\ density\ (g/cm^3)}{Theoretical\ density\ of\ dense\ anode\ composite\ (6.376\ g/cm^3)} \qquad (2.2)$$

and

$$RD^\# \equiv \frac{Bulk\ density\ (g/cm^3)}{Theoretical\ density\ of\ porous\ (TP = 12.84\%)\ anode\ composite\ (5.557\ g/cm^3)}$$

Where the theoretical density of fully dense anode (6.376 g/cm^3) composed by NiO and YSZ in 58:42 weight ratio (55:45 volume ratio) results from the rule of mixture adopting 6.67 and 6.01 g/cm^3 as density for NiO and YSZ powders, respectively (Radovich, 2004 (1); Ingel, 1986). The relative density RD[+] considers the volume of solid and all porosity (open and closed) within the anode composite and specifically not only the porosity left by burn-out of pore former but also the porosity related to the densification of anode composite, i.e. NiO and YSZ matrix. On the other hand, RD[#] considers the fired compact as porous anode composite where the matrix is fully dense with residual porosity derived only from the burn-out of pore former, i.e. 12.84 vol%; this is based on the assumption that porosity left by pore former remains constant during sintering in according to Slamovich results where large pores in a matrix with fine grains do not contribute to the matrix densification (Slamovich, 1992). The theoretical density for the anode composite with 12.84% as total porosity is 5.557 g/cm^3 and it is directly obtained from the relation between the bulk density, total porosity and theoretical density as the following expressions of TP and TP° which represent respectively the total porosity of compact and the total porosity of compact without considering pores left by pore former:

$$TP = \frac{TD_{(6.376\,g/cm^3)} - BD}{TD_{(6.376\,g/cm^3)}} = 1 - RD^+$$

and

$$TP° = \frac{TD_{(5.557\,g/cm^3)} - BD}{TD_{(5.557\,g/cm^3)}} = 1 - RD^\# \qquad (2.3)$$

Where TD and BD stands for theoretical and bulk density respectively. The porosity left by pore former in the compact TP_{pf} is calculated as (TP − TP°) then ($RD^\#$ − RD^+); subsequently the residual porosity of matrix TP_m, as (TP − TP_{pf}). It was observed that the total porosity of matrix TP_m evolves with the same rate of the open porosity of compact OP and their difference gives a constant value confirming that the porosity left by pore former remains constant during sintering in according to Slamovich results (Slamovich, 1992). The constancy of porosity during sintering is also provided by the affinity limit porosity ALP as proposed in (Gregorová, 2011). ALP relates the shrinkage during firing with the total porosity, since these quantities are complemetary, i.e. the higher the shrinkage, the lower the porosity, and the affinity limit porosity results constant for a body of given composition. On the other hand, ALP represents the free volume that is not occupied by ceramic powders and here it is shown that ALP depends on drying and burn-out conditions and not only on the powder composition of system. Therefore, it is possible to tailor the fired microstructure by controlling the conditions of drying and binder burn-out from a compact of fixed powder composition and sintering schedule.

2.3.2.2   Sintering

The thermal response of green compacts to conventional sintering (sample C and E) and multistage sintering (sample D) is investigated following the schedule conditions given in table 2.12. The conditions of drying and binder burn-out were common for all samples although a difference on the green density was observed from samples of different batches. This is ascribed to the drying at room temperature wherein variation of humidity and temperature affects the subsequent solvent evaporation in oven responsible for an enhancement of particle packing of green compacts due the action of capillary forces and lastly different density is expected. This observation suggests that controlled conditions of temperature and humidity during dip coating deposition can also improve the repeatability of results and reliability of the process.

Table 2.12. Conditions of treatment for conventional sintering (sample C and E) and multistage sintering (sample D).

Drying	Sintering °

	Dwell (T x holding time)	Temperature range [°C]	Heating rate [°C/min]	Dwell (T x holding time)
C		RT-800	2.5	300x1h-400x1h-800x1h
		800-1380	5	1380x3h
D	RTx12h-60°Cx12h-	RT-800	2.5	300x1h-400x1h-800x1h
	120°Cx12h	800-1400	5	1400x0.5h
		1400-1350	5	1350x5h
E		RT-800	2.5	300x1h-400x1h-800x1h
		800-1400	5	1400x2h

° Static air

Nonetheless, relevant indications on pore evolution of anode composites were delineated with regards to drying and sintering conditions. For instance, the final porosity of sample D and E is respectively 12.6 and 12.0%, close to the fraction of pore former (12.8%), mostly retained as open porosity, i.e. ~87 OP/TP. This implies that the pore structure left by pore former mainly persists even for prolonged sintering time between 1350 and 1400°C. Moreover, the evolution of porosity during reduction of anode into Ni/YSZ cermet was investigated. It is observed that microstructure of cermets at interface between electrolyte and anode is identical of the bulk microstructure as a consequence of complete NiO conversion suggesting that the pore structure of initial sintered anodes assures effective gas diffusion throughout the electrode as a result of percolating pores left by graphite particles even for porosity level around 12%. Then, the porosity is not a sufficient condition to assure effective gas permeation whereas a uniform distribution of pores with appropriate size, shape and interconnectivity is a relevant factor to sustain the gas diffusion as proved by the pore structure left by graphite particles for the current anode composites.

2.4 Electrolyte

Rheological analysis has identified the optimal concentration of dispersant corresponding to the minimum viscosity value. Then, the effect of additives was investigated for which a concentration of 2.5 and 5 wt%, respectively of binder and plasticizer, has assured appropriate rheological properties of YSZ slurries for dip coating process as well as good wettability toward anode substrates. Moreover, electrolyte coatings showed sufficient strength and no visible defects, i.e. pinholes, at green state. Prior to sintering, the binder burn-out was designed in order to minimize the probability of microstructural defects resulting from the exothermic degradation of acrylic-base additives enhanced by the catalytic effect of zirconia powder. A stepwise burn-out not only prevented blistering and cracking but also ensured a higher density of sintered compacts. The densification behaviour of conventional and

multistage sintering was described in term of pore evolution and grain growth on the basis of densification rate curves and a phenomelogical model. In addition, interactions between electrolyte and anode layers during co-sintering were analized. The densification of electrolyte films of µt-SOFCs was modified by the presence of transition metals migrated from the anode electrode toward the electrolyte during co-sintering. Effects of metal impurities on the electrical properties of YSZ film were also discussed.

2.4.1   Rheological analysis

2.4.1.1   Screening analysis

The rheological analysis is carried out similarly to the screening anode suspensions and identifies the optimum dispersant concentration of dispersant for YSZ slurries characterized by 70 wt% of solid loading. The slurry with 0.50 dwb%, i.e. the optimal suspension, shows the lowest viscosity and therefore the highest flowability which are related to the low degree of particle agglomeration (Liu, 1999).

2.4.1.2   Electrolyte suspensions for dip coating

The slurries for dip coating deposition involve the addition of binder and plasticizer to the optimal suspension with 0.50 dwb%. Different concentrations and ratio of binder and plasticizer were adopted where the YSZ suspension with 2.5 and 5 wt% of binder and plasticizer (slurry # 25) fulfilled several requirements. In fact, the slurry # 25 is characterized by good wettability toward anode substrates and the electrolyte coatings show sufficient strength and no visible defects, i.e. pinholes, at green state. In addition, the low viscosity of slurry allows to obtain thin layer for a given set of dip coating conditions, as required for the realization of solid electrolytes for SOFC applications.

2.4.2   Thermal analysis

2.4.2.1   Binder burn-out

The removal of additives follows a drying with identical conditions of anode compacts as described in table 2.12. Differently from anode samples, the binder burn-out of YSZ compacts is particularly critical as revealed by exothermic peaks between 300 and 400°C during dilatometric analysis which are associated to the release of gaseous products. This phenomenon depends on the catalytic activity of zirconia powder that enhances the degradation of additives and when large amount of gaseous products is released, blistering and cracking of compacts can occur. In

order to realize a milder burn-out and minimize the probability of defects and cracking, a stepwise burn-out is also carried out in comparison with the previous linear burn-out, whose conditions are described respectively, by sample C and B of table 2.11. The milder conditions of stepwise burn-out, i.e. lower heating rate and additional isothermal step, prevent the occurrence of exothermic peaks and then minimize the probability of microstructural defects, and secondly a higher green density and therefore a higher sintered density of YSZ compacts is assured. For these reasons, the stepwise burn-out is adopted for the development of dense electrolyte layers during the co-sintering of half-cells.

2.4.2.2   Sintering

The densification behaviour of YSZ compacts is subjected to conventional and multistage sintering as done for anode where the designation of samples is also maintained; electrolyte compacts, i.e. C, D and E, follow the schedule conditions of table 2.12. The densification behaviour is described in term of pore evolution and grain growth based on densification curves obtained by dilatometric anlaysis where a phenomelogical model proposed by Cameron is adopted (Cameron, 1982). The model is effective for examining the last sintering stage where grain growth controls the densification. In this stage, all samples are characterized by the same densification rate and therefore an estimate of final density (or porosity) of sintered compact is possible. Specifically, the sample D subjected to multistage sintering can achieve the same final density of sample E, exposed to conventional sintering for 2 h at 1400°C, after 10 h at 1350°C. Then, it is possible to tailor the sintering process, in term of temperature and time of last sintering stage, with regards to the fabrication requirements.

2.4.2.3   Interactions between electrolyte and anode layer

The co-sintering of half-cells involves interactions between the electrolyte coating and the anode substrate whose densification behaviour is generally different from that of free electrolyte and anode layers predicted by thermal analysis due to differential shrinkage and shrinkage rate of each layer. From thermal analysis, the densification initiates at 950 and 1100°C, respectively for the anode and electrolyte, while the shrinkage rate of electrolyte is higher than that of anode for temperature beyond 1280°C (Bonenti, 2012). In this condition, the electrolyte coating during co-sintering should experience tensile stresses which hinder its densification. From micrographs of µt-SOFCs, the electrolyte layer is ~20 µm and shows closed porosity suggesting a relative density > 93-95% and hence a consistent densification of electrolyte film. Then, other aspects have to do with the densification of YSZ films during co-sintering. The presence of transition metals within electrolyte layer of µt-

SOFCs, detected by X-ray energy-dispersive spectroscopy (EDS) analysis, is related to the diffusion of Ni and Pd from the anode and the embedded current collector during co-sintering, which are responsible for the densification behaviour of YSZ films. In fact, an increment of vacancy concentration is produced by the incorporation of Ni and Pd occurring as NiO and PdO within zirconia lattice, which causes a modification of YSZ densification mechanisms connected to lattice diffusion mechanism. In this condition, the sintering of YSZ layer with NiO and PdO is expected to be closer to the densification behaviour of anode substrates and eventual tensile stresses arising during co-sintering are offset or minimized. Possible effects of NiO and PdO on the electrical behaviour of YSZ layer during cell service is also provided on the basis of literature data.

2.5 Cathode

2.5.1 Thermal analysis

The thermal response of current collector layer and functional layer composed respectively by LSM and LSM/YSZ powders, is investigated for different sintering conditions, like atmosphere and maximum sintering temperature. Specifically, compacts produced by die pressing (~100 MPa for 2-3 min) were sintered in dilatometer under static air and argon flow (3 m^3/h) from room temperature to the maximum sintering temperature with a dwell of 1 h at 800°C at heating rate of 5°C/min. Compacts were sintered at maximum temperature of 1150 and 1180°C for 2 h for which the electrochemical performance of functional cathode layer is maximized and the eventual formation of resistive compounds as $La_2Zr_2O_7$ (LZ) reduced (Cronin, 2012; Kim, 2001; Soderberg, 2009).

2.6 Micro-Tubular Solid Oxide Fuel Cells

2.6.1 Production

The production of µt-SOFCs with embedded current collector follows the experimental procedure previously outlined in § 2.2.1 and profits of results and indications so far achieved from the rheological and thermal analysis of different cell components with the result of reliable fabrication process characterized by high reproducibility of cell characteristics. This point is particularly important for the electrochemical testing other than for a potential upscale production of ceramic fuel cells.

2.6.2 Electrochemical performance

The performance of µt-SOFCs is investigated by electrochemical testing where potentiostat (Autolab PGSTAT302N, Eco Chemie, Netherlands) was used in potentiostatic mode to obtain voltage vs. current plot and Tafel plot. The sintered cells were placed and sealed in an alumina tube used as setup with electrical connections realized at anode and cathode electrode in four-probe configuration in other to acquire separately (reliable outputs) the potential and current signals. The sintered cell prepared with anode and cathode connections is illustrated in figure 2.4 and the cell placed into alumina tube setup in figure 2.5.
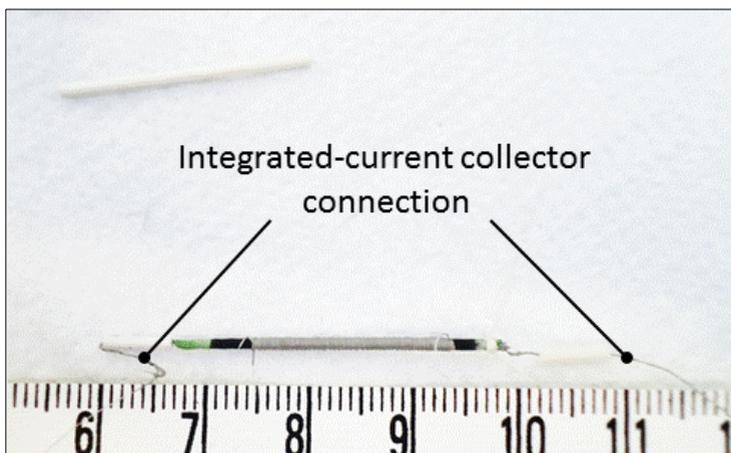

Figure 2.4. Photograph of µt-SOFC with Pd-current collector prepared with integrated-current collector connection for anode side.

The connection of anode side is the integrated-current collector connection as illustrated in figure 2.4 and 2.5 as proposed by (De la Torre García, 2013). On the other hand, this configuration of anode connections was found here not reliable during the electrochemical testing due to the breaking of low thickness wires at critical points as explained more detailed in § 3.6.3. Consequently, all electrochemical results were obtained with a straight wire of palladium passing along the fuel channel for anode connection while for the cathode side, silver wire (99.997%, Alfa Aesar, Germany) with 0.1 mm of diameter was wound around the
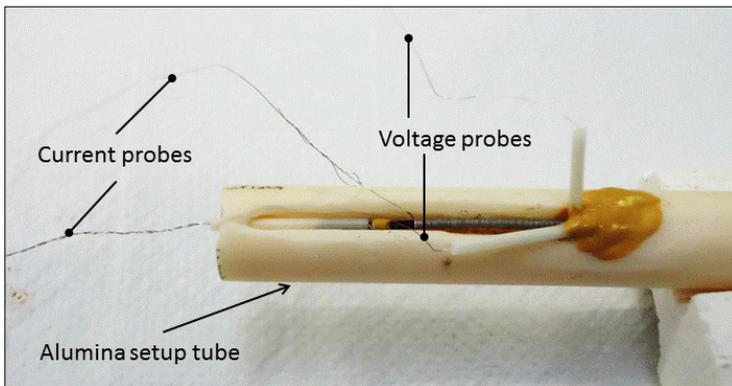
Figure 2.5. Setup for the electrochemical testing of µt-SOFCs.

cathode active area and a silver paste was added for increasing the electrical contact. A commercial ceramic-based sealant (Ultratemp 516, Aremco, Valley Cottage, NY) was usually used to fix the cell to the tube setup, where also a home-made sealant provided by SOFCpower was also proved for trials tests. A four-bores alumina tube with k-termocouples wires was fixed firmly to the setup tube of figure 2.5 and used to bring outside the two voltage and current terminals to the potentiostat. The tubes were place in a high temperature furnace where, along with the inner furnace thermocouple, an additional thermocouple was placed within 2 cm above the middle of µt-SOFC in order to control the temperature above the sample within ±1.5°C. The complete setup reached the temperature of 800°C with dwell of 2h in order to cure the sealant after dwells of 2 h at fixed temperatures of 93, 260 and 372°C as indicated by Aremco specifications; a heating rate of 2.5°C/min was used from RT to 800°C. Subsequently, the temperature of sample was set to the reduction temperature and thus 800 and 750°C, respectively for cells with nickel and palladium wire as current collector. Once reached the reduction temperature for 1-2 h, nitrogen was flow in the sample at 20 ml/min and stepwise turned off gradually to hydrogen humified at RT. The operative flow (20 ml/min) of electrochemical testing was thus a mixture of 97 and 3% of hydrogen and water, respectively. The cathode was exposed to static air of ambient (furnace) pressure. The potentiostat station employed Nova 1.6 software (Metrohm Autolab B.V.) in order to set and control the conditions of electrochemical measurements as well as to acquire the electrochemical data.

2.6.3   Engineering aspects

The current collector configuration of anode electrode was demonstrated to be a critical and crucial aspect for the improvement of cell performance. In the present study, the high performance integrated-current collector connection was not feasible for the electrochemical testing although it was realized and proved before the testing. For this reason, it was proposed an alternative current connection configuration for the promising palladium collector which assured an improvement of cell performance by a factor of 4 than the cell with nickel collector. Finally, an estimate of power output over manufacturing cost is provided as reference value for the development of μt-SOFCs with embedded current collector.

Chapter III

Results and Discussion

The results are presented and discussed with regards to the most relevant parameters of processing steps for the fabrication of μt-SOFCs in order to achieve a controlled and reliable ceramic process and to realize final composite products with specific microstructures and properties. Following this purpose, after the thermal analysis on the current collector components and pyrolisable materials, rheological results are presented and demonstrated the optimization of wet colloidal process where the effect of solid loading and additives concentration on the slurry properties was widely investigated by rheological models especially for anode suspensions as their main part for the production of anode-supported SOFCs. Then, thermal analysis concerned the drying, binder burn-out and sintering process of anode, electrolyte and cathode layers complying with the achievement of specific microstructures and properties of sintered products. Finally, electrochemical testing of μt-SOFCs pointed out the effect of the embedded current collector on cell performance. It was demonstrated the effectiveness of current collector in term of turns per unit length and the nature of metal, where the power density scaled with the square of turns per unit length and an outstanding improvement of cell performance was achieved by adopting palladium than nickel as current collector; at 800°C, the power output was increased by a factor ~4 than that of the cell with nickel collector.

3.1 Cell Supports

The cell supports are constituted by a metallic coil wound around a carbon-base composite rod as shown in figure 3.1. The coil made by nickel and palladium is 4 cm long and the carbon composite rod has a diameter of 0.5 and 0.7 mm. The features of cell supports are summerized in table 3.1.

Table 3.1. Characteristics of the cell supports.

| Rod diameter [mm]	Coil metal	Coil feature [turns/cm]
0.5	Ni and Pd	6
0.5	Ni and Pd	11
0.7	Ni and Pd	5-6
0.7	Ni and Pd	11
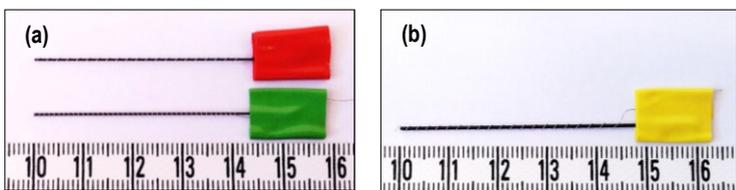
Figure 3.1. Examples of cell supports in nickel and palladium wire with rod diameter 0.5 mm (a) and palladium wire with rod diameter 0.7 mm (b).

The coils are in intimate contact with the rod and show regular and homogeneous distribution of turns along the support length regardless the rod diameter and metal nature as a prove of similar mealleability of nickel and palladium wire.

3.1.1   Thermal Analysis

3.1.1.1   *Current collector*

The oxidation behaviour of nickel and palladium was analyzed by TGA as shown in figure 3.2. Generally, most of metals and alloys are subjected to oxidation at high temperatures. This phenomenon is characterized by the growth of oxide layer and the material gains weigth by oxygen incorporation. From figure 3.2 both nickel and palladium gain weight due to oxidation but with different trends. Palladium mass reaches a plateau above 1100°C whereas the mass change of nickel increases rapidly with temperature especially above 1000°C. In particular, the palladium mass increase is 15 wt%, whereas for nickel is double, around 30 wt% at 1300°C in static air.
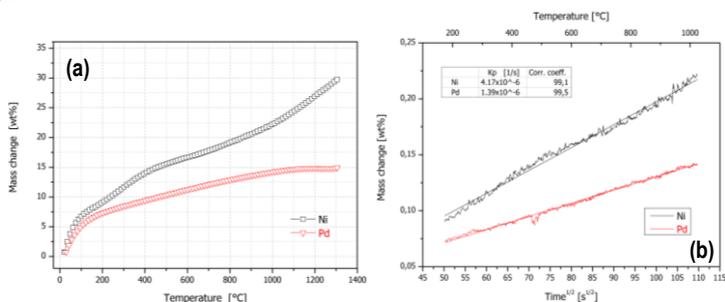

Figure 3.2. Thermogravimetric analysis (a) and parabolic law fitting between 200 and 1000°C for nickel and palladium.

At high temperatures, a parabolic law describes the oxidation of most metals and alloys. Specifically, a decreasing oxidation rate with the oxide growth was observed, represented as (Khanna, 2002):

54

$$\frac{dx}{dt} = \frac{k_p}{x} \tag{3.1}$$

And after integration:

$$x^2 = 2k_p t + c \tag{3.2}$$

Equation 3.1 is derived by Wagner where x is the oxide thickness or mass change, k_p the rate constant and t the time (Khanna, 2002). In this case, the oxide growth is governed by diffusion of ions through the oxide layer. In figure 3.2 the mass change is also plotted versus the square root of time for nickel and palladium; the inset reports the rate constants and the correlation coefficients of parabolic law fits for nickel and palladium. Both nickel and palladium follow a parabolic oxidation law between 200 and 1000°C. Above 1000°C, the parabolic oxidation law breaks down. In fact, between 1000 and 1300°C, the mass change of nickel increases linearly with temperature whereas that regarding palladium adjusts to a plateau. In the former case, the linear trend following a parabolic oxidation law occurs when the oxide layer (scale) cracks or scale spallation arises (Khanna, 2002). Figure 3.3 (c) shows a thick scale of nickel and its spallation. This confirms the linear oxidation of nickel in figure 3.2 (a) as well the critical thickness of scale reached at 1000°C. In fact, the stress causing the failure of Ni scale (NiO) is related to a build-up of stresses at Ni-NiO interface. At a certain critical thickness of the scale, the stresses can be only released by fracture and therefore the scale spallation occurs regardless the low mismatch of thermal expansion between oxide layer and metal as in this specific case where the thermal expansion for Ni-NiO and Ni is 17.1 and 17.6x10^{-6}, respectively, in the RT-1000°C range (Khanna, 2002). Conversely, the palladium behaviour above 1000°C displays an opposite trend compared to that of nickel. The palladium appearance is slightly tarnish and indicates the occurence of oxidation as shown in figure 3.3 (b); differently from nickel, palladium oxide (PdO) is very thin and does not show any spallation even after repeating bending. The constant mass gain of palladium above 1100°C is justified by its high vapour pressure (Arblaster, 2007; Khanna, 2002). Therefore, it is expected a competitive oxygen dissolution within the metal and the volatilization of PdO causing the constant mass change between 1000 and 1300°C as shown in figure 3.2. In fact, the melting point of NiO scale at atmospheric pressure is 1990°C whereas for PdO it is 870°C (Khanna, 2002), as a further prove of low stability of PdO at higher temperatures.
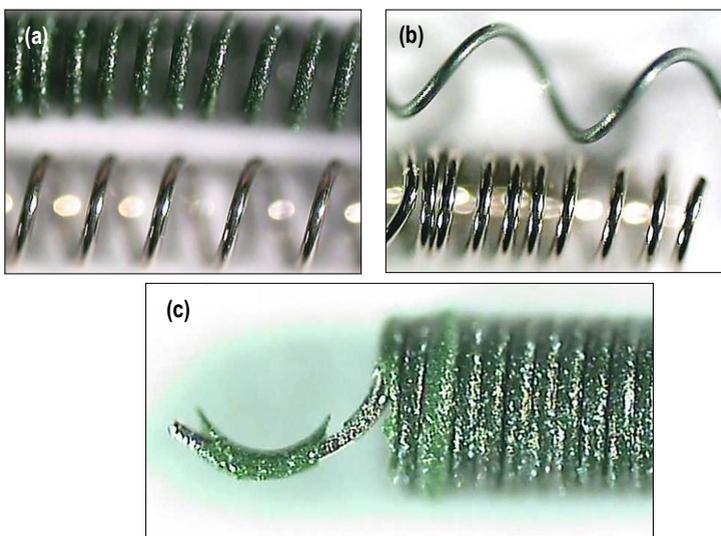
Figure 3.3. Micrographs of current collectors after treatment at 1400°C for 4 hours. Metallic coil after treatment (top) and coil from as-received metal (bottom) for nickel (a) and palladium (b). Spalliation of nickel scale (c).

In conclusion, nickel and palladium oxidize at high temperatures forming NiO and PdO. The thickness of nickel scale increases with temperature until it reaches a critical value where cracking and spallation of scale occur. On the other hand, palladium scale is thin with good adhesion to the substrate and the coil is still malleable after isothermal treatment at 1400°C in static air. Nickel and palladium scales are both cation deficient oxides ($M_{1-x}O$) and therefore p-type semiconductors (Khanna, 2002). In addition, for thin oxides above thermally activated semiconduction also electron tunnelling arises (Martin, 1997). From this point of view, an enhanced catalytic activity for thin oxide film derived from palladium compared to nickel it is predictable as well as an improved electrical conductivity. Consequently, the palladium coils after harsh treatment conditions offer several advantages upon nickel ones. First of all, the higher malleability that is essential for a good electrical connection of inner current collector. Moreover, an improved catalytic activity is expected to fuel oxidation as well a not shortage on electrical conductivity even after harsh treatment conditions such as co-sintering at 1400°C in static air.

3.1.1.2 Sacrificial inner core

Thermal behaviour of the sacrificial inner core was analyzed by thermogravimetric and differential thermal analysis (DTA) as shown in figure 3.4. In particular, the degradation of sacrificial inner core is carried out by different heating rate (HR), i.e. 150 (2.5°C/min) and 300°C/h (5°C/min), from room temperature to 1000°C in static air. The Thermal decomposition of sacrificial inner core is complete at 800 and 1000°C for the lower and higher HR, respectively, as from figure 3.4 (a). As expected, the decomposition is shifted to higher temperature with increasing HR. The decomposition of epoxy resin is accomplished by two steps at about 300°C and between 500 and 600°C. The former involves dehydration, bond scission and elimination of volatile chain fragments resulting in a carbon residue underwent to decomposition at higher temperature range, i.e. 500 and 600°C (Levchik, 1998). Instead, the oxidation of carbon fibers occurs above 600°C and it is complete between 800 and 1000°C as a function of HR (Ismail, 1992). In general, higher HR values delay the oxidation of carbon components of sacrificial inner core to higher temperatures especially for carbon fibers as clear in figure 3.4.
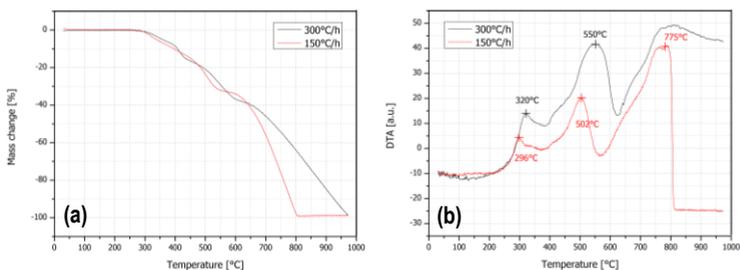

Figure 3.4. Thermogravimetric analysis (a) and differential thermal analysis (b) of the sacrificial inner core at 150 and 300°C/h in static air.

In figure 3.5 a comparison between the DTA and derivative of TGA is reported. The derivative of thermogravimetric curve identifies the mass change rate. Exothermic peaks entailing oxidation of carbon components correspond to maximum mass change rate for both HRs, i.e. 150 and 300°C/h. In particular, the highest value of maximum mass change rate for the treatment at 150°C/h corresponds to the lowest value of maximum mass change rate for the treatment at 300°C/h. In the last case, an additional peak of derivative of TGA at around 400°C (full circle) is clear in figure 3.5 (b).
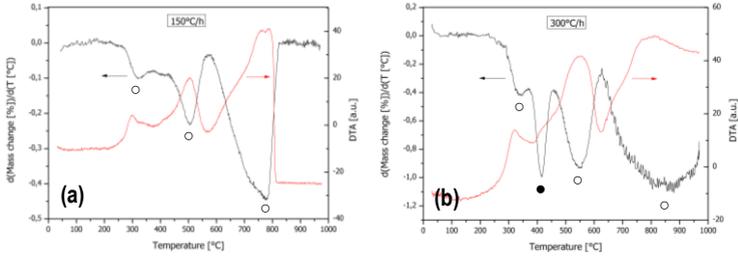
Figure 3.5. Derivative of the thermogravimetric analysis and differential thermal analysis for the sacrificial inner core tretated at 150°C/h (a) and at 300°C/h (b) in static air.

As a result, further investigation of the thermal behaviour of sacrificial inner core is performed by TGA and DTA from RT to 770°C at 300°C/h with dwell time of 1 h at 400°C (figure 3.6).
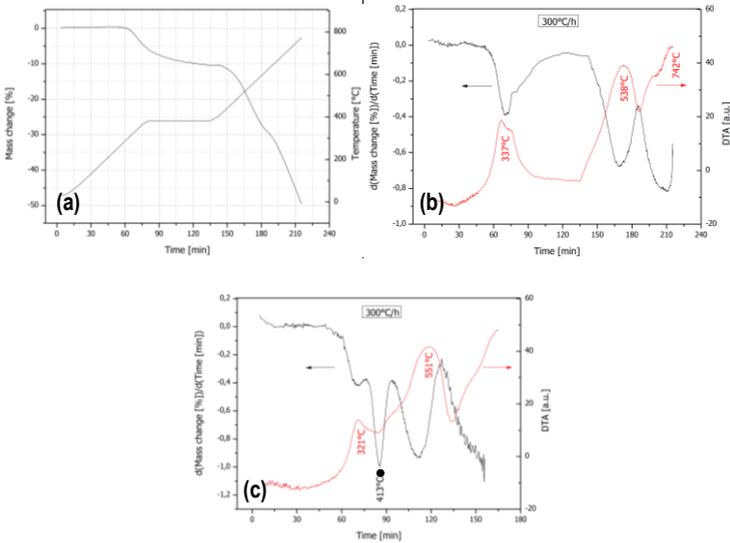
Figure 3.6. Sacrificial inner core tretated at 300°C/h with a dwell of 1 h at 400°C in static air. Thermogravimetric analysis and treatment profile (a) and derivative of the thermogravimetric analysis and differential thermal analysis (b). As comparison in panel (c) the treatment at 300°C/h without dwell.

The TGA (figure 3.6 (a)) indicates a mass loss of 10 wt% after isothermal dwell at 400°C. Similarly, a mass loss between 8 and 10 wt% is achieved at 400°C without dwell as from figure 3.4 (a). The unique difference between these treatments at 300°C/h consists of the peak of mass change rate at around 400°C as emphasised

58

in figure 3.6 where this peak takes out with a dwell at 400°C for 1 h. In this condition, it is expected a milder burn-out of epoxy resin and consequently crack-free samples after co-sintering. Unfortunately, this does not occur also at lower heating rate, i.e. 150°C/h, and dwell at 400°C as shown in figure 3.7 (a). The choice of decreasing HR to 150°C/h is further reducing the mass loss rate as demonstrated in figure 3.5 and avoid any additional peak with an isothermal step with the potential benefit of avoiding dentrimental decomposition of epoxy resin. It is clear that, mild burn-out conditions are not sufficient to obtain crack-free half-cells and consequently an alternative treatment was analyzed. Specifically, the sacrificial inner core was subjected to partial oxidation of epoxy resin before cell support fabrication and co-sintering. In this case, the as-received carbon-base rods were treated in a furnace at 150°C/h with a dwell at 375°C for 45' in static air in order to remove a precise amount of epoxy resin. Specifically, the proper amount of epoxy resin is between 16 and 18 wt% for the rod with diameter 0.5 mm and between 20 and 22 wt% for the 0.7 mm diameter rod. This quantity of epoxy resin prevents any cracking problems along sintering without compromising the integrity of sacrificial inner core during fabrication of cell supports as well as the wettability of cell supports during dip coating process.
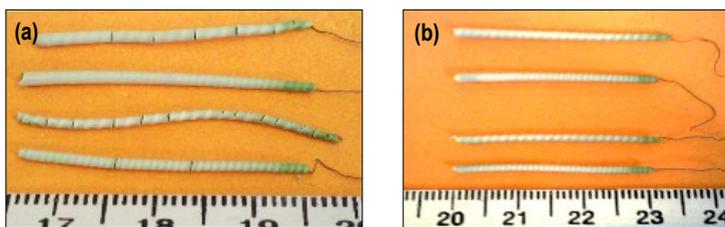

Figure 3.7. Half-cells after co-sintering with carbon-base rods as-received (a) and with preliminary treatment in muffle furnace (b).

Half-cells derived from preliminary treatment of sacrificial inner core exhibit regular shape and any cracks as shown in figure 3.7 (b). From this investigation, the integrity and regular shape of half-cells after co-sintering are related to the epoxy resin decomposition of the sacrificial inner core. As a matter a fact, the oxidation of carbon components involves a large amount of gases even for low amount of solid polymer (Evans, 1990). When the diffusion of these gases from the body surface is low, a pressure gradient can be established with the consequence of the stress build-up larger enough to cause cracks in the body (Ring, 1996). In this specific case, a removed amount of 16 to 18 wt% on the carbon-base rod is sufficient to guarantee the integrity of half-cells after co-sintering and points out the hypothesis of a critical amount of epoxy resin to eliminate. The removed amount of epoxy resin is estimated from the critical one, i.e. 16 to 18 wt%, the density and the volume fraction of epoxy

resin and carbon fibers. The epoxy resin covers 35 vol% of the sacrificial inner core and corresponds to 26 wt%, as estimated by the rule of mixtures and adopting 1.2 and 1.8 g/cm^3 as density respectively for the epoxy and carbon fiber (Zhou, 1999; Ismail, 1992). The amount of removed resin is the ratio of the critical amount (16-18%) upon the overall one (26%) and corresponds to 61 to 69% by weigth of epoxy resin fraction. Quantitatively, 5 cm fiber long of 0.5 mm in diameter weighs 16 mg and therefore the amount of removed resin is estimated to be between 2.5 and 2.9 mg leaving a void between 21.5 to 24.2%. Consequently, the porosity left by the removed resin during the preliminary treatment, around 22 vol%, allows a mild diffusion of gases along the sacrificial inner core thus avoiding cracking and warping of half-cells. Finally, this investigation points out the importance of burn-out or debinding of processing additives and other components which must be eliminated before the sintering treatment without introducing defects or cracks in the body. For this reason, the removal of such components is one of the most critical steps and therefore is fundamental for the optimization of ceramic processing. In addition, a mild thermal removal brings about uniform and fine microstructure of green compacts as well as improved mechanical properties of sintered bodies (Liu, 1997; Chartier, 1995). As a result, the elimination of the sacrificial inner core during co-sintering is performed at low HR, i.e. 150°C/h, with isothermal steps after a preliminary treatment of the as-received carbon-base rods.

3.1.1.3   *Pore former*

Thermal behaviour of pore former was analyzed by TGA as shown in figure 3.8. In static air, graphite is completely oxidized at 1050°C similarly to the sacrificial inner core of figure 3.4. A dwell at lower temperature enables the elimination of graphite already at 800°C after 1 h.
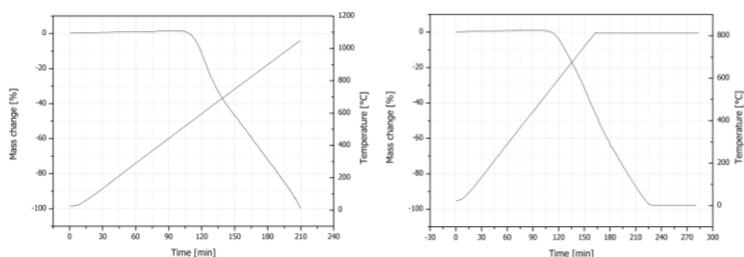

Figure 3.8. Thermogravimetric analysis at 5°C/min (300°C/h) in static air from RT to 1050°C (a) and from RT to 800°C with 2 h of dwell.

In addition, potential carbon residues after dwell at 800°C can be removed with the proceeding of firing, since co-sintering of half-cells is accomplished at temperature

as high as 1380°C. The elimination of graphite at lower temperature is preferred not only for economical issue but also because the oxidation of carbon is highly exothermic and high spots can be developed with the occurrence of dangerous thermal stresses (Ring, 1996). Moreover, the elimination of carbon at higher temperature can produce higher volume of CO and CO_2 gases, increasing the probability of cracking. For this reason, the burn-out of pore former is carried out with a dwell at 800°C for 1 h in static air during co-sintering and crack-free half-cells are obtained as shown in figure 3.7.

3.2 Ceramic Processing

3.2.1 Powders

Micrographs of NiO, YSZ and LSM powders are shown in figure 3.9. Any additives such as dispersant are intentionally not employed in order to avoid any preferential or bias adsorption of dispersant molecules by the surface of different powders. In addition, the agglomeration state of suspension may be altered due to degradation of dispersant during milling (Chartier, 1996). Consequently, in this investigation the agglomeration degree should be related only to the propensity of particles to form agglomerates upon milling step. Specifically during ball mixing soft agglomerates may be broken and reformed, whereas hard agglomerates or aggregates should survive. Consequently, micrographs of figure 3.9 should represent the powders affected only by the interactions of oxide particles in polar solvent, i.e. deionized water, avoiding any bias source and bearing a comparison of the agglomeration state for the powders in point. Here, the term agglomerates regards both soft and hard agglomerates.
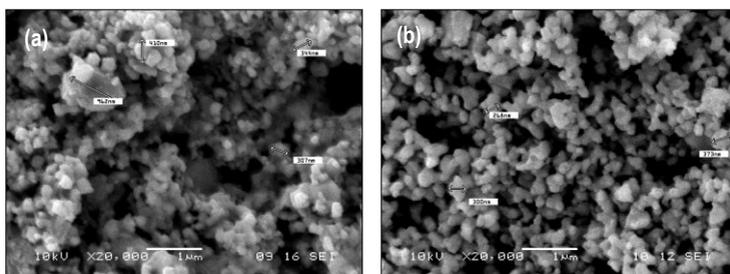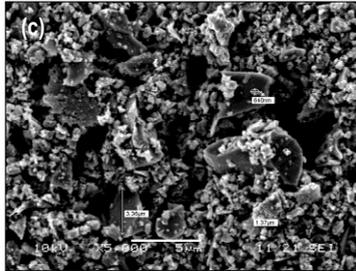
Figure 3.9. SEM micrographs of NiO (a), YSZ (b) and LSM (c) powders.

Most of NiO and YSZ particles are below 1 µm as well the largest agglomerates. Their constituents, primary particles, are characterized by round shape even if larger non-isometric agglomerates are pointed out especially for NiO powder. Particles and agglomerates of LSM are very irregular in shape as well as size and most of agglomerates are between 1 and 5 µm.
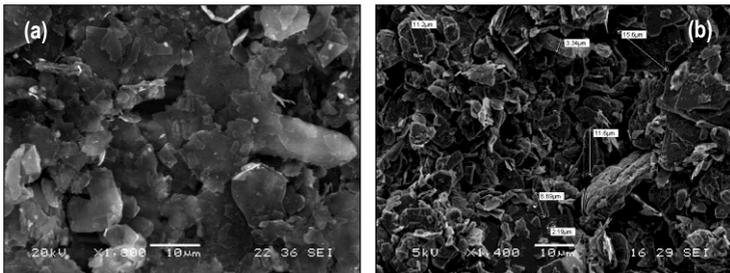
Figure 3.10. SEM micrographs of graphite powder after milling (a) and as received (b).

Graphite powders are investigated due to their nature. Graphite has a strong tendency to flake and its flaky nature is clear from figure 3.10 (a) where graphite particles display plate-like shape with angular edges after milling resembling a more exfoliation character than the as-received powder in figure 3.10 (b). Finally, the anisotropic shape of graphite flakes is peculiar for particles as-received and also after milling as evident in figure 3.10 where in both cases most of particles are larger than a few microns. The flaky and soft characteristics of graphite particles are crucial on flow behaviour of anode slurries as well as on the effect as pore former for green compacts.

62

3.3 Anode

Accurate rheological analysis concerned the realization of stable suspensions with optimal amount of dispersant. Then, the effect of solid loading, additives and temperature was studied for the stabilized slurries in order to optimize the wet colloidal process of dip coating. Rheological models were used to describe the flow behaviour of anode slurries elucidating the underlying mechanisms of particle interactions and on the other hand, to estimate flow properties of slurries as a function of solid loading and temperature. Thermal analysis on green compacts prepared from stabilized slurries identified the effects of drying, binder burn-out and sintering conditions on fired microstructures. The role of pore former on the porosity of sintered compacts was investigated where the pore evolution throughout sintering process is accompanied by models which provide porosity values in agreement with experimental results. Finally, the reduction process of anode pointed out the function of pore structure where an interconned porosity has assured effective gas permeation during reduction of NiO/YSZ electrode even for porosity of 12-13% as a result of uniform distribution of pores with appropriate size, shape and interconnectivity. A porosity of 30-33% was estimated for the Ni/YSZ cermet.

3.3.1   Rheological analysis

3.3.1.1   Screening analysis

The effect of dispersant concentration on the suspension viscosity is shown in figure 3.11 (a). The lowest viscosity value is obtained at dispersant concentration of 1.04 dwb% for which the surface coverage of dispersant onto particle surface is optimized and corresponds to the lower extent of powder agglomeration or flocculation (Liu, 1999). Experimental data are well fitted by a quadratic regression model and this allows the estimation of the viscosity at pristine value of dispersant that is 5.92 Pa s.
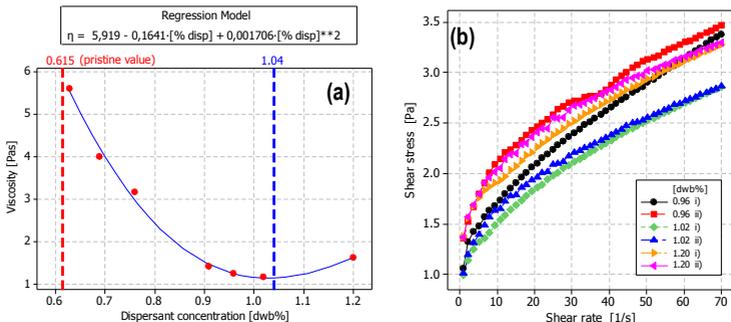
Figure 3.11. Rheological behaviour of screening suspensions. Viscosity versus dispersant concentration (a) and shear stress versus shear rate (b); i) ascending ramp and ii) descending ramp) for suspensions with 0.96, 1.02 and 1.20 dwb%.

For the optimum dispersant concentration of 1.04 dwb%, the viscosity value is 1.17 Pa s that is five times lower than the estimated viscosity in pristine condition, i.e. 0.615 dwb% of dispersant, for 70 wt% suspension evaluated at 0.85 s^{-1} shear rate at 23°C. Figure 3.11 (b) points out the shear stress along with the hysteresis loop for the three slurries with different dispersant amount; around the the optimum value, i.e. 1.04 dwb%. The lowest shear stress along with the lowest hysteresis loop regards the "optimal" suspension whose ascending and descending ramps are almost superimposed. As a result, the suspension microstructure with dispersant close to the optimum concentration, i.e. 1.02 dwb%, is weakly affected by the shear history due to higher stability for the duration of measurement (Barnes, 1997). For the other two suspensions, the hysteresis loops are quite evident especially for the slurry with lower dispersant concentration. In this case the suspension microstructures, with dispersant concentration different from the optimum value, depends much more on shearing compared to the suspension with dispersant amount close to the optimum. The hysteresis is related to the rearrangement of suspended powders during shear. The particle rearrangement tends to an equilibrium state corresponding to a specific microstructure of suspension along shearing conditions (Barnes, 1997). At low shear rates the Brownian forces dominates and their action is usually much longer than that derived from viscous or hydrodynamic forces predominating at higher shear rates. For this reason, the attainment of the equilibrium state and favourable arrangement of suspended particles can be delayed along the descending ramp revealing an apparent higher viscosity (Macosko, 1994). In addition, nonspherical objects such as rod-like or disk-like particles can adjust their principal axis along preferential direction and therefore are characterized by orientational order (Larson, 1999). As a consequence, by far nonspherical objects like fibers, flakes and flocs align under shearing in order to minimize the flow resistance and their restore to equilibrium state takes time with the consequence of an enhancement of time effects. This is the case for the suspensions with optimal and higher dispersant concentration where the level of shear stress at maximum and minimum values of shear rate coincide after the increasing and decreasing shear ramps, then the equilibrium state is expected to be achieved during the last portion of the descending ramp by the restoring of random distribution of nonsherical particles, i.e. graphite in figure 3.10. The higher viscous response of the slurry with higher dispersant concentration is probably related to the increase of solvent viscosity due to nonadsorbed dispersant molecules above the optimum concentration. For the suspension with lower dispersant concentration, the level of shear stress value at 70 s^{-1} increases during the dwell of 50 s and this suggests the occurrence of powder

agglomeration. In this case, at high shear rates hydrodynamic forces induce agglomeration that is known as orthokinetic flocculation (Everett, 1989). As a result, the hysteresis loop does not close at 0.85 s^{-1} due to the larger extent of agglomerates that increases the slurry viscosity and/or prevents the rearrangement of suspended powders with the result of further enhancement of time effects. The reversibility of suspension microstructure is related to the dispersion state of slurry systems (Mewis, 2009); in this case, the optimal suspension with dispersant concentration close to the optimum value exhibits the best dispersion state that is related to the lowest hysteresis loop and viscosity. On the other hand, irreversible changes of suspension microstructure can be related to evaporation of suspension solvent (Mewis, 2009). Under this assumption, the suspension stability over time was also evaluated by monitoring the solvent evaporation under laboratory conditions of relative humidity and temperature as shown in figure 3.12 (a).
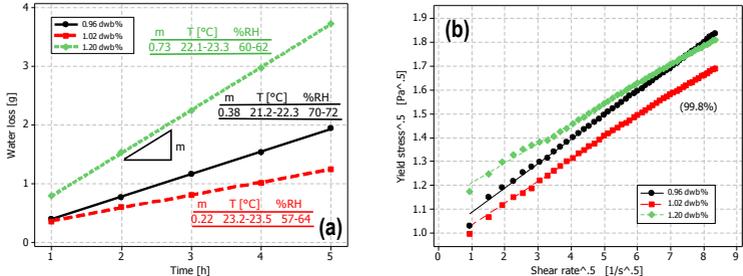
Figure 3.12. Water loss function versus time where m is the water loss coefficient and %RH the relative humidity (a) and yield stress$^{0.5}$ versus shear rate$^{0.5}$ calculated by Casson model with correlation coefficient of 99.8% (b) for the three screening suspensions under investigation.

As shown in figure 3.12 the lowest amount of water and water loss coefficient (m) correspond to the optimal suspension. In this case the relative humidity is between 57 and 64%, similarly to that regarding the suspension with higher dispersant concentration (60-62 %RH); this latter, in constrast to the optimal slurry, displays a much higher water loss in spite of lower temperature. Additionally, the lowest evaporation should occur at lower temperature and higher RH as for the conditions of the suspension with lower dispersant concentration, i.e. 21.3-22.3°C and 70-72 %RH. As a matter of fact, this does not occur and therefore the dispersant concentration should be expected to affect the evaporation of solvent, i.e. water loss. A linear dependence of water loss over the time is evident within 57-72 RH% and 21.2-23.5°C ranges for the three suspensions under investigation. This linear trend is similar to that regarding the rate of evaporation during constant rate period (CRP) involved during the first stage of drying for ceramic materials (Rahaman, 2003). Further insights on the effect of dispersant on suspension stability may arise from the

evaluation of solvent evaporation under controlled laboratory conditions of relative humidity and temperature adopting the following equation (Rahaman, 2003):

$$\dot{V}_E = H \ (P_W - P_A) \tag{3.3}$$

Where $\dot{V}_E$ is the evaporation rate, P_W the vapor pressure of the liquid at the surface and P_A the ambient vapor pressure. H is a factor depending on the surface area of evaporation and other conditions such as stirring. In the current investigation the surface area of evaporation and stirring velocity were maintained constant. As a consequence, the water loss of the suspensions should be related to the difference of vapor pressure terms in equation 3.3. As a further suggestion, the stirring can contribute to the solvent evaporation, and hence on H factor, since the dissipation of viscous energy into heat involves the flowing of the solvent around particles and flocs. Under this perspective, the solvent viscosity plays a significant role and is affected by the temperature as well as non-adsorbed molecules of dispersant. In addition, a certain amount of free dispersant molecules are always present throughout the slurry solvent regardless higher dispersant concentration than the optimum value as reported for acqueous slurries with high solid loading stabilized by polyelectrolyte (Guo, 1997). Moreover, the solvent consistency can affect the collision rate between flocs and particles; high viscosity solvent prevents collisions and conversely a solvent of low viscosity promotes them supporting perikinetic flocculation in regime of low shear rates. In this specific case, heat is released during the formation of flocs and therefore a rise on temperature of slurry is expected to enhance the solvent evaporation. Nonetheless, this contribution is thought to be negligible in comparison with the energy dissipation related to the shear field (Firth, 1976). Then, a detailed investigation on solvent evaporation should include the flocculation degree and control of shear conditions along with external conditions, i.e. temperature and humidity, in order to highlight the effect of dispersant upon the aforementioned concurrent phenomena. All screened suspensions displayed shear thinning behaviour even if in figure 3.12 (b) only two suspensions are reported other than the optimal suspension in according to the outline of panel (a). The yield stress τ_Y is calculated by extrapolating at zero the shear rate $\dot{\gamma}$ of Casson expression (Liu, 1998):

$$\tau^{1/2} = \tau_y^{1/2} + c\dot{\gamma}^{1/2} \tag{3.4}$$

Again the suspension with dispersant concentration of 1.02 dwb% displays, along with the lowest viscosity and water loss, also the lowest yield stress and flow resistance parameter as shown in figure 3.12 (b) and table 3.2. The flow resistance parameter ø/(A-ø) is the ratio of solid concentration ø in term of volume fraction to

the available space *(A-ø)* of particles freely moving throughout the system (Liu, 1998). *A* represents the maximum solid concentration at which the system ceases to flow and it is determined by rheological measurements. The lower is the flow resistance parameter the better is the dispersion of the slurry. As evident from table 3.2 the suspension with dispersant concentration close to the optimum value exhibits the best flow behaviour. In fact, the optimum concentration of dispersant guarantees the complete coverage of particle surface that is responsible for a good dispersion state of suspension with the result of low degree of powder agglomeration associated by low yield stress as well as flow resistance parameter values. In conclusion, the suspension with the optimum dispersant concentration shows a lower viscosity as well as a more stable microstructure along time in term of hystereris and water loss and consequently the stability of colloidal suspensions is enhanced. Then, the control and reliability of wet colloidal process is improved through the minimization of the influence of external conditions as humidity and temperature and a more homogeneous microstructure of the green body can also be expected (Tseng, 1999).

Table 3.2. Rheological parameters of the screening suspensions.

Dispersant concentration [dwb%]	Yield stress [Pa]	A	A-ø	ø/(A-ø)	Hysteresis area
0.96	0.97	0.380	0.090	3.22	19
1.02	0.89	0.398	0.108	2.69	4.5
1.20	1.27	0.395	0.105	2.76	6.2

3.3.1.2   Anode suspensions

Part I: Effect of solid loading on the flow behaviour of slurries and fired microstructures

The powder concentration has a significant influence on the rheological behaviour especially for high solid loading suspensions as shown in figure 3.13. The viscosity increases linearly from 70 to 83 wt% suspension while for the 85 wt% slurry, the viscosity increases greatly and agglomeration probably takes place in larger extent. Figure 3.13 (b) shows the shear thinning behaviour for 70, 80, 83 wt% suspensions and the viscosity increases with the solid loading as expected (Liu, 2000).
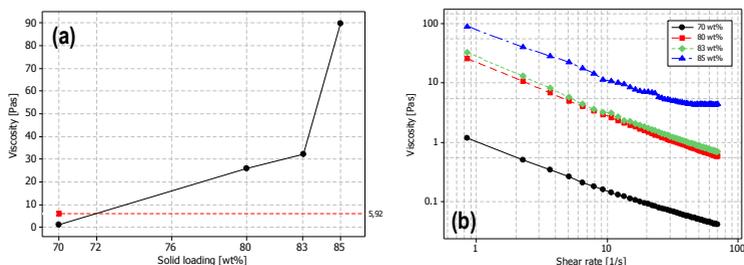
Figure 3.13. Rheological behaviour of anode suspensions. Viscosity versus solid loading (a) and viscosity versus shear rate in logarithmic scale (b).

The 85 wt% suspension moves partially away from a shear thinning behaviour and its viscosity curve tends to a constant value at higher shear rates. This trend resembles the behaviour of non-Newtonian fluids characterized by two plateau of constant viscosity, Newtonian regions, occurring at very low and very high shear rates (Barnes, 1989). It is clear that beyond a certain solid concentration, i.e. 83 wt%, repulsive forces between particles are not effective anymore regardless the good surface coverage by the dispersant. This occurs for the 85 wt% slurry where the attractive particle-particle interactions are favoured by the reduced interparticles distance occurring at high solid concentrations and prevail over repulsive forces at high shear rates (Liu, 2000). For 70, 80 and 83 wt% suspensions the shear thinning effect is evident and the viscosity decreases with the shear rate because of shear induced disruption of the agglomerates (Bonekamp, 1996). Conversely, for the 85 wt% slurry probably equilibrium between the formation and breakage of agglomerates is achieved at higher shear rates (Krieger, 1959). An alternative hypothesis considers the agglomerates as dense and compact when formed at high shear rate and therefore their breakage is prevented. In this way, at a given solid concentration, the effective distance between particles and/or agglomerates increases with the effect of more Newtonian flow behaviour. Moreover, the optimization of dispersant has the advantage of achieving higher solid concentration due to a better packing efficiency. In fact, as shown in figure 3.13 (a), at viscosity of 5.92 Pa s corresponds a 72 wt% solid loading for the slurry with optimized dispersant but also a 70 wt% solid loading suspension without optimized dispersant as pointed out in figure 3.11 (a) for the pristine suspension (0.615 dwb%). As a result, the optimization of the dispersant allows to obtain higher solid loading for a given viscosity value. In addition, the flow behaviour of suspensions can be described by an empirical power-law dependence (Reed, 1995):

$$\eta = K\dot{\gamma}^{n-1} \tag{3.5}$$

68

where η is the viscosity, K the consistency index and n is the power-law index or shear thinning constant. n values lower than 1 indicate a departure from Newtonian behaviour towards an increasing shear thinning behaviour.
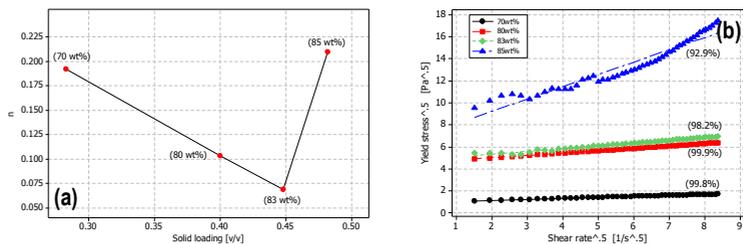

Figure 3.14. Power-law index n versus solid loading (a) and Casson model with correlation coefficient in parenthesis (b) for anode suspensions.

From figure 3.14 (a) and table 3.3 it is shown that the index n decreases with solid loading and consequently an increasing shear thinning behaviour occurs from 70 to 83 wt% solid loading. Beyond this solid concentration, i.e. 83 wt%, the trend changes to a greater n index value and another flow behaviour should be expected. The power-law model confirms the closer Newtonian trend of flow curve regarding 85 wt% slurry as shown in Figure 3.13 (b). Once again, the 85 wt% slurry is not well fitted by Casson's model as a further confirmation of the weak shear thinning behaviour compared to the 70, 80 and 83 wt% suspensions which are well fitted by the equation 3.4 with correlation coefficient between 98.2 and 99.9% as shown in figure 3.14 (b). For all suspensions, the yield stress increases with the solid loading according to previous results (Liu, 2000). The yield stress is also linearly related to the flow resistance parameter $ø/(A-ø)$ when shear thinning suspensions, i.e. 70, 80, 83 wt% ones, were taken in account as shown in figure 3.15 (a). The increase of flow resistance parameter reveals an increase of powder agglomeration with solid concentration for the 70, 80 and 83 wt% suspensions. When 85 wt% slurry is considered the linear trend between yield stress and flow resistance parameter is lost and this can be associated to the shift of shear thinning region to lower shear rates as shown in figure 3.13 (b). Once again, this can be explained by considering the presence of agglomerates characterized by a critical size where the disintegration is limited (Macosko, 1994).

Table 3.3. Rheological parameters of anode suspensions.

Suspension [wt%]	Yield stress [Pa]	Power-law index, n	(n-1)	A	ø	ø/(A-ø)
70	0.89	0.192	-0.808	0.3875	0.2822	2.68
80	20.8	0.103	-0.897	0.4335	0.3992	11.6
83	23.5	0.068	-0.932	0.4816	0.4460	12.5

| 85 | 50.6 | 0.210 | -0.790 | 0.4919 | 0.4814 | 46.0 |

In addition, the change in flow behaviour as indicated by figure 3.14 (a) corresponds to a critical solid concentration, i.e. 83 wt%, for the shift of shear thinning region as point out by de Kruif in (Larson, 1999; Macosko 1994) where a critical yield stress versus solid concentration reveals the shear thinning shift and resembles analogous trend of power-law index stressed in figure 3.14 (a). The rheological behaviour of slurries and especially for those highly concentrated is fitted by Krieger-Dougherty equation, here written in linear form (Everett, 1988):

$$ln(\eta_r) = -[\eta]Aln(1 - \frac{\phi}{A})$$ (3.6)

Where η_r is the relative viscosity, $[\eta]$ the intrinsic viscosity, A the maximum solid concentration, ϕ the volume fraction of particles including oxide powders as well pore former and ϕ/A represents the relative density or packing fraction of suspension.
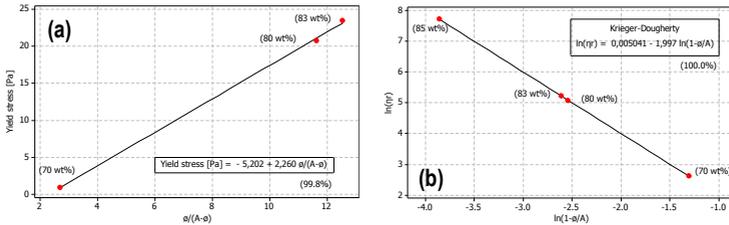
Figure 3.15. Yield stress vs flow resistance parameter (a) and Krieger-Dougherty model (b) with respective linear expression and correlation coefficient (99.8 and 100.0% respectively) for anode suspensions.

The rheology of suspensions is well fitted by Krieger-Dougherty model over the entire solid loading, 70-85 wt% with slope $[\eta]A$ of -1.997 very close to the theoretical value -2.0 and table 3.4 summarizes the rheological parameters along with the chemical compositions of anode slurries. From table 3.4 it is clear that the increase of ϕ/A with solid loading up to values larger than typically 0.64 and 0.74 respectively for the random and maximum close-packing of monosize spheres.

Table 3.4. Rheological parameters and chemical composition of anode suspensions.

Suspension [wt%]	ϕ	ϕ_{pf}	$\phi_{(pf+w)}$	A	$[\eta]$	ϕ/A
70	0.2822	0.0362	0.7397	0.3875	5.16	0.728
80	0.3992	0.0512	0.6317	0.4335	4.61	0.921
83	0.4460	0.0573	0.5886	0.4816	4.15	0.926
85	0.4814	0.0618	0.5559	0.4919	4.07	0.979

This is justified by the evidence of slurries far from a system characterized by monosize particles especially for the presence of graphite flakes. In fact, asymmetric particles such graphite ones (figure 3.10) can assume hexagonal order (two-dimensional) at high shear rates and in these conditions a good dispersion of highly concentrated suspensions can achieve packing fraction values close to 0.96 (Larson, 1999). In addition, particles stabilized by adsorbed layer like dispersant molecules experience a compression of such layer increasing with solid concentration. In this circumstance, the deformability of adsorbed layer has the effect of increasing the effective solid concentration. This effect can be supported by considering the 83 and 85 wt% suspension for which an increment of 7.9% in solid fraction corresponds to an increase of 5.7% on the relative density of suspension. Conversely, only a slight increase of 0.5% of relative density regards the 80 and 83 wt% slurries characterized by 11.7% solid concentration increment. Another observation from table 3.4 regards the value of intrinsic viscosity *[η]* that is different from 2.5 derived from Einstein formula describing an ideal dilute suspension of spherical particles for which the flow of one particle is practically not influenced by neighboring particles. For concentrated suspensions multiple interactions between particles increase, with the result of larger intrinsic viscosity and simultaneously the maximum solid concentration *A* diminishes to keep constant the product *[η]A* to 2. This assertion involves also suspensions with nonspherical particles, where the intrinsic viscosity raises as the increasing of the aspect ratio of particles keeping again constant the product *[η]A* to 2 (Genovese, 2012). From table 3.4 the intrinsic viscosity decreases with the increment of the solid loading *ø* and pore former volume fraction *$ø_{pf}$*. This apparent contradiction can be related to the arrangement of particles during high shear rates where equation 3.6 is applied. In this condition spherical and non-spherical particles, i.e. graphite flakes, align along shear direction minimizing their interactions though the reduction of free volume with solid loading. The ordering and packing density of particles are related to the free volume, in such case the solvent volume. Basically, as the ordering is established the free volume although contracts, results distributed more homogeneously over each particle (compared to a loose packing density) and this favours positional fluctuations of particles and rises their vibration entropy that largely compensates the decrease on the configurational entropy of the system giving rise a repulsive contribution to the particles (Larson, 1999). Then, orientational orderings are substantially controlled by repulsive forces determined by excluded-volume interactions which are short-ranged and responsible for instance for the short range structure of liquids and the ordering transition of liquid crystals (Larson, 1999; Frenkel, 1999). Similarly, excluded-volume forces conceive systems of colloidal charged particles where the repulsion mainly arises from the entropic (osmotic) pressure of counterions as particle surfaces approach each other (Israelachvili,

1996). Consequently, as the packing fraction of suspension increases with solid concentration, the free volume encompasses more efficiently the particles, which get closer and arrange in an ordered structure governed by excluded-volume interactions with the consequence of decreasing the intrinsic viscosity. Table 3.4 also points out the volume fraction of pore former and water $\varnothing_{(pf+w)}$, that represents the free volume not occupied by ceramic powders and therefore the total porosity of the body after firing when any shrinkage is prevented throughout drying, burn-out of pore former and sintering (Gregorová, 2011). As a result, $\varnothing_{(pf+w)}$ identifies the upper limit of porosity value for sintered compacts derived from slurries formulated with pore former; $\varnothing_{(pf+w)}$ decreases with solid concentration as expected and repoted in table 3.4. In addition, from equation 3.6 the relative viscosity is very sensitive to solid concentration and small error in the determination of $\varnothing$ leads to significant error in the estimation of suspension viscosity (Larson, 1999). Figure 3.15 (b) shows good fitting as a consequence of a good consistency of reological measurements justified by an appropriate preparation of the anode suspensions as well as estimation of the maximum solid concentration *A*. For this reason, it is reasonable to pursue a link between the slurry composition and rheological parameter of anode slurries. The graph of figure 3.16 (a) exhibits an interesting and tough relation between the chemical composition of suspension and the relative maximum solid concentration:

$$\frac{\varnothing_{(pf+w)}}{A} = 3.038 - 4.000\ \varnothing \qquad (3.7)$$
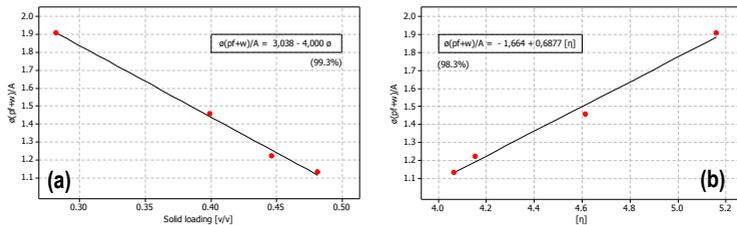
Figure 3.16 Relation of the normalized volume fraction of pore former and water vs solid loading (a) and vs intrinsic viscosity (b) with respective linear expression and correlation coefficient (99.3 and 98.3% respectively) for anode suspensions.

The volume fraction of pore former and water $\varnothing_{(pf+w)}$ should scale with the total porosity of fired body and it can be also conceived as the residual free volume existing after drying, burn-out and densification steps. Giving heed to slurry systems, this volume fraction when normalized to the maximum solid concentration *A* represents how this apparent free volume should spread over throughout the suspension and in particular over each suspension components at maximum packing density. From figure 3.16 (a) is clear that slurry components experience a

lower free volume fraction as the solid concentration rises. In addition, the normalized volume fraction of pore former and water $ø_{(pf+w)}/A$ displays an growing trend with the intrinsic viscosity $[\eta]$ as evident from the panel 3.16 (b); an analogous growing trend occurs when the normalized volume fraction of water $ø_w/A$ is considered. This latter can be considered more representative and close to the previously assertion on the exclude-volume regarding the ordering and packing of particles otherwise slurry structure. Nonetheless, the concept of the free volume concerning a more efficiently distribution of solvent with the packing and ordering of solid phase holds and is fundamentally confirmed by graphs of figure 3.16 where the lowest value of the intrinsic viscosity entails the slurry with the highest solid loading characterized by the lowest free volume. The linear relation of the normalized volume fraction of pore former and water $ø_{(pf+w)}/A$ with intrinsic viscosity $[\eta]$ is described by eq. 3.8 with correlation coefficient of 98.3%:

$$\frac{\emptyset_{(pf+w)}}{A} = -1.664 + 0.6877\,[\eta] \tag{3.8}$$

Equation 3.8 results more reliable compared to that considering the water volume fraction over the maximum solid concentration $ø_w/A$, regardless similar correlation coefficient, i.e. 98.0%. In fact, in this latter case when the right side of equation is set ≥ 0, the lowest value of $[\eta]$ is 2.62 whereas for eq. 3.8 is 2.42. In this case, the lower bound is closer to the theoretical value 2.5 for dilute suspensions while for anode slurries the evaluation of $[\eta]$ provides 5.20, 4.54, 4.20 and 4.06. These values are the same of those reported in table 3.4 within experimental error, i.e. 1.5%. Therefore, the expression 3.8 is consistent from a physical point of view and pave the way to a possible estimation of the intrinsic viscosity for a wide range of suspensions from those dilute to highly concentrated ones as demonstrated by anode slurries. Additionally, the maximum solid concentration A can be estimated from the composition of slurry in terms of the volume fraction of pore former and water $ø_{(pf+w)}$ and solid concentration $ø$ by rearranging the equation 3.7 that is valid for solid loading between 70 and 85 wt% with correlation coefficient of 99.3%:

$$A = \frac{\emptyset_{(pf+w)}}{3.038 - 4.000\,\emptyset} \tag{3.9}$$

Equation 3.9 is very interesting because it allows the estimation of maximum solid concentration A and the flow resistance parameter $ø/(A-ø)$ without any rheological measurements, only by know the slurry composition. Furthermore, the maximum solid loading is obtained by setting the right side of the equation ≤ 1 (and the denominator > 0). For the anode suspensions, the maximum solid concentration is 0.5095 v/v that corresponds to 85.5 wt% slurry or 0.4909 on volume base. At this

solid concentration, the available space *(A-ø)* of particles freely moving throughout the system tends to zero. As the solid loading approaches the value 85.5 wt% much of the colloidal suspension behaves as a paste. At this point the flow resistance parameter *ø/(A-ø)* can be easily calculated as well as the yield stress by adopting the equation in the inset of the figure 3.15 (a). This linear expression of yield stress with flow resistance parameter is valid in the range of 70-83 wt% suspensions with correlation coefficient of 99.8% and here expressed:

$$\tau_y = -5.202 + 2.260 \left(\frac{\phi}{A-\phi}\right) \tag{3.10}$$

Finally, the estimation of the yield stress τ_y of shear thinning suspensions is determined by know exclusively the composition of slurry thoroughout the equation 3.9 and 3.10 by determing sequentially the maximum solid concentration *A* and flow resistance parameter *ø/(A-ø)*. Again, it is possible to evaluate the maximum solid concentration for which the yield stress arises when the equation 3.10 is set equal to zero. This occurs when *ø/(A-ø)* is greater than 2.30, corresponding to a slurry of 0.2666 v/v solid concentration (or 68.3 wt%) characterized by *A* value equal to 0.3825. At solid loading larger than 68.3 wt% a yield stress even slight should appear; this estimation is based on the validity of the extrapolation of *A* value through the equation 3.9 beyond the lower bound, i.e. 70 wt%. So far, elements for the estimation of the yield stress are provided and merges into the equation 3.10.
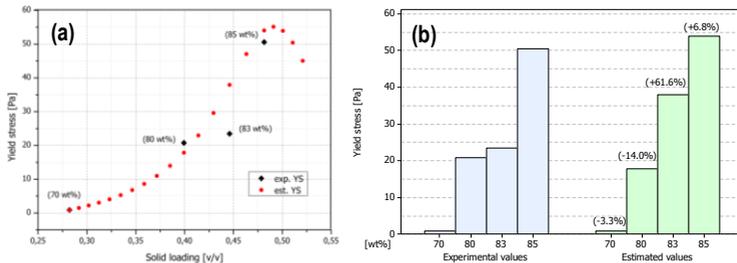
Figure 3.17 Yield stress with experimental and estimated values of the anode slurries vs solid loading throughout 70 and 87 wt% concentration (a) and bar chart of the experimental and estimated values for 70, 80, 83 and 85 wt% slurries with relative errors in parenthesis (b).

Figure 3.17 (a) shows the trend of the yield stress as a function of solid loading throughout the solid loading 70 and 87 wt%. Basically, the model of yield stress as a function of the flow resistance parameter fits very well experimental data for shear thinning slurries as reported by Liu et al. (Liu, 1998; 1999). Even in the current work, experimental yield stress values are well represented by flow resistance parameter derived from experimental values of *A* as displayed by the graph of figure 3.15 (a).

Conversely, when the flow resistance parameters result from the determination of the *A* value through the expression 3.9, the estimated values of yield stress are very different from the experimental ones in particular for 80, 83 and 85 wt% slurries as displayed in both panels of figure 3.17. The accuracy of the equation 3.10 is clearly low as indicated by large relative errors and depends probably on the determination of *A* at higher solid loadings. Nonetheless, interesting observations can be made in Fig. 3.17 (a). In fact, a change on the trend of the yield stress is revealed at concentration just above the 85 wt% slurry. Specifically, this divergence of yield stress curve occurs at 85.5 wt% solid loading, the same value previously predicted by the expression of *A*, i.e. Eq. 3.9, derived exclusively from the composition of suspensions. Hence, according to previous assessment, it is expected a transition of flow behaviour of colloidal suspension when the solid concentration approaches the maximum solid loading; this transition is here qualitatively dipected by the changeover of the graph 3.17 (a). These considerations reveal that flow resistance parameter derived from experimental *A* values well describes shear thinning suspensions, i.e. 70, 80 and 83 wt% ones as shown in figure 3.15 (a) whereas the determination of flow resistance parameter from slurry composition just indicates qualitatively the transition of the flow behaviour of the anode slurry system as the solid loading approaches the concentration of 85.5 wt%. Then the flow resistance parameter derived from slurry composition mantains same information of *A* values, determined by the expression 3.9 like the maximum solid loading, i.e. 85.5 wt% and consequently a connection between them evidently emerges. For these reasons, the following analysis focus more accurately on the relation of *A* with the slurry composition in order to predict the flow behaviour, in terms of yield stress, of high solid loading suspensions, i.e. 80, 83 and 85 wt% ones, for which the model described by equation 3.10 fails. The first step involves the determination of additional *A* values from the experimental ones between the range 80-85 wt% solid concentration, specifically at intermediate values, i.e. 81.5 and 84 wt% in order to pursue an enhanced fitting in case the linear one is not adequate. In fact the previous computation of the yield stress by the equation 3.10 is implicity not restricted to 70-83 wt% slurries since no constraints are applied for the calculation of the flow resistance parameter other than the solid concentration; this assumption can be not apt for the estimation of yield stress upon a larger range of solid concentrations and in particular for the higher ones. Then, intermediate *A* values are calculated and reported in table 3.5 along with composition data of the suspensions in term of solid concentration ø, pore former fraction $ø_{(pf)}$ as well as pore former and water fraction $ø_{(pf+w)}$ with their normalized values to the maximum solid concentration *A*.

Table 3.5. Composition of anode suspensions with normalized values respect to the maximum solid concentration.

Suspension [wt%]	ø	ø$_{pf}$	ø$_{(pf+w)}$	A	ø/A	ø$_{(pf+w)}$/A
80	0.3992	0.0523	0.6317	0.4335§	0.9209	1.457
81.5	0.4218	0.0553	0.6110	0.4563*	0.9243	1.339
83	0.4460	0.0586	0.5886	0.4816§	0.9261	1.222
84	0.4633	0.0609	0.5727	0.4867*	0.9519	1.177
85	0.4814	0.0633	0.5559	0.4919§	0.9787	1.130

§ Experimental values, * Intermediate values obtained by harmonic average of lower and upper experimental *A* values, i.e. 80 and 83 wt%, for the 81.5 wt% suspension

From table 3.5, the values of the packing density of suspension *ø/A* increases with solid concentration similarly to those in table 3.4 while the normalized volume fraction of pore former and water *ø$_{(pf+w)}$/A* decreases in according to the graph of figure 3.16 (a). This latter is represented as a function of solid loading for 80, 81.5, 83, 84 and 85 wt% suspensions and reported in figure 3.18 (a); the arrows indicate the values derived from experimental *A* values.
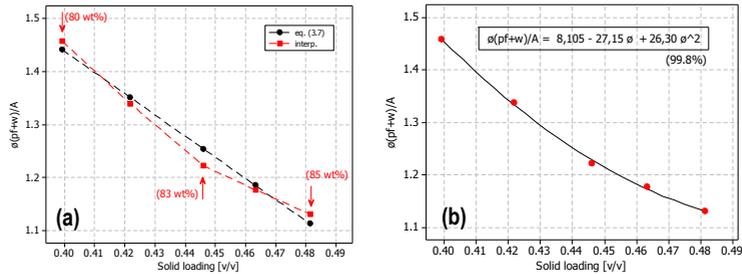
Figure 3.18 Normalized volume fraction of pore former and water versus solid loading from experimental and intermediate *A* values in comparison with that derived from the equation 3.7 (a) and the quadratic fitting with relative formula in the inset (b) for the suspensions in the table 3.5.

The normalized volume fraction of pore former and water *ø$_{(pf+w)}$/A* is considered as apparent free volume, AFV, for the slurry systems and is expressed as linear expression of the solid concentration, i.e. eq. 3.7, as shown in figure 3.18 (a) along with a nonlinear trend related to the extra intermediate values. Specifically, experimental and intermediate values of the AFV are well described by parabolic law at high solid loading, (i.e. greater than 80 wt%), with correlation coefficient of 99.8% as exhibited in figure 3.18 (b) and here reported:

$$AFV \equiv \frac{\varnothing_{(pf+w)}}{A} = 26.30\varnothing^2 - 27.15\varnothing + 8.105 \tag{3.11}$$

76

In order to find out a consistent expression of the AFV upon a wide range of solid loading, and in turn a reliable estimation of A values for modeling the yield stress of anode slurries, it is necessary to elucidate the validity interval for AFV expressions, i.e. linear and quadratic form, firstly focusing on this latter. The quadratic expression 3.11 of the experimental AFV is arranged in a more general form:

$$AFV \cong k\emptyset^2 - k\emptyset + c = k\emptyset(\emptyset - 1) + c \qquad (3.12)$$

The expression 3.12 is a quadratic equation and hence provides two solutions or roots for each concentration value. For $k < 4c$ the discriminant is negative and in such a case two complex (non-real) roots are the solutions of the equation as the case in point for the formula 3.11 as for its arranged form, i.e. equation 3.12, with constant k close to 27 and constant c equal to 8. This means that AFV assumes strickly positive values for any value of solid concentration. The constant c is independent with the solid concentration while the constant k is related to powder concentration and therefore to some characteristic of the system in point similarly to the A value that is correlated to the shape and particle-size distribution of powders (Barnes, 1989). In what follows, the general meaning of the equation 3.12 is not affected by the assignment of value 8 for the constant c since it is independent on the solid loading.

$$AFV = k\emptyset(\emptyset - 1) + 8 = \begin{cases} 8, & for \ \emptyset \to 0 \\ 8, & for \ \emptyset \to 1 \end{cases} \qquad (3.13)$$

Equation 3.13 is restricted between two limits such as extremely high concentration and extreme dilution. For this latter the solvent fraction overwhelms the pore former fraction and therefore the numerator $\emptyset_{(pf+w)}$ converges to $\emptyset_{(w)}$ that tends to 1 due to the extreme dilution; the corresponding A value is 0.124 determined by the formula 3.11. In this circumstance the solvent, i.e. water, surrounding the suspended powders is largely predominant and really represents the free volume of the suspension system at extreme dilution. The value of the free volume tends to 8 (that is 1/0.124); we just recognized this value corresponding to the excluded-volume of a sphere for the extreme dilution as well as extreme concentration. At this point, the expression 3.13 is further developed and the constant k hires the role of fitting parameter, i.e. 27.40, after keeping the value 8 for the constant c. Its trend is smooth and similar to that of the equation 3.11 as shown in figure 3.19 (a) along with the fitting formula.
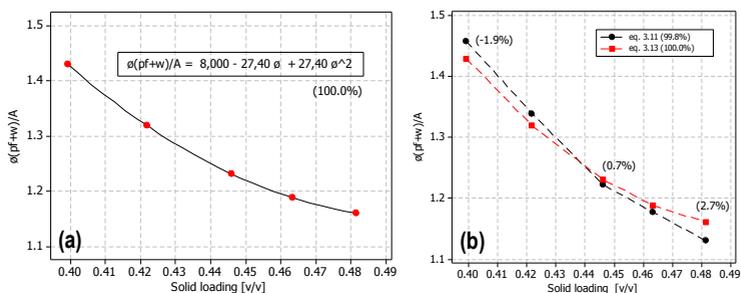
Figure 3.19 Normalized volume fraction of pore former and water or AFV as a function of solid loading with fitting parameter k equal to 27.40 for the equation 3.13 (a) and its comparison with the fitting formula 3.11 of figure 3.17 (b) with relative errors between experimental and fitted AFV values in parenthesis (b).

Nonetheless, the adjustment of constant c and parameter k brings about slight difference between AFV values derived from experimental A values and those fitted by the equation 3.13 as highlighted in figure 3.19 (b). The concistency of the equation 3.13, that is the approximate form of the 3.11, is evident after adjusting the c value as well ad-hoc choice for the parameter k with the implication of expressing the formula 3.11 in a more compact and general form without producing significant errors, i.e. $\leq 2.7\%$. Now it is interesting to perceive the impact on the estimation of A values from the different equations of AFV in comparison with the experimental A values. Table 3.6 sums up experimental A values along with those determined from equations 3.11, 3.13 and 3.7 with relative errors.

Table 3.6. Comparison of experimental A values with those estimated with equations 3.11, 3.13 and 3.7 with relative errors.

Suspension [wt%]	ø	A				Relative error [%]		
		Exp.	Eq. 3.11	Eq. 3.13*	Eq. 3.7	Eq. 3.11	Eq. 3.13*	Eq. 3.7
80	0.399	0.434	0.433	0.442	0.438	-0.03	2.04	1.13
81.5	0.422	-	0.459	0.464	0.452	-	-	-
83	0.446	0.482	0.480	0.479	0.469	-0.44	-0.62	-2.53
84	0.463	-	0.489	0.483	0.483	-	-	-
85	0.481	0.492	0.492	0.480	0.500	0.03	-2.53	1.61

* AFV = $27.40ø^2$ - $27.40ø + 8.0 = 27.40ø(ø - 1) + 8.0$

As expected, the values derived from the equation 3.11 are close with the experimental ones whereas any apparent difference arises between those yielded by the quadratic equation 3.13 and the linear equation 3.7 both with relative errors within 2.6%. In order to discern the underlying features of the linear and quadratic expressions, a graphical representation of A values along with the available space

78

(A-ø) representing the volume of particles freely moving throughout the suspension, is illustrated in figure 3.20 (a) and (b), respectively.
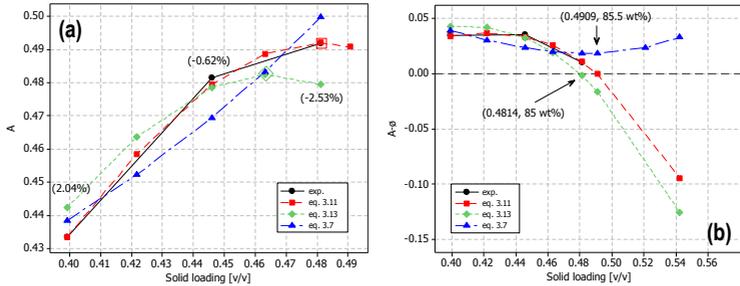

Figure 3.20 Maximum solid concentration *A* and available space *(A-ø)* behaviour as a function of solid loading respectively in (a) and (b). Estimated *A* values from equations 3.11, 3.13 (AFV = 27.40ø^2 - 27.40ø + 8.0) and 3.7 in comparison with experimental values.

From figure 3.20 (a) it is evident the difference of the trend for the maximum solid concentration estimated by the the quadratic and linear equation, respectively 3.11 and 3.7. This latter exhibits a linear increase of *A* with solid loading without point of maximum. Therefore, the maximum solid concentration for the system in point expands indefinitely with the addition of the solid phase. This is clearly unreal since it resembles a special case of ideal packing of particles avoiding any crowding effects in contrast with the expected reduction on the free volume with solid loading. On the contrary, the quadratic equation 3.11 and its approximate form, i.e. 3.13, show parabolic trends of the maximum solid concentration identified by maximum points where nearby the available space *(A-ø)* goes to zero respectively at solid loading 85 and 85.5 wt% as shown in figure 3.20 (b). Consequently, the parabolic trend of *A* suggests a difficulty on the packing of powders with solid concentration as expected by the inherent reduction on the free volume and thus crowding effects are conceived. Finally, experimental *A* values are well estimated by the equation 3.11 and also qualitatively by the approximate form 3.13 for anode suspensions of high solid loading. In addition, the resulting available space *(A-ø)* seizes negative values indicating the transition from a liquid-like system, i.e. colloidal suspensions, to a solid-like structure as the solid loading approaches the maximum solid concentration as highlighted in figure 3.21 (a) in contrast with *(A-ø)* derived from the linear equation 3.7 for which just an inflection point is showed at 0.4909 v/v precluding the zeroing of the function *(A-ø)*. The behaviour of highly concentrated slurries is described in a loose way by the linear AFV equation. This point further strengthens the validity of the quadratic equation of the AFV for which *(A-ø)* reaches zero and the negative values remind the Kauzmann's paradox where in place of the glass transition temperature, a critical or maximum solid loading identifies a transition of the system,

specifically from a liquid-like one to a solid-like system. The quadratic form of the AFV holds for highly concentrated slurries with solid loading between 80 (0.3992) and 85.5 wt% (0.4909 v/v) and its range of validity is shown in the graph of figure 3.21 (b) along with that of the AFV linear law.
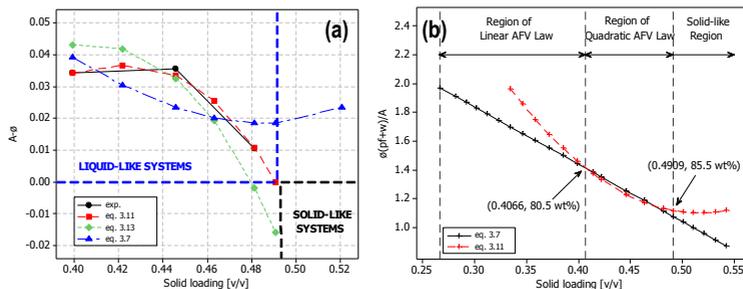

Figure 3.21 Available space *(A-ø)* behaviour as a function of solid loading where liquid and solid regions are highlighted (a) and range of validity of AFV expressions (b).

The slight difference on solid concentration concerning the boundary between the linear and quadratic expression of AFV, i.e. 0.3992 and 0.4066, corresponds to 1.9% and can be related to the approximation of *A* values from the equation 3.7 and 3.11. For the upper limit, the solid concentration value is determined by the zeroing of the function *(A-ø)*; it spans between 0.4814 and 0.4909 v/v by the equation 3.13 and 3.11 respectively. This variation is clearly associated with the expression adopted and hence to the approximation but the uncertainty can be also connected to other aspects. In fact, the function *(A-ø)* seizes zero sligthly beyond the maximum value of *A* as point out in the panel (a) of figure 3.20. This can be related to the compression of the dispersant adsorbed layer that arises just as the solid phase approaches the critical solid loading. So far, the assumption of hard-sphere interactions holds as conceived by the Kriegher-Dougherty model as well as the determination of *A* through the AFV functions with reasonable accuracy as proved by the comparison with experimental *A* values shown in table 3.6. Under this perspective the assumption of hard-sphere interactions is confirmed for the anode system and as proposed by Tadros, the change on the flow behaviour from liquid-like to solid-like can be identified by the maximum hard-sphere volume fraction instead of the generic aforementioned definition of critical or maximum solid loading (Tadros, 2011). In addition, the approximation of hard-spheres is related to the extent of screening length or Debye length, k^{-1}, that is shorter than the center-to-center distance between particles in contrast to soft-spheres which are characterized by not negligible thickness of adsorbed layer (Xia, 2000). The assumption of hard-spheres involves just a repulsive interaction when particles come to close contact and it is considered

to be of general validity even the likely compression of adsorbed layer occuring when the solid concentration is close to the maximum hard-sphere volume fraction that is 0.4909. In proximity to these high solid concentrations the particles arrange themselves to form an order array. For a monodisperse system governed by repulsive hard-spheres interactions, a phase transition is envisaged at 0.5 and it is known as Kirkwood-Adler fluid-solid transition (Greenwood, 1997). In particular, this transition results at solid concentration of 0.494 (freezing transition) and is completed at 0.545 (melting transition) if the system is monodisperse with standard deviation ≤ 5% as predicted by theoretical, simulation and experimental studies (Brader, 2010; Gasser 2009; Kose, 1974; Hachisu, 1974). This situation is not always found experimentally and a possible cause concerns the polydispersity (Anderson, 2002). For polydispersity higher than 5%, the freezing transition is expected to shift to higher volume concentration and eventually it is suppressed up to 0.60 volume fraction for polydispersity ≥ 8% as underlined by experiments and theoretical analysis (de Schepper, 1996). Other recent studies demonstrate the polydispersity does not necessary impede the formation of solid ordered structures (Gasser, 2009). Indeed, freezing transition occurs even for polydispersity up to 15% when the fractionation of larger particles is allowed. In this case the fractionation is differently distributed between the solid and fluid phases, i.e. nearly 6 and 12% respectively, and avoiding any glass transition for the liquid phase (Kofke, 1999; Martin, 2003). The so far systems have concerned binary mixture of spherical particles with different polydispersity degree and size ratio below 0.9 for which the fluid-solid or disorder-order transition is similar to that predicted for the monodisperse hard-sphere systems (Phan, 1996; Henderson, 1998). In addition, it is worth to note that monodisperse hard-sphere systems with standard deviation ≤ 5% exhibit a shift of the freezing and melting transitions to lower values, i.e. 0.38 and 0.42 respectively, when particles present a small charge (Gasser 2001; Anderson 2002). At this point, freezing and melting transions can occur either at higher or lower values than 0.494 and 0.545 depending on the polydispersity and charge effects. Under this point of view the value 0.4909 obtained here independently from the function *(A-ø)* as well 0.5 ensued by the minimum of the parabolic AFV function, i.e. equation 3.12, can represent either the freezing or melting transition of the anode system according to the extent of the polydispersity and charge effects. For the anode system, the assumption of hard-sphere interactions is reasonable for the highly concentrated suspensions and therefore the polydispersity issue results of main interest. Then, the solid phase of each anode slurries is composed by a mixture of 87.2% of NiO and YSZ powders and 12.8% of graphite powder by volume. The average size of this latter, i.e. 7 μm, is one order of magnitude greater than the NiO and YSZ ones, 0.3 μm, according to the manufacture specifications of the as-received powders that are indeed not monodisperse (within 5% of standard deviation). As a consequence, the

suspended powders can be perceived as a "sea" of small particles of spherical-like shape of similar size, i.e. NiO and YSZ, with relative few large and anisotropic particles, i.e. graphite ones. This observation is of general soundness even if the intrinsic brittleness and exfoliation features of pore former powder must be considered and thus a variation of size is also envisaged for the graphite flakes. In particular, it is likely a size reduction of the as-received graphite powder with the increase on the solid concentration due to higher extent of particle-particle interactions, i.e. during milling, with a consequent change of the PSD of graphite. Subsequently, the polydispersity of the anode system varies with solid loading and in turn, the difference of the PSD among the as-received powders is expected to change. This results on a decrease of the intrinsic viscosity with a concomitant increase of the maximum solid concentration values with solid loading as displayed by the table 3.4. The increase of A is ascribed to an improved ordering and packing efficiency of particles determined by the change of PSD, principally related to the reduction on the size and aspect ratio of graphite powder. On the other hand, the ordering and packing density is also attributed to a more efficient distribution of the free volume that is here expressed by the AFV. Then, the intrinsic viscosity is connected to the maximum solid concentration and thus it is immediate to predict a different trend of $[n]$ from the linear behaviour shown in figure 3.16 (b) similarly to the parabolic AFV law for the highly concentrated suspensions. Before reporting a graphical representation of $[n]$ and A with solid loading, it is necessary to return to the validity range of AFV laws. According to the figure 3.21 (b), the upper boundary is set to 0.4909 for the quadratic form of the AFV corresponding to 85.5 wt% slurry, whereas the linear equation of the AFV is restricted between 0.4066 (80.5) and 0.2666 v/v (68.3 wt%) for which the yield stress arises in agreement with equation 3.10. The following expression points out the validity interval for the AFV throughout the solid loading 68.3 and 85.5 wt%:

$$AFV = \begin{cases} 3.038 - 4.000\emptyset, & 0.2666 \leq \emptyset \leq 0.4066 \\ 26.30\emptyset^2 - 27.15\emptyset + 8.105, & 0.4066 \leq \emptyset \leq 0.4909 \end{cases} \qquad (3.14)$$

Therefore from eq. 3.14, the maximum solid concentration A is easily determined.

$$A = \begin{cases} \emptyset_{(pf+w)}/(3.038 - 4.000\emptyset), & 0.2666 \leq \emptyset \leq 0.4066 \\ \emptyset_{(pf+w)}/(26.30\emptyset^2 - 27.15\emptyset + 8.105), & 0.4066 \leq \emptyset \leq 0.4909 \end{cases} \qquad (3.15)$$

Equation 3.15 describes the behaviour of the maximum solid concentration as a function of the slurry composition. In particular, A can be defined exclusively by the solid concentration because of the existence of a relation between the pore former and water fraction $\emptyset_{(pf+w)}$ and solid concentration $\emptyset$.

$$\emptyset_{(pf+w)} = 1 - 0.9224\emptyset \tag{3.16}$$

Equation 3.16 is valid throughout the whole solid concentration range of slurry system under investigation. Immediately, on the basis of eq. 3.16 and 3.15:

$$A = \begin{cases} (1 - 0.9224\emptyset)/(3.038 - 4.000\emptyset), & 0.2666 \leq \emptyset \leq 0.4066 \\ (1 - 0.9224\emptyset)/(26.30\emptyset^2 - 27.15\emptyset + 8.105), & 0.4066 \leq \emptyset \leq 0.4909 \end{cases} \tag{3.17}$$

Finally, the maximum solid concentration for anode slurries is expressed entirely by the solid concentration through two functions defined by specific solid loading range as highlighted by expression 3.17. The lower range of solid loading, i.e. $0.2666 \leq \emptyset \leq 0.4066$, identifies the setting of yield stress throughout the validity of the linear AFV function. This range corresponds to flocculated slurries at regime of low solid concentration in contrast to the high solid concentration regime of slurries with solid loading between 0.4066 and 0.4909 for which the AFV follows the parabolic trend. Consequently the AFV functional, group of different AFV functions, allows the estimation of *A* for any solid concentration of suspensions comprehended by the validity interval of the AFV functional, i.e from nearly 0.27 to 0.49, under the assumption of hard-spheres even for the lower solid loading range. In fact for hard-sphere systems, Newtonian flow is exhibited for solid loading up to 0.20 and 0.30 as reported respectively by Krieger and Lewis in agreement with the system in point for which the shear thinning flow is established at the concentration of 0.2666 (Krieger 1959; Lewis 2000). The dependence of the maximum solid concentration and its derivative on solid loading is represented in figure 3.22.
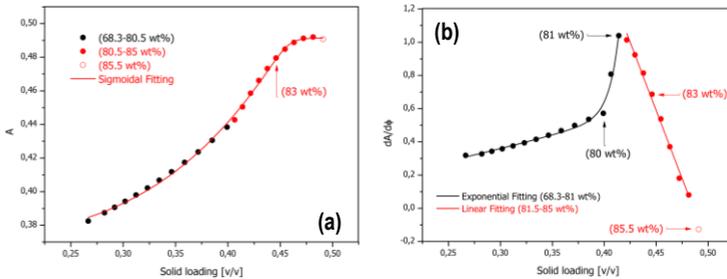
Figure 3.22 Maximum solid concentration (a) and its derivative on the solid loading (b) for the range ensued by the AFV functions, i.e. 0.2666-0.4909 v/v or 68.3-85.5 wt%.

The *A* vs *ø* graph of figure 3.22 (a) resembles a sigmoidal curve which is characterized by a positive derivative everywhere with a bell-like shape as shown in figure 3.22 (b). Generally many natural processes concerning biology, chemistry and so on are described by sigmoidal functions as well as other examples even arise

from the field of materials science such as the response of magnetic materials to an induced field (hysteresis loop) or the kinetics of certain solid state reactions. The common features of these phenomena is an initial stage of approximately exponential growth followed by a saturation period usually connected to a decaying phase. This is confirmed by the graph of the derivative of A which indicates a linear growth for the rate of A between 0.2666 and 0.3992 v/v (68.3-80 wt%) solid loading followed by a steep increase between 0.3992 and 0.4141 (80-81 wt%) and finally a linear decay up to 0.4814 (85 wt%). The empty circles in figure 3.22 denote the fluid-solid transition at 0.4909 (85.5 wt%) for which the derivative hires the only non-positive value. The maximum solid concentration A indicates the packing of particles and when it is determined at infinite shear rate as in the current analysis, it represents the maximum degree of ordering of particles for the specific system (Shapiro, 1992). At high shear rates, hydrodynamic force dominates over inter-particle interactions arising from dispersion forces, i.e. van der Waals one, and are intended to minimize the extent of particle flocculation (Doroszkowski, 1968). For a given solid loading, it is observed a reduction of A value with the increase on the flocculation degree of particles and of their aspect ratio (Liu, 1999; Genovese 2012). Additional experimental evidence indicates a constant and specific A value for suspensions composed by single ceramic powder even throughout an extensive range of the solid loading evaluated at infinite shear rate as reported by Liu (Liu, 2000). Similarly, A is a precise value even for polydisperse suspensions composed by multimodal ceramic powders or multi-PSD systems as proved by Farris. In this case, the maximum solid concentration can be optimized by a precise mixture of multimodal powders and it is reported an increase of A value from 0.84 to 0.94 respectively for bimodal to tetramodal system of spherical particles when flocculation is suppressed (Servais, 2002). Another parameter characterizing polydisperse suspensions is the size ratio of particles beloging to the different PSDs of the system. The highest packing fraction for polydisperse systems of spherical particles is attained with size ratio around 7 even for bi-, tri- and tetramodal PSD (Greenwood 1997; Servais 2002). Figure 3.22 (a) shows an increasing trend of the maximum solid concentration with solid loading up to a maximum value, i.e. 0.4909, recognized as the fluid-solid transition. This behaviour is ascribed to the variation of PSD since the determination of A is carried out in order to prevent any contributions from flocculation. In particular, the trend of A with solid concentration is suggested to rely on the PSD variation caused by the intrinsic brittleness and exfoliation feature of graphite (whose size and aspect ratio vary with solid loading) ensuing different arrangements of powders as shown in figure 3.22 (a) while the trend of packing density and intrinsic viscosity are displayed in figure 3.23.
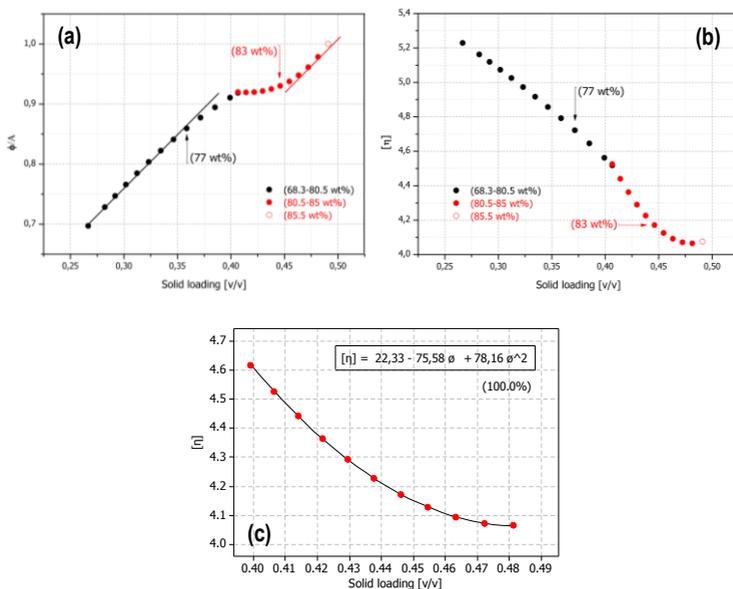
**Figure 3.23** Packing density (a) and intrinsic viscosity (b) and (c) as a function of solid loading for the range ensued by the AFV functions, i.e. 0.2666-0.4909 v/v or 68.3-85.5 wt%.

The packing density of the system *ø/A* should grow linearly with the solid concentration for those ceramic suspensions characterized by a precise *A* value as highlighted by Liu (Liu 2000). The variation of *A* is revealed by a change of the slope of *ø/A* versus *ø* graph scaling with *1/A* and emphasizes the effect of PSD change throughout the solid loading of interest as shown in figure 3.23 (a). Specifically, up to 77 wt% solid content, the linear growth of the packing allows to assume a constant value for *A*. Between 77 and 83 wt% the packing density increases with parabolic trend and levels off to 0.92 with the highest values of rate for *A* indicating higher efficiency of particle packing. Above 83 wt% (0.4460 v/v) the packing density takes again a nearly linear trend corresponding to an almost constant *A* value. The transition along 77 and 83 wt% concerns a region of high packing efficiency in the middle of two linear regimes of lower efficiency. Along this transition, the arrangement of particles is characterized by a specific blend ratio and size ratio with the free volume efficiently spread over throughout the solid phase although its reduction. The decreasing rate for *A* implies lower packing efficiency as a result of ineffective blend ratio and size ratio of particles. Under this point of view, the increasing fraction of smaller particles (due to the reduction size of graphite flakes) is a possible cause for the lower packing efficiency for solid concentrations exceeding 0.4460. At the same time, a significant diminution of the free volume and interparticle

distance is another possible reason for the hindered arrangement of particles. The plateau of packing density at 0.92 results between 0.3992 and 0.4296 (80 and 82 wt%), just lower than 0.4460 (83 wt%); this limit is fixed in regards to rheological properties of slurries as pointed out by the graphs of figure 3.13 where particle aggregation occurs extensively for concentrations greater than 04460. Up to this point, only the effect of PSD variation is considered for the particle packing excluding any effects arising from flocculation. In the following, the anode system will be outlined in a more realistic framework including the aggregation process and phase separation at high solid concentrations both driven by entropy as the fluid-solid transition (Kaplan, 1994). So far, the anode system is assumed as hard-spheres (HS) colloidal suspension composed predominantly by small spherical-like particles while the fraction of larger particles, i.e. graphite ones, is low and decreases with the solid loading. By assuming only repulsive interaction, a certain degree of polydispersity and fractionation of large particle, a fluid-solid transition has been predicted at solid concentration in agreement with that concerning monosize HS systems. For these systems, the colloidal particles experience only repulsive force of entropic origin, which also drives the phase transitions (Frenkel, 1999). A detailed investigation of systems composed by a binary mixture of HS involves phase separation and attraction force together the typical repulsive force (Biben, 1991; Kaplan, 1994). This attraction is analogous to the attractive "depletion" force arising in colloidal suspensions with non-absorbing polymer causing flocculation (Meijer 1991; Rahaman, 2003). Specifically, when small spheres outnumber the larger ones, the former provide the main contribution to the entropy of system (Kaplan, 1994). Each large sphere is characterized by a region of excluded volume where the small spheres cannot penetrate (depletion zone) as large spheres approach each other. When the depletion zones of large spheres overlap, the accessible volume for small spheres increases so that their entropy rises, resulting in a decrease of the system's free energy (Crocker, 1999). At the same time as the entropy of small spheres increases, an attractive depletion force acts between large spheres driving the phase separation and clustering of them (Biben 1991; Dinsmore, 1995). In addition, for binary HS systems the attraction force depends on the size ratio and fraction of small spheres. Then for a given size ratio, there is a critical solid concentration promoting attraction force of adequate magnitude for the occurrence of phase separation (Biben 1991, Xia, 2001). Experimental results and theoretical models demonstrate that phase separation precedes the fluid-solid transition and occurs at concentration lower than 0.494 concerning monodisperse systems (Kaplan 1994; Dinsmore, 1995). The role of the attraction force is evident and suggests the assumption of binary HS system accurate for the anode suspensions extending their understanding of rheological and structural properties as well as thermodynamic behaviour in term of phase transitions. Following this assumption, the substantial change of rheological

behaviour of slurries for concentration greater than 0.4460 (83 wt%) is related to the occurrence of particle aggregation due to the attraction force as pointed out by the graphs of Fig. 3.13. The shear thinning behaviour of 70, 80 and 83 wt% slurries involves the breakage of agglomerates for moderate shear rates, i.e. 1-70 s^{-1}. For the 85 wt% slurry, the lower extent of shear thinning region as stressed by the Newtonian plateau is related to the formation of dense and compact aggregates due to irreversible flocculation already at low shear rate, i.e. 40 s^{-1}. This means that A is affected by the presence of aggregates above the critical concentration of 0.4460 suggesting that the irreversible flocculation cannot be prevented below a critical distance between particles, regardless the estimation of A at infinite shear rate, because of the dominance of attractive interaction over hydrodynamic and repulsive forces at short distances. This experimental evidence is also proved by simulation studies of concentrated colloidal suspensions where van der Waals and contact forces dominate Brownian, hydrodynamic and electrostatic forces at short interparticle distance (Fujita, 2007; Fujita, 2008). At this point, the trend of $ø/A$ beyond the critical concentration 0.4460 is explained by the occurrence of irreversible flocculation extending the role of PSD not only on the packing density but also on the aggregation process for a binary HS system whose PSD changes along the overall solid loading not only due to the exfoliation of graphite but also to the formation of particle agglomerates. Then, as long as the occurrence of attraction force, the PSD variation is related to the exfoliation of graphite and has a beneficial effect on the packing density until its plateau at 0.92 arising between 80-82 wt% (0.3392-0.4296 v/v) where the slurry composition is characterized by an optimal blend ratio and size ratio of particles as affirmed by high efficiency of packing. Above 0.4460, as the interparticle distance reduces with solid concentration and the fraction of smaller particles increases due to the reduction size of graphite, the depletion zones of residual large particles are esteemed to overlap. As a result, attractive depletion force arises and causes the phase separation of larger particles and their cluster along with the likely aggregation of smaller particles promoted by the reduced interparticle distance. The overall effect of both aggregation processes is the slowing down the rate of A where the linear trend $ø/A$ identifies the region of lower packing efficiency for concentration above 0.4460 as shown in figure 3.22 and 3.23, respectively. Secondly, the irreversible flocculation does change the PSD of system concurrently to the size reduction of graphite powder and this renders difficult to distinguish their own contribution to the overall PSD of system. Nonetheless, the role of PSD and solid loading on the rheological behaviour of suspensions is outlined. A theoretical study dealing the effect of PSD and solid concentration on the suspension stability was carried out by Strauss et al. based on Derjaguin-Landau-Verwey-Overbeck (DLVO) theory (Strauss, 1989). In that study the slurry structure was not addressed, whereas the current investigation relying on rheology and

thermodynamics of binary HS systems, provides indications on the structure of anode slurries. In particular, the optmization of dispersant ensures good dispersion and homogeneous structure for 80 and 83 wt% slurries provided by the dominance of repulsive interparticle force and the microstructure after sintering is expected to be uniform and fine (Pugh, 1994; Tseng, 1999). Conversely, for higher solid loading, attractive interparticle force prevails and the suspension structure is affected by particle aggregation and phase separation of larger particles; fired microstructure derived from the 85 wt% slurry is expected to be coarse and inhomogeneous with large voids (Bonekamp, 1996). As a result, the benefit of highly concentrated and well dispersed suspensions for the production of ceramics with high reliability is limited to anode suspensions with solid loading at the most 83 wt% (Lange, 1989). The microstructure of fired samples derived from 80, 83 and 85 wt% slurries will be presented by micrographs in the last part of this section. The behaviour of the intrinsic viscosity versus solid concentration is shown in figure 3.23 (b) and (c) and its values are obtained from the expression *[η]A=2* where *A* is estimated by equation 3.17. As predicted this formula is more accurate for the higher range of solid loading, i.e. 0.4066 and 0.4814, than equation 3.8 which remains valid for the lower range, 0.2666-0.4066. Graph 3.23 (c) shows an interesting relation of *[η]* with solid concentration when obtained by equation 3.17:

$$[\eta] = 78.16\emptyset^2 - 75.58\emptyset + 22.33 \qquad (3.18)$$

Equation 3.18 bears a similarity with the parabolic AFV law described by eq. 3.11 and 3.12.

$$[\eta] \cong k'\emptyset^2 - k'\emptyset + c' = k'\emptyset(\emptyset - 1) + c' \qquad (3.19)$$

Then by rearranging the equation 3.19 on the basis of eq. 3.13, one obtains:

$$[\eta] = k''AFV = 2.8[27.40\emptyset(\emptyset - 1) + 8.0] \qquad (3.20)$$

Equation 3.20 provides the same expression 3.18 within experimental error and supplies a linear relation of the intrinsic viscosity with AFV for highly concentrated suspensions where *k''* is a parameter connected to some features of free volume. The reduction of the intrinsic viscosity *[η]* with solid concentration is related to the inherent increment of *A* which is ascribed to an improved packing and ordering that minimize interactions between particles. Specifically, the decrease of *[η]* up to 77 wt% follows approximately a linear trend similarly to the packing density and indicates a lower extent of particle interactions which are further reduced between 77 and 83 wt% as proved by the steeper slope of *[η]* that corresponds to the region of

high efficient packing. This suggests that the improved particle packing provided by the optimal blend ratio and size ratio, entails the reduction of particle interactions. The decrease of *[η]* is also associated to the diminution of aspect ratio of particles validating the postulate of PSD variation for graphite powder (Barnes, 1989; Macosko, 1994). Above 83 wt%, intrinsic viscosity is affected by particle aggregation. As the solid loading increases, aggregates become larger and their relative distances increase with the consequence of decreasing *[η]* with solid concentration; the changeover of curves of figure 3.23 indicates the occurrence of flocculation. Now the effect of PSD and packing density on the slurry viscosity will be delineated. Farris has demonstrated a remarkable reduction of suspension viscosity, also 50-fold for a given solid loading, when the packing density is optimized by a proper mixture of fine and large particles with size ratio 5 for a bimodal PSD suspension of high solid concentration, i.e. 0.60 v/v (Barnes, 1989; Larson, 1999). Moreover, specific viscosity curves as a function of solid fraction and characteristics of particles, i.e. shape and aspect ratio, have been experimentally acquired and fitted by the Krieger-Dougherty model (Barnes, 1989; Genovese, 2012). Figure 3.24 (a) points out the behaviour of the relative viscosity according to the Krieger-Dougherty model estimated at infinite shear rate where two distinct curves are distinguished, suggesting specific and different characteristics of powders throughout the solid loading range 0.2666-0.4909 (68.3-85.5 wt%). The inflection point at solid fraction of 0.4066 (80.5 wt%) highlighted by the inset of figure 3.24 (a) essentially supports the previous assertion on the variation of PSD of the system related to the change of size and aspect ratio of graphite particles and agglomerates along the solid loading range of interest.
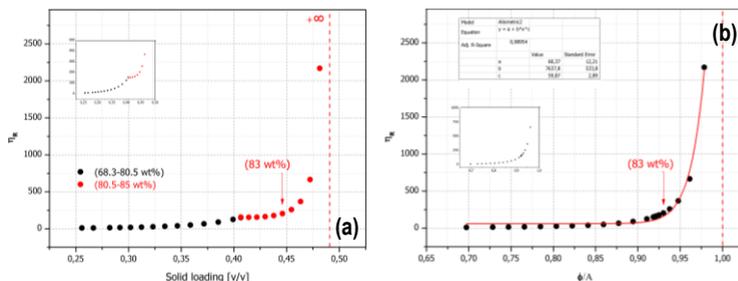
Figure 3.24 Relative viscosity versus solid loading (a) and packing density ø/A (b) for 0.2666-0.4909 v/v or 68.3-85.5 wt% solid loading range.

Conversely, the relative viscosity as a function of the packing density *ø/A* of figure 3.24 (b) displays a regular trend without inflection points and this feature descends from the peculiar behaviour of *ø/A* versus solid loading. The packing density bears the change of PSD of the system throughout the entire solid range differently from

the solid concentration. The advantage of regular and smooth trend for the relative viscosity with packing density is to adopt a power law model for the rheology of slurry system as shown in figure 3.24 (b); coefficient values of the model are present in the inset. Another benefit from the linear form of the Krieger-Dougherty model (eq. 3.6) concerns the following arrangement setting the product *[η]A=2*:

$$ln(\eta_r) = -2ln\left(1 - \frac{\phi}{A}\right) = -2ln\left[\left(1 - \sqrt{\frac{\phi}{A}}\right)\left(1 + \sqrt{\frac{\phi}{A}}\right)\right] \qquad (3.21)$$

The factorization provides the terms *(1-√ ø/A)* and *(1+√ ø/A)* defined as the crowding factor and ordering factor respectively and tagged as *C* and *O*. Moreover, the harmonic average of just two numbers *x* and *y* is expressed as $H_{(x,y)}=2(xy)/(x+y)$ and equation 3.21 is outlined into a more compact form as follows:

$$ln(\eta_r) \equiv -2ln[(C)(O)] = -2ln\left[H_{(C,O)}\right] = -2[ln(C) + ln(O)] \qquad (3.22)$$

Equations 3.21 and 3.22 underline the contribution of the two factors on the suspension viscosity. The crowding factor *C* is limited between 0 and 1 so that provides always a positive contribution to the slurry viscosity through *-2ln(1-√ ø/A)* or crowding term, while the domain of the ordering factor *O* is between 1 and 2 leading to a negative value to the viscosity through *-2ln(1-√ ø/A)* or ordering term. Consequently, although the viscous response of slurries always rises with solid concentration as shown in figure 3.24, there is even an all-present term which modulates the viscosity in regards to the solid content increment through the ordering term according to equation 3.23. It is also remarkable to recognize that the product of two factors is equivalent to their harmonic average and this supplies a further account about the underlying mechanisms for rheological properties of the system since the harmonic average implies different situations involving rates as well as processes working in parallel. Essentially, as solid loading rises, the viscosity increases but also the particle ordering according to HS system. On the other hand, the optimization of packing density gives rise a reduction of viscosity for a given powder concentration of appropriate PSD as proved by Farris. Then, the particle order enhances the flow of slurries for a given solid loading and this aspect is bore by the ordering term arising from the factorization of Krieger-Dougherty model, i.e. equations 3.21 and 3.22. Figure 3.25 confirms the viscous response of slurries as a function of solid loading and packing density previously exhibited by figure 3.23 and also underlines the concurrent effects of the crowding and ordering terms, respectively *-2ln(C)* and *-2ln(O)*.
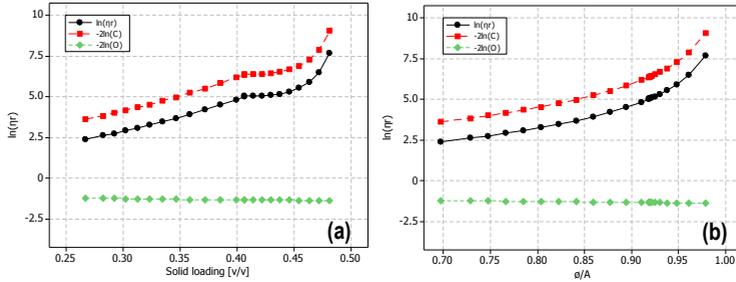
**Figure 3.25** Relative viscosity versus solid loading (a) and packing density ø/A (b) for 0.2666-0.4909 v/v or 68.3-85.5 wt% solid loading range in according to the equation 3.22.

The ordering term supplies a negative contribution to the viscosity that means a positive effect on the flow properties of the system whereas the crowding term shifts the viscosity curve $ln(\eta_r)$ to higher values. The crowding term is connected to the resistence of the relative motion of particles and/or agglomerates throughout the liquid phase so that particle-particle interactions and particle-solvent interactions are largely involved for the dissipation of viscous energy. For these interactions, the free volume plays a significant role for the viscous response of slurries. Instead, the ordering term stands for the suspension fluidity provided by an ordered structure that, differently from a disordered array, minimizes the energy dissipation experienced by the relative motion of particles and fluid. In order to verify these characteristics of crowding and ordering terms with certain physical quantities, an extension of the model 3.22 is required.

$$ln(\eta_r) \equiv -2ln[(C)(O)] = -[ln(C)^2 + ln(O)^2] =$$
$$= -[ln(1 - 2\sqrt{\frac{\phi}{A}} + \frac{\phi}{A}) + ln(1 + 2\sqrt{\frac{\phi}{A}} + \frac{\phi}{A})] \qquad (3.23)$$

Equation 3.23 avails of the logarithmic properties where the square crowding factor C^2 and the square ordering factor O^2 explicity characterize respectively the viscous and fluid contribution to the slurry viscosity. The physical quantities designed for describing the underlying relation of O^2 with the ordered structure is the packing density ø/A whereas the relation of C^2 with the free volume is (A-ø)/ø resulting from the available space (A-ø) of particles freely moving throughout the liquid phase normalized to the solid concentration; it corresponds to the inverse of the flow resistance parameter and here is defined as the normalized free volume (NFV).
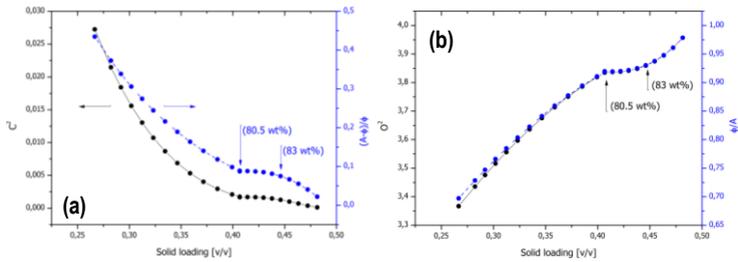
Figure 3.26 Relation of the square crowding factor C^2 with the normalized free volume *(A-ø)/ø* (a) and the square ordering factor O^2 with the packing density *ø/A* (b) vs solid loading.

NFV decreases while the packing density increases with solid loading as expected and the behaviour of C^2 and O^2 are well represented by these physical quantities as shown in figure 3.26. The curves of O^2 and packing density are superimposed and thus a linear relation is established as shown in figure 3.27 (c). Instead, the square crowding factor follows a power law with NFV and this implies that for high solid concentrations a small reduction of free volume strongly affects C^2 corresponding to a large increase of slurry viscosity especially for concentration exceeding 0.4460 as highlighted by figure 3.24 and 3.27.
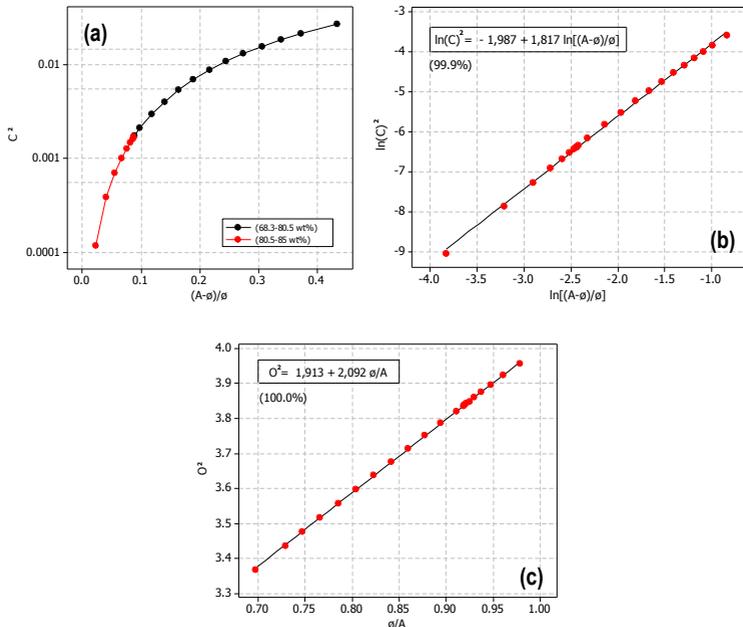
Figure 3.27 Square crowding factor C^2 versus the normalized free volume $(A\text{-}ø)/ø$ in semilogarithmic scale (a) and in double logarithmic scale (b) and the square ordering factor O^2 with the packing density $ø/A$ (c) both with fitting relation and correlation coefficient.

This increment of viscosity results from the solvent entrapped within agglomerates that reduces the free volume necessary for the suspension flow. Another source of flow resistance concerns the reducing gaps between particles and agglomerates where the solvent migration is constrained as well as the arrangement of particles whose mobility is sustained by the liquid phase with the result of low packing efficiency and high viscosity. The specular trend of NFV with packing density of figure 3.26 indicates a plateau between 0.3992 and 0.4296 (80 and 82 wt%). In this range, the value of NFV remains constant regardless the increment of solid content confirming the efficient distribution of free volume along the region of high packing efficiency where the system achieve high packing density, i.e. 0.92, without the occurrence of particle aggregation. Along this concentration interval, the positive contribution of PSD is emphasized in regards to the relative viscosity whose value remains practically constant in spite of the increment of solid concentration. This clearly supports that a proper mixture of small and large particles well dispersed ensures high packing density and in turn controls slurry viscosity according to the Farris effect (Barnes, 1989; Larson, 1999). Figure 3.28 (a) highlights the region of high packing density where the relative viscosity is constant and pointed out by decreasing values of the incremental relative viscosity, between 0.3992 and 0.4296 (80 and 82 wt%), corresponding to the plateau of NFV and packing density of figure 3.26. The incremental viscosity is defined as $(\eta_{r(i+1)} - \eta_{r(i)})/\eta_{r(i)}$ with $i=0,\dots,22$ for the solid concentration range 0.2666-0.4814 (68.3-85 wt%).
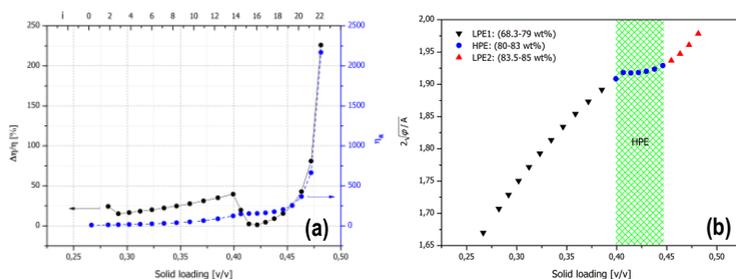
**Figure 3.28** Incremental relative viscosity (a) and packing efficiency parameter (b) as a function of solid loading.

The specular trend of NFV and packing density with solid concentration is attributed to $\pm 2\sqrt{ø/A}$, the only unlike term arising from C^2 and O^2 of equation 3.23. This term $2\sqrt{ø/A}$ scales as $ø/A$ with solid concentration (figure 3.23 (a)) and its comparison

with figure 3.28 (a) outlines immediately the relation of viscosity with packing efficiency. For this reason $2\sqrt{\phi/A}$ is defined as packing efficiency parameter and provides a pratical evaluation of packing efficiency for those systems characterized by a variable A as the current anode system. Figure 3.28 (b) displays two regions of low packing efficiency, i.e. LPE1 and LPE2, and a region of high packing efficiency, namely HPE. This latter is characterized by low values of incremental viscosity where the relative viscosity is almost independent from the solid loading between 80 and 83 wt%. Conversely, incremental viscosity increases linearly between 68.3 and 79 wt% (LPE1) and exponentially between 83.5 and 85 wt% (LPE2) as a result of irreversible flocculation. So far, the influence of solid concentration and PSD on the rheological behaviour is emphasized especially for highly concentrated suspensions whose high packing density between 80 and 83 wt% ensures relative low viscosity as well as low shrinkage of derived compacts upon drying and sintering assuring respectively easily forming of green body and reliability of final product. Another point for the anode system concerns the phase transitions. The previous fluid-solid transition at 0.4909 is assumed here as the melting transition according to the binary HS system whose attraction force shifts the transition at lower concentration than a monodisperse HS system (Kaplan, 1994; Dinsmore, 1995); in turn the freezing transition is also expected to occur at lower concentration and its estimation relies on the calculation of osmotic pressure. The osmotic pressure is a thermodynamic property taking part in equation of state (EOS) concerning hard-sphere systems as colloidal suspensions (Ring, 1996; Dinsmore, 1995). The determination of EOS is a challenging task for systems far from the ideal (diluite) case as liquid systems where attractive forces can not be neglected. The most widespread expression of EOS for fluid systems of hard-spheres is that proposed by Carnahan and Starling; this equation is a close-form solution which agrees with molecular dynamics computation better than other expressions (Carnahan, 1969). Several studies, focusing on the determination of phase diagram for colloidal HS suspensions, are based on EOS of Carnahan-Starling and provides good predictions of fluid-solid phase transitions with experimental results (Dinsmore, 1995; Rutgers, 1996; Phan, 1996). For ordered structures, EOS is given by virial expression whose includes not only the solid concentration as for Carnahan-Starling equation but also the maximum solid concentration (Ring, 1996; Phan, 1996). The following EOS and hence phase diagram of anode system involves an expression of osmotic pressure based on a modified Carnahan-Starling equation where the maximum solid concentration A arises at denominator as $(A-\phi)^3$ replacing $(1-\phi)^3$ as proposed by Guo et al. (Guo, 1999):

$$\Pi = \frac{RT}{\bar{V}} \frac{(1+\phi+\phi^2-\phi^3)}{(A-\phi)^3}$$

(3.24)

Where $\prod$ is the osmotic pressure, $\underline{V}$ the molar volume of particle, T the temperature and R the gas constant (8.314 J/Kmol). The normalized osmotic pressure $\prod/(RT/\underline{V})$, that is a form of EOS, represents the phase diagram of anode system as shown in figure 3.29 (a) similarly to those determined by sediment tests for colloidal HS suspensions (Phan 1996; Rutgers, 1996).
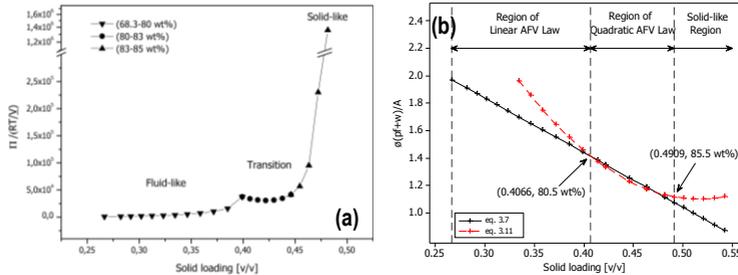

Figure 3.29 Equation of state of anode system (a) and range of validity of AFV expressions (b).

The phase diagram displays three regions where the system behaves as a disordered fluid (fluid-like region) up to 0.4066, here recognized as freezing transition; beyond 0.4066, the transition region is characterized by the arrangement of particles towards an ordered structure tipical of a solid, which is accomplished at 0.4909, the melting transition that identifies the solid-like region. The determination of osmotic pressure through equation 3.24 highlights the close correspondence of phase diagram with the range of validity of AFV expressions of figure 3.29 (b). In particular, the linear AFV function bears the fluid-like behaviour of slurries up to the freezing transition (0.4066) while the quadratic AFV, the transition region characterized by increasing order of the system. In addition, the osmotic pressure of colloidal suspension not only specifies the phase and structure of the system but also the interparticle interactions (Ring, 1996). In particular, Brady describes analytically the properties of colloidal HS systems considering the osmotic pressure of suspension as the isotropic and macroscopic stress component of particles. Brady also provides a mechanical derivation of osmotic pressure in agreement with the thermodynamic one (Brady, 1992). In addition for Guo et al., the osmotic pressure descibes the stress transmitted between particles and highpoint a correlation between the osmotic pressure and drying stress for a dispersed colloidal suspensions (Guo, 1999).
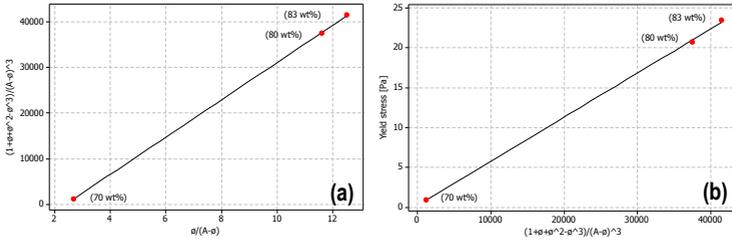
Figure 3.30 Relation of the normalized osmotic pressure with flow resistance parameter (a) and yield stress (b) for 70, 80 and 83 wt% slurries.

Figure 3.30 shows a linear behaviour of the yield stress with normalized osmotic pressure (derived from equation 3.24) as a consequence of the relation of flow resistance parameter with osmotic pressure. These graphs clearly demonstrate the correspondence of yield stress with osmotic pressure that represents the macroscopic force between particles for 70, 80 and 83 wt% slurry similarly to figure 3.15 (a) where the model 3.10 based on the flow resistance parameter fails for higher solid loadings. The motive lays on the fast divergence of osmotic pressure near the melting transition, i.e. 0.4909 (85.5 wt%), where linear trends in figure 3.30 are lost when the 85 wt% suspension is considered, similarly to figure 3.15 (a). For this reason, an alternative model is required for the yield behaviour of highly concentrated slurries. The model in point is that proposed by Flatt which displays a good fitting of experimental data for colloidal suspensions over a wide range of solid concentration at isoelectric point (IEP) (Flatt, 2006):

$$\tau_y = m \frac{\emptyset^2(\emptyset - \emptyset_0)}{A(A - \emptyset)}$$ (3.25)

Where τ_y is the yield stress, Φ the solid concentration, A the maximum solid concentration, Φ_0 the percolation threshold and m a coefficient depending on the interparticle force, particle size and PSD that will be described in more detail later. The yield stress model 3.25, namely YODEL (Yield stress mODEL), is based on hard-sphere interaction of particles (pairs) with different size and describes the rheological behaviour of cement systems (Flatt, 1999). These systems are characterized by multimodal particle size distribution and the key point for the estimation of yield stress concerns the determination of maximum solid concentration for the powder mixture (Flatt, 2007). In those studies A is evaluated by independent experiments as filter-pressing or by packing model which needs the PSD of powders as main input (Flatt, 2006; Flatt, 2007). In the current analysis, A is determined experimentally and hence PSD of powders is not required. In addition, both A and yield stress are derived from the same rheological measurement and thus a

96

comparison of experimental values of yield stress with values predicted by YODEL is directly delivered without any additional experiments for the evaluation of A. Indeed, an alternative expression of YODEL is proposed by Flatt (Flatt, 2006):

$$\tau_y = m \frac{\emptyset(\emptyset - \emptyset_0)^2}{A(A - \emptyset)} \tag{3.26}$$

The difference between the two expressions of YODEL, i.e. 3.25 and 3.26, derives from a different account of percolation (of undisperded particles, i.e. flocs) during the development of the model (Flatt, 2006). Nonetheless, since in that study experimental data are determined at IEP where the percolation threshold Φ_0 is 0.026 and turns out zero, no distinction on fitting arises by using equation 3.25 or 3.26 as both expressions merge into:

$$\tau_y = m \frac{\emptyset^3}{A(A - \emptyset)} \tag{3.27}$$

The coefficient m is a fitting parameter and depends on the interparticle force, particle size and PSD. It is expressed as follows:

$$m = \frac{1.8}{\pi^4} G_{max} \left(\frac{f_{\sigma,\Delta} u}{R_{v,50}} \right) = \frac{1.8}{\pi^4} \frac{A_0}{12 H^2} \left(\frac{f_{\sigma,\Delta} u}{R_{v,50}} \right) \tag{3.28}$$

Where G_{max} designates the maximum attractive interparticle force normalized by the radius of curvature at the contact points of particle pair and is estimated by the ratio of non-retarded Hamaker constant A_0 and the minimum separation distance H of particle pair. The effect of PSD on the yield stress is given by the terms in parenthesis; the normalized particle size distribution $f_{\sigma,\Delta}$, the median volume radius $R_{v,50}$ and u the normalization factor which makes $f_{\sigma,\Delta}$ unity for monodispersed systems (Flatt, 2007). In addition, $f_{\sigma,\Delta}$ accounts for the volume increment of particles when they form doublets during flocculation; at a critical solid concentrion, Φ_0, doublets form a percolating network whereby a certain shear stress, τ_Y, breaks down this continuos structure and induces the flow of slurry. The ratio of $f_{\sigma,\Delta}$ and $R_{v,50}$ must be derived from the same sort of distribution, i.e. surface or volume, in order to obtain consistent results; in this case $f_{\sigma,\Delta}$ comes from volume distribution (Flatt, 2006). In the current study, the determination of coefficient m through the fitting of experimental yield stress of 80, 83 and 85 wt% slurries gives high correlation coefficients (> 99.9%) for both models 3.25 and 3.26; figure 3.30 (a) shows the fitting by using equation 3.25. At this stage, the difference on adopting the models 3.25 and 3.26 is not clear, but both fit well the experimental values. These values and the additional ones, i.e. 0.4218 (81.5) and 0.4633 (84 wt%), obtained from YODEL lie

down on red curve obtained from a power-law fitting as shown in figure 3.31 (b). This sets a connection between YODEL and yield stress models based on power law as that proposed by Zhou et al. in (Flatt, 2007).
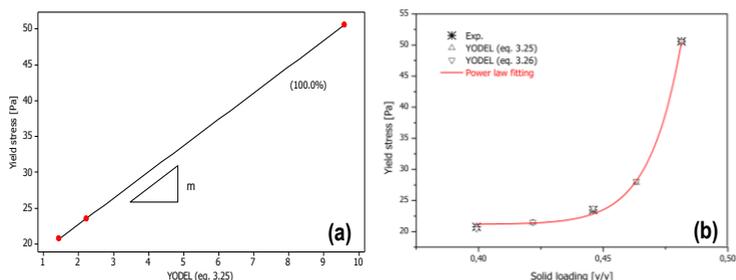

Figure 3.31 Determination of coefficient *m* from the equation 3.25 by the fitting experimental values of 80, 83 and 85 wt% slurries (correlation coefficient in parenthesis) (a) and values of yield stress predicted from YODEL, eq. 3.25 and 3.26, in comparison with experimental values.

It is worth to note that YODEL predicts the yield stress for the highly concentrated anode slurries where the model 3.10 fails. In addition, the percolation threshold Φ_0 is fixed 0.2666 which is obtained by setting zero equation 3.10 wherein *A* values come from the linear AFV function. The validity of AFV functional, i.e. eq. 3.17, is confirmed by the percolation threshold Φ_0 and *A* values which are the main inputs for YODEL and derive from the linear and quadratic AFV functions. Moreover *A* values, for those system whose maximum solid concentration changes throughout the solid loading of interest, are here determined with a limited number of rheological measurements. Furthermore, YODEL predictions are consistent with experimental data also for system far from IEP so that with non-zero Φ_0 . As a result, YODEL provides good estimation of yield stress throughout the solid loading range 0.3992-0.4814 (80-85 wt%) with relative errors within ± 1.5% as shown in table 3.7.

Table 3.7. Experimental and estimated yield stress values from YODEL equations with input parameters as Φ, *A* and Φ_0 for highly concentrated anode suspensions.

Suspension [wt%]	ø	A		$\emptyset_0$	Yield Stress [Pa]		
		Exp.	Eq. 3.11		Exp.	YODEL (Eq. 3.25)*	YODEL (Eq. 3.26)*
80	0.399	0.434	0.433		20.75	20.65 (-0.49%)	20.46 (-1.38%)
81.5	0.422	-	0.459		-	21.42	21.48
83	0.446	0.482	0.480	0.267	23.46	23.57 (0.47%)	23.79 (1.41%)
84	0.463	-	0.489		-	27.84	28.09
85	0.481	0.492	0.492		50.58	50.57 (-0.03%)	50.55 (-0.06%)

* Relative errors in parenthesis

The behaviour of m in figure 3.31 (a) is lost when the overall solid loading range 0.2666-0.4814 (68.3-85 wt%) is considered. Then, an additional value of m needs for the lower lower range 0.2666-0.4066 (80.5 wt%). In this range just two data are available, i.e. 70 and 80 wt%, but the trend of figure 3.31 (a) makes possible the assumption of linear fitting also for m between 70 and 80 wt%; the coefficient m is then defined as m_L and m_U respectively for the lower and upper range, i.e. 70-80 wt% and 80-85 wt%. The behaviour of yield stress of figure 3.32 (a) resembles the trend of viscosity and the phase diagram of figure 3.24 and 3.29 differently from that reported by Flatt where a single smooth curves describe the rheological behaviour of slurries upon the overall interval of solid concentration without any changeover (Flatt, 2006). This is not unexpected since in Flatt analysis, regardless the interparticle distance decreases with solid concentration, the minimum separation distance H is set constant where the attractive interparticle force is maximum.
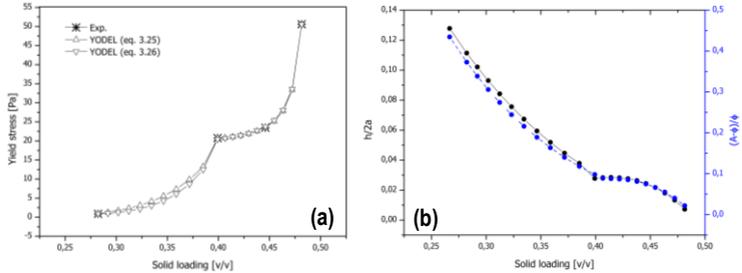
Figure 3.32 Yield stress predicted from YODEL, eq. 3.25 and 3.26, in comparison with experimental values (a) and interparticle distance along with the normalized free volume (b) for 0.2666-0.4814 (68.3-85 wt%) solid loading range.

Moreover, also A is assumed constant as well as the Hamaker constant and then m depends only on the term in parenthesis of equation 3.28 concerning the PSD that does not change for a specific ceramic suspension if particles are not subjected to exfoliation or variation in size as for graphite ones. For the anode system, A changes as a consequence of variation of PSD and then also the distance between particles changes according to (Greenwood, 1995):

$$\frac{h}{2a} = \left[\left(\frac{A}{\emptyset}\right)^{1/3} - 1\right]$$

(3.29)

Where h is the distance between particle surfaces that corresponds to the minimum separation distance H when A is determined at infinite shear rate as the current study and a is the particle radius. From figure 3.32 (b), the normalized interparticle distance $h/2a$ decreases with solid loading and approaches zero as Φ tends to A as

expected and pointed out by the equation of inset in figure 3.33; the trend of interparticle distance behaves as that of NFV especially at higher solid fractions where the two curves are superimposed and are described with good approximation by a linear relation as shown in figure 3.33.
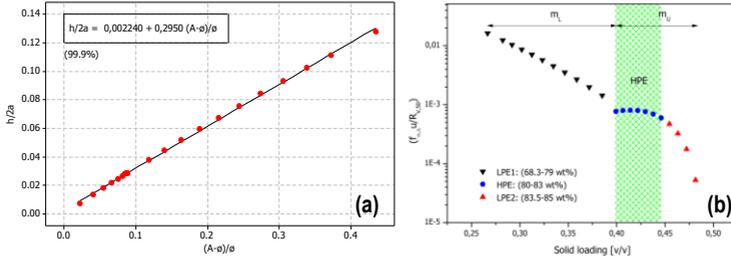

Figure 3.33 Normalized interparticle distance versus NFV (a) and PSD term of YODEL versus solid loading in semilogarithmic scale (b).

From equation 3.28, the non-retarded Hamaker constant A_0 does not depend on the interparticle distance and is assumed constant for a given system, then m depends on the PSD term in parenthesis, i.e. $(f_{\sigma,\Delta u}/R_{v,50})$, that offsets the variation of H and thus $h/2a$ in order to keep constant m. The two regimes of m, i.e. m_L and m_U, and thus of yield stress of figure 3.32 can be associated to the inflection point at 0.4066 where the curvature of $h/2a$ curve changes sign. This implies that $(f_{\sigma,\Delta u}/R_{v,50})$ decreases as far as it sets constant along the region of high packing efficiency or maximum order, i.e. 0.3992 and 0.4296 (80 and 82 wt%), and finally strongly reduces beyond 0.4460 (83 wt%) as a result of aggregation processes as shown in figure 3.33. In particular, along LPE1 the decrease of PSD term is associated to the reduction size of graphite powder where m_L is the fitting parameter for YODEL. Instead, the region of high packing efficiency HPE, is characterized by almost constant value of PSD term where the packing relies on an efficient arrangement of particles with specific size and blend ratio. Beyond 83 wt% along the LPE2, the irreversible flocculation causes a strong decrease of PSD term; the regions of HPE and LPE2 are characterized by m_U as fitting parameter for YODEL.
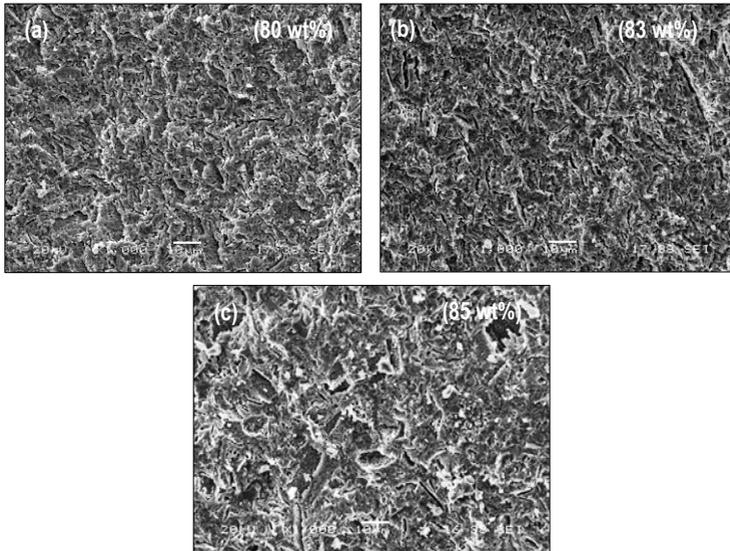
Figure 3.34 SEM micrographs of fired sample derived from 80 wt% suspension (a), 83 wt% (b), 85 wt% (c).

As last point, the effect of solid loading on the fired microstructure is presented through SEM micrographs in figure 3.34 for samples sintered at 1380°C for 3 h as reported in (Casarin, 2012). The fired microstructure depends on the green body microstructure which in turn is determined by the slurry structure. In fact, the fired microstructure of samples derived from well dispersed slurries, i.e. 80 and 83 wt%, is homogeneous and the porosity is distributed uniformly throughout the section of samples where the pores resemble the graphite particles left after burn-out. Instead, the microstructure of 85 wt% sample is inhomogeneous and coarse with large pores and dimples. It is evident that fine and homogeneous microstructures from highly concentrated and well dispersed slurries is restricted to anode suspensions with solid loading at the most 83 wt%. Additional indications on the sintering behaviour of samples derived from 80, 83 and 85 wt% slurries are shown in table 3.8.

Table 3.8. Properties of fired samples derived from 80, 83 and 85 wt% slurries such as open porosity (OP), total porosity (TP), and shrinkage.

Suspension [wt%]	ø	OP [%]	TP [%]	OP/TP	Shrinkage [%]
80	0.399	13.34±0.05	13.72±0.08	0.97±0.01	-14.69
83	0.446	12.63±0.10	14.12±0.09	0.89±0.01	-14.14
85	0.481	11.64±0.04	13.66±0.06	0.85±0.01	-14.89

The total porosity of all samples is very close (within 5%) to the graphite fraction, i.e. 12.84%, that is actually adopted for realizing a residual porosity after complete densification of the matrix, i.e. NiO and YSZ. The open (and interconnected) porosity is useful for transport properties of electrode and it decreases with solid loading from 13.3 to 11.6%; specifically, 85 wt% sample exhibits only 85% of open porosity (OP/TP) and thus 15% of close pores while 80 wt% sample shows almost exclusively open porosity. The densification of samples is accomplished already after 2 h during the dwell at 1380°C where dilatometric curves reach a plateau (Casarin, 2012). During the last stage of sintering, for prolonged time of heat treatment, grain growth can be pronounced and has an important influence on the evolution of microstructure (Rahaman, 2003). The microstructure of fired body is affected by the microstructure of green body and in turn by the structure of slurries, i.e. dispersed or flocculated; samples derived from 80 and 85 wt% slurries are chosen for highlighting the effect of slurry structure on the final product as shown in figure 3.35.
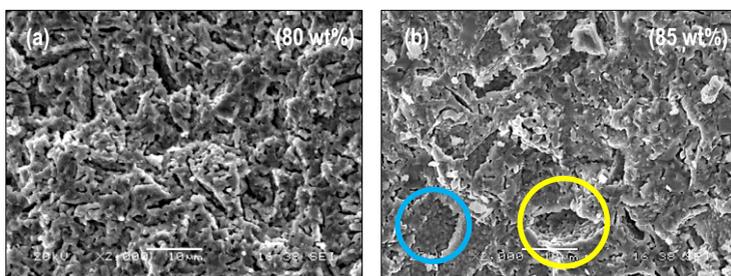
Figure 3.35 SEM micrographs of fired sample derived from disperded slurry, i.e. 80 wt%, (a) and flocculated slurry, i.e. 85 wt%, where the blue and yellow circle highlights respectively a region of high density and a void left by aggregation of graphite particles (b).

Both 80 and 85 wt% samples have similar sintering response in term of final shrinkage and shrinkage rate (derivative of shrinkage over time) but show different fired microstructures (Casarin, 2012). Large voids, around 10 μm, characterize 85 wt% sample (yellow circle of figure 3.35) differently from 80 wt% sample that is characterized by uniform and fine microstructure. Both samples show similar sintering response and grain growth is not expected to be the main cause for the diverse microstructural evolution. Then, the dispersion degree and aggregation process of slurry can be responsible for the final microstructure. In particular, 80 wt% samples (as well as 83 wt%) shows an extended porosity with small as well as large and sharp pores; these latter resemble the shape of singular graphite flake with the largest size nearly 10 μm. The large pores of 85 wt% have spherical-like shape and derive from aggregation process as postulated from thermodynamics issue of binary hard-sphere system. In this case, for a specific size and blend radio of particles as

well as solid fraction, attractive force prevails and the larger particles, i.e. graphite ones, aggregates forming clusters that leave voids after burn-out and sintering as shown in figure 3.35 (yellow circle). These pores appear isolated one other within a matrix of high density where interconnected porosity is restricted as also suggested by low OP/TP ratio; interconnected pores act as constraint for the grain growth of a single phase material (Cameron, 1988). Nonetheless, no neat grain growth arises neither for 85 wt% sample where interconnected porosity is expected to be limited. This means that the sinterability of a dual solid phase, i.e. NiO and YSZ, is different compared to that of a single phase. This is fair clear if one imagines a layer composed by NiO onto a substrate of YSZ. For a weak interface between the top layer and substrate, the sintering response of each single phase (insoluble each other) proceeds independently, whereas for a mixture of two powders the densification process of one phase is expected to be affected by the other one. Specifically, the compact derived from a well dispersed slurry conceives a homogeneous mix of each constituents if segregation is prevented so that when the composition is near 50:50 in volume, as the current anode, i.e. 55:45 (NiO:YSZ), one particle of NiO, is sorrounded by a large number of particles of the other phase, i.e. YSZ, and vice versa. In this condition, the domain of each phase (particle) for a binary mixture is restricted with longer diffusion paths in comparison of a single-phase system and eventual grain growth is controlled by particles of the second phase which act as pinning barrier for migration of grain boundary when these particles are insoluble and immobile in the matrix (Rahaman, 2003; Tekeli, 2004). Indeed, the solubility of NiO in YSZ is near 2 mol% at high temperatures, i.e. 1600°C, so that it is expected a limited grain growth even after the occurrence of pore transition during last stage of sintering (Kuzjukevics, 1997 (2)). Therefore, the inhomogeneous microstructure of 85 wt% sample relies principally on the aggregation process of graphite particles induced by attractive depletion force while NiO and YSZ particles arrange towards a high density array with limited grain growth where primary particles can be recognized (blue circle of figure 3.35). This is not really unexpected since the aggregation of graphite particles releases extra free volume, available for the sorrounding particles, which favours particle arrangement into ordered structures of high particle coordination number responsible for dense and uniform fired microstructures without excessive grain growth (Novich, 1990). This indicates that the repulsive force of binary HS suspensions can be conceived as proceeding all over the system with the exception of some zones where the attractive depletetion force locally acts and provokes the aggregation of larger graphite particles forming large pores (voids) and adjacent regions of high order where grain growth is limited especially for systems composed by phases insoluble each other. Finally, the fine microstructure with uniform open porosity of 80 wt%

sample is surely desirable for the anode electrode application since ensures good mechanical, electrical and transport properties.

Part II: Effect of the solid loading and temperature on the flow behaviour of slurries for dip coating

A comparison of rheological behaviour for anode slurries with only dispersant and with other additives (slurries for dip coating) respectively labelled as (D) and (D+A) is given in figure 3.36 (a).
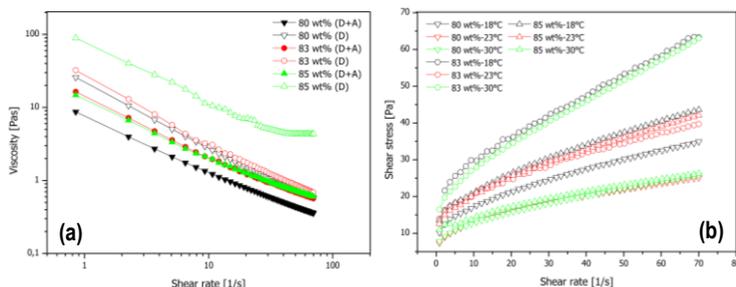
Figure 3.36 Viscosity versus shear rate in double logarithmic scale for suspensions with only dispersant (D) and with other additives (D+A) at 23°C (a) and shear stress versus shear rate of suspensions for dip coating (D+A) as a function of temperature (b).

All suspensions show shear thinning behaviour with the exception of 85 wt% (D) slurry at higher shear rates. The suspensions with binder and plasticizer (D+A) are less viscous in comparison with those with only dispersant as a result of dilution coming from the water of additive emulsions. The effect of temperature and solid loading on the flow behaviour of slurries is shown in figure 3.36 (b). It is interesting to note that the flow behaviour of 80 and 85 wt% slurries is similar. In particular, the shear stress (and viscosity) decreases with temperature as expected in contrast to the flow behaviour of 83 wt% slurry. Moreover, the highest shear stress values concern 83 wt% slurry and its lowest flow curve lays between the highest curves of 80 and 85 wt% slurries. Other indications on flow behaviour are provided by the power-law index *n* as shown in figure 3.37 (a).
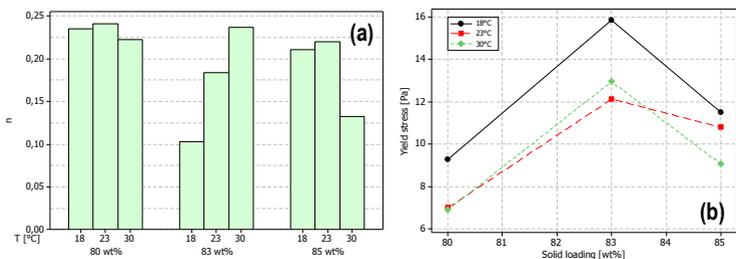
Figure 3.37 Power-law index *n* (a) and yield stress (b) of anode suspension for dip coating as a function of temperature.

In general, the values of *n* are relatively low (< 0.25) and confirm the dependence of slurry flow on shear rate of figure 3.36. It is worth to note that the highest difference of *n* concerns 83 wt% slurries for 18 and 30°C whose corresponding flow curves are nearly superimposed. Conversely, flow curves of 80 wt% slurry for 23 and 30°C are superimposed with very close *n* values. This implies that the slurry flow is caught in more detail by flow curves than the power-law index but, yet this latter indicates a constancy character. Specifically, similar *n* values within a group of slurries, i.e. 80 wt% one, indicate flow curves almost superimposed or possible superimposition by rigid shift of curves like for 80 wt% slurry 23 and 30°C or 85 wt% slurry 18 and 23°C; for this feature, the power-law index can be conceived as controlling tool for the reliability of rheological measurements. The higher values of shear stress and viscosity for 83 wt% slurry suggest higher flocculation degree as proved by high yield stress values shown in figure 3.37 (b). The yield stress values of 80 and 85 wt% slurries are lower than those of 83 wt% slurry for all temperatures considered. This unexpected trend of 83 wt% slurry can be explained by considering the corresponding suspension of Part I which marks a limit for the occurring of extensive flocculation. Under this perspective, the molecules of binder encompass the particles whose limited separation favours the aggregation process with the result of high yield stress and viscosity. For 80 wt% slurry, the larger separation between particles hinders the flocculation prompted by binder molecules and the flow has a higher Newtonian character than 83 wt%slurry, following the viscosity dependence with temperature. The same occurs for 85 wt% slurry whose nature is close to Newtonian behaviour already after dispersant addition due to the relative large distance between dense agglomerates. Nonetheless, the distribution of binder throughout 80 and 85 wt% slurry is expected to differ and in turn the green and fired microstructures derived from these suspensions. Another difference concerns 80 wt% slurry which exhibits a more limited variation of flow behaviour with temperature than 85 wt% slurry (figure 3.36 (b)), with the benefit of more reliable wet colloidal process. Finally, the effect of solid loading and additive addition on the

microstructure of fired samples sintered at 1380°C for 3 h is shown in figure 3.38 with the purpose to highligh the influence of slurry structure of 80 and 85 wt% suspensions whose similar rheological behaviour does not entail similar sintering microstructures.
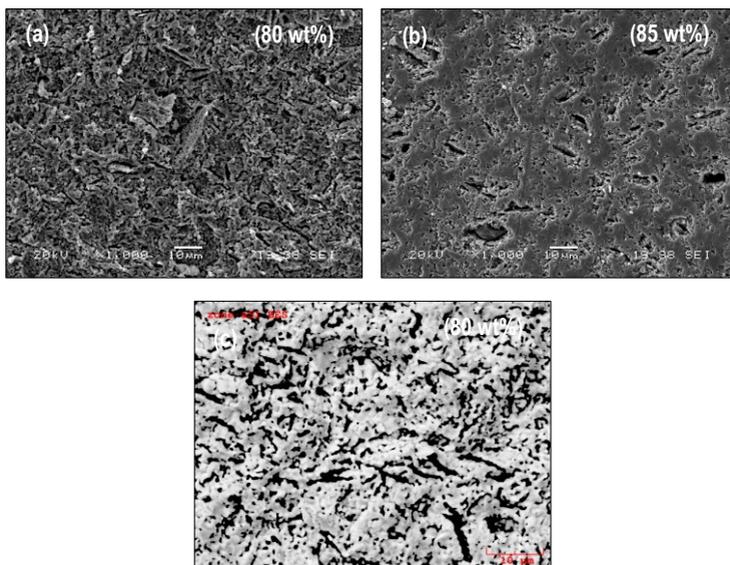
Figure 3.38 SEM micrographs of fired sample derived from 80 wt% (a) and 85 wt% slurry (b) in secondary electrons mode. Micrograph of fired 80 wt% sample obtained with back scattered electrons where dark zones represent pores (c).

As a matter of fact, the fired microstructures of figure 3.38 resembles that of 80 and 85 wt% samples of figure 3.35. The role of dispersant is deemed to be fundamental also for the subsequent addition of additives for the anode suspensions here investigated; a suspension with low degree of flocculation, i.e. 80 wt% one, preserves a good dispersion also after binder and plasticizer additions and finally shows a homogeneous fired microstructure as clear in figure 3.38. For the fired sample derived from 85 wt% slurry, the microstructure is nonuniform with zones well sintered and zones of higher porosity along with large voids. The inhomogeneous microstructure of 85 wt% sample is related to a nonuniform distribution of additives from a slurry characterized by aggregates and low degree of dispersion after dispersant addition. Then, 80 wt% anode suspension assures reliable dip coating process in regards to external condition as temperature and ensures uniform microstructure with homogeneous distribution of pores of fired product which meets the requirements for the application of anode electrode.

3.3.2　Thermal analysis

3.3.2.1　*Drying and binder burn-out*

The effect of drying on sintering behaviour is pointed out by sample A and B which are respectively dried at room temperature (RT) and in oven with dwell at 60 and 110°C. The main evidence of dilatometric curves of figure 3.39 concerns the stage of sintering where sample B achieves most of shrinkage before the dwell at maximum temperature, i.e. 1380°C, differently from the sintering of sample A that proceeds until the end of heat treatment. In table 3.9, the lower shrinkage is connected to higher density (bulk and relative density) and lower porosity of sample B whose sintering behaviour is boosted than sample A.
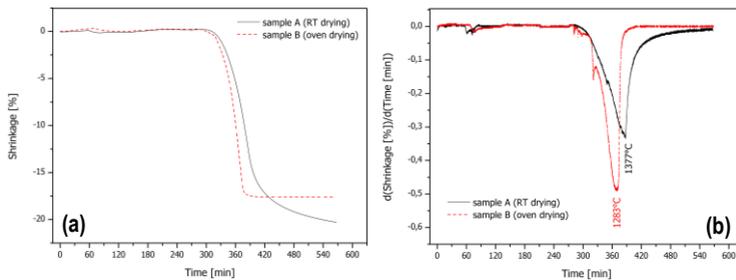
Figure 3.39 Dilatometric curves of sample A and B respectively dried at RT and oven. Shrinkage versus time (a) and shrinkage rate versus time (b).

The sintering response of sample B reflects a uniform green microstructure which is characterized by homogeneous pore-size distribution and supports the achievement of high sintered densities (Roosen, 1988). Moreover, Carbone suggests that the shrinkage during the last stage of sintering is controlled by the pore structure of green body whose distribution of pores, when uniform with pore dimension similar to particle size, assures high density of sintered compacts (Carbone, 1978). An interesting relation between pore structure of green compacts and sintering behaviour is supplied by Roosen that remarks a tough correspondence between curves of pore-size distribution and shrinkage-rate curves; specifically, the maximum of pore-size distribution (most frequent pore size) matches the maximum of shrinkage rate at a certain temperature (Roosen, 1984). Then, the higher sinterability of sample B is determined by the green microstructure with narrower pore-size distribution (and finer pore size) which can be related to the shrinkage-rate curves of figure 3.39 (b) according to Roosen results; in particular, the higher sinterability of sample B is marked by a temperature of maximum shrinkage rate about 100°C lower than that of sample A, respectively 1283 and 1377°C. The different pore-size

107

distribution and sintering behaviour of sample A and B are related to the drying step. Specifically, sample A is dried at RT while the drying of sample B occurs in an oven at 60 and 110°C for 12 h each after 12 h at RT. During the drying in oven, capillary pressure develops compressive stress during the constant rate period (CRP) of drying which is characterized by the drawing of liquid from the interior of the body to its surface where evaporation proceeds (Rahaman, 2003). As long as this stage of drying occurs, the compressive stress whose entity is proportional to the evaporation rate enables particles to arrange in a denser packing characterized by narrower pore-size distribution and smaller pores. As additional proof of capillary pressure whose effect is deemed to modify significantly the pore structure of green compacts, a green sample B# was dried at 150°C for 18 h after 12 h at RT and sintered with same schedule of sample A and B. The open and total porosity of sample B#, respectively 10.9 and 13.0%, were significantly lower than sample A and B confirming not only the existence of capillary pressure effect, but also its magnitude with evaporation rate as proved for sample B#. Figure 3.40 points out the effect of binder burn-out on sintering behaviour where the underlying mechanisms of additive removal are highlighted for sample A, B, C and A#; sample A# is dried and fired as sample A and B but it is prepared with only dispersant as additive.
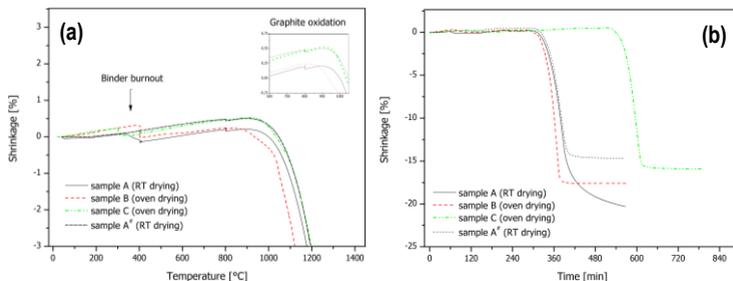
Figure 3.40 Dilatometric curves of sample A, B, C and A# which correspond to sample A without additives (only dispersant). Shrinkage versus temperature (a) and shrinkage versus time (b).

The inset of figure 3.40 (a) shows a slight contraction of green samples during the dwell at 800°C where graphite oxidation is accomplished. Similarly, knees between 300 and 400°C identify the removal of binder, plasticizer and/or dispersant occurring at different burn-out conditions. Basically, sample A reveals a knee of shrinkage curve which is related exclusively to the removal of binder and plasticizer since the corresponding sample A# prepared without binder and plasticizer (with only dispersant) does not display any contraction. The removal of additives depends on burn-out conditions but also on the drying step. In fact, sample B and C dried in oven exhibit a clear and higher expansion than sample A dried at RT, during the earlier

stage of heat treatment. This expansion is determined by the additive layer which experiences a contraction during oven drying that is later released and converted to dilation during heating by thermal expansion of molten binder as evident for sample B and C in figure 3.40 (a). The expansion of additive layer for sample B and C is controlled by burn-out conditions. Specifically, the burn-out of sample C is longer with low heating rate (HR), i.e. 2.5°C/min, and two dwell of 1 h each at 300 and 400°C. Instead, the binder removal for sample B is faster, 5°C/min as HR, with one dwell of 1 h at 400°C. For both sample B and C, the binder burn-out is complete after the isothermal knees respectively at 400 and 300°C since any contraction occurs beyond these temperatures as shown in figure 3.40 (a). After burn-out, the lower contraction implies a higher density for green compact C than compact B which favours the sintering behaviour as confirmed by the higher sintered density and lower final shrinkage of sample C than sample B as shown in figure 3.40 and table 3.9. On the other hand, for higher sintered porosity it is expected higher porosity of green compacts after drying and burn-out, implying an increasing green density passing from sample A to sample C.

Table 3.9. Bulk density (BD), relative density (RD), open porosity (OP), total porosity (TP) and shrinkage for sintered compacts.

	BD [g/cm^3]	RD[+] [%]	RD[#] [%]	OP [%]	TP [%]	OP/TP	Shrinkage [%]
A	4.93	77.3	88.7	22.90	22.73	1.01	-20.30
	(±0.01)	(±0.2)	(±0.2)	(±0.34)	(±0.20)	(±0.02)	
B	5.23	82.0	94.0	17.24	18.03	0.96	-17.58
	(±0.02)	(±0.3)	(±0.3)	(±0.19)	(±0.26)	(±0.02)	
C	5.47	85.7	98.4	12.83	14.27	0.90	-15.92
	(±0.01)	(±0.2)	(±0.2)	(±0.27)	(±0.22)	(±0.02)	

[+] Relative density = Bulk density / Theoretical density of dense anode composite (6.376 g/cm^3)

[#] Relative density = Bulk density / Theoretical density of porous (TP = 12.84%) anode composite (5.557 g/cm^3)

The different sintering behaviour between sample B and C relies on the underlying mechanisms concerning the thermal degradation of organic additives during burn-out. Low-molecular weight additives like plasticizers are eliminated primarily by evaporation, while compounds of high-molecular weight as binders soften and melt prior evaporation. Then, the liquid binder migrates from the interior of compact under capillary pressure to its surface where further evaporates (Liu, 1998). This mechanism of binder removal is similar to that regarding the drying of solvent from green compacts (Cima, 1989). Then for sample C, the prolonged time at lower temperatures promotes the migration of molten binder which maintains the evaporation at surface throughout the complete burn-out already at 300°C. In the case polymer-gas interface recedes within compacts, the low temperature ensues

lower production of volatile species minimizing the occurrence of defects and cracking. In addition, the liquid binder supports the arrangement of particles into denser packing with expected narrow pore-size distribution of green compact and hence higher sinterability for sample C. Conversely for sample B, the expansion occurs up to 400°C suggesting that evaporation shifts to higher temperatures with increasing heating rate. In this condition, the binder burn-out is accomplished with higher evaporation rate as a result of higher vapour pressure with temperature according to Clausius-Clayperon equation. The dominant role of evaporation at higher temperatures not only causes an increasing probability of cracking but also reduces the action of molten binder on the particle arrangement resulting in a broader pore-size distribution of green compact with the effect of lower sinterability of sample B than sample C. As last point of the interplay of drying and burn-out conditions with green microstructure, the thermal response of sample A is highlighted so that binder removal begins at 330°C and is complete before the dwell at 400°C even at 5°C/min HR. The drying of sample A occurs at RT where capillary forces are minimal if not absent, and so the green microstructure is characterized by broad pore-size distribution with large pore size. The larger pores of sample A have the following effects. First, the transport of volatile products is improved and in turn the evaporation mechanism of binders (German, 1987). The combined effects of evaporation of binders at lower temperatures and the limited contraction of sample A during drying can explain the low expansion of sample A during the earlier stage of heat treatment. Secondly, the flow of binder is limited by large pores since capillary pressure scales with the inverse of pore size. As a result of partial or absent effect of capillary flow during drying and binder removal, sample A has higher porosity and broader size-pore distribution than sample B and C at green state with the result of lower sinterability as confirmed by the lowest density and the highest porosity among sintered compacts. It is remarkable to observe that, the prominent effect of capillary forces on green compacts is expected to depend on the graphite powder whose lubricant nature can support the particle arrangement into denser packing. Finally, the drying and burn-out processes are characterized by similar mechanisms which control the green microstructure of compacts and subsequent sintering behaviour.
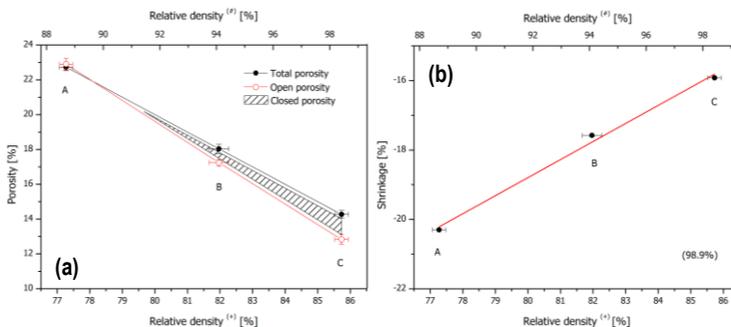
Figure 3.41 Sintering behaviour of sample A, B and C in term of porosity (a) and shrinkage (b) versus relative density (RD+ and RD#) with correlation coefficient of linear fitting of 98.9% in parenthesis.

Figure 3.41 provides a graphical representation of experimental data of table 3.9 concerning the thermal response of compacts A, B and C sintered at 1380°C for 3 h. As high the porosity and shrinkage, as low the density, as expected and shown in figure 3.41; in particular, porosity and shrinkage exhibit fair good relation with relative densities RD+ and RD#. Here, relative densities are expressed as bulk density (BD) in reference to the theoretical density of anode composite fully dense (6.376 g/cm^3) and to the theoretical density of porous (TP=12.84%) anode composite (5.557 g/cm^3), respectively labelled as RD+ and RD#. The theoretical density of porous anode composite conceives the compact with a solid phase fully dense (matrix) and a porous phase, i.e. 12.84%, developed exclusively from the burn-out of pore former. Then, the relative density# (RD#) of fired compacts describes the sintering behaviour (or pore evolution) of the matrix considering the porosity fraction left by pore former as a constant value during sintering. This assumption is valid for matrix with fine grains where large pores do not contribute to the matrix densification and they just shrink in the same measure of the matrix; this suggests that after sintering, the porosity left by pore former depends on the density of the matrix (Slamovich, 1992). In other words, since the shrinkage of large pores does not reduce the porosity of the fired compact, a difference between the total porosity after sintering and porosity predicted by burn-out of pore former, indicates a matrix not fully dense. Under this perspective, RD# is useful for determining the porosity left by pore former TP$_{pf}$ as (RD# − RD+) and then the residual porosity of matrix after sintering TP$_m$, as (TP − TP$_{pf}$). The derivation of these expressions is reported in § 2.3.2.1 while here an example is outlined with the support of table 3.10.

Table 3.10. Bulk density (BD), relative density in reference to theoretical density of fully dense anode (RD+), relative density in reference to theoretical density of porous anode (RD#) with

residual porosity 12.84%, total porosity (TP), total porosity left by pore former (TP$_{pf}$), total porosity of matrix (TP$_m$) and total porosity of pore former from Slamovich-Lange relation (TP$_{S-L}$).

	BD [g/cm³]	RD⁺ [%]	RD# [%]	TP [%]	TP$_{pf}$ [%]	TP$_m$ [%]	TP$_{S-L}$ [%]
A	4.93	77.3	88.7	22.7	11.4	11.3	11.6
B	5.23	82.0	94.0	18.0	12.0	6.0	12.2
C	5.47	85.7	98.4	14.3	12.7	1.6	12.7
D$	5.56	87.2	100.0	12.8*	12.8	0.0	12.8

$ Model sample with matrix fully dense, * value obtained from linear extrapolation of experimental data

For complete densification of the matrix, i.e. sample D of table 3.10, the anode composite is characterized by 5.56 g/cm³ as bulk density (BD), 87.2% RD⁺, 100.0% RD#, and 12.8% TP. The total porosity TP of sample D is obtained from linear extrapolation of experimental data of figure 3.41 (a) and its value is also confirmed by the total porosity left by pore former TP$_{pf}$ and TP$_{S-L}$ here calculated respectively by (RD# − RD⁺) and Slamovich-Lange equation (Slamovich, 1992):

$$TP_{S-L} = \frac{\varnothing_{pf}\rho_m}{1-\varnothing_{pf}+\varnothing_{pf}\rho_m} \qquad (3.30)$$

Where Φ_{pf} is volume fraction of pore former computed as volume of pore former over volume of pore former and ceramic powders, i.e. NiO and YSZ, and results 0.1284 independently from the density of matrix, while ρ_m is the density of matrix after burn-out of pore former, so that RD# is adopted for the calculation of TP$_{S-L}$. Equation 3.30 provides an upper limit for the porosity left by pore former whose behaviour increases with matrix density equally to the relation (RD# − RD⁺) as shown in table 3.10 and figure 3.42 (a).
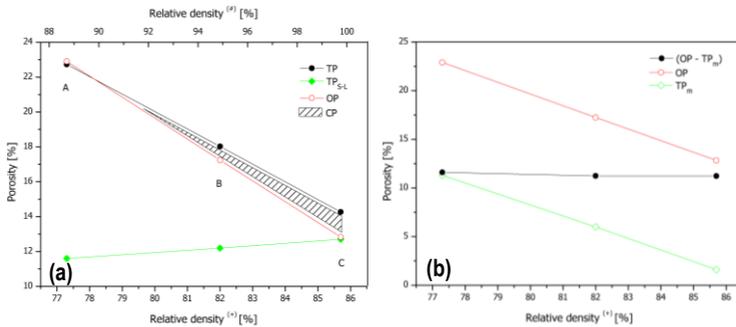

Figure 3.42 Total porosity (TP), total porosity left by pore former (TP$_{pf}$), open porosity (OP) and closed porosity (CP) versus relative densities (RD⁺ and RD#) (a) and sintering behaviour in term of relative density (RD⁺) (b) for sample A, B and C.

Figure 3.42 (a) shows a clear reduction of open porosity for relative density RD[#] greater than 89% where sample A exhibits 100% of OP/TP. In particular, the diminution of the open porosity of compact OP is accompanied by reduction of the matrix porosity TP_m as shown in figure 3.42 (b), suggesting that the decrease of OP and OP/TP is related to the microstructural evolution of matrix. In fact, the evolution of the open porosity of compact and porosity of matrix has same rate and their difference, i.e. (OP − TP_m), gives a constant value supporting that the porosity left by pore former remains constant during sintering according to Slamovich results. Large pores of graphite do not contribute to the densification of fine-grain matrix, and shrink as the matrix retaining their structure during sintering of sample A, B and C. Conversely, the microstructure of matrix evolves from open and interconnected porosity to closed porosity (CP). For sample C, the open porosity and porosity left by pore former have the same value (figure 3.42 (a)) for almost fully dense matrix, i.e. 98.4% RD[#], suggesting that the pore network left by pore former is continous and percolating. For higher fired density, i.e. sample D, it is evident a crossover of OP and TP_{S-L} with the arising of closed porosity. Nonetheless, a large fraction of total porosity is retained as open porosity with estimated OP/TP as high as 87% for full dense fired matrix where most of pore network derived from pore former is continous and interconnected as also supported by micrographs of figure 3.35 and 3.38. The microstructural evolution of matrix involves the transition from open to closed porosity at relative density RD[#] of 89%. It is well known that with the proceeding of sintering, the continous and interconnected pore structure becomes unstable and changes to isolated porosity, typically for density around 90% (Rahaman, 2003). Experimental results of alumina compacts derived from colloidal processing, provide the porosity transition at 92% of relative density, in agreement with theoretical predictions, i.e. 91%, for sintering models conceiving porosity as cylindrical pore channels (Cameron, 1988). In that study the pore transition is associated with grain growth which is limited as long as the porosity is interconnected. It was observed that homogeneous particle packing and high green density delays the pore transition and then the grain growth at higher densities. In the current study, the transition occurs at density as high as 89%, proving the homogeneous green microstructure here obtained from colloidal methods. At this point it is interesting to estimate the green density from experimental data and find a relation with the sintered density. For this purpose, the affine limit porosity (ALP) suggested by Gregorová comes to the aid; it is defined as (Gregorová, 2011):

$$ALP = dl_v + (1 - dl_v)TP \qquad (3.31)$$

Where TP is the total porosity and dl_v the volumetric shrinkage which is related to the linear shrinkage dl, as $dl_v = 3dl – 3dl^2 + dl^3$ under the assumption of isotropic volume

change of the body. ALP relates the shrinkage during firing with the total porosity and since these quantities are complemetary, i.e. the higher the shrinkage, the lower the porosity, ALP results a constant value for a body of given composition. In other words, it is an invariant parameter characterizing the microstructure of compact during sintering whether partial or complete densification. ALP represents also the free volume that is not occupied by ceramic powders and then it has a fixed value for a given compact composition; it is given by ALP = $\emptyset_{(pf+w)}$ where $\emptyset_{(pf+w)}$ is the volume fraction of pore former and water emerged during rheological analysis. Under this perspective, ALP represents the maximum porosity of a compact when any shrinkage is prevented, for instance if only nondensifying mechanisms are actived. Following this idea, when the final shrinkage and total porosity are computed into equation 3.31, it provides the total porosity of green compact (and then the green density) at very initial stage of sintering after burn-out of pore former. On the other hand, from dilatometric curves it is possible to obtain the relative density (ρ/ρ_0) by using the equation (Rahaman, 2003):

$$\rho = \frac{\rho_0}{(1-dl)^3} \tag{3.32}$$

Where ρ_0 is a precise value of density necessary for the normalization of $(1-dl)^3$ function. Equation 3.32 provides the equivalent RD+ and is valid for isotropic shrinkage and for constant weight of compact. For this reason, curves of relative density for sample A, B and C in figure 3.43 (a) are obtained from 801°C (after burn-out of graphite) until the last stage of sintering, i.e. 1380°C for 3 h, with sintered density in table 3.10 as normalization values.
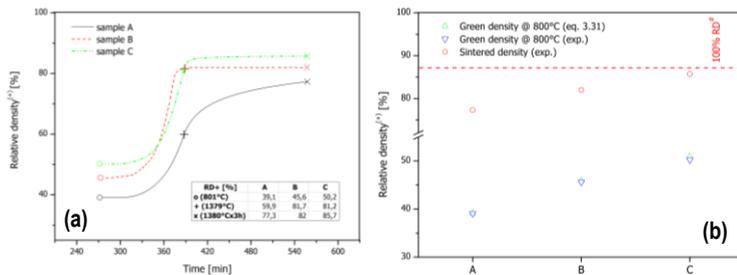
Figure 3.43 Relative density RD+ obtained from dilatometric curves versus time (sample C is shift for ease of comparison) with density values at 800°C (after burn-out of pore former) and 1380°C (at beginning and end of dwell) (a) and comparison of green density at 800°C from equation 3.31 and experimental data with sintered density (b) for sample A, B and C.

Green density values reflect the trend of sintered density ones for sample A, B and C which are characterized respectively by 39.1, 45.6 and 50.2% as relative green

114

density at 800°C; same values within 1.5% error are obtained from the equation of affine limit porosity as shown in figure 3.43 (b). At initial stage, constant values of green density indicate that densification commenced not earlier than 950°C for all samples, suggesting the occurrence of same sintering mechanisms. The plateau of green density confirm nondensifying mechanisms at initial stage of sintering as assumed for the determination of green density from ALP equation. On the other hand, ALP is assumed constant for a given compact composition during sintering. Figure 3.43 emphases that for a given composition of system, i.e. compacts prepared from 80 wt% slurry, ALP also depends on the specific conditions of drying and burn-out.
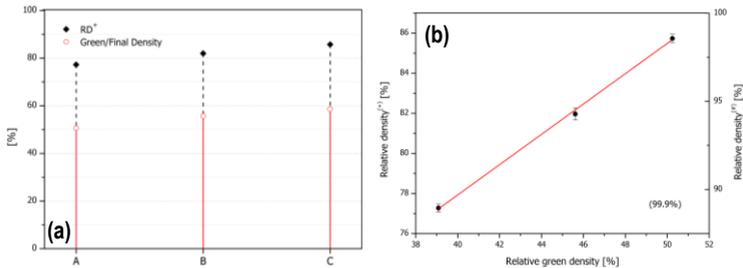
Figure 3.44 Relative (final) density RD+ and ratio between green and final density (a) and linear relation of relative density with relative green density (b) for sample A, B and C with correlation coefficient of 99.9%.

Consequently, the free volume of a green compact with fixed powder compositon is affected by drying and burn-out process. Specifically, it is recognized an increment of green density from sample A to C due to capillary forces acting during drying and burn-out. Precisely the green density increases by 16.7% from sample A to B due to the effect of capillary pressure developed during drying in oven, and an increment of 28.6% from sample A to C attributed to the combined action of capillary force during drying and elimination of binder with milder conditions. The drying and binder burn-out affect the green microstructure which in turn influence the sintering behaviour of sample A, B and C as highlighted in figure 3.44. The ratio between green and final density (GD/RD+) results 50.6, 55.6 and 58.6% respectively for sample A, B and C whose sintered density RD+ is 77.3, 82.0 and 85.7%. It is clear that as higher (GD/RD+), as higher the final density, according to the linear increment of figure 3.44 (b) suggesting that the final microstructure is controlled by the same densification mechanisms. Comparison of figure 3.41 with figure 3.44, sets a connection between green microstructure in term of green density with the properties of sintered body as shrinkage, porosity and density stressing the effect of drying and burn-out steps on the successive sintering process. Then, it is possible to tailor the fired microstructure

by controlling the conditions of drying and binder burn-out for a compact of fixed powder composition and sintering schedule. In the specific case, compacts obtained from dip coating of colloidal suspension, i.e. 80 wt%, provides a uniform and fine microstructure of sintered body with total porosity extending from nearly 13 to 23% which is mostly retained as open porosity, i.e. 90 to 100% of OP/TP. The conditions of sample C fulfill the demands for the production of anode layer with specific properties of porosity for fuel cell applications.

3.3.2.2   *Sintering*

Thermal response of sample C, D and E to different sintering processes is shown in figure 3.45 where drying and binder burn-out follows the same conditions of sample C previously outlined. Sample C and E experience a conventional sintering with a dwell at maximum temperature, respectively 3 h at 1380°C and 2 h at 1400°C. Instead, a multistage sintering involves sample D where a first step at 1400°C for 30 min precedes the last step at 1350°C for 5 h. Basically, as higher the shrinkage as lower the porosity (higher density) as shown in figure 3.45 and table 3.11. The highest density corresponds to the sample E sintered at the highest temperature whereas it is interesting to observe that sample D has higher sintered density than sample C although its lower sintering temperature, i.e. 1350°C. At this stage, it is necessary to point out that the green density after the graphite oxidation at 800°C is different for each sample, while conditions of drying and binder burn-out steps were
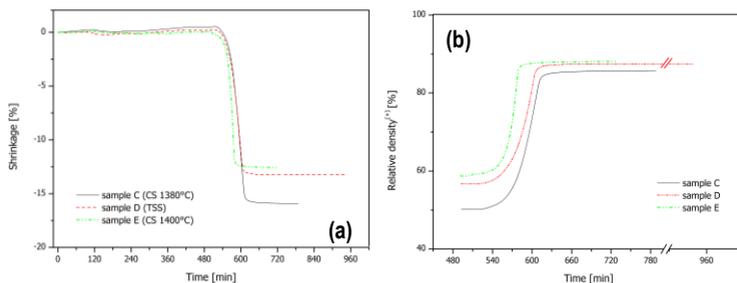
Figure 3.45 Shrinkage versus time (a) and relative density RD+ obtained from dilatometric analysis versus time at 800°C (after burn-out of pore former) for sample C, D and E.

the same. The reason is attributed to the level of water within compacts throughout drying at RT and in oven. After oven drying sample were sealed and weighed before dilatometric analysis in order to verify any weight change due to humidity. As a result, the drying at RT is expected to influence the response of successive drying in oven and firing process similarly to sample A (§ 3.3.2.1). The effect of drying at RT was investigated for compacts derived from the same batch and dried at RT for 12 h

Table 3.11. Bulk density (BD), relative density (RD[+] and RD[#]), open porosity (OP), total porosity (TP), total porosity of pore former from Slamovich-Lange relation (TP$_{S-L}$) and shrinkage for compact C, D and E.

	BD [g/cm³]	RD[+] [%]	RD[#] [%]	OP [%]	TP [%]	TP$_{S-L}$ [%]	OP/TP [%]	Shrinkage [%]
C	5.47 (±0.01)	85.7 (±0.2)	98.4 (±0.2)	12.83 (±0.27)	14.27 (±0.22)	12.7	89.9 (±0.2)	-15.92
D	5.57 (±0.01)	87.4 (±0.1)	100.3 (±0.1)	11.05 (±0.07)	12.62 (±0.20)	12.9	87.6 (±0.1)	-13.23
E	5.61 (±0.01)	88.0 (±0.1)	101.0 (±0.1)	10.37 (±0.18)	11.97 (±0.15)	13.0	86.6 (±0.2)	-12.56

under different conditions, i.e. evaporation surface. These compacts were sintered with same firing schedule and shown diverse (even slight) values of density confirming the influence of drying at RT on the subsequent process steps. In particular, the magnitude of solvent evaporation at RT influences the oven drying where capillary forces modify the green microstructure in the measure of the water content within compacts. This implies that variation of temperature and humidity during drying at RT affects the evaporation of water and then the evolution of green microstructure along the following steps. On the other hand, controlled conditions of temperature and humidity are also recommended during dip coating deposition in order to increase the reliability of the process. Nonetheless, the variance of relative green density due to external conditions is relatively low as proved by samples of the same batch such as sample D and E whose relative green density at 800°C is respectively 56.8 and 58.8% with a difference within 3.5%. It is interesting to observe that the sintering response of compacts is characterized by similar trends regardless the drying conditions.
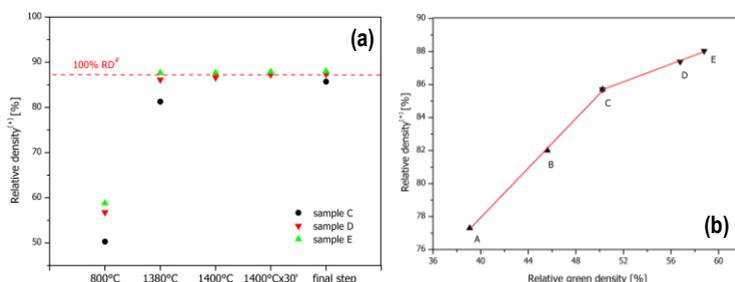

Figure 3.46 Densification behaviour of sample C, D and E for common conditions of sintering (a) and relation of relative density with relative green density for sample A, B, C, D and E (b).

Figure 3.46 (a) provides a comparison of the densification behaviour for sample C, D, E through common conditions of sintering schedules. The trend of green density

117

evaluated at 800°C reflects the corresponding values of the final sintering density. The relative density at 1380, 1400°C and 1400°C after 30 min follows similar trends as a result of similar densification mechanisms. Specifically, for a specific sintering condition, the higher sinterability is determined by the lower size and fraction of larger pores proper to compacts with high bulk density (Lange, 1984 (1)). In particular, processes which promote the reduction of the size of pores and their coordination number, such as isopressing, improve the sinterability of compacts similarly to the capillary forces developed during drying (Lange, 1984 (2)). The sintering behaviour of sample C and E in figure 3.46 (a) clearly indicates that at 1380°C, after nearly 2 h from 800°C, the densification of sample E is practically complete, i.e. 99.6% of its final density, while sample C reaches 94.8% of its final density whose value is 2.7% lower than that of sample E. Therefore for common conditions of sintering, the higher sinterability of sample D and E than sample C is determined by lower porosity and pore size (and hence average pore coordination number) of green compacts as a result of larger extent of compressive stress developed during drying. In figure 3.46 (b), the relative sintered density scales linearly with the relative green density for all samples but with lower slope beyond the inflection point corresponding to sample C; the reason for this behaviour relies on the evolution of pore structure.
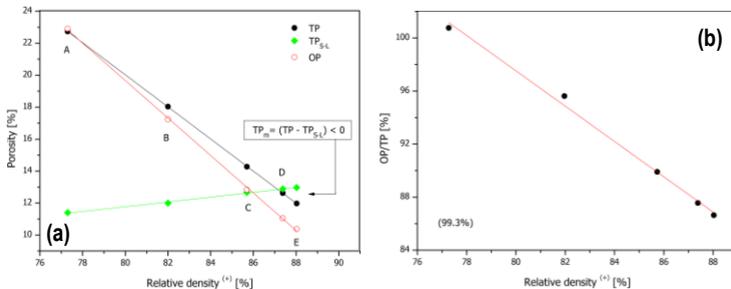
Figure 3.47 Total porosity (TP), total porosity left by pore former (TP$_{S-L}$) and open porosity (OP) (a) and OP/TP ratio versus relative density (RD[+]) with correlation coefficient in parenthesis (b).

Figure 3.47 describes the pore evolution for sample A, B, C, D and E where open and total porosity decrease linearly with densification of samples. For relative density greater than 86%, i.e. sample C, the porosity left by pore former TP$_{S-L}$ first crosses the open porosity and then total porosity at 87.4% RD[+], i.e. sample D, where TP$_{S-L}$ can not exceed 12.84% for full dense matrix in according to equation 3.30; higher value for TP$_{S-L}$ implies a modification of the pore structure. For instance, the negative value of matrix porosity TP$_m$ for sample D and E has no physical meaning, unless a reduction of the porosity left by pore former is allowed. In this case, the assumption that larger pores do not contribute to the densification of compact fades away.

118

Indeed, the assumption is still correct when most of pores left by removal of graphite are large enough to avoid their densification and only a minor fraction of them have similar size of matrix pores and then subjected to densification. At this point the distinction between porosity related to the matrix densification and porosity derived from pore former is not neat since both porosity classes preserve similar feature and densification behaviour. Therefore, as the densification of matrix proceeds, also a fraction of smaller pores left by graphite are exposed to densifying mechanisms with the result of reducing the overall porosity of compact to values lower than 12.84%. The lower slope of RD^+ with relative green density for sample D and E of figure 3.46 is determined by the densification of this fraction of smaller pores left by pore former as also indicated by the crossover of TP_{S-L} of figure 3.47. Moreover, the amount of this pore fraction is very low as also suggested by the constant rate of OP/TP reduction. Again, the densification rate is low as revealed by figure 3.46 where sample D and E achieve the boundary of 100% $RD^\#$ (87.2 RD^+) between 1380 and 1400°C and only exceed it at the final stage of sintering, respectively after 5 h at 1350°C and 2 h at 1400°C. Conversely for sample C, the pore structure left by pore former does not experience densification but just shrink as the same amount of matrix without reduction of compact porosity. Then it is expected that, the sintering behaviour of sample D and E, characterized by relative green density higher than 55.6%, is due to the pore structure derived from pore former whose variation in term of pore size, pore coordination number and porosity results from the breakage and splintering of graphite phase into smaller spots due to the capillary forces acting during drying and binder burn-out; this produces a fraction of smaller pores subjected subsequently to densifying mechanisms. For sample C, these capillary forces just reduce the porosity of green compact and whether producing smaller pores from the graphite phase, these latter do not undergo to densification (upon 3 h at 1380°C) with the result of preserving the pore structure left by pore former during sintering. At this point the porosity of anode composite is delineated in term of pore structure and kinetics with regards to processing variables as drying and sintering conditions. Specifically, the porosity of sintered compact D and E is respectively 12.6 and 12.0%, close to the fraction of pore former, and most of it is retained as open porosity, i.e. 87.6 and 86.6% OP/TP, supporting that the pore structure left by pore former mainly persists even for the severest conditions of sintering, i.e. 1400°C for 2 h, as shown in figure 3.48.
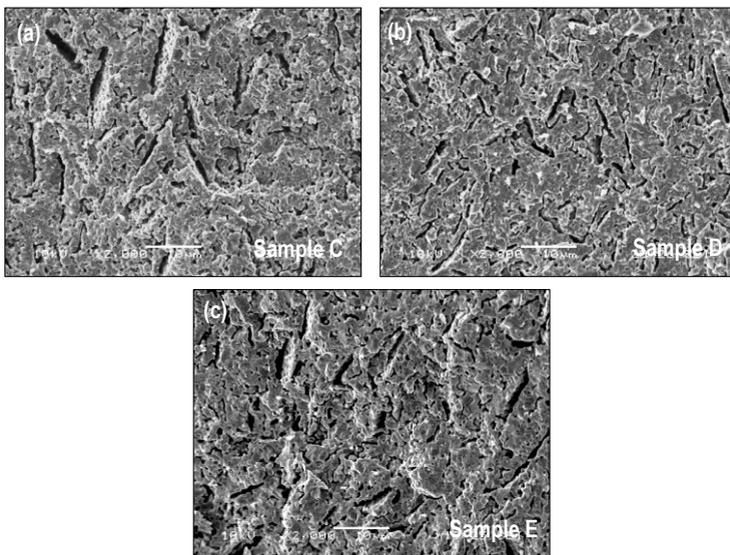
Figure 3.48 SEM micrographs of fired sample C (a), sample B (b) and sample D (c).

The microstructures of fired compact C, D and E are uniform with homogeneous distribution of pores for both conventional and multistage sintering processes. In particular, the pore-size distribution and bulk density of green compacts influence the densification rate but not the final fired microstructure which remains substantially the same for all samples C, D and E. At this point, it is interesting to investigate the further evolution of sintered microstructure after the reduction process which converts the ceramic matrix composed by NiO and YSZ oxides into Ni/YSZ cermet through the flow of hydrogen or its mixture during the first service cycle. The effect of the reduction of NiO into Ni is a microstructural modification of anode whose physical and mechanical properties change substantially and are found to be dependent on porosity which increases as a result of volume change from NiO to Ni due to the loss of oxygen. The porosity of anode composite after reduction p is described by the following expression (Radovich, 2004 (1)):

$$p = p_0 + (1 - p_0)\rho x_{NiO}[\frac{1}{\rho_{NiO}} - \frac{1}{\rho_{Ni}} + \frac{m_O}{m_{NiO}}\frac{1}{\rho_{Ni}}] \tag{3.33}$$

Where p_0 is the porosity of composite before reduction, ρ the density of anode composite fully dense (6.376 g/cm³), x_{NiO} the NiO weight fraction of composite (0.58), ρ_{NiO} the density of NiO (6.67 g/cm³), ρ_{Ni} the density of Ni (8.88 g/cm³), m_O the molecular weight of oxygen (16 amu) and m_{NiO} the molecular weight of NiO (74.7

120

amu). Equation 3.33 assumes that the volume change of anode composite after reduction is negligible as confirmed by dilatometric analysis (Pihlatie, 2009). In addition, Eq. 3.33 provides the porosity upon partial reduction when the term within square brackets is moltiplied by a factor r representing the weight fraction of reduced NiO (Radovich, 2004 (2)). Here, the reduction of sample C, D and E is assumed complete and hence the porosity is calculated from equation 3.33 and represented in figure 3.49.
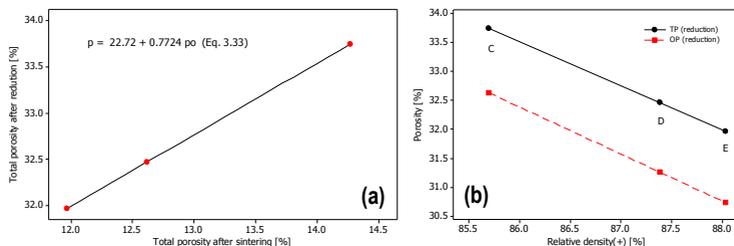
Figure 3.49 Relation between total porosity of sintered and reduced samples C, D and E where Eq. 3.33 is expressed as a function of only sintered porosity p_0 (a) and total and open porosity after reduction versus relative density (RD[+]) (b).

After reduction, the porosity of compact C, D and E increases linearly with sintered porosity when calculated by equation 3.33 which is also expressed as a function of only sintered porosity as reported in figure 3.49 (a). The total porosity of reduced sample C, D and E is estimated to be 33.7, 32.5 and 32.0% respectively, while the open porosity is 32.6, 31.3 and 30.7%. These values are consistent with the appropriate porosity of Ni/YSZ cermets for SOFC application corresponding to 30-40% (Lee, 2002; Dong, 2007). The microstructure of reduced anodes of µt-SOFCs produced by conventional sintering at 1380 and 1400°C are shown in figure 3.50.
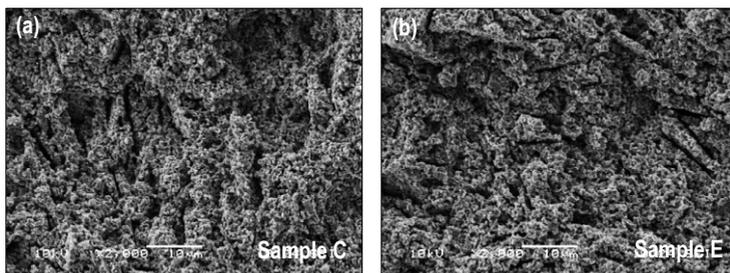
Figure 3.50 SEM micrographs of µt-SOFCs with reduced anode derived from conventional sintering at 1380°C (as sample C) (a) and from conventional sintering at 1400°C (as sample E) (b).

The microstructures of reduced anodes are practically indistinguishable as well as the porosity level, confirming qualitatively its estimation through Eq. 3.33. In particular, the microstructure at interface between electrolyte and anode is identical of the bulk microstructure as a consequence of complete NiO conversion under the current conditions of reduction as shown in figure 3.50 and 3.51. This indicates that the pore structure of initial sintered anodes assures effective gas diffusion throughout the electrode as a result of percolating pores left by graphite particles even for porosity level lower than 13% (Lee, 2002; Lee, 2003).
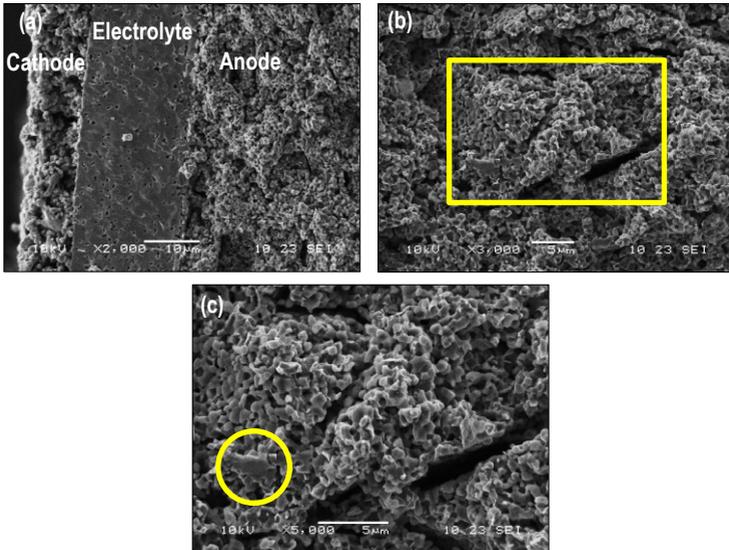
Figure 3.51 SEM micrographs of μt-SOFCs where the reduced anode is fired with conventional sintering at 1400°C (a) and with multistage sintering wherein the marked zone in (b) highlights an agglomerate at higher magnification (c).

On the other hand, the increment of porosity after reduction is related to the oxygen loss due to the conversion of NiO/YSZ into Ni/YSZ cermet which produces small pores tipically well below 1 μm as shown in figure 3.51. The smaller pores determine larger interfacial area per unit volume and hence larger number of reaction sites, beneficial for the cell performance (Jono, 2007). Conversely, agglomerates derived from coarsening of nickel phase during reduction and service, determine a decrease of the reaction area and electrical conductivity of cermet with the effect of degradation of cell performance (Lee,1997; Simwonis, 2000). In figure 3.51, the cermet microstructure derived from multistage sintering is fine and homogeneous

even at larger magnification where the largest agglomerates when present are below 5 μm (yellow circle); also cermets obtained from conventional sinterings present same features as a result of similar behaviour upon reduction in hydrogen at 750°C on the part of sintered microstructures from different firing processes. The benefit of fine microstructure without agglomerates for the current cermets is relevant not only for the cell performance but also for long term operation where agglomeration or coarsening of Ni particles is particularly dentrimental as source of fracture for the cermet failure (Li, 2010; Radovich, 2004 (1)). Moreover, for Ni/YSZ cermets of given powder composition, electrical and mechanical properties were higher for fine microstructures characterized by enhanced percolation (continuity) of Ni and YSZ phases (Yu, 2007). Furthermore, for cermets of given composition and fine microstructure, as low the porosity as high the electrical conductivity and fracture strength (Hu, 1998; Radovich, 2004 (1)). These indications lead the control of each single step for the anode processing, from the preparation of colloidal suspensions to the sintering of compacts and their reduction, in order to produce cermets with fine microstructure and low porosity assuring good electrical conductivity and mechanical strength for the anodes of μt-SOFCs. In conclusion, it was observed that drying and sintering conditions influence the densification behaviour of anode composites but not their final sintered microstructures where the pore structure left by graphite phase is preserved even for the severest conditions of sintering, i.e. 1400°C for 2 h. In this case, the total porosity is 12%, most of it retained as open porosity, i.e. 86.6% OP/TP, resulting appropriate for gas diffusion throughout the electrode for the anode reduction indicating that the porosity level is not a sufficient condition to assure effective gas permeation. Instead, a uniform distribution of pores with appropriate size, shape and interconnectivity is a relevant factor to sustain the gas diffusion as proved by the pore structure left by graphite particles for the current anode composites. The aforementioned value of porosity, i.e. 12%, is also in agreement with investigations of percolation for systems characterized by anisotropic objects as the present graphite flakes whose percolation threshold is lower than 16% typical value for systems of monosize rigid spheres (Balberg, 1984 (1); Balberg 1984 (2)). Moreover, the anode microstructure after reduction do not show agglomeration or coarsening phenomena which are dentrimental for cell performance and the fine microstructure along with low porosity (30-33%) provide good electrical and mechanical properties for the Ni/YSZ cermets here fabricated.

3.4   Electrolyte

Rheological analysis identified the optimal concentration of dispersant corresponding to the minimum viscosity value. Then, the effect of additives was investigated in order to assure appropriate rheological properties of YSZ slurries for dip coating

process as well as good wettability toward anode substrates and finally sufficient green strength of YSZ coatings. Prior to sintering, the binder burn-out was designed in order to minimize the probability of microstructural defects resulting from the exothermic degradation of acrylic-base additives enhanced by the catalytic effect of zirconia powder. A stepwise burn-out not only prevented blistering and cracking but also ensured a higher density of sintered compacts. The densification behaviour of YSZ compacts subjected to conventional and multistage sintering processes was studied in term of pore evolution and grain growth through densification rate curves and phenomelogical model. In addition, interactions between electrolyte and anode layers during co-sintering were analized. The densification of electrolyte films of μt-SOFCs was modified by the presence of transition metals migrated from the anode electrode toward the electrolyte layer during co-sintering. Effects of metal impurities on the electrical properties of YSZ film were also discussed.

3.4.1   Rheological analysis

3.4.1.1   *Screening analysis*

The flow behaviour of electrolyte slurries with different concentration of dispersant is shown in figure 3.52. The effective dispersion of 70 wt% suspensions is evaluated for 0.85 s^{-1} shear rate at 23°C and is achieved for dispersant concentration of 0.50 dwb% corresponding to the optimal coverage of surface particles by the polyelectrolyte molecules. Specifically, the slurry prepared with 0.50 dwb%, i.e. the optimal suspension, shows the lowest viscosity and therefore the highest flowability which are related to the low degree of particle agglomeration (Liu, 1999).
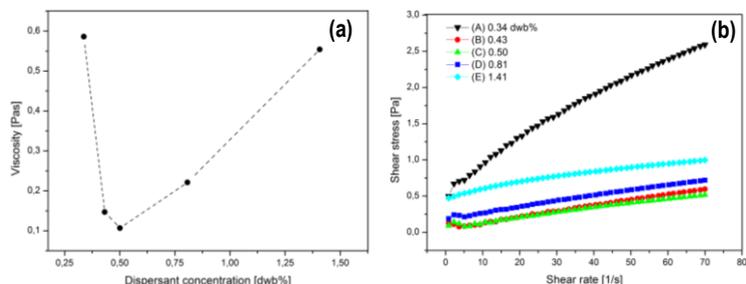
**Figure 3.52** Rheological behaviour of electrolyte suspensions: viscosity versus dispersant concentration at 0.85 s^{-1} shear rate (a) and shear stress versus shear rate (b) at 23°C.

It is interesting to observe that the viscosity increases and the agglomeration is different for dispersant concentration far from the optimum value, i.e. 0.50 dwb%. For concentration lower than the optimum value, the viscosity increases rapidly and

extensive agglomeration occurs due to insufficient particle coverage by dispersant molecules which offers a low barrier to flocculation as proved by sharp increment of shear stress, i.e. curve A in figure 3.52 (b). Conversely, the increase of shear stress and viscosity is limited for dispersant concentration larger than the optimum value, suggesting different mechanism of flocculation. If the concentration is larger than 0.50 dwb%, free polyelectrolyte is present in the solvent with the effect of increasing the solvent viscosity as well as screening the electrical double layer and hence enhancing particle agglomeration although the complete particle coverage by the polyelectrolyte; the former effect induces a slight increase of viscous response as for curve D, while the flow of E slurry is probably produced by both, increment of solvent viscosity and screening of double layer (Briscoe, 1998).
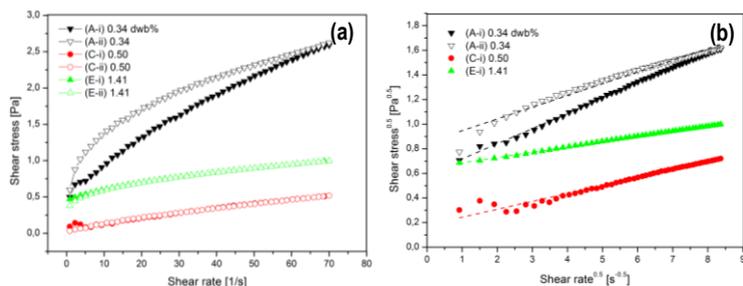
Figure 3.53 Shear stress versus shear rate for ascending i) and descending ramp ii) (a) and and yield stress$^{0.5}$ versus shear rate$^{0.5}$ calculated by Casson model (Eq. 3.4) with correlation coefficient between 96.8-99.9% (b).

Another consequence of the dispersant addition concerns the hysteresis of shear stress curves in figure 3.53. Indeed, all electrolyte suspensions show superimposed flow curves during the ascending and descending ramps with the exception of E slurry characterized by the lowest dispersant concentration, i.e. 0.34 dwb%. This suggests that only the flow of highly agglomerated suspensions shows a dependence on shear the history under the current shear conditions; for instance, slurry prepared with 0.43 dwb% dispersant, i.e. -14% than optimum value, does not display any hysterisis loop regardless higher flocculation than the optimal suspension. The limited hysteresis for electrolyte slurries is a valuable feature for wet colloidal deposition techniques like dip coating where the thickness of coating is unaffected by the shear history for the same suspension with the benefit of higher reliability of the deposition process (Bonekamp, 1996). The current results indicate that the flow behaviour in term of viscosity and shear stress is much less influenced for dispersant concentration higher than the optimum value. In particular, the stability of aqueous slurries stabilized by polyelectrolyte is observed to be significantly affected by temperature (Guo, 1997). Specifically, the adsorption of dispersant on

the part of particles increases with temperature, so that for higher dispersant concentration than the optimum value, the free polyelectrolyte can further adsorb on the particle surface with the result of suspensions more stable and less sensitive to temperature variation (Guo, 1997; Wang, 2007). Nevertheless, free dispersant in the solvent can induce flocculation by screening effect of double layer as well as interact adversely with eventual addition of other additives as binders and reduce the stability of slurry (Khan, 2000). Then, it is important to point out that the present 70 wt% electrolyte slurry is here prepared and charaterized at 23°C temperature where 0.50 dwb% concentration of dispersant assures the lowest viscosity and yield stress indicating a low flocculation degree from which homogeneous green microstructure of coating is also expected (Liu, 1999; Tseng, 1999). In table 3.12 the rheological parameters of slurries with dispersant concentration lower and higher than the optimum value along with the optimal suspension are reported.

Table 3.12. Rheological parameters of 70 wt% electrolyte suspensions with different concentration of dispersant.

Dispersant concentration [dwb%]	Solid loading [v/v]	Yield stress [Pa]	Viscosity# [Pa s]	Hysteresis
(A) 0.34		0.353-0.510$	0.586	Yes
(C) 0.50	0.276	0.032	0.107	No
(E) 1.41		0.413	0.554	No

$ value for ascending and descending ramp respectively, # at 0.85 s^{-1} (23°C)

3.4.1.2   *Electrolyte suspensions for dip coating*

The electrolyte slurries for dip coating are composed by dispersant, binder and plasticizer and derived from the optimal electrolyte slurry characterized by 70 wt% solid loading and 0.50 dwb% dispersant concentration. The concentration of additives and rheological parameters of the slurries are reported in table 3.13, while their rheological behaviour is shown in figure 3.54 in comparison with the optimal suspension, here indicated as C.
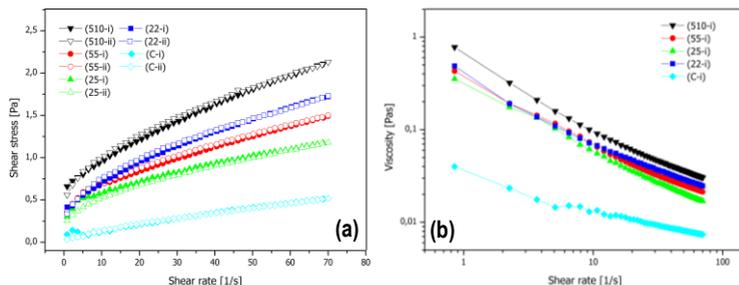
Figure 3.54 Shear stress versus shear rate for ascending i) and descending ramp ii) (a) and and viscosity versus shear rate in double logarithmic scale (b) at 23°C.

The suspensions with additives have a distinct shear thinning behaviour as indicated by the low power-law index (table 3.13) and hence are characterized by larger flocculation in comparison with the suspension with only dispersant (C) whose behaviour is closer to a Newtonian one. The additive addition does not cause hysterisis but only an increment of shear stress and viscosity in comparison to the suspension with only dispersant, i.e. C, as shown in figure 3.54. Altough binder and plasticizer induce flocculation, here their effect on the flow behaviour is different in comparison with that of anode slurries whose viscosity is systematically reduced by dilution coming from emulsions in contrast to the viscosity increment of electrolyte slurries. Under this point of view it is interesting to clarify the effect of binder and plasticizer for electrolyte slurries with the support of table 3.13.

Table 3.13. Composition and rheological parameters of electrolyte slurries.

	Additives[+]			Yield stress [Pa]	Viscosity[#] [Pa s]	η_r[*]	Power law-index, n
	Conc. [wt%]		Ratio B:P				
	B	P					
510	5	10	1:2	0.49	0.78	12.62	0.186
55	5	5	1:1	0.34	0.43	9.36	0.278
25	2.5	5	1:2	0.31	0.35	6.52	0.289
22	2.5	2.5	1:1	0.30	0.49	10.81	0.256
C[§]	-	-	-	0.03	0.11	4.71	0.618

§ Optimal suspension with only dispersant, [+] B (binder), P (plasticizer)
# at 0.85 s^{-1} and 23°C, * Relative viscosity extrapolated at infinite shear rate (23°C)

In general, the viscosity and yield stress increase with additive concentration, as proved by moving from the suspension without additives to that with 5 wt% binder and 10 wt% plasticizer (C and 510, respectively) regardless the concurrent increment of dilution with the exception of slurry # 25. This latter, among the slurries with additives, shows the lowest viscosity at 0.85 s^{-1} and infinite shear rate (η_r) and yield stress along with 22 slurry which difference in composition concerns the platicizer concentration. Under this perspective, for the fixed binder concentration, i.e. 2.5 wt% for 22 and 25 systems, the increment of plasticizer brings about a reduction of viscosity while the yield stress is practically constant. On the other hand, for the fixed plasticizer concentration, i.e. 5 wt%, the increment of binder causes an increase of viscosity and yield stress as evident for 25 and 55 system. Then, the binder is principally responsible for an increment of flocculation, but for lower concentration of binder such as 2.5 wt%, the plasticizer acts as diluent or "co-solvent" and the system is less viscous. This effect involves that the higher the plasticizer concentration the more Newtonian the suspension behaves as proved by the highest power-law index

of 25 system. This effect typically arises for systems without significant network structures, i.e. slurries with low flocculation degree, where free polymers molecules in the solvent increases the dispersion of system through the mechanism of depletation stabilization which occurs for 25 slurry (Rahaman, 2003; Goodwin, 2004). Instead, for higher binder concentration, i.e. 5 wt%, the suspensions are more flocculated and the higher the plasticizer concentration, the higher the flocculation, as proved by the significant increment of yield stress and reduction of power-law index passing from 55 to 510 suspension. In this case, the plasticizer acts as deplethent than diluent and is responsible for the increasing particle agglomeration through depletion mechanism (Goodwin, 2004). Then, suspension # 25 is the most stable suspension among the slurries with additives due to its low particle agglomeration related to its moderate shear thinning behaviour. It is experimentally observed that film obtained from stable suspensions are more dense than film from agglomerated slurries and also the surface of coatings results more smooth (Bonekamp, 1996). In addition, the adhesion of electrolyte film on the anode substrate is proved for the dip coating deposition of slurry # 25 whose wettability properties are assured by 2.5 and 5 wt% of binder and plasticizer which reduces the surface tension of the slurry with only dispersant. This additive concentration also ensures adequate green strength to the electrolyte coatings for the subsequent processing steps of the half-cells. Moreover, the low viscosity of slurry # 25 allows to obtain thin layer for a given set of dip coating conditions. These features are essential for a reliable wet colloidal deposition process and for the realization of thin electrolyte layer for SOFC applications.

3.4.2   Thermal analysis

3.4.2.1   Binder burn-out

The removal of additives from the electrolyte slurries is investigated by dilatometric analysis after drying in oven as done for anode compacts, i.e. 12 h at 60 and 110°C, after 12 h at room temperature. Figure 3.55 and 3.56 show the thermal response of YSZ compacts of different additive concentrations along with the optimal, i.e. 2.5 and 5 wt% binder and plasticizer, respectively. In particular, green compacts with lower additive concentrations correspond to slurries with lower additive (emulsion) concentrations and hence lower dilution with the result of higher solid concentrations for compacts # 22 and 25.
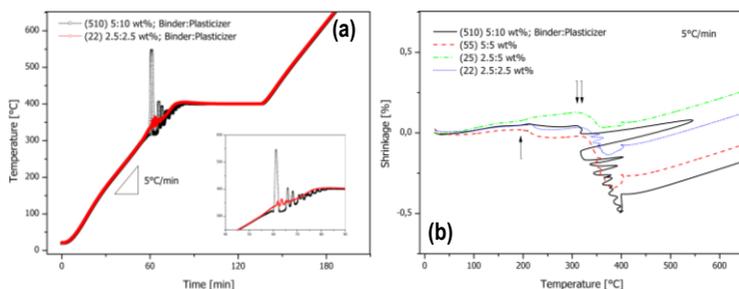
Figure 3.55 Temperature profile of binder burn-out with exothermic peaks in the inset (a) and relative dilatometric curves for electrolyte compacts with different concentration of additives (b).

Dilatometric analysis points out exothermic peaks revealed from the thermocouple placed upon the mid point of samples. Compacts with different concentration of binder and plasticizer as well as their ratio, i.e. samples # 510 and 22, show peaks throughout the same temperature range, i.e. 315-390°C, suggesting identical degradation mechanism of additives regardless the solid concentration as shown in figure 3.55 (a). Previous experiments confirmed the minor influence of solid loading on the activation energy and mechanism of thermal degradation of additives for zirconia compacts (Liu, 1999 (2)). In addition, anode compacts with different solid loadings do not show any exothermic peaks during binder burn-out even at 5°C/min, suggesting the influence of powder composition as main cause for the marked exothermic oxidation of additives, so that zirconia powders are responsible for the burn-out behaviour of YSZ compacts. This assumption agrees with the catalytic effect of oxide powders on the binder burn-out (Masia, 1989; Knapp, 2006). In particular, it was observed that oxide powders extensively alter binder burn-out by retarding the early stage of degradation and accelerating the later stages (Knapp, 2006; Liu, 1999 (2)). The burn-out of current acrylic-base additives is in agreement with thermal behaviour in air of polyacrylate film whose degradation occurs in one single stage with exothermic peak at 370°C (Liufu, 2005). Then, the exothermal degradation of acrylic binder and plasticizer is further enhanced by the catalyc effect of zirconia powder with the effect of larger volume of volatile species which can produce rapid pressure build-up within compacts especially when diffusion of degradation products outward is the rate limiting step (Shulka, 1989; Knapp, 2006). In this case, blistering and cracking of compacts can occur with possible release of gaseous products which should be accompanied by exothermal peaks. For these reasons, binder removal for YSZ compacts is particularly critical as shown in figure 3.55 (b). The burn-out of compacts with different addititive concentrations is complete before the isothermal step at 400°C and is characterized by more or less fuzzy shrinkage curves between 300 and 400°C. This particular behaviour is related to the harsh additive oxidation with release of gases, i.e. 550°C for compact # 510,

and then hot spots cause thermal expansion of compacts as indicated by upward peaks of shrinkage curves regardless the continuous contraction of samples up to 400°C, with the exception of the sample with optimal additive concentration. In fact, compact # 25 shows a smooth shrinkage behaviour as a result of mild burn-out without evident exothermic peaks as shown in figure 3.56 (a) even at 5°C/min. This compact is characterized by constant expansion up to 310°C (↓↓) beyond that it shrinks, in contrast with the other samples whose expansion stops around 210°C (↑) which is followed by a nearly constant dimensional change before an evident contraction beyond 310°C. Another difference of compact # 25 concerns its dimensional change that remains positive even during shrinkage connected to binder burn-out between 300 and 400°C. In fact, for the other samples there is an inflection of shrinkage curves close to 210°C indicating a volume reduction due to the loss of more volatile additive species. This contraction causes a denser particle packing with smaller pore channels and this microstructure hinders the subsequent degradation of remaining additive of higher molecular weight. In fact, although a slight thermal expansion is expected at 300°C, the expansion for compacts # 22, 55 and 510 is zero, suggesting a denser packing before the last stage of burn-out that is exothermic and the most critical. In this condition, gaseous products of degradation accumulate within compacts and their release causes microstructural defects and so the corresponding fired compacts are expected to be more brittle. Conversely, after drying, compact # 25 is characterized by higher packing density and smaller pores than compacts # 22, 55 and 510 as indicated by the lowest final shrinkage, which is not shown here. Consequently, additive layer expands as long as pore channels are sufficiently large to promote the evaporation and migration of gaseous species occurring at 310°C. Similarly, larger expansion during the ealier stage of burn-out has also involved green anode compacts (§ 3.3.2.1) with higher packing density characterized by lower final shrinkage and higher sintered density. Then, a higher green density for compact # 25 is not unexpected as a result of the optimization of rheological behaviour of slurry # 25 which assures a homogeneous structure of suspension necessary for achieving a uniform and dense green microstructure. In turn, the green microstructure influences the diffusion of degradation products and therefore the thermal behaviour of YSZ compacts, under specific conditions of burn-out as atmosphere and heating rate. Now, it is interesting to investigate the thermal response of compact # 25 for different burn-out schedules as shown in figure 3.56.
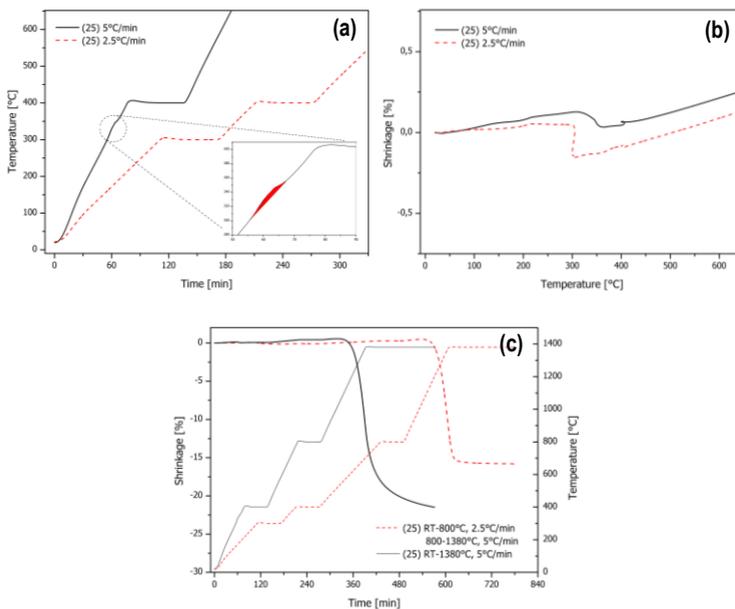
Figure 3.56 Thermal behaviour of 25 compact for different burn-out schedules as shown in (c) with relative temperature profile (a) and dilatometric curves (b) and (c).

So far, the binder burn-out of YSZ compacts is carried out by linear heating rate of 5°C/min up to a dwell of 1 h at 400°C. In this condition, compact # 25 shows a slight increment on temperature as shown by the temperature profile of figure 3.56 (a). In order to achieve a milder burn-out to minimize the probability of defects and cracking, binder removal is also carried out at lower heating rate (HR), i.e. 2.5°C/min, with additional dwell at 300°C for 1 h before the dwell at 400°C. Secondly, this milder burn-out (here referred as stepwise burn-out in contrast to the previous linear burn-out) is expected to have the additional advantage of increasing the green density and so the sintered density of electrolyte compact according to the preceding results for anode compacts. Figure 3.56 points out the achievement of the first goal because no exothermic peaks arise along the heating ramp as a result of mild evaporation of degradation products. In fact, as lower HR as lower the thermal expansion with the result of denser microstructure which moderates the evaporation. Moreover, evaporation at 300°C is further reduced than 400°C due to the lower vapour pressure of additives. As clear from figure 3.56 (b), the binder burn-out is achieved before the dwell at 400°C for both linear and stepwise burn-out, but for this latter the removal of additives is complete already after 1 h at 300°C. The lower evaporation of stepwise burn-out supports the formation of liquid binder which promotes the arrangement of particles into denser packing with the result of narrower

131

pore-size distribution of green compact which favours the subsequent densification. In fact, the final shrinkage of compact derived from stepwise burn-out reaches a plateau around 15.8% after 1h at 1380°C because of higher sinterability than the green compact obtained from conventional burn-out whose complete densification is not achieved after 3 h at 1380°C. Finally, the lower shrinkage indicates higher sintered density for compact with stepwise burn-out whose progress without exothermal peaks also assures low probability of defects and cracking. Then, the stepwise burn-out ensures higher density minimizing the probability of microstructural defects which are essential demands for the development of dense electrolyte layer for SOFC applications.

3.4.2.2   *Sintering*

The densification behaviour of YSZ compacts is shown in figure 3.57 where samples experience identical conventional and multistage sintering of anode compacts and maintain their designation. Then, sample C and E undergo conventional sintering with a dwell at maximum temperature, i.e. 3 h at 1380°C and 2 h at 1400°C, respectively, while for sample D a multistage sintering involves a first step at 1400°C for 30 min prior the last step at 1350°C for 5 h. The dilatometric curves of YSZ compacts are practically superimposed with very close final values, yet as low the shrinkage, as high the sintered density as also pointed out in table 3.14. This implies an increasing densification response from sample C to F as proved by reduction of porosity as evident in figure 3.57 (b); sample F is fired with conventional sintering for 2 h at 1420°C. A transition from open to closed pores is also expected, within experimental errors, for relative density ≥ 95% as proved by sample F whose open porosity and OP/TP ratio is nearly 0.3 and 6% at 94.6% of theoretical density.

Table 3.14. Relative green density at 800°C and relative sintered density, open porosity (OP), total porosity (TP), ration between open and total porosity (OP/TP) and shrinkage for YSZ compacts.

	Relative density [%]		OP [%]	TP [%]	OP/TP [%]	Shrinkage [%]
	800°C	Sintered				
C	52.7	89.4	6.72	10.61	63.4	-15.82
D	54.2	92.2	1.01	7.82	12.9	-15.69
E	55.3	92.6	0.55	7.40	7.4	-15.33
F$	-	94.6	0.32	5.35	5.9	-

$ Sample fired in furnace with conventional sintering for 2 h at 1420°C

It is interesting to observe that the porosity of YSZ compacts follows an exponential-decay law which indicates common and general mechanisms of densification in spite of different sintering schedules as pointed out in figure 3.57 (b). As densification

proceeds, microstructural evolution involves diminution of pores per unit volume and grain growth which are controlled by diffusion mechanisms and therefore matter transport paths (Rahaman, 2003). When relative density increases, the pores per unit volume (or pore density) decrease while their relative distance increases and in turn the average diffusion distances with the effect of slowing down the pore densification (Slamovich, 1992).
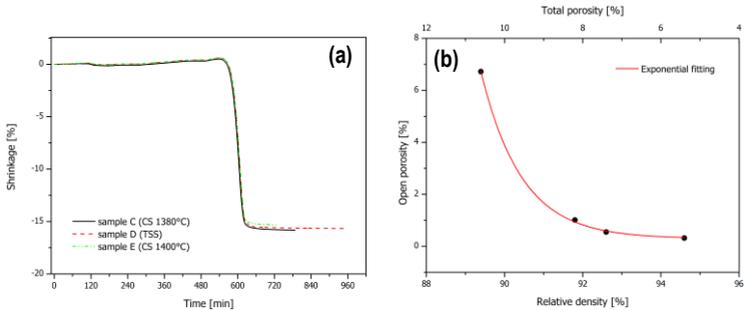
Figure 3.57 Dilatometric curves versus time for sample C, D and E (a) and porosity evolution for sample C, D, E and F fitted by exponential law (b).

Similarly, the grain growth reduces the densification rate by increasing distances of matter transport into pores through grain boundary diffusion when pores are trapped within grains (abnormal grain growth), and by reducing the number of grain boundaries intersecting pores which are paths of preferential matter transport for reduction of pores during normal grain growth (Slamovich, 1993; Rahaman, 2003). Although normal grain growth reduces the densification rate, it is useful for the shrinkage of larger pores through the reduction of their coordination number ensuing higher sintering density for compacts where grain growth is not inhibited as experimentally demonstrated (Lange, 1984 (2); Lange, 1984 (1)). At this point, it is interesting to investigate deeply the densification behaviour in term of pore evolution and grain growth.

133
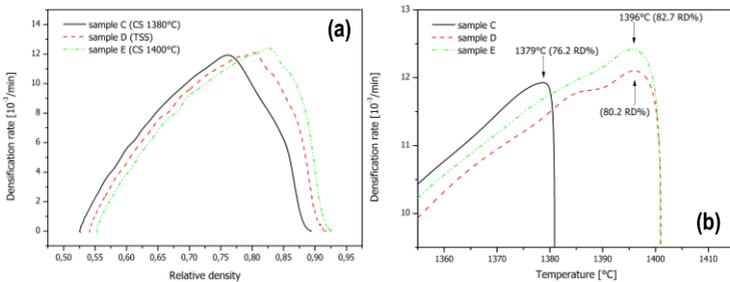
Figure 3.58 Densification behaviour of YSZ compacts. Densification rate versus relative density (a) and densification rate versus temperature (b) for sample C, D and E.

The densification behaviour of YSZ compacts in figure 3.58 (a) is typically encountered for oxide systems subjected to either conventional and multistage sintering as a result of common densification mechanims (Roosen, 1984; Lange1984 (2); Lange 1989, Lin, 1997). The green density at 800°C is proportional to sintered density, confirming that the final density is proportional to the bulk density of green compacts. For final density value lower than the theoretical density, the full densification is limited by the presence of residual pores. Despite kinetics, pores with large coordination number (usually larger pores) do not shrink during sintering if microstructural rearrangements as grain growth or interfacial instability of elongated pores are prevented (Lange, 1984 (1)). In this condition, large pores control the final density when are developed during sintering, as well as the initial bulk density of green compact if they are present after forming process with the effect of reducing the final density of sintered compact (Lange, 1984 (1)). Conversely, smaller pores control the densification behaviour during first stage of sintering and thus shrink at lower temperatures; for a given temperature, as higher the fraction of smaller pores has higher the densification rate of compact (Roosen, 1984; Lange, 1984 (2)). The shrinkage of zones with smaller pores can cause local densification with concurrent pore enlargement of surrounding zones, so that a redistribution of pore sizes occurs prior the last stage of densification. It was also observed that densification rate increases as long as local densification depletes smaller pores (Lange, 1984 (2)). At this stage of maximum densification rate, compact is characterized principally by larger pores which can subsequently undergo shrinkange when microstructural rearrangements as grain growth occur and kinetics permits (Lange, 1984 (1)). In figure 3.58, the thermal response of YSZ compacts is described by densification curves almost parallel and then with similar slopes so that the rate of densification rate at given value of relative density and temperature is independent of the initial compact density. This agrees with Rahaman experiments on compacts prepared with different initial density whose densification during the initial stage of sintering is characterized by the same densification rate (Rahaman, 1986). The same densification rate up to the the maximum of densification-rate curves implies the same mechanism of densification which concerns the fraction of smaller pores, according to Lange results (Lange, 1984 (2)). As a consequence, any difference in the densification behaviour for YSZ compacts in figure 3.58 is related to specific characteristics of smaller pores, i.e. distribution, most frequent pore size (MFPS) and volume, during the first stage of sintering which ends at maximum of densification-rate curve wherein the sintering schedule is common for all samples. Although densification curves are very similar, indications on the pore structure of green compacts can be obtained from Roosen observations based on the relation between

the pore-size distribution (PSD) and densification rate. Specifically, the maximum of PSD of the green compact, that is the MFPS, matches the maximum of densification-rate curve (at a certain temperature) whose height is related to the pore volume for that specific pore size, suggesting that each pore size needs a specific temperature for its densification (Roosen, 1984). In figure 3.58, the maximum of densification rate of all samples is achieved before the isothermal dwell at the highest temperature so that the sintering of smaller pores is expected to be completed at 1379°C for sample C and 1396°C for sample D and E where the temperature profile of sintering processes is common for all samples. It is evident a small difference on the temperature and height of maximum peaks, which identify respectively MFPS and pore volume for a specific pore size, suggesting almost identical features of small pore fraction for green compact C, D and E. Nonetheless, for sample C the peak at 1379°C indicates a MFPS at lower pore size than sample D and E and therefore it is expected higher densification rate for sample C. Indeed, for a given relative density and temperature the densification rate of sample C is higher than other samples as a result of relative higher portion of smaller pores as represented qualitatively by PSD curves of green YSZ samples in figure 3.59. The representation in figure 3.59 (a) is oversimplified but it is useful to highlight that MFPS of sample C at lower pore size, although causes a relative increment of fraction of smaller pore, does not imply an absolute increase of volume of smaller pores (as represented by rigid shift of PSD curve) because a higher fraction of small pores should produce a higher final density
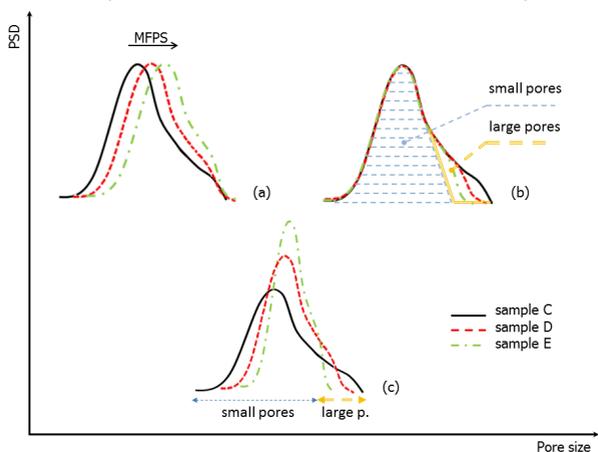

Figure 3.59 Representation of PDS curves from densification curves of YSZ compacts where it is shown the effect of shift of MFPS (a) a comparison of small and large pore fractions (b) and a qualitative sketch of PSD curves for green compact C, D and E (c).

for sample C, in contrast to its lowest sintered density as shown in table 3.14. As a result, the shift of PSD curve toward lower pore size also involves a wider tail of PSD toward larger pore size accompanied by concurrent reduction of height of MFPS for the constancy of pore volume as depicted in figure 3.59 (c). Similarly, the maximum peak at higher temperature for sample D and E, i.e. 1396°C, entails a MFPS at larger pore size whose height is proportional to the peak height at 1396°C and hence the MFPS of sample E is higher than sample D. In turn, the variation of MFPS heigth influences the fraction of larger pores that results inversely proportional to the MFPS height; among sample E and D, this latter should have higher fraction of larger pores. Finally, the PSD curves for green YSZ compacts are derived from densification-rate curves and are illustrated in a qualitative outline in figure 3.59 (c) where the pore structure of sample C is charaterized by the lowest and smallest MFPS with the largest fraction of large pores while sample D and E are characterized by larger fraction of smaller pores with "average" (most frequent pore size) larger size than sample C, but with narrower PSD. These indications on pore structure of green compacts are important to understand the evolution of microstructure during sintering. In this respect, table 3.15 provides a further support with values of relative density at 800°C, at maximum densification rate and after sintering expressed in term of total porosity respectively as TP_G, TP_{MDR} and TP. The values of total porosity in table 3.15 are complementary with those in table 3.14 with the advantage of underlining the pore evolution throughout the sintering process and in particular during the last stage of densification where the evolution of grain growth is controlled by the pore structure (Cameron, 1988).

Table 3.15. Total porosity of YSZ compacts at green state (800°C) (TP_G), at maximum densification rate (TP_{MDR}) and total porosity after sintering (TP) and relative ratio.

	Total porosity [%]			FSD[+] [%]	FLD[°] [%]	FLP[#] [%]
	TP_G (a)[§]	TP_{MDR} (b)[¶]	TP (c)[$]	(a−b)/a	(b−c)/b	c/a
C	47.3	23.8	10.6	49.7	55.5	22.4
D	45.8	19.8	7.8	56.8	60.6	17.0
E	44.7	17.3	7.4	61.3	57.2	16.6

[§] at green state (800°C), [¶] at maximum densification rate, [$] after sintering

[+] fraction of small pores sintered between [§] and [¶], [°] fraction of larger pores sintered between [¶] and [$],

[#] ratio of large pores after sintering over initial porosity

The evolution of porosity (considered as the total porosity) from green state (TP_G) to the sintered state (TP) follows the same trend for all samples as highlighted in figure 3.60. The final porosity is controlled by pores with high coordination number (usually large pores) which do not shrink during the last stage of sintering and limit the final density. The ratio between the final porosity over the porosity at green state (FLP) scales with the final porosity suggesting that larger pores effectively control the final density and can derive either from green state and binder burn-out. The decrease of

136

larger pores FLP from sample C to sample E basically confirms PSD of green YSZ compacts as well as the much higher fraction of smaller pores for sample D and E which shrink up to the maximum of densification rate (FSD). On the other hand, FLD represents the fraction of larger pores which shrink during the last stage of sintering (beyond the maximum of densification rate) under the assumption that smaller pores are completely depleted at the maximum of densification rate.
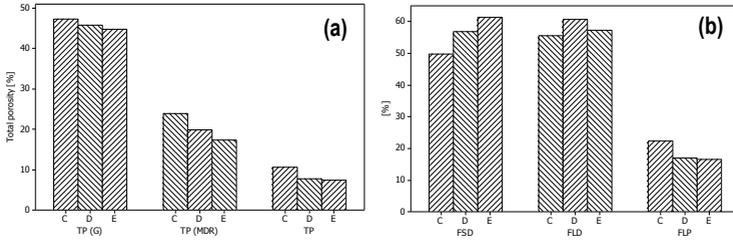
Figure 3.60 Representation of PDS Total porosity at green state (TP$_G$), at the maximum densification rate (TP$_{MDR}$) and after sintering (TP) (a) and relative relations as reported in table 3.14 (b).

The densification during the last sintering stage is tipically accompanied by grain growth which is controlled by pore evolution. Then, grain growth of YSZ compacts is expected to occur beyond the maximum of densification rate where the pore evolution can be described by a phenomenological model proposed by Cameron et al. in which for a given grain size, the rate of densification of porosity is proportional to the remaining porosity and it is expressed as (Cameron, 1982):

$$\frac{d(P)}{dt} = -\frac{1}{\tau}P \tag{3.34}$$

where P is the porosity (total porosity) and τ a time constant that depends on the grain size and temperature. Integration of Eq. 3.34 with the initial condition as $P = P_o$ at $t = 0$, provides:

$$P = P_o \exp(-\frac{t}{\tau}) \tag{3.35}$$

Equation 3.35 describes the reduction of porosity similarly to the exponential-decay law for the present experimental data as shown in figure 3.57. Equation 3.35 can be expressed as a function of relative density ρ through the relation $P = 1 - \rho$ where ρ is obtained from dilatometric curves (Eq. 3.32), and thus:

$$ln\left[\frac{(1-\rho)}{(1-\rho_0)}\right] = -\left(\frac{1}{\tau}\right)t \tag{3.36}$$

137

The slope of equation 3.36 scales with τ that depends on the grain size and therefore a change of the slope indicates the onset of grain growth from an initial condition. For YSZ compacts, the initial condition ρ_o concerns the density at maximum densification rate which corresponds to the compact density at the beginning of isothermal dwell at 1380°C for sample C and at 1400°C for sample D and E.
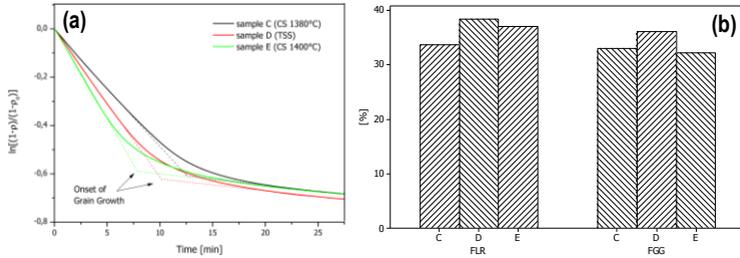
Figure 3.61 Densification behaviour of experimental data fitted by Eq. 3.36 (a) and FLR and FGG from table 3.16 (b).

As expected, grain growth occurs at a certain point as supported by the change of slope of experimental data fitted by Eq. 3.36 as shown in figure 3.61 (a). The onset of grain growth occurs as soon the isothermal dwell at maximum temperature is reached and in less than 15 minutes for all samples. In particular, the onset of grain growth, determined by the intersection of the two approximately linear regions, is inversely proportional to the initial relative density at maximum densification rate (complementary to TP_{MDR}) and therefore follows E, D and C order. This relation is also maintained for the relative density at the end of the first linear region (complementary to TP_{LR}) as pointed out in table 3.16, so that grain growth arises first for sample E at corresponding relative density of 89.1%, followed by sample D and C at 87.2 and 84.2% relative density, respectively. In this linear region, where relative density is < 90%, the porosity of compact is expected to be predominately interconnected with pore channels located at grain edges (Cameron, 1982); these pores, previously referred as large pores, can either derive from forming process and additive burn-out as well as from local densification during the first stage of sintering. For higher relative density, the interconnected pore channels collapse into smaller isolated pores with concurrent grain growth suggesting that interconnected (extensive) pores along grain junctions have greater resistance to grain boundary motion than isolated (small) ones. During this stage, as the relative density (RD) increases, the microstructure is controlled by the volume reduction of pores and simultaneous grain growth (Rahaman, 2003). The occurrence of grain growth largely

reduces the densification rate as evident in figure 3.61 where sample C, D and E are characterized by parallel curves indicating similar mechanisms of grain growth with identical densification rate, in spite of different temperature during the last stage of sintering, i.e. 1380°C, 1350°C (after 30' at 1400°C) and 1400°C for sample C, D and E, respectively. Then, the densification rate during grain growth is independent from the compact density, but it also evident that as high the RD at maximum densification rate (as low the TP_{MDR}) as high the relative density at pore transition (as low the TP_{LR}) and as high the final relative density (as low the TP). Under this perspective, it is reasonable to believe that as higher the compact density at maximum densification rate as higher the final density for constant densification rate along grain growth regime throughout the temperature 1350 and 1400°C. Nonetheless, when densification behaviour of sample D and E, the reduction of porosity for sample D is improved as shown in figure 3.61 (b). The same densification rate of YSZ compacts during grain growth allows to compare the final density and FLD of sample D and E under same dwell conditions. For instance, when the sintering of sample E is extrapolated to 5 h, it produces a relative final density of 93.2% that is only 1.1% greater than that of sample D, i.e. 92.2%, while FLD and FGG are respectively 60.7% and 37.6% which are equivalent to those of sample D as shown in table 3.16. On the other hand, sample D can achieve 93.2% RD after 10 h at 1350°C. Despite the prolonged permanence of multistage sintering, the lower temperature of last stage, i.e. 50°C below the temperature of conventional sintering as for sample D, can be useful for those heat treatments limited for instance by compounds of high vapour pressure or by oxidation of metal components.

Table 3.16. Total porosity of YSZ compacts at maximum densification rate (TP_{MDR}), at the end of linear regime (TP_{LR}) and total porosity after sintering (TP) and relative ratio.

	Total porosity [%]			FLR[+] [%]	FGG[°] [%]	FLD[#] [%]
	TP_{MDR} (b)	TP_{LR} (b")[¶]	TP (c)	(b−b")/b	(b"−c)/b"	(b−c)/b
C	23.8	15.8	10.6	33.6	32.9	55.5
D	19.8	12.2	7.8	38.4	36.1	60.6
E	17.3	10.9	7.4	37.0	32.1	57.2

[¶] at the end of linear regime (before grain growth), [+] fraction of pores sintered between maximum densification rate and grain growth, [°] fraction of pore sintered [#] fraction of pores sintered between (b) and (c)

As a result, sintering of YSZ compacts can be tailored according to the process requirements and the thermal response based on densification curves. For YSZ compacts, it was observed similar densification behaviour during the initial stage of sintering (from 800°C to the maximum of densification rate, i.e. 1380-1400°C), although slight difference on densification rate is deemed to depend on the different fraction of smaller pores even present for almost same initial green density, i.e. 54.0±1.3%. At the end of this stage, smaller pores were sintered while larger pores

evolved from interconnected to isolated pores (pore transition) between the maximum of densification rate and the last sintering stage controlled by grain growth (grain growth regime). The pore transition is proportional to the relative density so that it occurs at 87.8 and 89.1%, respectively, for sample D and E, under identical sintering condition, i.e. at 1400°C. In turn, the onset of grain growth is related to the pore transition and therefore to the relative density of compacts, whereas the rate of grain growth (indicated by the slope of negative inverse of time constant $,-1/\tau$) is similar for all samples, suggesting similar grain growth mechanisms during the last sintering stage throughout the temperature 1350 and 1400°C. Under this point of view, equivalent values of final density can be achieved for prolonged permanence at lower sintering temperature as for sample D. Nevertheless, final density above certain limit, i.e. 95% of theoretical density, can be achieved in reasonable short dwell only at higher temperature as 1420°C for sample F.

3.4.2.3   *Interaction between electrolyte and anode layer*

The densification behaviour of YSZ samples with initial green density of 54.0±1.3% was previously evaluated for conventional and multistage sintering processes which ensue a final relative density of ~93% with open porosity ≤ 1%, i.e. sample D and E. However, the thermal response of YSZ films can be different during co-sintering of half-cells, as a result of interaction with the anode substrate. For instance, a thin film on a rigid substrate shows a lower densification rate than the unconstrained film (Garino, 1990). In addition, the structure and microstructure of electrolyte layer can be affected by the diffusion of elements from the anode during the cell fabbrication and service (Linderoth, 2001; Zhou, 2010; Liu, 2003). In figure 3.62, micrographs of µt-SOFCs derived from conventional and multistage sintering (as for sample D and E) of half-cells with nickel wire as inner current collector.
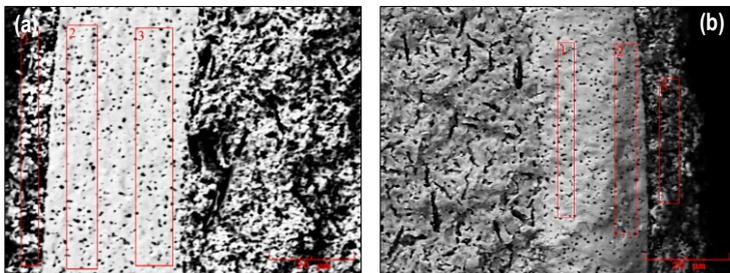

Figure 3.62 SEM micrographs of µt-SOFCs with nickel wire as current collector where co-sintering of electrolyte and anode involves multistage sintering (30' at 1400°C and 5 h at 1350°C) (a) and conventional sintering (2h at 1400°C) (b) with detection areas of EDS analysis.

The electrolyte layer is nearly 20 µm thick and not completely dense; small pores appear isolated and not interconnected thus preventing gas leakage between electrodes. The closed porosity of both samples derived from conventional (CS) and multistage sintering (TSS) indicates relative density > 93-95% (in comparison with 87% of anode) in agreement with previous results of table 3.14 and literature data. From thermal analysis, the densification of anode commences at 950°C while that of electrolyte does not initiate before 1100°C and therefore the anode substrate is expected to act as a rigid support for the electrolyte layer during co-sintering process. In addition, the densification rate of electrolyte is higher than that of anode for temperature above 1280°C (Bonenti, 2012). For adherent films on rigid substrates, the densification of electrolyte is constrained and the film experiences transient stresses, typically tensile, which can cause its delamination and cracking as much as shrinkage and densification rate of film are higher than those of substrate (Bordia, 1985). In figure 3.62, the absence of delaminations at interface between the anode and the electrolyte as well as cracks across the electrolyte, suggests that during co-sintering the constrained YSZ films are able to relax tensile stresses through its reduction of densification rate (Garino, 1990). In figure 3.63, the micrographs of µt-SOFCs obtained from conventional and multistage sintering of half-cells with palladium wire as inner current collector, reveal microstructure of YSZ layers similar to those of figure 3.62 suggesting same thermal response during co-sintering.
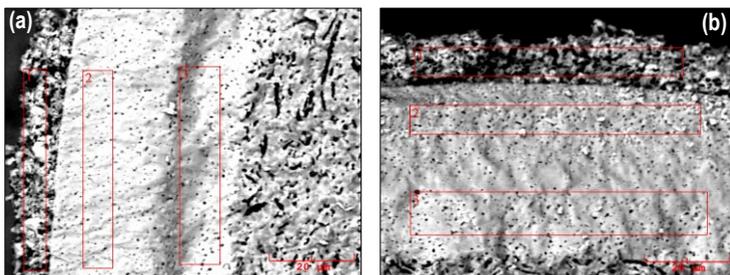
Figure 3.63 SEM micrographs of µt-SOFCs with palladium wire as current collector where co-sintering of electrolyte and anode involves multistage sintering (30' at 1400°C and 5 h at 1350°C) (a) and conventional sintering (2h at 1400°C) (b) with detection areas of EDS analysis.

The observation of closed porosity and good adhesion of YSZ layer to substrate indicates a consistent densification of electrolyte in spite of the reduction of densification rate due to the effect of tensile stresses caused by the rigid substrate. An improvement of sinterability was observed for YSZ compacts with addition of NiO powder below the solubility limit, i.e. ~1.5 mol% in 8 mol% yttria-doped zirconia (8YSZ) at 1350°C (Batista, 2011 (2)). On the other hand, doped-zirconia powders

with different Y_2O_3 and impurity contents showed diverse densification behaviour where phase precipitation and segregation of impurities along grain boundaries were related to sintering conditions and YSZ compositions (Badwal, 1995). At this stage, it is evident that the densification of constrained YSZ films not only depends on the stresses with substrates but also on eventual contaminations from anodes at temperatures as high as 1400°C where the mobility of ions is high. Indeed during fabrication of SOFCs, interaction of transition metals with YSZ electrolyte is almost inevitable at high temperatures when protective interlayers at electrolyte interfaces are not present as proved by Ni migration through 3 and 8 mol% yttria-doped zirconia electrolytes from screen printed NiO substrates (Delaforce, 2007). Then, for a thorough description of densification behaviour of YSZ films during co-sintering, it is important to identify eventual interaction of transition metals with electrolyte and their sources as NiO-based cermet and Ni- and Pd-current collectors embedded in the anodes of present µt-SOFCs. For this purpose, the microstructural analysis of figure 3.62 and 3.63 is accompanied by chemical investigation through X-ray energy-dispersive spectroscopy (EDS) analysis of electrolyte layers near the anode and cathode interfaces checking for the transition metals present in µt-SOFC anodes, i.e. nickel and palladium. Table 3.17 points out the concentrations of nickel and palladium (balanced by Y and Zr) measured at electrolyte interfaces (rectangular windows in figure 3.62 and 3.63). Before the examination of composition data of electrolyte, it is necessary to remark that EDS is a semi-quantitative analysis from which significant relative errors (~10%) arise for element concentrations near to the detection limit alike the values of table 3.17. In spite of this, the systematic presence of nickel and palladium in other samples than those of figure 3.62 and 3.63 does not impair the following considerations and confirms the idea of interaction of transition metals with electrolyte layer during co-sintering.

Table 3.17. Concentration of nickel and palladium at electrolyte-cathode and electrolyte-anode interfaces for µt-SOFCs with nickel and palladium wire as inner current collectors.

| [%]* | Nickel-current collector | | | | Palladium-current collector | | | |
| | TSS | | CS | | TSS | | CS | |
	Ni	Pd	Ni	Pd	Ni	Pd	Ni	Pd
Electrolyte-cathode	1.3 (1.9)	-	0.6 (0.9)	-	0.3 (0.5)	1.9 (1.6)	0.5 (0.8)	0.9 (0.8)
Electrolyte-anode	1.5 (2.3)	-	1.7 (2.6)	-	0.9 (1.3)	2.8 (1.9)	0.9 (1.3)	1.6 (1.4)

* % mol in parenthesis

The concentration gradient of Ni and Pd between the electrolyte interfaces, i.e. anode-electrolyte and electrolyte-cathode, indicates the occurrence of diffusion processes and the absence of precipitates throughout YSZ electrolytes suggests concentration of Ni and Pd lower than the solubilty limit; consequently, values in

table 3.17 are probably overestimated than ~1.5 mol% of NiO in 8 mol% yttria-doped zirconia (8YSZ) at 1350°C, but do not undermine the occurrence of diffusion of transition metals from anode toward electrolyte. It is remarkable to note that, palladium is not detected in the electrolyte of the fuel cell with Ni-current collector, while it is present along with nickel for the cell with Pd-current collector. This implies that the embedded current collector in the anode is a source for metal diffusion, i.e. Ni and Pd cations, as well as the cermet NiO-YSZ which provides Ni ions for the fuel cell with Pd-current collector. For this latter, it is interesting to note the higher concentration of Pd than Ni at both electrolyte interfaces and sintering processes, i.e. conventional and multistage sintering. As a consequence, it is expected a higher rate of matter transport for Pd than Ni which probably depends on the diffusion coefficient as the Ni source (cermet) is present at interface with electrolyte whereas Pd source is the current collector placed at much larger distance from the electrolyte interface, ~200 μm. Nickel and palladium belong to the same group of transition metals and are characterized by similar physical and chemical properties. Their diffusion coefficients are expected to be close for the same diffusion mechanism, even lower for Pd whose ion size in 12-coordination number is 10.4% larger than that of Ni (Kittel, 1996). Nonetheless, it was observed a linear relation of diffusion coefficient with size of (acceptor) cations in yttria- and calcia-stabilized zirconia for lattice diffusion mechanism. In particular, the cation diffusion coefficient increases in the order $Ca^{2+} > Y^{3+} > Sc^{3+}$ whose radius in octhaedral coordination is respectively 1.12, 1.02 and 0.87 Å. The reason of this astounding behaviour of lattice diffusion coefficient can be ascribed to the ionic field strength of cation resulting from the ratio of its charge over the square of radius, so that as higher the charge density as "harder" the cation, and as lower its diffusion coefficient; for instance, the diffusion coefficient of Sc^{3+} is 1.8 times that of Zr^{4+} whose radius is only 3.5% lower than scandium one, i.e. 0.84 Å. On the other hand, the diffusion coefficient of Sc^{3+} and Y^{3+} is respectively 1.8 and 4.3 times that of Zr^{4+}, underlining the ion-charge density effect for ions of same charge wherein the radius ratio of Y^{3+}/Sc^{3+} is 1.17 (Kilo, 2003). For palladium and nickel, the estimation of radius ratio is 1.10 (1.38/1.25 for 12-fold coordination), responsible for a larger diffusion coefficient of Pd^{2+} than Ni^{2+} through YSZ lattice. Migration of ions involves not only lattice mechanism but also grain boundary (GB) diffusion usually favoured at lower temperatures because of lower activation energy although segregation of impurities and secondary phase along GB region rises the activation energy and at higher temperatures both lattice and GB diffusion can occur concurrently. This latter transport mechanism depends on the structural properties of GB interphase as probably on the aforementioned effect of ion-charge density and hence the diffusion coefficient of palladium is expected to be larger than nickel one even through GB interphase of YSZ. An estimation of nickel diffusion was carried out by using values from literature of activation energy and

lattice diffusion coefficient of nickel into 9 mol% Y_2O_3-doped ZrO_2 (Zhou, 2010; Kilo 2003). The results obtained from Fick's second law provide, for a nickel profile of 0.5 mol% from a semi-infinite source as boundary condition, a diffusion depth of ~5 µm for the current sintering conditions (Zhou, 2010; Delaforce, 2007); this estimate is essentially in agreement with values obtained by EDS analysis when considering GB diffusion also active and a higher diffusion coefficient for palladium. Then, the effective presence of transition metals within electrolyte layer results from diffusion of nickel and palladium from the anode cermet and current collector embedded in the anode; for µt-SOFCs with Pd-current collector, the higher diffusion coefficient of Pd in YSZ ensues higher concentration of palladium than nickel at both electrolyte interfaces indicating a larger interaction of palladium with electrolyte elements for temperatures as high as 1350-1400°C. At this point, possible interaction mechanisms of metals impurities with electrolyte elements are provided in order to highlight their effects on the material structure and densification behaviour of constrained electrolyte film where nickel and palladium are considered as dopant elements. First, it is important to point out that zirconia doped with 8 mol% of yttria (8YSZ) is stable as cubic phase at room temperature, while the pure cubic zirconia (without dopant elements) is stable at temperature higher than ~2370°C (Goff, 1999; Badwal, 1992). The addition of metal oxides in ZrO_2 as M_2O_3 (M = Y, Nd, Sm, Er) but also CeO_2 stabilizes the tetragonal and cubic phase of zirconia at room temperature in the measure of oxygen vacancy present in the ZrO_2 lattice (Shibata, 2001; White, 2011). Recently, it was demonstrated that the stabilization of zirconia is controlled by the structural disorder induced by oxygen vacancies in zirconia crystal so that the role of dopant cations, i.e. Y, Nd, Ce, etc, is limited to the extent of formation of oxygen vacancy (Fabris, 2002; White, 2011). For yttria-stabilized systems, 3 mol% Y_2O_3 ensues the metastable tetragonal phase, while 8 mol% Y_2O_3 is appropriate for the complete stabilization of cubic zirconia phase at room temperature (Guo, 2001). The addition of Y_2O_3 solute into ZrO_2 involves a structural change of material that is described as a chemical reaction through the Kröger-Vink notation (Rahaman, 2003):

$$Y_2O_3 \xrightarrow{ZrO_2} 2Y'_{Zr} + V_O^{\cdot\cdot} + 3O_O^x \qquad (3.37)$$
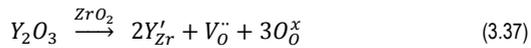
where Y'_{Zr} is a Y^{3+} ion placed in a zirconium lattice site, $V_O^{\cdot\cdot}$ an oxygen vacancy double positively charged and O_O^x an oxygen neutral atom placed in an oxygen lattice site. Equation 3.37 observes three rules involving i) mass conservation (vacancies have zero mass and electronic defects are considered to have no effect on the mass balance), ii) electroneutrality (conservation of charges of the overall reaction) and iii) site ratio conservation for which the number of regular cation sites and anion sites maintain the same ratio. For 8 mol% Y_2O_3-doped ZrO_2 (8YSZ), the

substitutional exchange of zirconium with yttrium produces one oxygen vacancy for every two yttrium atoms for which 8 mol% of Y_2O_3 provides a sufficient concentration of oxygen vacancy for the stabilization of cubic (fluorite structure) zirconia. The oxygen vacancies not only stabilize the cubic zirconia phase but also assist the ionic conductivity of YSZ which achieves a maximum around 8-10 mol% of yttria concentration (Dixon, 1963; Weller, 2004). This implies that the maximum of conductivity is achieved with the minimum concentration of dopant to fully stabilize the cubic phase which is the most conductive among zirconia phases, i.e. monoclinic, tetragonal and cubic (Badwal, 1992). For doping greater than 8-10 mol% of yttria, a higher vacancy concentration although assuring stabilization of cubic structure, causes a reduction of ionic conductivity as a result of association of point defects (dopants-oxygen vacancies) that limit the mobility of charged defects (oygen vacancies) even at high temperatures (Goff, 1999; Weller, 2004). The metal impurities within yttria-stabilized zirconia, i.e. Ni and Pd, are expected to be in the form of oxides under not reducing conditions and therefore NiO and PdO when below to the solubility limit are incorporated substitutionally into ZrO_2 lattice in the following way:

$$ NiO \xrightarrow{ZrO_2} Ni''_{Zr} + V_O^{\cdot\cdot} + O_O^x \tag{3.38} $$
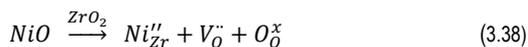
and for palladium oxide:

$$ PdO \xrightarrow{ZrO_2} Pd''_{Zr} + V_O^{\cdot\cdot} + O_O^x \tag{3.39} $$
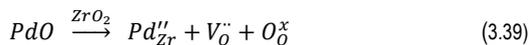
Eq. 3.38 and 3.39 fulfill rules i), ii) and iii) and indicate that one oxygen vacancy is formed from one cation, either Ni or Pd, substituting one zirconium atom and then twice as many vacancies for substitutional cation are formed in comparison with equation 3.37. Therefore, the dissolved NiO and PdO into ZrO_2 lattice produces an increment of vacancy concentration which can be considered as extra addition of yttria alike 3 mol%, on the basis of complete solid solution of either NiO or PdO with solubility limit of 1.5 mol% into zirconia lattice for the current sintering temperatures. Then, for complete solid solution of NiO and PdO addition into 8YSZ, the vacancy concentration is equivalent to that of 11 mol% yttria-doped ZrO_2. On the other hand, it is experimentally well recognized the segregation of yttrium along grain boundaries (Stemmer, 1998; Badwal, 1995; Guo 2001; Lei, 2002; Shibata, 2001). In this case, the diffusion of yttrium to GB, leaves behind vacancies within zirconia lattice supporting the substitutional process proposed by equation 3.38 and 3.39. As a result, the substitutional process of NiO and PdO not only depends on their concentrations and solubility limits but also on the segregation of yttrium; in turn, the oxygen vacancy concentration is also determined by yttrium segregation. It is

145

expected that as higher the concentration of yttrium along GB as extensive the substitutional process of NiO and PdO into zirconia lattice and as higher the vacancy concentration. Following this idea, the apparent concentration of 11 mol% of yttria can increase with the segregation of yttrium if the solubility limit of NiO and PdO into zirconia lattice concurrently increases. Theoretically, dopants can also occupy interstitial sites with concurrent creation of cation vacancies for electroneutrality preservation, although for ZrO_2 systems anionic (oxygen) vacancies prevail and therefore substitutional process of cations is the predominant mechanism (Dixon, 1963). In addition, stable cubic phase of YSZ was obtained for yttria content lower than 8 mol% when NiO is added to 6 mol% Y_2O_3-doped zirconia, supporting the substitutional processes of Eq. 3.38 as possible mechanism of stabilization of cubic zirconia phase obtained by Kuzjukevic et al. (Kuzjukevic, 1997 (1)). As a result, it is expected that nickel and palladium occurring in the electrolyte layer as NiO and PdO act as stabilizing agents for the cubic zirconia phase by producing oxygen vacancies into zirconia lattice following the mechanisms of Eq. 3.38 and 3.39. In addition, the vacancy concentration is deemed to depend also on yttrium segregation which in turn can alter the solubility limit of dopants, i.e. ~1.5 mol% of NiO in 8YSZ in the temperature range of 1350-1400°C. The introduction of dopants also produces structural changes of lattice whose strain depends on dopant size and concentration. The lattice strain has a significant effect on the conduction properties when single-phase material is considered (Badwal, 1992). For instance, the ionic conductivity of zirconia stabilized with 8-10 mol% of yttria or scandia (Sc_2O_3) shows a maximum at 1000°C that is twice as higher for scandia-doped zirconia than yttria-doped one, respectively 0.32-0.25 S/cm and 0.18-0.13 S/cm (Badwal, 1992; Minh, 1995; Gibson, 1998). The different conductivity behaviour is basically attributed to a possible "blocking effect" of larger dopants to vacancy migration (steric effect), but more probably to the lattice strain caused by different host and dopant cation size; specifically, the size of Y^{3+} and Sc^{3+} into zirconia lattice is 1.02 and 0.87 Å respectively, while that of Zr^{4+} is 0.84 Å (Kilo, 2003; Kharton, 2004). As a result, dopant ions of similar size of Zr^{4+}, i.e. scandium, should assure the highest ionic conductivity while it is expected a reduction of conductivity and an increment of activation energy of (lattice) conduction with increasing of dopant size (Badwal, 1992). It is also important to point out the influence of dopant concentration on the conductivity and phase stability of material which are reciprocally related to the electrolyte behaviour with time (Badwal, 1992; Kondoh, 1998 (1)). In fact, a reduction of ionic conductivity was observed with time at constant temperature (aging) for different electrolytes, among them yttria- and scandia-doped zirconia ones (Hattory, 2004; Kondoh, 1998 (1); Badwal, 2000). The main causes of aging are ascribed to the decomposition-transformation of phases and ordering of vacancies and their association with point defects, i.e. dopant cations, both related to the dopant

concentration (Badwal, 1992; Badwal, 2000; Kondoh, 1998 (1), Hattori, 2004). For instance, aging of 8YSZ was observed for prolonged time at high temperature (1000 h at 1000°C) where the reduction of conductivity is mainly attributed to the presence of tetragonal phase. An increment of dopant, although suppressing the aging phenomenon by preventing the formation of tetragonal phase, does not account for the reduction of ionic conductivity of the cubic phase of YSZ with higher yttria contents than 8 mol%; in particular, a constant ionic conductivity of 0.135 and 0.122 S/cm was measured along 1000 h at 1000°C respectively for 9.5 and 10 mol% yttria-doped zirconia as reported by Hattory, in agreement with values of other studies (Hattori, 2004; Kondoh, 1998 (1); Badwal, 1992). A detailed investigation on the relation between structure and conductivity of YSZ systems is carried out by Kondoh et al. where the aging of electrolyte is also related to the short range ordering of oxygen vacancies aroud zirconium ion, necessary for the relaxation of lattice strain induced by the solid solution of yttrium ion with the effect of reducing the mobility of oxygen vacancies caused by the shorter distance of cations-vacancies (Kondoh, 1998 (2)). The lattice relaxation through short range ordering of vacancies accounts not only for the aging phenomenon but also for the decreasing conductivity with increasing dopant concentration beyond the optimal concentration, i.e. 8-10 mol% for yttria- and scandia-doped zirconia; in general the lattice relaxation and its effect also encompasses multi-phase systems with different structures (Kondoh, 1998 (2)). At this point, it is possible to predict a possible relation between the structure and the ionic conductivity of electrolyte layers containing NiO and PdO. At first, the presence of NiO and PdO into electrolyte layer during co-sintering of half-cells enhances the stabilization of cubic structure, the most conductive among zirconia phases. Then, assuming the cubic structure as only existing phase, the cation size of Ni^{2+} is smaller than Zr^{4+} (0.69 and 0.72 Å respectively in sixfold coordination) and therefore after nickel substitution, a lattice contraction of the cubic zirconia structure is expected as experimentally observed (Zhou, 2010; Park, 1999). In this case, the relative distance between cations and oxygen vacancies is shorter and favours their interaction with the effect of decreasing the mobility of charged defects. In addition, the higher vacancy concentration of electrolyte with NiO than pure 8YSZ, corresponding to ~11 mol% YSZ, produces a lattice strain which is relaxed via short range ordering (SRO) of vacancies whose shorter distance with cations further reduces the defect mobility. Then, the higher the vacancy concentration and the difference between dopant and host ion size are, the shorter the distance between cations and oxygen vacancies is; it is expected a lower conductivity of NiO-doped (8)YSZ than pure (8)YSZ; the parentheses of (8) indicate the nominal molar content of yttria whose value can vary in the measure of yttrium segregation along GB. It is supposed that the segregation of yttrium modifies the solubility limit of NiO and PdO into zirconia and this would justify the high concentration values of EDS analysis for electrolyte layers with total

147

concentration of NiO and PdO higher than 1.5 mol% (µt-SOFC with Pd-current collector). On the other hand, the increment of vacancies due to NiO and PdO can influence the diffusion of yttrium and therefore its segregation along GB. The higher concentration of NiO and PdO (and oxygen vacancies) for electrolyte layers of µt-SOFC with Pd-current collector, suggests a further reduction of conductivity than NiO-doped (8)YSZ and pure (8)YSZ electrolyte as the SRO of vacancies increases with dopant concentration, although the eventual larger size of palladium ion than nickel ion would induce a lower contraction and strain of zirconia lattice. Under this perspective, for the same dopant content, the layer containing PdO should demonstrate a higher conductivity than that containing NiO. These indications are of particular interest when supported by structural and electrochemical characterization which are fundamental for the development of solid electrolytes especially when structural changes may occur during operation as aging and degradation phenomena causing variation of material conductivity. Under this perspective, a brief overview on electrochemical techniques for conductivity measurements is outlined with regards to solid electrolytes made by polycrystalline materials as for most of practical applications, where the ionic conductivity depends at structural level on existing phase, vacancy concentration, dopant content, etc while at microstructural level depends on grain boundaries, pores, cracks, etc. The contribution of lattice and grain boundary conductivity to the material conductivity can be measured and distinguished by electrochemical impedance spectroscopy (EIS) analysis. In this case, the lattice conductivity of a full dense electrolyte reflects the material conductivity at structural level (Zhang, 2009 (2)). Alternatively, four-probe d.c. electrical conductivity technique does not distinguish the contribution of lattice and grain boundary to the overall conductivity of material but it is suitable for studying aging phenomena and phase transformations through a continuous monitoring of conductivity over a wide range of temperatures in contrast to EIS (Badwal, 1991). In addition, for material whose grain boundary resistance is negligible at high temperatures, like in YSZ at 1000°C, the conduction is practically provided by the lattice conductivity even for samples with high content of impurities along grain boundaries (Badwal, 1991; Minh, 1995). Conductivity measurements provide also the pre-exponential term and activation energy of conduction law; the former is proportional to the concentration of charged defects, i.e. oxygen vacancies for YSZ electrolytes, while the activation energy depends on dopant content and defect interactions and therefore can deliver structural information as substitution degree (and solubility limit) of dopants (Park 1999; Coors, 2009; Badwal, 1991). Therefore, conductivity measurements and structural investigations, i.e. diffractometric analysis, provide complementary information on the electrolyte behaviour such as phase stability as well as aging and degradation phenomena as a fuction of time and temperature. At this point, the effects of transition metals on the structure of 8YSZ

electrolyte have been discussed as well as the dependence between ionic conductivity and structure. Now, the relation of densification behaviour with structure is dealt by considering the cubic zirconia as the only existing phase for YSZ electrolyte layers in agreement with the stabilizing effect of NiO and PdO for the cubic structure. It was observed different thermal response for tetragonal and cubic phase (Badwal, 1995). In particular, the grain growth is related to the phase content and results significantly suppressed for dual-phase zirconia while for single-phase YSZ the grain growth of cubic structure is much faster than that of tetragonal one (Allemann, 1995; Delaforce, 2007). For the current 8YSZ layer, it is expected that the increment of oxygen vacancy resulting from the solid solution of NiO and PdO into 8YSZ not only stabilizes the cubic structure but also plays an important role on the matter transport and hence diffusion mechanisms during sintering. Batista observed an increment of final density and reduction of temperature for the onset of shrinkage and maximum shrinkage rate for 8YSZ compacts with NiO contents below the solubility limit in comparison with undoped 8YSZ compacts for sintering up to 1350°C (Batista, 2011 (1)). In that study, the initial stage of sintering for NiO-doped 8YSZ was not affected by NiO contents while the improvement of sinterability concerned the last stage of densification where lattice diffusion prevails. As a result, it was suggested the main effect of NiO for the lattice diffusion mechanism during sintering of 8YSZ (Batista, 2011 (1)). Then, the improved densification of 8YSZ compacts with NiO is related to the enhancement of lattice diffusion as a result of the increment of vacancy concentration, in agreement with the substitutional process here proposed by Eq. 3.38. In addition, the lower temperature for the onset of shrinkage and maximum shrinkage rate suggests a lower activation energy for lattice diffusion when dopant is present. Similar trend concerns other dopants as Fe, Mn and Co which act as sintering aids for 8YSZ whose densification behaviour, in comparison with undoped 8YSZ, is characterized by lower temperature of maximum shrinkage rate whose peak height even results lower as analogously depicted by curves of figure 3.59 (c) (Zhang, 2009 (2)). For 8YSZ with 1 wt% NiO the temperature of maximum densification rate was even ~100°C lower than the undoped 8YSZ whose height of maximum densification rate was higher than doped 8YSZ (Zhang, 2009 (1)). Consequently, the addition of NiO to 8YSZ was responsible for higher sintered density at lower temperatures with lower densification rates. This behaviour is also expected here for 8YSZ electrolytes during co-sintering where the densification of 8YSZ layers with either NiO and PdO is expected to occur at lower temperature (than 1100°C predicted by thermal analysis) with lower densification rate and therefore closer to the densification behaviour of anode substrates with the effect of minimizing eventual tensile stresses experienced by constrained electrolyte layers. From figure 3.62 and 3.63, the electrolyte layer appears dense and the closed porosity suggests relative density > 93-95% confirming the positive effect of

NiO and PdO into 8YSZ during co-sintering through an enhanced lattice diffusion which assures higher density at lower temperatures and densification rates which also minimize eventual detrimental effects of constrained densification of thin layers on rigid substrates. The increment of relative density of electrolyte layers is benificial for ionic conductivity since pores act as barrier to the migration of charged species and a linear reduction of conductivity was observed from 5 to 25% of porosity (Steil, 1997; Gibson, 1998). For relative density > 95%, the effect of porosity on either lattice and grain boundary (GB) conductivity is minimal (Gibson, 1998; Zhang, 2009 (2)). Then, for polycrystalline electrolytes of high relative density is possible to determine the effect of dopants on lattice and GB conductivity through EIS although in a limited temperature range where lattice and GB contributions can be separated, i.e. usually temperature around 400°C for YSZ (Badwal, 1987; Zhang, 2009 (2)). Alternatively, four-probe d.c. technique allows to determine the effects of dopants on a wider temperature range. For instance, Park et al. demonstrated that the conductivity of full dense 8YSZ decreases with NiO contents within solubility limit (~2 mol%) in the temperature range of 400-1000°C (Park, 1999). This reduction of conductivity is related to the SRO of vacancies due to their increasing concentration resulting from the effective solid solution of NiO into 8YSZ as supported by increasing pre-exponential term and activation energy. Another important effect of interaction of dopants with YSZ involves the grain growth of cubic zirconia. In particular, 8YSZ doped with NiO contents within solubility limit shows an enhancement of grain growth than undoped 8YSZ (Batista, 2011 (1); Kuzjukevic, 1997 (2); Delaforce, 2007; Zhang, 2009 (2)). The grain growth affects the conductivity behaviour of cubic YSZ whose GB conductivity increases with grain size whereas the lattice conductivity results independent of grain size for relative high-purity YSZ (Badwal, 1987; Verkerk, 1982). On the other hand, GB conductivity is also influenced by segregation of impurities and precipitation of secondary phases along GB (Badwal, 1987, Batista, 2011 (2)). In particular for 8YSZ with 1 mol% NiO, Batista observed segregation of nickel along GB for prolonged sintering time, i.e. greater than 5 h, at 1350°C. For prolonged time at high temperature, the positive effect of grain growth on GB conductivity is ruled by the dentrimental effect of segregation (Batista, 2011 (2)). Moreover, considering segregation of yttrium and of eventual other dopants as well as precipitation of secondary phases, the prediction of conductivity behaviour of 8YSZ with even low NiO and PdO contents is difficult even more the interplay of dopants and secondary phases with grain growth (Allemann, 1995). Furthermore, during service in addition to aging phenomenon, other possible structural changes involve electrolytes with dopants where the reducing operational conditions can induce the transformation of NiO and PdO into metallic nickel and palladium with dentrimental effects on long-term performance of electrolytes (Linderoth, 2001). Indeed, it was observed for 8YSZ with NiO a

decreasing performance in hydrogen atmosphere as a result of precipitation of nickel particles with concurrent transformation of a fraction of cubic phase into tetragonal one with the effect of decreasing the ionic conductivity similarly to aging phenomenon of undoped 8YSZ (Linderoth, 2001). A comparison of 8YSZ and 10YSZ with 1 wt% NiO shows a precipitation of nickel particles in reducing conditions for both electrolytes although only NiO-doped 8YSZ is characterized by degradation of conductivity in short time while NiO-doped 10YSZ presents a constant conductivity along 600 h at 1000°C without aging phenomena. This suggests that the degradation of ionic conductivity is related to the phase stability of electrolyte rather the precipitation of metallic phases itself for low dopant contents (Coors, 2009). So far, possible effects of interactions of transition metals with 8YSZ electrolytes during fabrication and service are outlined as guidelines for further structural, microstructural and electrochemical characterization which are fundamental for the development of the solid electrolyte in term of long-term performance. From the current investigation, the nickel and palladium migrating from the anode cermet and current collector toward 8YSZ electrolyte layers during co-sintering, have a positive effect on the densification of 8YSZ layers whose relative density is estimated > 93-95% which is higher than that predicted from thermal analysis of undoped 8YSZ layers for the same sintering conditions.

3.5 Cathode

Thermal analysis of current collector layer (LSM) and functional layer (LSM/YSZ) concerned sintering at 1150 and 1180°C under static air and argon flow. An enhanced densification occurred for compacts sintered at 1150°C under argon flow, while at 1180°C no significant benefit is shown for sintering in protective atmosphere.

3.5.1 Thermal analysis

Thermal response of cathode compacts constituted by LSM powder and a mixture of LSM and YSZ powders denoted respectively as current collector layer (c-layer) and functional layer (f-layer), is here investigated under different sintering conditions, like atmosphere and maximum sintering temperature as shown in table 3.18 and 3.19. The pore evolution is shown in figure 3.64 where the open and closed porosity of c-layer and f-layer follow the same decreasing trend with increasing sintering temperature and the porosity of f-layer is higher than c-layer as expected for densification of dual-phase composites.

151
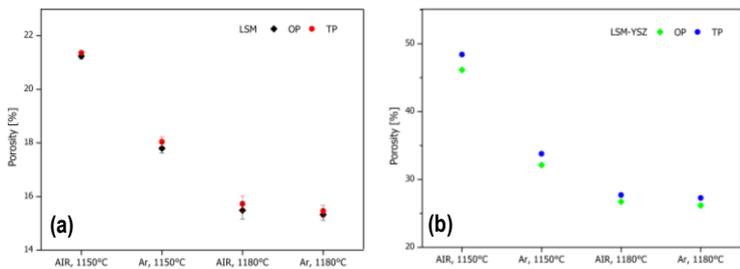
Figure 3.64 Porosity, open and closed, for LSM compacts (c-layers) (a) and LSM/YSZ compacts (f-layers) (b) for different sintering conditions of atmosphere, static air and under argon flow, and sintering temperature, i.e. 1150 and 1180°C.

In addition, the effect of atmosphere on densification of c- and f-layer is evident for the lower sintering temperature, i.e. 1150°C, while no significant difference on porosity arises for samples sintered at 1180°C either in static air or under argon flow. The effect of oxygen partial pressure (PO_2) on oxygen stoichiometry of $LaMnO_{3+\delta}$ was investigated; for a given PO_2 well below the atmospheric PO_2, i.e. 0.21 atm, the oxygen vacancy concentration increases ($\delta < 0$) with temperature (Miyoshi, 2003; Minh, 1995). In particular, the densification of LSM ($La_{0.8}Sr_{0.2}MnO_{3+\delta}$) was enhanced in nitrogen atmosphere ($PO_2 < 10^{-5}$ bar) as a result of increasing oxygen vacancy concentration (Poirson, 1997). The role of atmosphere and temperature on the densification behaviour of LSM compacts is shown in figure 3.65 where the effect of atmosphere on the relative density is given by the incremental relative density defined as $(RD_{(Ar, T)} − RD_{(AIR, T)})/RD_{(AIR, T)}$.
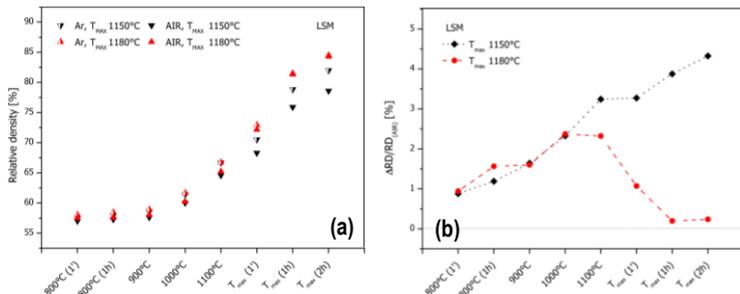
Figure 3.65 Densification behaviour of LSM compacts (c-layers) under common sintering conditions as a function of relative density (RD) (a) and incremental relative density (b).

The relative green density of LSM compacts, evaluated at 800°C, is approximately the same, i.e. 57-58%, while the final density is in the range of 78-85% of theoretical density (6.5 g/cm³) (Armstrong, 2002). It is interesting to observe that for any temperature of sintering process, LSM compacts are characterized by higher relative

density (RD) when sintered in argon than in air, although there is an evident difference of densification behaviour during the dwell at maximum sintering temperature as pointed out in figure 3.65 (b). Specifically, the incremental relative density of compacts sintered at 1180°C decreases during the isothermal dwell at sintering temperature as long as a plateau is reached densification shows no appreciable enhancement in comparison with the sintering in static air. For compacts sintered at 1150°C in argon atmosphere, the incremental relative density is steadily increasing. This difference can be related to experimental conditions where the argon flow is kept constant from room temperature to the maximum temperature while a dilution of gas flux at higher temperatures is expected. As a consequence, the partial pressure of argon it is expected to decrease at 1180°C while PO_2 reaches the atmospheric one, i.e. 0.21 atm, and so the benefit of low PO_2 on densification of LSM is taken out. On the other hand, the improvement on densification behaviour of compacts sintered at 1150°C under argon flow is related to the increment of oxygen vacancies due to reduced PO_2 supporting the role of defect concentration for the densification of LSM.

Table 3.18. Relative density at green and sintered state, open porosity (OP), total porosity (TP) and shrinkage (dl%) of LSM compacts (c-layers) under under different sintering conditions of atmosphere and maximum sintering temperature.

Sintering conditions		Relative density [%]		OP [%]	TP [%]	dl [%]
Atmosphere°	T_{MAX}	800°C [+]	Sintered			
AIR	1150°C	57.02	78.64±0.06	21.24±0.10	21.36±0.08	-9.67
Ar		57.53	81.95±0.15	17.80±0.19	18.05±0.18	-10.74
AIR	1180°C	57.52	84.28±0.25	15.49±0.32	15.72±0.29	-11.54
Ar		58.06	84.54±0.19	15.33±0.22	15.46±0.22	-11.36

° Static air, and 50 ml/min as argon flow, [+] from dilatometric analysis

The densification behaviour of LSM/YSZ compacts (f-layers) is described in figure 3.66. The relative green and sintered density of f-layers are respectively in the range of 49-52% and 66-73% which are lower than those of c-layers as shown in table 3.19. The anomalous lower density of f-compact sintered at 1150°C in static air derives from die pressing where the higher residual porosity is probably due to the presence of hard aggregates of YSZ as detected after the breaking of sample. For this reason the incremental relative density of f-layers sintered at 1150°C presents apparent higher values as shown in figure 3.66 (b); for comparison purpose the curve is shifted to lower values on the basis of previous results of LSM (figure 3.65 (b)). The role of argon atmosphere is different for f-compacts where the incremental relative density assumes also negative values which represent a higher density of compacts sintered in static air than under argon flow for temperature > 1000°C, as the compact sintered at 1180°C in static air which is characterized by the highest
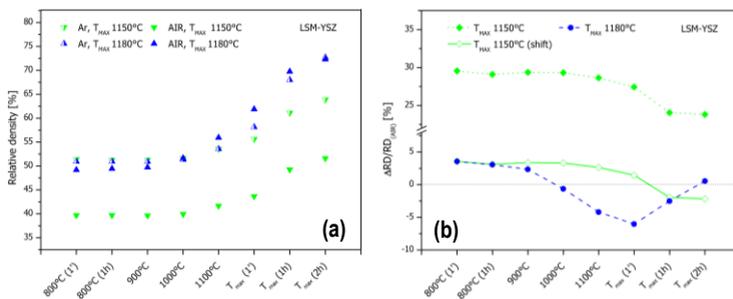
Figure 3.66 Densification behaviour of LSM/YSZ compacts (f-layers) under common sintering conditions as a function of relative density (RD) (a) and incremental relative density (b).

density at 1100°C although its lowest green density (without considering the sample with higher residual porosity from die pressing). However, the densification under argon flow is ehnanced during the dwell at 1180°C as indicated by the final sintered density and the growth of incremental relative density. The densification behaviour of f-layers is characterized by reaction between LSM and YSZ with formation of $La_2Zr_2O_7$ (LZ) and $SrZrO_3$ (SZ) phases at elevated temperature during cell fabbrication and cell service (Tsai, 1997). The LZ and SZ phases are dentrimental for the performance and long-term stability of the fuel cell and their formation depends on the composition and stoichiometry of LSM, LSM/YSZ ratio, temperature and atmosphere, i.e. PO_2 (Tsai, 1997; Chen, 2009). For instance, the formation of LZ is promoted by diffusion of manganese from LSM into YSZ which is related to temperature and PO_2; as low the partial pressure of oxygen, as high the solubility of Mn into YSZ and as high the amount of LZ formed (Mahapatra, 2012). On the other hand, the diffusion of Mn into YSZ not only promotes the formation of LZ but also changes the defect concentration within LSM with the result of far complicated dependence of densification on atmosphere conditions. Although, low PO_2 during sintering can promote the formation of dentrimental secondary phases, the reactions between LSM and YSZ are reversible and therefore eventual LZ and SZ phases can dissolve with subsequent heat treatment in air (Mahapatra, 2012; Chen, 2009). The densification of c-layer is enhanced at 1150°C under argon flow assuring the minimal porosity of ~20% for gas diffusion of cathode layer, while no particular advantage of argon flow appear for the densification of LSM compact at 1180°C (Kim, 2001). For f-layers, the densification at low PO_2 can favour the formation of dentrimental secondary phases without significant enhancement of densification behaviour. Then, the densification of cathode layers is desirable in static air when proctective atmosphere is not necessary for avoiding oxidation of metal components or adverse reactions between cell components.

Table 3.19. Relative density at green and sintered state, open porosity (OP), total porosity (TP) and shrinkage (dl%) of LSM/YSZ compacts (f-layers) under under different sintering conditions of atmosphere and maximum sintering temperature.

Sintering conditions		Relative density [%]		OP [%]	TP [%]	dl [%]
Atmosphere°	T_{MAX}	800°C [+]	Sintered			
AIR	1150°C	39.69	51.58±0.03	46.14±0.05	48.42±0.06	-7.80
Ar		51.42	66.21±0.06	32.13±0.21	33.79±0.09	-8.46
AIR	1180°C	49.18	72.30±0.07	26.72±0.16	27.70±0.10	-11.58
Ar		50.93	72.73±0.08	26.17±0.26	27.27±0.12	-10.66

3.6 Micro-tubular solid oxide fuel cells

The geometric characteristics of the micro-tubular solid oxide fuel cells produced with different cell diameter and configuration of current collector are described. The cell performance was anlyzed and a relation between power density and current collector configuration (turns per unit length) was established; these findings also provided an estimate of cell power output on costs. In addition, a development of current collector design was suggested for the improvement of cell performance in order to achieve comparable power density with that of planar cells.

3.6.1 Fabrication

The micro-tubular solid oxide fuel cells (µt-SOFCs) with embedded current collector are shown in figure 3.67 and their specific dimensions are reported in table 3.20. The cells are characterized by common features independent from the sintering process and current colllector characteristics. For instance, the fuel channel diameter (ID in table 3.20) corresponds to a reduction 20-25% of initial diameter of sacrificial inner core, i.e. 0.5 and 0.7 mm. Moreover, the design of anode supports is devised in order to keep as low as possible the anode thickness for reducing the resistance of gas transport without compromising the mechanical integrity of the cell and the quality of upper coating. For this purpose, the cell support (sacrificial inner core with metallic coil wound around) is completely covered by anode layers after dip coating in order to obtain a smooth surface without irregularities suitable for the subsequent deposition of electrolyte layer. In addition, the anode substrate of appropriate thickness assures the mechanical strength and regular shape of the µt-SOFCs after sintering, where the cells with lower and higher diameter , i.e. ID of 0.37 and 0.55 µm, are characterized respectively by ID/OD ratio ≤ 0.40 and 0.45 and anode thickness ≤ 0.35 and 0.45 mm.

Table 3.20. Dimensions of µt-SOFCs in figure 3.67 with different diameter and turns/cm for the current collector.

Cell	Diameter [mm]			Anode thickness [mm]	Cell length [mm]	Cathode length [mm]	Active area [cm²]
	ID	OD	ID/OD				
6-5	0.365	1.04	0.35	0.338			~0.65
11-5	0.381	1.04	0.37	0.330	~30	~20	
6-7	0.543	1.38	0.39	0.418			~0.87
11-7	0.560	1.30	0.43	0.370			~0.82

Cell 6-5: 6 turns/cm as current collector and 0.5 mm diameter of sacrificial inner core, ID: inner diameter, OD: outer d., Active area = π x OD x Cathode length
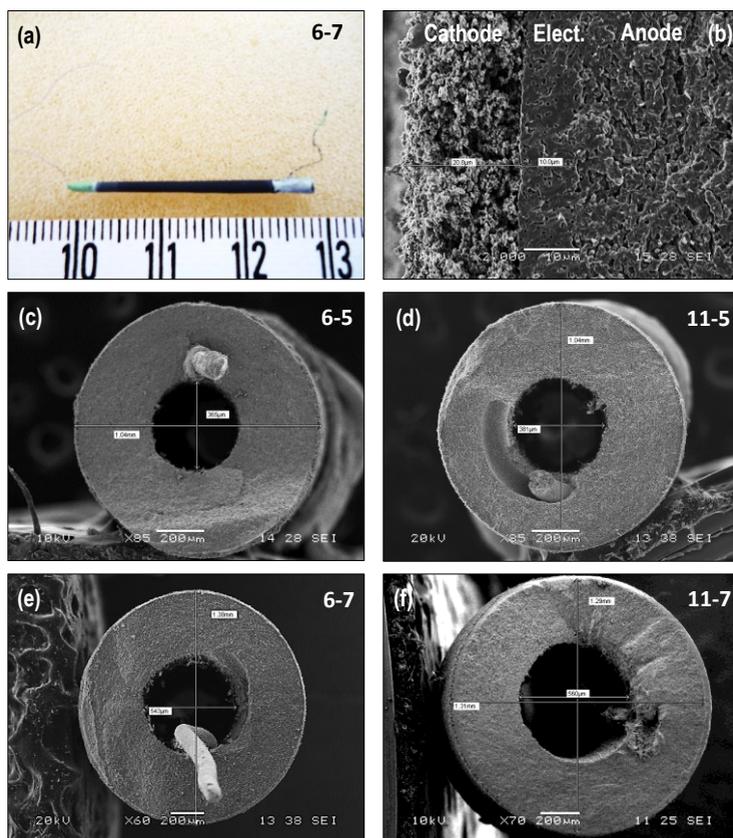

Figure 3.67 µt-SOFCs with palladium as current collector. Photograph of 6-7 cell (6 turns/cm as current collector and 0.5 mm diameter of sacrificial inner core) (a). SEM micrographs of: cathode, electrolyte and anode (b), 6-5 cell (c), 6-11 cell (d), 6-7 cell (e) and 11-7 cell (f).

The length of the cell is fixed to ~30 mm in order to guarantee a uniform distribution of fuel gas along the fuel channel in order to minimize chemical and thermal gradients occurring from the gas inlet and outlet of the cell with the benefit of reducing eventual thermomechanical stresses. Figure 3.67 (a) shows a µt-SOFCs with palladium leads at both cell extremes which result malleable even after co-sintering and sintering of cathode in air. Conversely, the cells with nickel-current collector presents brittle metallic leads after sintering processes even under argon atmosphere as anticipated by thermal analysis in § 3.1.1.1 which is here supported by SEM investigation.
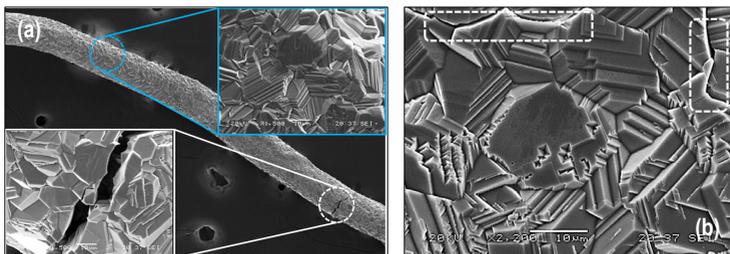

Figure 3.68 SEM micrographs of nickel lead after sintering processes in air of µt-SOFCs. Macroscopic fracture (a) and microscopic fracture (marked areas) (b).

Figure 3.68 shows the nickel lead after the cell fabrication where a macroscopic (a) and microscopic cleavage (marked areas in (b)) are pointed out and indicate the distinctive brittle fracture occurring along crystallographic planes (Dieter,1988). The brittle fracture is common for metals with bcc and hcp structures, although it can also involve the more ductile fcc metals, as for the current nickel wire. In fact, fcc metals deformed and subsequently annealed present grain growth characterized by straight bands across the grains, denoted as growth twins or annealing twins (Smallman, 1995). In particular, the formation of annealing twins depends on the metal purity and the twin formation is as extensive as higher the purity level of metal (Horton, 1995). The broad presence of twins in figure 3.68 (b) confirms, first the high purity grade of nickel (99.994%), and secondly the occurrence of grain growth. The twins act as barrier for migration of dislocations resulting in a reduction of plastic deformation mechanism and therefore a brittle fracture of fcc material is endorsed (Smallman, 1995). Secondly, the increasing of grain size due to grain growth determines a reduction of yield stress and hardness of material (Edalati, 2011; Dieter, 1988). Conversely in figure 3.69, the palladium wire shows the characteristic ductile fracture characterized by dimples formed by microvoids during plastic deformation (Dieter, 1988; Smallman, 1995); in this case the palladium lead was repeatedly bent before rupture.

157
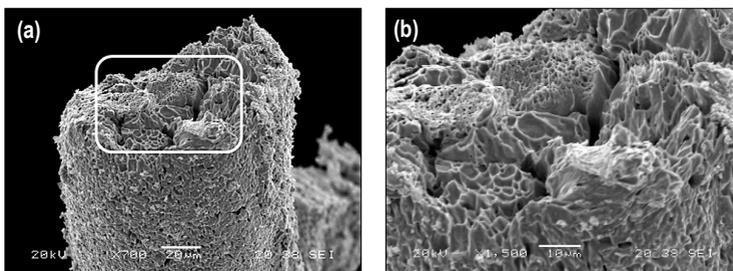
Figure 3.69 SEM micrographs of palladium lead after sintering processes in air of µt-SOFCs. Macroscopic fracture (a) and magnification of marked area in (b).

Generally, plastic deformation is particularly active in metals with high value of stacking fault energy (or surface energy) which assures relative high dislocation mobility while a fine grain size sustains ductile fracture (Dieter, 1988). Palladium is characterized by higher stacking fault energy than nickel, respectively 180 and 125 mJ/m^2, and finer grain size when assuming the dimple size (< 10 µm) in figure 3.68 (b) proportional to the grain size (Edalati, 2011). These characteristics provide good malleability of palladium even after sintering processes in air at 1400 and 1180°C. Palladium is an effective alternative as material for the anode current collector also for severe conditions of cell fabrication. On the other hand, the present anlysis suggests that a lower grade purity and a lower initial grain size of nickel can reduce the formation of growth twins and grain growth with the effect of lessening the brittle behaviour. Nonetheless, sintering at temperatures < 1350°C under protective atmosphere is recommended in order to reduce the oxidation of nickel and assure its integrity as current collector.

3.6.2 Electrochemical performance

The performance of µt-SOFCs with nickel current collector is shown in figure 3.70 and table 3.21 as a fuction of temperature and configuration of current collector, i.e. turns per unit length, which is the only variable parameter of the cell design. The power density increases with temperature and turns per unit length so that the performance of cell # 11-5 is higher than that of cell # 6-5 for a fixed operative temperature. The maximum power density (MPD) of either cell # 6-5 or 11-5 increases of ~1.7 times from 750°C to 800°C, while a much more significant increment of MPD is connected to the current collector configuration as indicated by MPD ratio which is defined as the MPD of cell with 11 turns/cm over MPD of cell with 6 turns/cm. In particular, the MPD of the cell # 11-5 is ~4 times than cell # 6-5 either at 750 or 800°C, underlining that as twice the turns per unit length, as fourfold the

maximum power density. The reason for this performance improvement depends on a more efficient gathering of electrons for the current collector with higher turns per unit length as suggested by the current density values at which MPD occurs as reported in table 3.21.
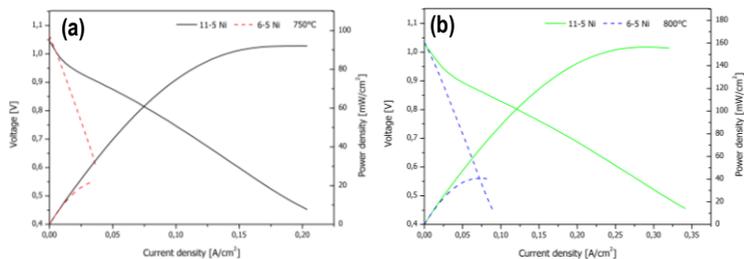

Figure 3.70 Performance of µt-SOFCs with nickel as current collector as a funtion of turns per unit length and operative temperature at 750°C (a) and 800°C (b).

Table 3.21. Performance of µt-SOFCs with nickel as current collector in term of open circuit voltage (OCV), and its comparison with thermodynamic value (EMF), maximum power density (MPD) and voltage (V) and current density (j) at which occurs and maximum power density ratio of 11-5 over 6-5 cell (MPD ratio).

	T [°C]	OCV [V]	OCV/EMF[‡] [%]	MPD [mW/cm²]	V [V]; j [A/cm²] at MPD	MPD ratio[§]
6-5 Ni	750	1.064	95.6	22.2	0.61;0.04	4.2
11-5 Ni		1.045	93.9	92.1	0.47;0.19	
6-5 Ni	800	1.035	93.7	40.6	0.52;0.08	3.9
11-5 Ni		1.028	93.1	156.4	0.49;0.32	

‡ thermodynamic voltage of hydrogen mixture (H2:H2O; 97:3) on the basis of higher heating value of enthalpy: EMF = 1.113 and 1.105 V, respectively at 750 and 800°C (Chen; 2007),
§ MPD ratio = MPD$_{(11-5)}$ / MPD$_{(6-5)}$

The maximum performance is achieved at voltage between 0.47 and 0.52 V, equivalent to half of open circuit voltage (OCV) (lower than the theoretical values), while the current density of cell with 11 turns/cm is 4 times the current density of cell with 6 turns/cm for a fixed temperature; the performance of cell # 6-5 at 750°C, i.e. 22.2 mW/cm², is estimated to be just lower than its most level as a result of interruption of electrochemical measurement at 0.6 V, prior of one-half of OCV, as also confirmed by figure 3.70. Then, the current density at maximum cell performance, is clearly dependent on the current collector configuration, here expressed by Ohm's law:

$$j = \sigma \frac{\delta E}{\delta x} \qquad (3.40)$$

Where j is the current density [A/cm^2], $\delta E/\delta x$ the gradient of electrical potential [V/cm] and σ the conductivity [1/Ωcm] or [S/cm]. For a fixed operative voltage, the current density across the current collector is proportional to the conductivity of electrons and Eq. 3.40 becomes:

$$j \propto \sigma_e = |z_e|Fc_eu_e \propto c_e \qquad (3.41)$$

Where σ_e is the conductivity of electrons as a function of the charge, concentration and mobility of electrons and Faraday constant, respectively z_e, c_e, u_e and F. From Eq 3.41, the charge of electrons and their mobility u_e (material property) is constant for a given material, and therefore the current density depends only on the concentration of electrons which is assumed to depend on the current collector configuration (CCC) and precisely to be proportional to the turns per unit length:

$$c_e = f(current\ collector\ configuration) \equiv c_{(CCC)}$$

$$c_{(11-5)} = 2c_{(6-5)} \qquad (3.42)$$

The concentration of electrons per unit length for 11 turn/cm configuration is twice as high than that of 6 turns/cm one. In general, the cell performance of SOFC is mainly controlled by the electrical property of the electrolyte whereas for the present cell design, the configuration of current collector is also pointed out to significantly affect the cell power output as shown in figure 3.70. Consequently, the power density (PD) [W/cm^2] of the cell with embedded current collector is accounted by the area-specific resistance of electrolyte (ASR) [Ωcm^2], constant for the present cell design, while the current density depends on the concentration of collected electrons per unit length and therefore collector configuration, and results:

$$PD = ASR(j)^2 \propto (j)^2 \propto c_e{}^2 \qquad (3.43)$$

On the basis of Eq. 3.42 and 3.43, the relation of power density at maximum performance MPD as a function of current collector configuration is:

$$MPD_{(11-5)} = 4MPD_{(6-5)} \qquad (3.44)$$

The effect of current collector on the cell performance is pointed out with experimental results well described by a simple model based on the gathering of electrons as a function of the configuration of collector embedded within the anode for operative cell conditions where the ohmic losses control the performance. In particular, as higher the collector turns per unit length are as higher the collection of electrons is and thus as higher the cell performance is. At maximum performance condition, the power density increases with the square of concentration of collected

electrons and therefore as twice the collector turns per unit length are as double the current density is making the power density 4-fold either at 750 and 800°C. On the other hand, the improvement of cell performance is associated to the reduction of cell resistance (given by the slope of V-j plot) which depends only on the current collector configuration (CCC) as other cell design parameters were here fixed. The CCC affects the distribution of current flow across the anode that is as homogeneous and extended over a larger effective area as higher the turns per unit length. Therefore for a fixed current flow, the resulting current density is lower with the effect of reduction of ohmic and polarization losses as reported in (Sasaki, 1996; Jiang, 2003; De la Torre García, 2011). As a consequence, the CCC with 11 turns/cm is responsible for a more homogeneous current density distribution than CCC with 6 turns/cm which minimize the cell resistance and therefore a significant increment of cell performance is obtained for a specific operative cell condition. The present analysis agrees with the results obtained by De la Torre García for similar μt-SOFCs with embedded current collector where a homogeneous current density distribution and an improved contact between electrode and current collector is obtained with CCC with 11 turns/cm, which is responsible for the improvement of cell performance as confirmed by current results (De la Torre García, 2013). Another benefit of the embedded collector is the availability of terminals at both ends of the cell avoiding the classical electrical connection with a straight wire along the fuel channel for the anode electrode of anode-supported SOFCs. This possibility was not feasible here for the brittleness of nickel collector after current sintering conditions as previously shown in figure 3.68. A further increment of cell performance is thus expected for an integrated electrical connection with embedded cell collector as demonstrated in (De la Torre García, 2013; 2012); this aspect will be dealt in the following section. At this point, the effect of palladium current collector on the cell performance is investigated as reported in 3.71 and table 3.22 where also the performance of cells with nickel current collector is shown for comparison.

Table 3.22. Performance of μt-SOFCs with nickel and palladium as current collector in term of open circuit voltage (OCV), and its comparison with thermodynamic value (EMF), maximum power density (MPD) and voltage (V) and current density (j) at which occurs and maximum power density ratio (MPD ratio).

	T [°C]	OCV [V]	OCV/EMF[‡] [%]	MPD [mW/cm²]	V [V]; j [A/cm²] at MPD	MPD ratio
(a) 6-5 Ni		1.035	93.7	40.6	0.52;0.08	4.4 (c/a)
(b) 11-5 Ni		1.028	93.1	156.4	0.49;0.32	
(c) 6-5 Pd	800	1.015	91.9	178.8	0.46;0.39	1.25 (c/d)
(d) 6-7 Pd		1.024	92.7	143.4	0.49;0.30	
(e) 11-5 Pd		-	-	710 [§]	-	4.0 (e/c)

[‡] EMF = 1.105 V at 800°C (Chen; 2007), [§] value estimated on the basis of Eq. 3.44

The cell resistance of Ni-collector cells shows a dependence with temperature but also with the current collector configuration. As shown in figure 3.71 (a), the cell resistance of cell # 11-5 Ni at 750°C is lower than that of cell # 6-5 Ni at 800°C, although it is expected a higher cell performance with increasing temperature as a result of higher ionic conductivity and electrochemical reaction rates that contribute to reduce the overall cell resistance. This observation is very important because points out the significant positive effect of 11 turns/cm-CCC on the ohmic and polarization losses of anode whose decrease is associated to a more homogeneous and higher current density which outweigh the negative effect of temperature reduction on cell performance. On the other hand, the cell performance is influenced by the nature of current collector as shown by comparing the cell # 6-5 Pd with cell # 11-5 Ni characterized by comparable cell resistance at 800°C. In this case, the benefit of homogeneous current distribution on cell performance resulting from the 11 turns/cm-CCC is considerably exceeded by the higher electrochemical activity of Pd-current collector than Ni-current collector although an unfavourable CCC. The effect of catalytic activity of current collector for hydrogen oxidation is demonstrated by comparing the MPD of the cell # 6-5 Pd with cell # 6-5 Ni whose cell performance differs by a factor more than 4.
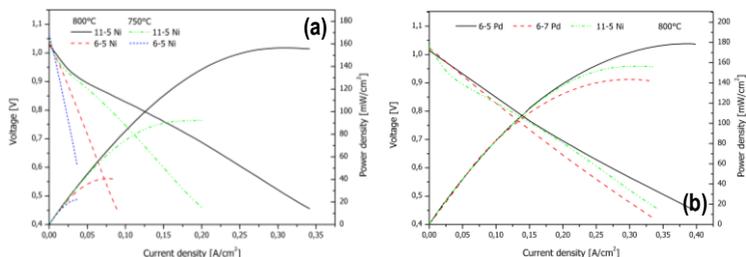
Figure 3.71 Performance of μt-SOFCs with nickel as current collector at 750 and 800°C (a) and palladium current collector at 800°C (b).

The cell with Pd-collector demonstrates an outstanding performance than the cell with Ni-current collector as supported by the estimate of maximum power density for the cell # 11-5 Pd from equation 3.44, corresponding to ~700 mW/cm². These results are consistent with the performance of SOFCs characterized by an anode functional layer with 1 wt% Pd as catalist whose MPD was 4 times higher than the same cell without palladium (Gross, 2007). The significant improvement of performance relies on the catalytic activity of palladium for the hydrogen oxidation where electrons are produced following the possible reactions at anode electrode:

$$PdO + H_2 \rightleftharpoons PdOH + H^+ + e^- \leftrightharpoons Pd + H_2O$$

162

$$Pd + H_2 \rightarrow Pd + 2H^+ + 2e^- \tag{3.45}$$
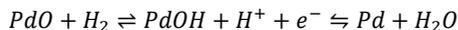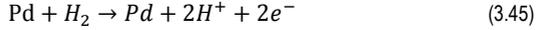
The electrochemical activity of Pd(O)-current collector is described by equation 3.45 consisting of different possible reactions in reducing environment where also steam is present. The native metallic collector is characterized by a thin PdO layer still present after sintering process. The embedded Pd-collector during electrochemical testing is exposed to hydrogen atmosphere at temperature as high as 800°C where the reduction of thin PdO layer to Pd with releasing of electrons is expected (Kalimeri, 2006). Alternatively, the metallic palladium can either directly oxidize the feeding hydrogen or react with steam derived from the classical hydrogen oxidation in SOFCs through oxygen ions at electrolyte/electrode interface and triple phase boundaries (TPBs) as:

$$H_2 + O^{2-} \rightarrow H_2O + 2e^- \tag{3.46}$$
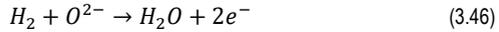
The reactions in equation 3.45 and 3.46 are controlled by H_2/H_2O ratio that depends on the gas transport of hydrogen from the fuel channel to the electrolyte/electrode interface and TPBs as well as to the migration of steam from the reaction interface to Pd-collector while the direct hydrogen oxidation by palladium wire is believed to have an important role due to the location of embedded collector near the fuel channel of hydrogen flow. Independently from the prevailing reaction in Eq. 3.45 and 3.46, the higher catalytic activity of palladium and/or palladium oxide than nickel is responsible for a significant extra release of electrons as supported by higher current density and therefore higher power density. At this point, the effect of current collector nature on cell performance is outlined while a difference on OCV arises between the µt-SOFCs with Ni- and Pd-current collector. In fact, the reversible potential of Ni-collector cells is lower than theoretical value but higher than Pd-collector cells. A possible cause is the temperature of reduction, 800 and 750°C, respectively for Ni- and Pd-collector cells. Nonetheless, during reduction process certain Ni-collector cells achieved OCV of 1.09-1.10 V close to the theoretical value, while OCV for Pd-collector cells was at most 1.05 V after reduction of some samples at 800°C. A potential cause of low OCV is attributed to the leakages and crossover of hydrogen across the electrolyte layer especially for the cell with Pd-collector whose difference on coefficient of thermal expansion with the anode cermet is expected to be higher than that of nickel collector. Although after co-sintering processes, no evident difference on shrinkage between Ni- and Pd-collector cells was observed and ascribed to the current collector expansion at higher temperatures, the OCV of Pd-collector cells was sytematically lower than theoretical value under different conditions of reduction. This suggests an eventual instability of electrolyte layer of Pd-collector cells during

reduction where phase transformations of PdO/NiO-YSZ layer can occur as previously described in § 3.4.2.3. An additional investigation of reduction response of electrolyte as well as anode (differential thermal expansion) of Pd-collector cells is therefore recommended; a last observation is provided with regards to the conditions of electrochemical testing. In fact, both reduction and electrochemical measurements were planned to be accomplished in a day while the reduction of Pd-collector cell can involve more prolonged reduction time. In fact, the potential direct hydrogen oxidation by palladium collector can compete with the interfacial hydrogen oxidation through oxygen ions with the effect of larger fraction of fuel involved at the interface of current collector/fuel channel and thus reducing the hydrogen migration to the electrolyte interface and TPBs necessary for a complete reduction of anode for which OCV values close to the thereotical voltage are expected when leakages and crossover of fuel are prevented. Nevertheless, the performance of μt-SOFCs with palladium current collector is remarkable superior than the performance of cells with Ni-collector under present experimental conditions. The effect of cell diameter on power density is evaluated by comparison of the cell # 6-5 Pd and cell # 6-7 Pd characterized by a difference of inner and outer diameter of 50 and 25%, respectively. The reduction of diameter causes an improvement of cell performance resulting from a larger ratio of reaction surface/volume scaling with the inverse of outer diameter while a possible decrease of cell performance can arise from a lower hydrogen concentration due to the pressure drop along fuel channel which is proportional to the fourth inverse power of inner cell diameter for laminar flow of a Newtonian fluid according to Poiseuille equation (Kendall, 2010; Barnes, 1989). The MPD of the cell # 6-5 Pd with lower diameter is 25% higher than that of the cell # 6-7 Pd charecterized by larger diameter as evident from figure 3.71 and table 3.22. Consequently, the adverse contribution of pressure drop on cell performance seems outweighed by the positive effect of larger reaction site per unit volume with the reduction of cell diameter. On the other hand, the current collector configuration has been demonstrated to have a great influence on cell performance and it must be considered when a possible difference of turns per unit length arises as for the cell # 6-7 Pd which is characterized by intermediate 5-6 turns/cm as shown in table 3.1. On the basis of Eq. 3.42 and 3.43, the difference on MPD between the cell # 6-7 and 6-5 Pd is proportional to the ratio of turns per unit length and therefore by considering 5.5 turns/cm for the cell # 6-7 Pd, the ratio of power density is:

$$\frac{MPD_{(6-7)}}{MPD_{(6-5)}} \propto \left(\frac{c_{(6-7)}}{c_{(6-5)}}\right)^2 = \left(\frac{5.5}{6}\right)^2 = 0.84 \tag{3.47}$$

Eq. 3.47 indicates a factor of 0.84 on MPD which is indeed in good agreement with 0.80 given by the MPD ratio 143.4/178.8 of the cell # 6-7 and 6-5 Pd, within 5%

relative error. Then, the reduction of MPD for cell # 6-7 Pd is accounted by the lower turns per unit length where the contribution of cell diameter on reaction area/volume ratio, if present, is reasonable overwhelmed by the prominent effect of current collector whose minimal difference on configuration (turns/cm) has a substantial impact on power density as demonstrated by Eq. 3.47. Then, the present experimental conditions does not enable to detect possible effects of cell diameter on performance altough the scaling down to 0.365 mm inner diameter of cells here produced, does not reasonable cause a pressure gradient along the fuel channel 3 cm long with adverse effect on power density. On the other hand, the role of current collector on cell performance is experimentally pointed out and well described by the proposed model as a result of regular and uniform characteristics of current collectors as shown in figure 3.1. The catalytic activity of palladium conceives not only the oxidation of hydrogen at anode but also the reduction of oxygen at cathode side where an enhanced electrochemical performance was observed for LSM and other SOFC cathodes (Babaei, 2011; Sahibzada, 1998). The EDS analysis on cathode layers of µt-SOFCs with Pd-collector (figure 3.63) has revealed traces of palladium, i.e. 1-2 wt%, derived from the diffusion of Pd from current collector to cathode layer during the sintering processes. The kinetics parameters derived from the Tafel plot of figure 3.72 (a) and table 3.23, i.e. exchange current density and charge transfer coefficient, are a useful tool for evaluating the effect of palladium on electrode performance. As higher the exchange current density as higher the rate of electrochemical reactions while indications on reaction mechanisms are given by the charge transfer coefficient (van Heuveln, 1997; Kalimeri, 2006).
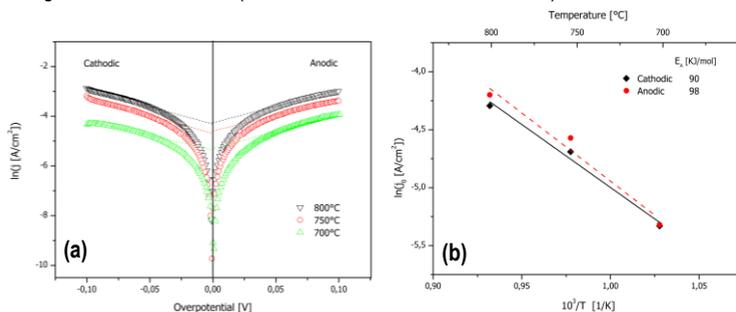
Figure 3.72 Electrochemical behaviour of a µt-SOFC with Pd-collector evalueted by Tafel plot (a) and Arrhenius plot (b) for oxygen reduction and hydrogen oxidation reactions at 700, 750 and 800°C.

Table 3.23. Kinetics parameters of µt-SOFCs with Pd- current collector derived from Tafel plot; exchange current density i_0 (intercept of plot) for anodic and cathodic polarization, i_{0a} and i_{0c}, respectively and charge transfer coefficient $α$ (slope of plot) for anodic and cathodic polarization, $α_a$ and $α_c$, respectively.

T [°C]	Cathodic polarization		Anodic polarization	
	i_{0c} [mA/cm²]	α_c	i_{0a} [mA/cm²]	α_a
700	4.9	0.48	4.8	0.41
750	9.2	0.62	10.3	0.47
800	13.7	0.64	15.0	0.44

The rate of electrochemical reactions of oxygen reduction and hydrogen oxydation, respectively represented by i_{0c} and i_{0a} and obtained by the intercept of Tafel plot of figure 3.72 (a), increases with temperature as typically for activated systems and results in an enhanced kinetics of electrochemical reactions as supported by the increment of cell power density with temperature. The activation energy of the overall reduction and oxidation reaction is obtained by plotting $ln(j_0)$ versus $1/T$ as shown in figure 3.72 (b), where the value of activation energy for the oxygen reduction and hydrogen oxidation is 90 and 98 KJ/mol, respectively. These values are lower than values generally reported in literature for hydrogen oxidation on Ni/YSZ cermet electrodes, i.e. 100-170 KJ/mol, and for oxygen reduction on LSM and LSM/YSZ cathodes, i.e. 120-210 KJ/mol (Jiang, 1999; Barbucci, 2005; Sodeberg, 2009). The origin of scattering data in literature derives from the properties of material system like chemical composition and microstructure, but also on the experimental measurement technique. For the oxygen reduction reaction, the activation energy values are generally 120-140 KJ/mol for LSM and LSM/YSZ system, independently from the measurement technique adopted, either impedance or polarization analysis (Barbucci, 2005; Sodeberg, 2009). This is related to the reaction mechanisms so that oxygen ions produced during reduction as are incorporated into the electrolyte as do not longer take part to the oxygen reduction. Conversely, the water (steam) produced during hydrogen oxidation can further partecipate to the oxidation reaction at anode and influences the reaction kinetics; as higher the water concentration as lower the activation energy up to 14 vol% water concentration (Jiang, 1999). In addition, the water concentration produced by hydrogen oxidation depends also on the current density eventually imposed by electrochemical measurement and thus the activation energy value is affected by the adopted technique; galvanostatic current interruption (GCI) technique imposes a current density and the concentration of water is then higher than technique in condition of zero current density as electrochemical impedance analysis (EIS) at OCV with the result of apparent lower activation energy of hydrogen oxidation for GCI than EIS measurement (Jiang, 1999). Therefore, the activation energy of hydrogen oxidation (98 KJ/mol) here obtained by polarization technique can be influenced by measurement dynamics (production and diffusion of water, local polarization, etc), yet indicates a large amount of water generated and thus a high rate of hydrogen oxidation as a result of the catalytic activity of palladium, responsible in part of low activation energy. A concomitant EIS analysis can shed light on the effect of palladium as catalyst for

hydrogen oxidation. On the other hand, the activation energy of oxygen reduction is expected to be related to material property. The value of activation energy of 90 KJ/mol, 33% lower than the typical 120 KJ/mol of similar LSM/YSZ systems, suggests an improved electrochemical performance of cathode. In addition, the charge transfer coefficient i_{0c} pass from a value close to 0.5 to 0.6 with temperature indicating a probable change on reaction mechanisms (van Heuveln, 1997). The relative large coefficient increment of ~30% at 750°C suggests a different electrochemical activity of cathode. A transition from PdO to Pd is observed at temperature above 700°C under usual operative SOFC conditions at cathode side suggesting the variation of oxidation state of palladium as possible reason for the change of mechanisms and kinetics of oxygen reduction (Kalimeri, 2006). Again, further electrochemical analysis can unravel underlying reaction mechanisms and properties of electrode materials and promote the performance improvement of μt-SOFCs with regards to temperature where the catalytic effect of palladium can support the use of methane or other hydrocarbons as fuels as well as lessening the service temperature without compromising the kinetics of oxygen reduction. Finally, the electrochemical performance of μt-SOFCs with embedded current collector was analysed in term of configuration and nature of current collector. It has been demonstrated that, the power density scales with the square of turns per unit length of metallic collector while an outstanding performance improvement was achieved for the cell with palladium collector where for a fixed collector configuration the power output was increased by a factor ~4 than the cell with nickel collector at 800°C. An additional enhancement of cell performance is expected for an improvement of current connection architecture as dealt in the following section.

3.6.3 Engineering aspects

The embedded current collector of the present μt-SOFCs has a significant effect on the cell performance which is related to the configuration and nature of the collector. The embedded current collector is also designed for a direct electrical connection for the anode electrode through the avaliability of terminal leads at both ends of cell as demonstrated by De la Torre García and designed as integrated-current collector architecture (De la Torre García, 2013; 2012). Here, the electrochemical performance of μt-SOFCs was analyzed by a straight wire passing along the fuel channel although it has been demonstrated the feasibility of integrated-current collector architecture as shown in figure 3.74. Indeed, the leads of palladium at both ends of the cell are available after sintering and are also enough ductile to realize the integrated-current connection (ICC) but the reduced thickness of wire, i.e. 0.1 mm, seriously compromises the reliability of anode connection during testing due to the inherent weakness of points indicated by arrows in figure 3.73.
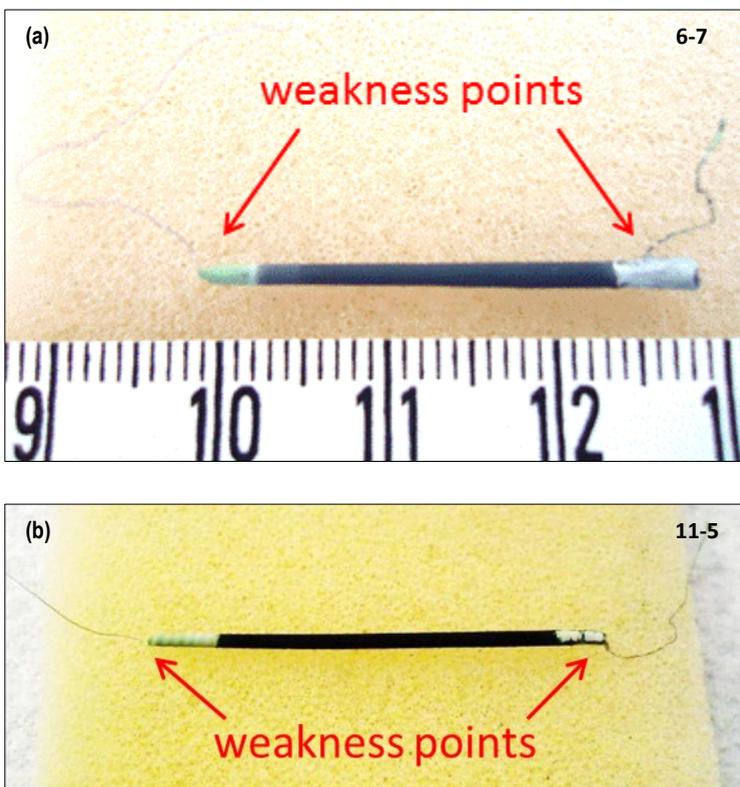
Figure 3.73 Photographs of µt-SOFC with Pd-collector configuration 6-7 (a) and 11-5 (b) where critical points of current collector are highlighted.

In addition, the heat treatment for curing the sealant before testing was a critical step as the metallic wires enveloped by the sealant were broken by the shrinkage of ceramic-based sealant during curing. A potential solution conceived the use of alumina capillaries with the fuction of shielding the metallic leads from the contact with sealant and other potential sources of damage as shown in figure 3.74.
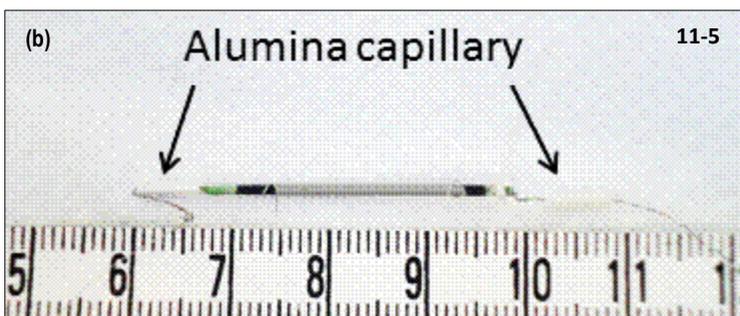
Figure 3.74 Photographs of µt-SOFC with Pd-collector configuration 11-5 where integrated-current collector connection is shown whithout alumina shielding capillaries (a) and with capillaries (b).

This solution assured the integrity of electrical connection during the curing of sealant but a reliable ICC was not realized for the electrochemical testing due to the weakness of wires at critical points as illustrated in figure 3.73. For this reason, a straight wire passing along the fuel channel was adopted as electrical connection for the anode electrode. This strategy, although more reliable, does not ensure the best performance of the fuel cell due to the higher contact resistance between the anode electrode and metallic wire and at the same time fades the potential effortless anode connection available already after the cell fabrication without the need of complicated operations for the realization of electrical connection which is particularly challenging for devices of reduced size as µt-SOFCs. In order to pursue the innovative ICC strategy and improve the cell performance, a potential solution is proposed on the basis of ecomical issues regarding the expensive cost of palladium wire. In fact, the palladium wire of 0.1 mm diameter used for the current collector was chosen not only for its superior properties as catalyst and high temperature resistant metal but also for the comparable prize in comparison with the nickel wire 99.994% purity grade. Under this perspective, the prize of nickel and palladium wire was respectively 18.7

and 15.3 €/m for the wire 0.1 mm thick. For higher diameter, i.e. 0.127 mm, the prize of palladium wire of 99.99% purity grade was twice as high than nickel one and therefore unfeasible for an appreciable power density over manufacturing costs. Under this point of view, an alternative collector configuration is envisaged for the palladium wire which fulfills the demanding wire thickness without using wires of prohibitive cost.
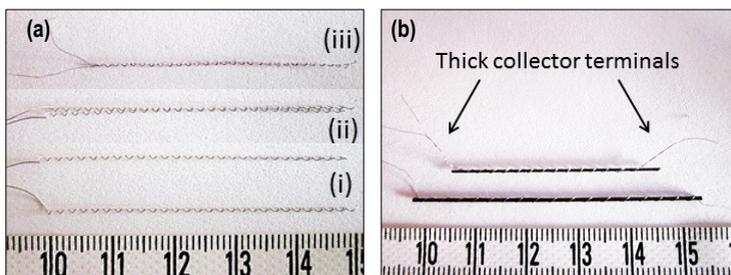

Figure 3.75 Photographs of nickel current collectors with 6 turns/cm; single collectors (i), (ii) and two collectors wrapped together to form a single collector (iii) (a) with larger thickness of both extremes ends (b).

Figure 3.75 shows the uniform and regular characteristics of current collectors as screw pitch through the whole length (i) where single collectors can be perfectly superimposed (ii) into a single-double coil (SDC) whose terminals are wrapped (iii) and therefore characterized by larger thickness. Concurrently, the inner diameter of SDC is smaller than the initial diameter of single coil and therefore a thinner carbon rod is necessary for the realization of cell supports as pointed out in figure 3.75 (b); the wire in figure is nickel, but same behaviour and flexibility is expected for palladium wire whose malleability is also higher than nickel wire. Commercial carbon rods are available in a wide range of size with diameter as low as 0.25 mm and hence a wide design of cell supports is possible for μt-SOFCs with embedded current collector whose configurations can potentially involve three or more coils wrapped into a single collector. Consequently, it is possible to realize alternative designs of micro-tubular fuel cells with embedded collector with terminals of palladium sufficiently thick for an integrated-current connection withstanding during electrochemical testing. As a consequence, the potential design of cell supports with single-double collectors (SDC) combines the superior performance of palladium collector with the possibility of integrated-current collector architecture as proposed in (De la Torre García, 2013; 2012). As a final remark, an estimate of power density over manufacturing cost is given on the basis of the maximum performance of 11 turns-CCC cell over the cost of Pd current-collector which is certainly the principal material/fabrication cost of present cell for lab-scale production and as probably for

an upscale fabrication. Then, the maximum performance of single μt-SOFCs with palladium collector of 11 turns-CCC, based on experimental data and equation 3.44, is 0.7 W/cm^2 where 17 cm of Pd wire were used for the collector. The cost of collector for one cell is 2.6 € (15.3 €/m for Pd wire) and thus the normalized cost per unit power density is 3.7 €/W, otherwise 3700 €/KW for a potential upscaling to stack size. This value is a rough estimate of eventual production costs over power output based on a single device but it offers a useful reference for the cell development. In addition, it provides a comparison with standard targets for the commercialization of SOFC technology. For instance, the US Department of Energy (DOE) fixed a target of 400 $/KW in 2010 addressing the market of stationary power generation of 10 KW power supply. As a result, the value for the present μt-SOFC is much far from the target fixed by DOE but on the other hand the current status of MT-SOFCs with embedded current collector can upturn toward higher power output than 0.7 W/cm^2. This value is in good agreement with the state of art for micro-tubular cells even if the present study demonstrated that an improvement of electrolyte and cathode layers is attainable and the potential innovative connection of single-double collector design can further enhance the cell performance (Liu, 2010; Sarkar, 2007; Suzuki, 2006). In fact, above the lower contact resistance resulting from the integrated-current collector connection, it is also expected a higher capability of electron collection for two metallic coils than a single coil with the effect of larger current density. Then, it was demonstrated that the current density is proportional to turns per unit length and if this relation holds also for two parallel coils, the current density of μt-SOFC with SDC configuration is expected to be twice as high than the present collector with single coil, while the power density would rise by a factor 4, fixing 2.8 W/cm^2 as upper limit of power density. Eventual adverse effect on current density flux and distribution, as possible eddy currents arising from the intimate contact of the two coils of SDC, can reduce the cell performance although a power output between 0.7 and 2.8 W/cm^2 is reasonable foreseen. This possibility pave the way to a possible alternative design of μt-SOFCs with significant performance improvement in the case the validity of previous assumption on the effect of collector configuration on cell performance would proved by forthcoming experimental investigation. Finally, aspects of ceramic processing of μt-SOFCs with embedded current collector were dealt in accordance to an improvement of control and reliability of fabrication process along with indications for a further development of cell design.

Chapter IV

Conclusions and Future Perspectives

4.1 Fabrication of Micro-Tubular Solid Oxide fuel cells

In the present work, micro-tubular SOFCs (µt-SOFCs) with embedded current collector and well-defined characteristics and geometry were fabricated through a reliable ceramic process based on wet colloidal deposition technique from ceramic suspensions. The optmization of anode slurries in term of solid loading and additive concentration ensured not only appropriate rheological properties and stability of suspensions throughout the dip coating process, but also a significant effect on the final properties of sintered products. The microstructure and porosity of sintered anode substrates was particularly homogeneous and uniform when the optimized anode slurry was used. The control of drying, burn-out and sintering conditions allows to tailor the porosity of sintered anode substrates. In particular, the total porosity spanned from 13 to 23% by controlling the conditions of drying and binder burn-out for the compact of fixed powder composition and sintering schedule. The residual porosity of anode substrates, designed for the gas transport and derived from the burn-out of pore former (graphite particles), was mainly retained as open porosity, i.e. 87-90%, independently from the sintering temperature. It was demonstrated that, during reduction process, the pore structure assured gas diffusion throughout the anode substrate even for porosity level ~13% as as a result of percolating pores left by graphite particles underlining that a uniform distribution of pores with appropriate size, shape and interconnectivity is a relevant factor to sustain effective gas diffusion rather the initial level of porosity. Consequently, it was possible to achieve adequate gas transport properties even for anode substrates with low porosity with the positive effect of improving the electrical and mechanical properties of anode cermets. An important observation concerns the diffusion of transition metals during co-sintering of anode and electrolyte, not only from the anode substrate but also from the current collector embedded within the anode. Experimental procedure was outlined in order to study the effect of transition metals, i.e. nickel and palladium, on electrical and structural properties of the electrolyte.

4.2 Electrochemical Performance

The realization of micro-tubular (µt-SOFCs) cells with well-defined characteristics and geometry consented to examine the effect of the embedded current collector on cell performance. The effectiveness of current collector was examined by comparing coils with different configurations (turns per unit length) as well as nature of the metal. The cell performance was demonstrated to be related to the current collector configuration. In particular, as twice the turns per unit length are as double the current density is, thus making the power density 4-fold. An additional improvement of the cell performance was found for the palladium current collector where the power density was increased by a factor more than 4 in comparison with the cell made with nickel collector due to the higher catalytic activity of palladium for electrochemical reactions. On the basis of these findings, an alternative design of palladium current collector (single-double collectors (SDC design)) was conceived for the improvement of cell performance with an estimate of power density higher than 0.7 W/cm^2 at temperature of 800°C. This innovative current collector design is an effective strategy to enhance the electrochemical performance of µt-SOFCs to values of power density comparable with those of planar SOFCs, making the tubular design more competitive on the basis of cell performance.

4.3 Future Perspectives

The achievement of reliable fabrication process complied with the reproducibility of µt-SOFCs characteristics and properties from which it was possible to establish the effectiveness of the current collector. In particular, the design of current collector was demonstrated to be an essential point for the development of µt-SOFCs. Under this perspective, the development of µt-SOFCs with embedded current collector should focus on the realization of reliable current collector design, similar to the single-double collectors (SDC design) here proposed. In this condition, an enhancend diffusion of palladium toward the electrolyte is expected to occur in comparison with the current collector with single coil, and therefore its effects on electrical properties as well as phase stability of 8YSZ electrolyte are advised to be studied. Once, eventual dentrimental effects of palladium on the properties and stability of 8YSZ are established, it is possible to either adopt a protective interlayer between the anode and electrolyte or a sintering process at lower temperature as the multistage sintering here proposed in order to reduce the diffusion of palladium. Alternatively, 10 mol% Y_2O_3-doped ZrO_2 (10YSZ), more stable than the current 8YSZ to degradation phenomena as aging, can be also a reasonalble alternative electrolyte. The Author hopes these indications, along with the results obtained from rheological and thermal analyses, useful for the next development of µt-SOFCs.

Acknowledgements

I wish to express my deep gratitude to my supervisor, Prof. Vincenzo M. Sglavo, to give me the great opportunity to work on the intriguing as intricate theme of ceramic fuel cells, a really elating challenge, and the possibility to present my results to international audiences. I appreciated his constant support and confidence, especially in those moments I would have hung my lab-coat, and the trust in the way I developed this project.

I am grateful to all my collegues who supported and helped me throughout this research. Special thanks go to Alexia, Livio, Prof. Dirè and Prof. Ceccato for their valuable support and advices.

For accepting my mood in common oxidizing but also reducing atmospheres, I thank all my office mates, in particular Aylin, Aravind, Tatiane, André, Pradeep, John, Federico, Mirko, Emanuele, Artan and Lam who shared glad and amazing experiments beyond the laboratory. I wish to thank Elisa, Giulia, Claudia, Francesca, Marzio, Saliou, Thiago and Maurizio for their appraised support and fruitful discussions. I also reveled in reveal the ripples arising from twenty microns of electrolyte with Claudio, who I really thank for his help. I also thank Stefano Modena and Massimo Bertoldi for the opportunity to accomplish the electrochemical testing in SOFCpower and Alessandro, Lorenzo, Marco, Anna Rita and Dario for their support in this important activity. Eleonora, Daniele, Enrico, Marco, Emanuele and Mirko for their friendship, tolerance, dinners and libations, I am grateful for.

I owe to Ricardo De la Torre G. for his steadfastness and perseverance supported by endless patience to introduce me in this project whose current stage would have been impossible to achieve without Ricardo support; for his friendship and valuable appraisal in different circumstances, my warmest gratitude.

During these years, I also appreciated the beautiful landscapes and sunrises in Trento, in the good times and bad times. Far from my home, the constant and unlimited encourangement of my family supported me, so that I was able to realize and appreciate this experience under different perspectives; for this and many other things, I am grateful to my family.

References

Allemann, J.A., Michel, B., Märki, H.-B., Gauckler, L.J., and Moser, E.M., *Grain Growth of Differently Doped Zirconia*, J. Eur. Ceram. Soc., **1995**, 15: p. 951-958.

Anderson V.J., and Lekkerkerker, H. N. W., *Insights into phase transition kinetics from colloid science*, Nature, **2002**, 416: p. 811-815.

Andújar, J.M., and Segura, F., *Fuel cells: History and updating. A walk along two centuries*, Renewable and Sustainable Energy Rev., **2009**, 13: p. 2309-2322.

Arblaster, J.W., *Vapour Pressure Equations for the Platinum Group Elements*, Platinum Metals Review, **2007**, 51(3): p. 130-135.

Armit, H.W., *The Toxicology of Nickel Carbonyl-Part I*, Journal of Hygiene, **1907**, 7(4): p. 525-551.

Armstrong, T.J., and Virkar, A.V.*, Performance of Solid Oxide Fuel Cells with LSGM-LSM Composite Cathodes*, J. Electrochem. Soc., **2002**, 149(12): A1565-A15571.

Atkinson, A., Barnett, S., Gorte, R.J., Irvine, J. T. S., McEvoy, A.J., Mogensen, M., Singhal, S. C., and Vohs, J., *Advanced anodes for high-temperature fuel cells*, Nature, **2004**, 3: p. 17-27.

Babaei, A., Zhang, L., Liu, E., and Jiang, S.P., *Performance and stability of $La_{0.8}Sr_{0.2}MnO_3$ cathode promoted with palladium based catalysts in solid oxide fuel cells*, J. Alloys and Compounds, **2011**, 509: p. 4781-4787.

Badwal, S.P.S., Drennan, J., *Yttria-zirconia: effect of microstructure on conductivity*, J. Mater. Sci., **1987**, 22: p. 3231-3239.

Badwal, S.P.S., Ciacchi, F.T., and Ho, D.V., *A fully automated four-probe d.c. conductivity technique for investigating solid electrolytes*, J. Appl. Electrochem., **1991**, 21: p: 721-728.

Badwal, S.P.S., *Zirconia-based solid electrolytes: microstructure, stability and ionic conductivity*, Solid State Ionics, **1992**, 52: p. 23-32.

Badwal, S.P.S., *Grain boundary resistivity in zirconia-based materials: effect of sintering temperatures and impurities*, Solid State Ionics, **1995**, 76: p. 67-80.

Badwal, S.P.S., Ciacchi, F.T., and Milosevic, D., *Scandia-zirconia electrolytes for intermediate temperature solid oxide fuel cell operation*, Solid State Ionics, **2000**, 136-137: p. 91-99.

Bakalis, D., and Stamatis, A.G., *Incorporating available micro gas turbines and fuel cell: Matching considerations and performance evaluation*, Appl. Energy, **2013**, 103: p. 607-617.

Balberg, I., Anderson, C.H., Alexander, S., and Wagner, N., *Excluded volume and its relation to the onset of percolation*, Phys. Rew. B, **1984**, 30(7): p. 3933-3943.

Balberg, I., Binenbaum, N., and Wagner, N., *Percolation Thresholds in the Three-Dimensional Sticks System*, Phys. Rew. Lett., **1984**, 52(17): p. 1465-1468.

Barbucci, A., Viviani, M., Panizza, M., Delucchi, M., And Cerisola, G., *Analysis of the oxygen reduction process on SOFC composite electrodes*, J. Appl. Electrochem., **2005**, 35: p. 399-403.

Barnes, H.A., Hutton, J.F., and Walters, K., *An Introduction to Rheology*. **1989**, Elvesier Science Publishing Company Inc.

Barnes, H.A., *Thixotropy a Review*, J. Non-Newtonian Fluid Mech., **1997**, 70: p. 1-33.

Batista, R.M., and Muccillo, E.N.S., *Densification and grain growth of 8YSZ containing NiO*, Ceram. Int., **2011**, 37: p. 1047-1053.

Batista, R.M., and Muccillo, E.N.S., *Structure, microstructure and electrical conductivity of 8YSZ containing NiO*, Ceram. Int., **2011**, 37: p. 1929-1934.

Biben, T., and Hansen, J.-P., *Phase Separation of Asymmetric Binary Hard-Sphere Fluids*, Phys. Rev. Lett., **1991**, 66(17): p. 2215-2218.

Bonekamp, B.C., *Preparation of asymmetric ceramic membrane supports by dip-coating*, in *FUNDAMENTALS OF INORGANIC MEMBRANE SCIENCE AND TECHNOLOGY*, A.J. Burggraaf and L. Cot, Editors **1996**, Elvesier Science B.V. p. 141-225.

Bonenti, C., *Ottimizzazione della sospensione di zirconia impiegata nella realizzazione di SOFC microtubolari*, **2012**, B.Sc. Thesis, University of Trento, Italy.

Bordia, R.K, and Raj, R., *Sintering Behavior of Ceramic Films Constrained by Rigid Substrate*, J. Am. Ceram. Soc., **1985**, 68(6): p. 287-292.

Boschi, A.O., and Gilbart, E., *Wet Forming Processes as a Potential Solution to Agglomeration Problems*, in *ADVANCED CERAMIC PROCESSING AND TECHNOLOGY Volume 1*, J.G.P. Binner, Editor **1990**, Noyes Publications. p. 73-92.

Brader, J.M., *Nonlinear rheology of colloidal dispersions*, J. Phys.: Condens. Matter, **2010**, 22: p. 363101.

Brady, J.F., *Brownian motion, hydrodynamics, and the osmotic pressure*, J. Chem. Phys., **1992**, 98(4): p. 3335-3341.

Briscoe, B.J., Khan, A.U., and Luckham, P.F., *Stabilising Zirconia Aqueous Suspensions using Commercial Polyvalent Electrolyte Solutions*, J. Eur. Ceram. Soc., **1998**, 18: p. 2169-2173.

Buergler, B.E., Siegrist, M.E., and Gauckler, L.J., *Single chamber solid oxide fuel cells with integrated current-collectors*, Solid State Ionics, **2005**, 176: p. 1717-1722.

Bujalski, W., Dikwal, C.M., and Kendall, K., *Cycling of three solid oxide fuel cell types*, J. Power Sources, 171, **2007**: p. 96-100.

Cameron, C.P., and Rishi, R., *Grain-Growth Transition During Sintering of Colloidally Prepared Alumina Powder Compacts*, J. Am. Ceram. Soc., **1988**, 71(12): p. 1031-1035.

Carbone, T.J., and Reed, J.S., *Dependence of Sintering Response with a Constant Rate of Heating on Processing-Related Pore Distributions*, Am. Ceram. Soc. Bull., **1978**, 57(8): p. 748-750.

Carlström, E., *Surface Chemistry in Dry Pressing*, in *SURFACE AND COLLOIDAL CHEMISTRY IN ADVANCED CERAMIC PROCESSING*, R.J. Pugh and L. Bergström, Editors **1994**, Marcell Dekker. p. 245-278.

Carnahan, N.F., and Starling, K., *Equation of State for Nonattracting Rigid Spheres*, J. Chem. Phys., **1969**, 51(2): p. 635-636.

Casarin, M., Ceccato, R., and Sglavo. V.M., *Tailoring the Anode Microstructure in Micro-Tubular SOFCs by the Optimization of the Slurry*. in ICACC, 36th International Conference and Exposition on Advanced Ceramics and Composites. **2012**. Daytona Beach.

Cesarano III, J., Aksay, I.A., and Bleier, A., *Stability of α-Aqueous Al₂0₃ Suspensions with Poly(methacrylic acid) Polyelectrolyte*. J. Am. Ceram. Soc., **1988**, 71(4): p. 250-255.

Cesarano III, J., and Aksay, I.A., *Processing of Highly Concentrated Aqueous α-Alumina Suspensions Stabilized with Polyelectrolytes*. J. Am. Ceram. Soc., **1988**, 71(12): p. 1062-1067.

Chartier, T., Ferrato, M., and Baumard J.-F., *Influence of the debinding method on the mechanical properties of plastic formed ceramics*. J. Eur. Ceram. Soc., **1995**, 15: p. 899-903.

Chartier, T., Souchard, S., Baumard, J.F., and Vesteghem H., *Degradation of dispersant during milling*. J. Eur. Ceram. Soc., **1996**, 16: p. 1283-1291.

Chaston, J.C., *Reactions of Oxygen with the Platinum Metals-III The Oxidation of Palladium*. Platinum Metals Review, **1965**, 9(4): p. 126-129.

Chen, X.J., Khor, K.A., Chan, S.H., and Yu, L.G., *Influence of microstructure on the ionic conductivity of yttria-stabilized zirconia electrolyte*, Mater. Sci. Eng. A, **2002**, 335: p. 246-252.

Chen, C.-N., and Tseng, W.J., *Effect of polymeric surfactant on particulate structure in nickel-terpineol suspensions*. J. Mater. Sci., **2004**, 39: p. 3471- 3473.

Chen, M., Liu, Y.-L., Hagen, A., Hendriksen, P. V., and Poulsen, F.W., *LSM-YSZ Reactions in Different Atmospheres*, Fuel Cells, **2009**, 6: p. 833-840.

Chen, X.J., Liu, Q.L., Chan, S.H., Brandon, N.P., and Khor, K.A., *High performance cathode-supported SOFC with perovskite anode operating in weakly humidified hydrogen and methane*, Electrochem. Communic., **2007**, 9: p. 767-772.

Cima, M.J., Lewis, J.A., and Devoe, A.D., *Binder Distribution in Ceramic Greenware during Thermolysis*, J. Am. Ceram. Soc., **1989**, 72(7): p. 1192-1199.

Coors, W.G., O'Brien, J.R., and White, J.T., *Conductivity degradation of NiO-containing 8YSZ and 10YSZ electrolyte during reduction*, Solid State Ionics, **2009**, 180: p. 246-251.

Crocker, J.C., Matteo, J.A., Dinsmore, A.D., and Yodh, A.G., *Entropic Attraction and Repulsion in Binary Colloids Probed with a Line Optical Tweezer*, Phys. Rev. Lett., **1999**, 82(21): p. 4352-4355.

Cronin, J.S., Muangnapoh, K., Patterson, Z., Yakal-Kremski, K.J., Dravid, V.P., and Barnett, S.A., *Effect of Firing Temperature on LSM-YSZ Composite Cathodes: A Combined Three-Dimensional Microstructure and Impedance Spectroscopy Study*, J. Electrochem. Soc., **2012**, 159(4): p. B385-B393.

De la Torre García, R., *FABRICACIÓN DE MULLITA A PARTIR DE MEZCLAS DE CIANITA CON BAUXITA Y PSEUDOBOHEMITA,* **2006**, M.Sc. Thesis, National Polytechnic Institute, Mexico.

De la Torre García, R., *Production of Micro-Tubular Solid Oxide Fuel Cells*, **2011**, PhD Thesis, University of Trento, Italy.

De la Torre García, R., and Sglavo, V.M., *Fabrication of Innovative Compliant Current Collector-Supported Microtubular Solid Oxide Fuel Cells*, Int. J. Appl. Ceram. Technol., **2012**, 9(6): p. 1058-1063.

De la Torre García, R., Avila-Paredes, H.J., and Sglavo, V.M., *Comparative Performance Analysis of Anode-Supported Micro-Tubular SOFCs with Different Current-Collection Architectures*, Fuel Cells, **2013**, 5: p. 729-732.

de Schepper, I.M., Cohen, E.G.D., and Verberg, R., *Comment on "Viscosity and Structural Relaxation in Suspensions of Hard-Sphere Colloids"*, Phys. Rev. Lett., **1996**, 77: p. 584.

de Souza, S., Visco, S.J., and De Jonghe, L.C., *Thin-film solid oxide fuel cell with high performance at low temperature*, Solid State Ionics, **1997**, 98: p. 57-61.

Delaforce, P.M., Yeomans, J.A., Filkin, N.C., Wright, G.J., and Thomson, R.C., *Effect of NiO on the Phase Stability and Microstructure of Yttria-Stabilized Zirconia*, J. Am. Ceram. Soc., **2007**, 90(3): p. 918-924.

Dieter, G.E., and Bacon, D., *Mechanical Metallurgy, SI Metric Edition*. **1988**, McGraw-Hill Series in Materials Science and Engineering.

Ding, J., and Liu, J., *Fabrication and Electrochemical Performance of Anode-Supported Solid Oxide Fuel Cells by a Single-Step Cosintering Process*, J. Am. Ceram. Soc., **2008**, 91(10): p. 3303-3307.

Dinsmore, A.D., Yodh, A.G., and Pine, D.J., *Phase diagrams of nearly hard-sphere binary colloids*, Phys. Rev. E, **1995**, 52(4): p. 4045-4059.

Dixon, J.M., LaGrange, L.D., Merten,U., Miller, C.F., and Porter II, J.T., *Electrical Resistivity of Stabilized Zirconia at Elevated Temperatures*, J. Electrochem. Soc., **1963**, 110(4): p. 276-280.

Dong, D., Gao, J., Liu, X., and Meng, G., *Fabrication of tubular NiO/YSZ anode-support of solid oxide fuel cell by gelcasting*, J. Power Sources, **2007**, 165: p. 217-223.

Dong, D., Liu, M., Dong, Y., Lin, B., Yang, Y., and Meng, G., *Improvement of the performances of tubular solid oxide fuel cells by optimizing co-sintering temperature of the NiO/YSZ anode-YSZ electrolyte double layers*, J. Power Sources, **2007**, 171: p. 495-498.

Doroszkowski, A., and Lambourne R., *A Viscometric Technique for Determining the Layer Thickness of Polymer Adsorbed on Titanium Dioxide*, J. Colloid Interf. Sci., **1968**, 26: p. 214-221.

Du, Y., Finnerty, C., and Jian, J., *Thermal Stability of Portable Microtubular SOFCs and Stacks*, J. Electrochem. Soc., **2008**, 155(9): p. B972-B977.

Dyer, C.K., *Fuel cells for portable applications*, J. Power Sources, 106, **2002**: p. 31-34.

Edalati, K., and Horita, Z., *High-Pressure Torsion of Pure Metals: Influence of Atomic Bond Parameters and Stacking Fault Energy on Grain Size and Correlation with Hardness*, Acta Mater., **2011**, 59: p. 6831-6836.

Erning, J.W., Hauber, T., Stimming, U., and Wippermann, K., *Catalysis of the electrochemical processes on solid oxide fuel cell cathodes*, J. Power Sources, **1996**, 61: 205-211.

Evans, J.R.G., *Injection Moulding of Fine Ceramics*, in *ADVANCED CERAMIC PROCESSING AND TECHNOLOGY Volume 1*, J.G.P. Binner, Editor **1990**, Noyes Publications. p. 215-246.

Everett, D.H., *Basic Principles of Colloid Science*. **1988**, Royal Society of Chemistry Paperbacks.

Fabris, S., Paxton, A.T., and Finnis, M.W., *A stabilization mechanism of zirconia based on oxygen vacancies only*, Acta Mater., **2002**, 50: p. 5171-5178.

Fergus, J.W., *Sealants for solid oxide fuel cells*, J. Power Sources, **2005**, 147: p. 46-57.

Firth, B.A., and Hunter, R.J., *Flow Properties of Coagulated Colloidal Suspensions III. The Elastic Floc Model*, J. Colloid and Interf. Sci., **1976**, 57 (2): p. 266-275.

Flatt, R.J., *Interparticle Forces and Superplasticizers in Cement Suspensions*, **1999**, PhD Thesis, EPFL, Switzerland.

Flatt, R.J., and Bowen, P., *Yodel: A Yield Stress Model for Suspensions*, J. Am. Ceram. Soc., **2006**, 89(4): p. 1244-1256.

Flatt, R.J., and Bowen, P., *Yield Stress of Multimodal Powder Suspensions: An Extension of the YODEL (Yield Stress mODEL)*, J. Am. Ceram. Soc., **2007**, 90(4): p. 1038-1044.

Frenkel, D., *Entropy-driven phase transitions*, Physica A, **1999**, 263: p. 26-38.

Fujita, M., and Yamaguchi, Y., *Multiscale simulation method for self-organization of nanoparticles in dense suspension*, J. Computational Physics, **2007**, 223: p. 108-120.

Fuel Cells Bulletin, *Hydrogenics fuel cell for US Army armored vehicle, Purolator truck*, , **2005**, 7: p. 7.

Fujita, M., and Yamaguchi, *Simulation of concentrated colloidal nanoparticulate flows*, Phys. Rew. E, **2008**, 77: p. 026706-1-026706-14.

Garino, T.J., and Bowen, H.K., *Kinetics of Constrained-Film Sintering*, J. Am. Ceram. Soc., **1990**, 73(2): p. 251-257.

Gasser, U., *Crystallization in three- and two-dimensional colloidal suspensions*, J. Phys.: Condens. Matter, **2009**, 21: p. 203101.

Gasser, U., Weeks, E. R., Schofield, A., Pusey, P. N., and Weitz, D.A., *Real-Space Imaging of Nucleation and Growth in Colloidal Crystallization*, Science, **2001**, 292: p. 258-262.

Genç, G., Çelik, M., and Genç, M.S., *Cost analysis of wind-electrolyzer-fuel cell system for energy demand in Pinarbaşi-Kayseri*, Int. J. Hydrogen Energy, **2012**, 37: p. 12158-12166.

Genovese, D.B., *Shear rheology of hard-sphere, dispersed, and aggregated suspensions, and filler-matrix composites*. Adv. Colloid and Interf. Sci., **2012**, 171-172: p. 1-16.

German, R.M., *Theory of Thermal Debinding*, Int. J. Powder Metall., **1987**, 23(4): p. 237-245.

Gibson, I.R., Dransfield, G.P., and Irvine, J.T.S., *Sinterability of commercial 8 mol% yttria-stabilized zirconiapowders and the effect of sintered density on the ionic conductivity*, J. Mater. Sci., **1998**, 33: p. 4297-4305.

Goff, J.P., Hayes, W., Hull, S., Hutchings, M.T., and Clausen, K.N., *Defect structure of yttria-stabilized zirconia and its influence on the ionic conductivity at elevated temperatures*, Phys. Rev. B, **1999**, 59(22): p. 14202-14219.

Goodenough, J.B., and Huang, Y.-H., *Review: Alternative anode materials for solid oxide fuel cells*, J. Power Sources, **2007**, 173: p. 1-10.

Goodwin, J.W., Hughes, R.W., Reynolds, P.A., and Kwaambwa, H.M., *Viscosity behaviour of particles with non-adsorbing polymers, Part III-experimental study*, Colloids Surfaces A: Physicochem. Eng. Aspects, **2004**, 233: p. 163-170.

Greenwood, R., Luckham, P.F., and Gregory, T., *The effect of particle size on the layer thickness of a stabilising polymer adsorbed onto two different classes of polymer latex, as determined from rheological experiments*, Colloids Surfaces A: Physicochem. Eng. Aspects, **1995**, 98: p. 117-125.

Greenwood, R., Luckham, P.F., and Gregory, T., *The Effect of Diameter Ratio and Volume Ratio on the Viscosity of Bimodal Suspensions of Polymer Latices*, J. Colloid Interf. Sci., **1997**, 191: p. 11-21.

Gregorová, E., and Pabst, W., *Process control and optimized preparation of porous alumina ceramics by starch consolidation casting*, J. Eur. Ceram. Soc., **2011**, 31: p. 2073-2081.

Gross, M.D., Vohs, J.M., and Gorte, R.J., *A Strategy for Achieving High Performance with SOFC Ceramic Anodes*, Electrochemical and Solid-State Letters, **2007**, 10(4): p. B65-B69.

Guo, L.C., Zhang, Y., Uchida, N., and Uematsu, K., *Influence of Temperature on Stability of Aqueous Alumina Slurry Containing Polyelectrolyte Dispersant*, J. Eur. Ceram. Soc., **1997**, 17: p. 345-350.

Guo, L.C., Zhang, Y., Uchida, N., and Uematsu, K., *Adsorption Effects on the Rheological Properties of Aqueous Alumina Suspensions with Polyelectrolyte*. J. Am. Ceram. Soc., **1998**, 81(3): p. 549-556.

Guo, J.J., and Lewis, J.A., *Aggregation Effects on the Compressive Flow Properties and Drying Behavior of Colloidal Silica Suspensions*, J. Am. Ceram. Soc., **1999**, 82(9): p. 2345-2358.

Guo, X., and Maier, J., *Grain Boundary Blocking Effect in Zirconia: A Schottky Barrier Analysis*, J. Electrochem. Soc., **2001**, 148(3): p. E121-E126.

Hachisu, S., and Kobayashi, Y., *Kirkwood-Adler Transition in Monodisperse Latexes II. Aqueous Latexes of High Electrolyte Concentration*, J. Colloid Interf. Sci., **1974**, 46(3): p. 470-476.

Hattori, M., Takeda, Y., Sakaki, Y., Nakanishi, A., Ohara, O., Mukai, K., Lee, J.-H., and Fukui, T., *Effect of aging on conductivity of yttria stabilized zirconia*, J. Power Sources, **2004**, 126: p. 23-27.

Hassmann, K., *SOFC Power Plants, the Siemens-Westinghouse Approach*, Fuel Cells, **2001**, 1: p. 78-84.

Hiraoka, K., Shin, H., and Yokoyama, T., *Density Measurements of Poly(Acrylic Acid) Sodium Salts,* Polymer Bulletin, **1982**, 8: p. 303-309.

Henderson, S.I., and van Megen, W., *Metastability and Crystallization in Suspensions of Mixtures of Hard Spheres*, Phys. Rev. Lett., **1998**, 80: p. 877-880.

Horton, D., Thomson, C.B., and Randle, V., *Aspects of Twinning and Grain Growth in High Purity and Commercially Pure Nickel*, Mater. Sci. Eng. A, **1995**, 203: p. 408-414.

Hu, W., Guan, H., Sun, X., Li, S., Fukumoto, M., and Okane, I., *Electrical and Thermal Conductivities of Nickel-Zirconia Cermets*, J. Am. Ceram. Soc., **1998**, 81(8): p. 2209-2212.

Ingel, R.P., and Lewis III, D., *Lattice Parameters and Density of Y_2O_3-Stabilized ZrO_2*, J. Am. Ceram. Soc., **1986**, 69(4): p. 325-332.

Ismail, M.K.I., Hurley, W.C., *Modelling Carbon Fibers Oxidation in Air at Constant Heating Rates*. Carbon, **1992**, 30(3): p. 419-427.

Israelachvili, J., and Wennerström, *Role of hydration and water structure in biological and colloidal interactions*, Nature, **1996**, 379: p. 219-225.

Ivers-Tiffée, E., Weber, A., and Herbstritt, D., *Materials and technologies for SOFC-components*, J. Eur. Ceram. Soc., **2001**, 21: p. 1805-1811.

Jiang, S.P., *Development of lanthanum strontium manganite perovskite cathode materials of solid oxide fuel cells: a review*, J. Mater. Sci., **2008**, 43: p. 6799-6833.

Jiang, S.P., and Chan, S.H., *A review of anode materials development in solid oxide fuel cells*, J. Mater. Sci., **2004**, 39: p. 4405-4439.

Jiang, S.P., Love, J.G., and Apateanu, L., *Effect of contact between electrode and current collector on the performance of solid oxide fuel cells*, Solid State Ionics, **2003**, 160: p. 15-26.

Jiang, S.P., and Ramprakash, Y., *H_2 oxidation on Ni/Y-TZP cermet electrodes_a comparison of electrode behaviour by GCI and EIS techniques*, Solid State Ionics, **1999**, 122: p. 211-222.

Jono, K., Suda, S., and Hattori, M., *Effect of Graded Porous Structure on Ni-YSZ Anode Performance*, ECS Transactions, **2007**, 7(1): p. 1541-1546.

Jiang, S.P., and Wang, W., *Sintering and grain growth of (La,Sr)MnO3 electrodes of solid oxide fuel cells under polarization*, Solid State Ionics, **2005**, 176: p. 1185-1191.

Kalimeri, K., Pekridis, G., Vartzoka, S., Athanassiou, C., and Marnellos, G., *Effect of palladium oxidation state on the kinetics and mechanism of the charge transfer reaction taking place at the Pd/YSZ interface*, Solid State Ionics, **2006**, 177: p. 979-988.

Kaplan, P.D., Rouke, J.L., Yodh, A.G., and Pine, D.J., *Entropically Driven Surface Phase Separation in Binary Colloidal Mixtures*, Phys. Rev. Lett., **1994**, 72(4): p. 582-587.

Kenjo, T., and Nishiya, M., *$LaMnO_3$ air cathodes containing ZrO_2 electrolyte for high temperature solid oxide fuel cells*, Solid State Ionics, **1992**, 57: p. 295-302.

Kendall, K., *Progress in Microtubular Solid Oxide Fuel Cell*, Int. J. Appl. Ceram. Technol., **2010**, 7(1): p. 1-9.

Khan, A.U., Briscoe, B. J., and Luckham, P. F., *Interaction of binders with dispersant stabilised alumina suspensions*. Colloids and Surfaces A: Physicochemical and Engineering Aspects, **2000**, 161: p. 243-257.

Khanna, A.S., *Introduction to High Temperature Oxidation and Corrosion*. **2002**, ASM International.

Kharton, V.V., Marques, F.M.B., and Atkinson, A., *Transport properties of solid oxide electrolyte ceramics: a brief review*, Solid State Ionics, **2004**, 174: p. 135-149.

Kharton, V. V., Naumovich, E.N., and Vecher, A.A., *Research on the electrochemistry of oxygen ion conductors in the former Soviet Union. I. ZrO2-based ceramic materials*, J. Solid State Electrochem., **1999**, 3: p. 61-81.

Kharton, V. V., Yaremchenko, A.A., and Naumovich, E.N., *Research on the electrochemistry of oxygen ion conductors in the former Soviet Union. II. Perovskite-related oxides*, J. Solid State Electrochem., **1999**, 3: p. 303-326.

Kilo, M., Taylor, M.A., Argirusis, C., Borchardt, B., Lesage, B., Weber, S., Scherrer, S., Scherrer, H., Schroeder, M., and Martin, M., *Cation self-diffusion of ^{44}Ca, ^{88}Y, and ^{96}Zr in single-crystalline calcia- and yttria-doped zirconia*, J. Appl. Phys., **2003**, 94(12): p. 7547-7552.

Kim, J.-D., Kim, G.-D., Moon, J.-W., Park, Y.-i., Lee, W.-H., Kobayashi, K., Masayuki, N., and Kim, C.-E., *Characterization of LSM–YSZ composite electrode by ac impedance spectroscopy*, Solid State Ionics, **2001**, 143: p. 379-389.

Kittel, C., *Introduction to Solid State Physics*. **1996**, John Wiley & Sons, Inc.

Knapp, A.M., and Halloran, J.W., *Binder Removal from Ceramic-Filled Thermoplastic Blends*, J. Am. Ceram. Soc., **2006**, 89(9): p. 2776-2781.

Kofke, D.A., and Bolhuis, P.G., *Freezing of polydisperse hard spheres*, Phys. Rev. E, **1999**, 59: p. 618-622.

Kondoh, J., Kawashima, T., Kikuchi, S., Tomii, Y., and Ito, Y., *Effect of Aging on Yltria-Stabilized Zirconia_I. A Study of Its Electrochemical Properties*, J. Electrochem. Soc., **1998**, 145(5): p. 1527-1536.

Kondoh, J., Kikuchi, S., Tomii, Y., and Ito, Y., *Effect of Aging on Yltria-Stabilized Zirconia_III. A Study of the Effect of Local Structures on Conductivity*, J. Electrochem. Soc., **1998**, 145(5): p. 1550-1560.

Kose, A., and Hachisu, S., *Kirkwood-Adler Transition in Monodisperse Latexes I. Nonaqueous Systems*, J. Colloid Interf. Sci., **1974**, 46(3): p. 460-469.

Krieger, I.M., and Dougherty, T.J., *A Mechanism for the Non-Newtonian Flow in Suspensions of Rigid Spheres*, Trans. Soc. Rheol., **1959**, III: p. 137-152.

Kuhn, M., Napporn, T., Meunier, M., Therriault, D., and Vengallatore, S., *Fabrication and testing of coplanar single-chamber micro solid oxide fuel cells with geometrically complex electrodes*, J. Power Sources, **2008**, 177: p. 148-153.

Kuzjukevics, A., and Linderoth, S., *Influence of NiO on phase stabilization in 6 mol% yttria-stabilized zirconia*, Mater. Sci. Eng. A, **1997**, 232: p. 163-167.

Kuzjukevics, A., and Linderoth, S., *Interaction of NiO with yttria-stabilized zirconia*, Solid State Ionics, **1997**, 93: p. 255-261.

Laguna-Bercero, M.A., Kilner, J.A., and Skinner, S.J., *Development of oxygen electrodes for reversible solid oxide fuel cells with scandia stabilized zirconia electrolytes*, Solid State Ionics, **2011**, 192: p. 501-504.

Lange, F. F., *Sinterability of agglomerated powders*, J. Am. Ceram. Soc., **1984**, 67(2): p. 83-88.

Lange, F.F*., Powder Processing Science and Technology for Increased Reliability*, J. Am. Ceram. Soc., **1989**, 72(1): p. 3-15.

Lange, F. F., and Davis, B.I., *Sinterability of ZrO$_2$ and Al$_2$O$_3$ Powders: The Role of Pore Coordination Number Distribution*, in *Advances in Ceramics, Vol. 12, Science and Technology of Zirconia II*, N. Claussen, M. Ruhle and H. Heuer, Editors **1984**, American Ceramic Society, Columbus, OH: p. 699-713.

Larminie, J., and Dicks, A., *Fuel Cell Explained, Second Edition*. **2003**, John Wiley and Sons Ltd.

Larson, R.G., *The Structure and Rheology of Complex Fluids*. **1999**, Oxford University Press, Inc.

Lawlor, V., Griesser, S., Buchinger, G., Olabi, A.G., and Cordiner, S., and Meissner, D., *Review of the micro-tubular solid oxide fuel cell Part I. Stack design issues and research activities*, J. Power Sources **2009**, 193: p. 387-399.

Lee, C.-H., Lee, C.-H., Lee, H.-Y., and Oh, S.M., *Microstructure and anodic properties of Ni/YSZ cermets in solid oxide fuel cells*, Solid State Ionics, **1997**, 98: p. 39-48.

Lee, J.-H., Moon, H., Lee, H.-W., Kim, J., Kim, J.-D., and Yoon, K.-H., *Quantitative analysis of microstructure and its related electrical property of SOFC anode, Ni-YSZ cermet*, Solid State Ionics, **2002**, 148: p. 15-26.

Lee, J.-H., Heo, J.-W., Lee, D.-S., Kim, J., Kim, G.-H., Lee, H.-W., Song, H.S., and Moon, J.-H., *The impact of anode microstructure on the power generating characteristics of SOFC*, Solid State Ionics, **2003**, 158: p. 225-232.

Lewis, J.A., *Colloidal Processing of Ceramics*. J. Am. Ceram. Soc., **2000**, 83(10): p. 2341-2359.

Lei, Y., Ito, Y., and Browning, N.D., *Segregation Effects at Grain Boundaries in Fluorite-Structured Ceramics*, J. Am. Ceram. Soc., **2002**, 85(9): p. 2359-2363.

Levchik, S.V., Camino, G., Luda, M.P., Costa, L., Muller, G., and Costes, B., *Epoxy resins cured with aminophenylmethylphosphine oxide-II. Mechanism of thermal decomposition*. Polymer Degradation and Stability, **1998**, 60(1): p. 169-183.

Lewis, J.A., *Colloidal Processing of Ceramics*, J. Am. Ceram. Soc., **2000**, 83(10): p. 2341-2359.

Li, T.S., Wang, W.G., Miao, H., Chen, T., and Cheng, X., *Effect of reduction temperature on the electrochemical properties of a Ni/YSZ anode-supported solid oxide fuel cell*, J. Alloys and Compounds, **2010**, 495: p. 138-143.

Li, T., Wu, Z., and Li, K., *Single-step fabrication and characterizations of triple-layer ceramic hollow fibres for micro-tubular solid oxide fuel cells (SOFCs)*, J. Membrane Sci., **2014**, 449: 1-8.

Lin, F.J.T., De Jonghe, L.C., and Rahaman, M.N., *Initial Coarsening and Microstructural Evolution of Fast-Fired and MgO-Doped Al_2O_3*, J. Am. Ceram. Soc., **1997**, 80(11): p. 2891-2896.

Linderoth, S., Bonanos, N., Jensen, K.V., and Bilde-Sørensen, J.B., *Effect of NiO-to-Ni Transformation on Conductivity and Structure of Yttria-Stabilized ZrO_2*, J. Am. Ceram. Soc., **2001**, 84(11): p. 2652-2656.

Liu, D.-M., *Effect of Dispersants on the Rheological Behavior of Zirconia-Wax Suspensions*. J. Am. Ceram. Soc., **1999**, 82(5): p. 1162-1168.

Liu, D.-M., *Particle packing and rheological property of highly-concentrated ceramic suspensions: Φ_m determination and viscosity prediction*, J. Mater. Sci., **2000**, 35: p. 5503-5507.

Liu, D.-M., and Tseng, W.J., *Porosity development in ceramic injection mouldings via different burnout strategies*. J. Mater. Sci. Lett., **1997**, 16(6): p. 482-484.

Liu, D.-M., and Tseng, W.J., *Influence of Debinding Rate, Solid Loading and Binder Formulation on the Green Microstructure and Sintering Behaviour of Ceramic Injection Mouldings*, Ceram. Int., **1998**, 24: p. 471-481.

Liu, D.-M., and Tseng, W.J., *Yield behavior of zirconia-wax suspensions*. Mater. Sci. Eng. A, **1998**, 254: p. 136-146.

Liu, D.-M., and Tseng, W.J., *Influence of Powder Agglomerates on the Structure and Rheological Behavior of Injection-Molded Zirconia-Wax Suspensions*. J. Am. Ceram. Soc., **1999**, 82 (10): p. 2647-2652.

Liu, D.-M., and Tseng, *Binder removal from injection moulded zirconia ceramics*, Ceram. Int., **1999**, 25: p. 529-534.

Liu, M., Gao, J., Dong, D., Liu, X., Meng, G., *Comparative study on the performance of tubular and button cells with YSZ membrane fabricated by a refined particle suspension coating technique*, Int. J. Hydrogen and Energy**, 2010**, 35: p. 10489-10494.

Liu, Y.L., Primdahl, S., and Mogensen, M., *Effects of impurities on microstructure in Ni/YSZ–YSZ half-cells for SOFC*, Solid State Ionics, **2003**, 161: p. 1-10.

Liufu, S.-C., Xiao, H.-N., and Li,Y.-P., *Thermal analysis and degradation mechanism of polyacrylate/ZnO nanocomposites*, Polymer Degradation and Stability, **2005**, 87: p. 103-110.

Macosko, C.W., *Rheology_Principles, Measurements and Applications*. **1994**, Wiley-VCH, Inc.

Mahapatra, M.K., Bhowmick, S., Li, N., and Singh, P., *Role of oxygen pressure on the stability of lanthanum strontium manganite-yttria stabilized zirconia composite*, J. Eur. Ceram. Soc., **2012**, 32: 2341-2349.

Maiti, A. K., and Rajende, B., *Terpineol as a dispersant for tape casting yttria stabilized zirconia powder*. Mat. Sci. Eng. A, **2002**, 333: pp. 35-40.

Martin, M., and Fromm, E., *Low-temperature oxidation of metal surfaces*. J. Alloys and Compounds, **1997**, 258: p. 7-16.

Martin, S., Bryant, G., and van Megen, W., *Crystallization kinetics of polydisperse colloidal hard spheres: Experimental evidence for local fractionation*, Phys. Rev. E, **2003**, 67: p 061405-1-061405-11.

Masia, S., Calvert, P.D., Rhine, W.E., and Bowen, H.K., *Effect of oxides on binder burnout during ceramics processing*, J. Mater. Sci., **1989**, 24: p. 1907-1912.

McIntosh, S., Adler, S. B., Vohs, J.M., and Gorte, R.J., *Effect of Polarization on and Implications for Characterization of LSM-YSZ Composite Cathodes*, Electrochem. Solid-State Lett., **2004**, 7(5): p. A111-A114.

Meijer, E.J., and Frenkel, D., *Computer Simulation of Polymer-Induced Clustering of Colloids*, Phys. Rev. Lett., **1991**, 67(9): p. 1110-1113.

Mewis, J., and Wagner, N.J., *Thixotropy*. Adv. Colloid Interf. Sci., **2009**, 147-148: p. 214-227.

Minh, N.Q., *Ceramic Fuel Cells*, J. Am. Ceram. Soc., **1993**, 76(3): p. 563-588.

Minh, N.Q., *Solid oxide fuel cell technology-features and applications*, Solid State Ionics, **2004**, 174: p. 271-277.

Minh, N.Q., and Takahashi, T., *Science and Technology of Ceramic Fuel Cells*. **1995**, Elsevier.

Miyoshi, S., Honga, J.-O., Yashiro, K., Kaimai, A., Nigara, Y., Kawamura, K., Kawada, T., and Mizusaki, J., *Lattice expansion upon reduction of perovskite-type $LaMnO_3$ with oxygen-deficit nonstoichiometry*, Solid State Ionics, **2003**, 161: p. 209-217.

Moreno, R., *The role of slip additives in tape-casting technology: Part II - Binders and Plasticezers*. Am. Ceram. Soc. Bull., **1992**, 71(11): p. 1521-1531.

Novich, B.E., and Pyatt, D.H, *Consolidation Behavior of High-Performance Ceramic Suspensions*, J. Am. Ceram. Soc., **1990**, 73(2): p. 207-212.

O'Hayre, R., Cha, S.-K., Colella, W., and Prinz, F.B., *Fuel Cell Fundamentals*. **2006**, John Wiley & Sons, Inc.

Othman, M. H. D., Wu, Z., Droushiotis, N., Kelsall, G., and Li, K., *Morphological studies of macrostructure of Ni-CGO anode hollow fibres for intermediate temperature solid oxide fuel cells*, J. Membrane Sci., **2010**, 360: p. 410-417.

Pagnoux, C., Chartier, T., de F. Granja, M., Doreau, F., Ferreira, J. M., and Baumard, J. F., *Aqueous Suspensions for Tape-casting Based Acrylic Binders*. J. Eur. Cer. Soc., **1998**, 18: p. 241-247.

Park, Y.M., and Choi, G.M., *Mixed Ionic and Electronic Conduction in YSZ-NiO Composite*, J. Electrochem. Soc., **1999**, 146(3): p. 883-889.

Phan, S.-E., Russel, W.B., Cheng, Z., Zhu, J., Chaikin, P.M., Dunsmuir, J.H., and Ottewill, R.H., *Phase transition, equation of state, and limiting shear viscosities of hard sphere dispersions*, Phys. Rev. E, **1996**, 54(6): p. 6633-6645.

Pihlatie, M., Kaiser, A., Larsen, P.H., and Mogensen, M., *Dimensional Behavior of Ni-YSZ Composites during Redox Cycling*, J. Electrochem. Soc., **2009**, 156(3): p. B322-B329.

Poirson, A., Decorse, P., Caboche, G., and Dufour, L.C., *A dilatometric study of the $La_{0.8}Sr_{0.2}MnO_3$ sintering behaviour*, Solid State Ionics, **1997**, 99: p. 287-295.

Primdahl, S., *Nickel/yttria-stabilised zirconia cermet anodes for solid oxide fuel cells*, **1999**, PhD Thesis, University of Twente, Netherlands.

Pugh, R.J., Dispersion and Stability of Ceramic Powders in Liquids, in *SURFACE AND COLLOIDAL CHEMISTRY IN ADVANCED CERAMIC PROCESSING*, R.J. Pugh and L. Bergström, Editors **1994**, Marcell Dekker. p. 127-192.

Radovich, M., and Lara-Curzio, E., *Mechanical properties of tape cast nickel-based anode materials for solid oxide fuel cells before and after reduction in hydrogen*, Acta Materialia, **2004**, 52: p. 5747-5756.

Radovich, M., and Lara-Curzio, *Elastic Properties of Nickel-Based Anodes for Solid Oxide Fuel Cells as a Function of the Fraction of Reduced NiO*, J. Am. Ceram. Soc., **2004**, 87(12): p. 2242-2246.

Rahaman, M.N., De Jonghe, L.C., and Brook, R.J., *Effect of Shear Stress on Sintering*, J. Am. Ceram. Soc., **1986**, 69(1): p. 53-58.

Rahaman, M.N., *Ceramic processing and sintering, second edition*. **2003**, Marcel Dekker, Inc.

Rajeswari, K., Suresh, M.B., Hareesh, U.S., Rao, Y.S., Das, D., and Johnson, R., *Studies on ionic conductivity of stabilized zirconia ceramics (8YSZ) densified through conventional and non-conventional sintering methodologies*, Ceram. Int., **2011**, 37: p. 3557-3564.

Reed, J.S., *Principles of Ceramic Processing, second edition*. **1995**, John Wiley & Sons, Inc.

Ring, T.A., *Fundamentals of Ceramic Powder Processing and Synthesis*. **1996**, San Diego, CA, USA: Academic Press, Inc.

Rödel, C., Müller, M., Glorius M., Potthoff A., and Michaelis A., *Effect of varied powder processing routes on the stabilizing performance and coordination type of polyacrylate in alumina suspensions*. J. Eur. Ceram. Soc., **2012**, 32: p. 363-370.

Roosen, A., and Hausner, H., *Sintering Kinetics for ZrO_2 Powders,* in *Science and Technology of Zirconia II*, N. Claussen, M. Rühle, and A.H. Heuer, Editors **1984**, American Ceramic Society. p. 714-726.

Roosen, A., and Bowen, H.K., *Influence of Various Consolidation Technique on the Green Microstructure and Sintering Behaviour of Alumina Powders*, J. Am. Ceram. Soc., **1988**, 71(11): p. 970-977.

Rutgers, M.A., Dunsmuir, J.H., Xue, J.-Z., Russel, W.B., and Chaikin, P.M., *Measurement of the hard-sphere equation of state using screened charged polystyrene colloids*, Phys. Rev. B, **1996**, 53(9): p. 5043-5046.

Sahibzada, M., Benson, S.J., Rudkin, R.A., and Kilner, J.A., *Pd-promoted $La_{0.6}Sr_{0.4}Co_{0.2}Fe_{0.8}O_3$ cathodes*, Solid State Ionics, **1998**, (113-115): p. 285-290.

Sarkar, P., Yamarte, L., Rho, H., and Johanson, L., *Anode-Supported Tubular Micro-Solid Oxide Fuel Cell*, Int. J. Appl. Ceram. Technol., **2007**, 4(2): p. 103-108.

Sasaki, K., Wurth, J.-P., Gschwend, R., Gödickemeier, M., and Gauckler, L.J., *Microstructure-Property Relations of Solid Oxide Fuel Cell Cathodes and Current Collectors_Cathodic Polarization and Ohmic Resistance*, J. Electrochem. Soc., **1996**, 143(2): p. 530-543.

Servais, C., Jones, R., and Roberts, I., *The influence of the particle size distribution on the processing of food*, J. Food Eng., **2002**, 51: p. 201-208.

Shapiro, A.P., and Probstein, R.F., *Random Packings of Spheres and Fluidity Limits of Monodisperse and Bidisperse Suspensions*, Phys. Rev. Lett., **1992**, 68(9): p. 1422-1425.

Shackelford, J.F., and Alexander, W., *Materials Science and Engineering Handbook, Third Edition*. **2001**, CRC Press LLC.

Shibata, N., Katamura, J., Kuwabara, A., Ikuhara, Y., and Sakuma, T., *The instability and resulting phase transition of cubic zirconia*, Mater. Sci. Eng. A, **2001**, 312: p. 90-98.

Shojai, F., Pettersson, A.B.A., Mäntylä, T., and Rosenholm, J.B., *Electrostatic and electrosteric stabilization of aqueous slips of 3Y-ZrO2 powder*. J. Eur. Ceram. Soc., **2000**, 20: p. 277-283.

Shukla, V.N., and Hill, D.C., *Binder Evolution from Powder Compacts: Thermal Profile for Injection-Molded Articles*, J. Am. Ceram. Soc., **1989**, 72(10): p. 1797-1803.

Simwonis, D., Tiezt, F., and Stöver, D., *Nickel coarsening in annealed Ni/8YSZ anode substrates for solid oxide fuel cells*, Solid State Ionics, **2000**, 132: p. 241-251.

Singhal, S.C., *Advances in solid oxide fuel cell technology*, Solid State Ionics, **2000**, 135: p. 305-313.

Singhal, S.C., *Review: Solid oxide fuel cells for stationary, mobile, and military applications*, Solid State Ionics, **2002**, 152-153: p. 405-410.

Slamovich, E.B., and Lange, F.F*., Densification of Large Pores: I, Experiments*, J. Am. Ceram. Soc., **1992**, 75(9): p. 2498-2508.

Slamovich, E.B., and Lange, F.F*., Densification of Large Pores: II, Driving Potentials and Kinetics*, J. Am. Ceram. Soc., **1993**, 76(6): p. 1584-1590.

Smallman, R.E., and Bishop, R.J., *Metals and Materials_Science, processes, applications*. **1995**, Butterworth-Heinemann.

Soderberg, J.N., Sun, L., Sarkar, P., and Birss, V.I., *Oxygen Reduction at LSM-YSZ Cathodes Deposited on Anode-Supported Microtubular Solid Oxide Fuel Cells*, J. Electrochem. Soc., **2009**, 156(6): p. B721-B728.

Steele, B.C.H., *Material science and engineering: The enabling technology for the commercialization of fuel cell systems*, J. Mater. Sci., **2001**, 36: p. 1053-1068.

Steil, M.C., Thevenot, F., and Kleitz, M., *Densification of Yttria-Stabilized Zirconia_ Impedance Specfroscopy Analysis*, J. Electrochem. Soc., **1997**, 144(1): p. 390-398.

Stemmer, S., Vleugels, J., and Van Der Biest, O., *Grain Boundary Segregation in High-purity, Yttria-stabilized Tetragonal Zirconia Polycrystals (Y-TZP)*, J. Eur. Ceram. Soc., **1998**, 18: p. 1565-1570.

Strauss, M., Ring, T., and Bowen, H.K., *Coagulation in processing of ceramic suspensions: Powder size distribution effects*, J. Appl. Phys., **1985**, 58(10): p. 3871-3879.

Sun, C., Hui, R., and Roller, J., *Cathode materials for solid oxide fuel cells: a review*, J. Solid State Electrochem., **2010**, 14: p. 1125-1144.

Suzuki, T., Funahashi, Y., Hasan, Z., Yamaguchi, T., Fujishiro, Y., and Awano, M., *Fabrication of needle-type micro SOFCs for micro power devices*, Electrochemistry Communic., **2008**, 10: p. 1563-1566.

Suzuki, T., Yamaguchi, T., Fujishiro, Y., and Awano, M., *Improvement of SOFC Performance Using a Microtubular, Anode-Supported SOFC*, J. Electrochem. Soc., **2006**, 153(5): p. A925-A928.

Tadros, T., *Interparticle interactions in concentrated suspensions and their bulk (Rheological) properties*, Adv. Colloid Interf. Sci., **2011**, 168: p. 263-277.

Tang, F., Yu, L., Huang, X., and Guo, J., *Characterization of Adsorption and Distribution of Polyelectrolyte on Stability of Nano-Zirconia Suspensions by Auger Electron Spectroscopy*. NanoStructured Materials, **1999**, 11(4): p. 441-450.

Tang, X., and Donato, A.T., Aqueous Emulsion Acrylic Binders for Low-Foaming Ceramic Slips. J. Am. Ceram. Soc., **1996**, 79(2): p. 510-512.

Tasa, S., and Aapro, T., *Fuel Cells as Energy Sources for Future Mobile Devices*, J. Fuel Cell Sci. Technol., **2006**, 3: p. 492-494.

Tekeli, S., Erdogan, M., and Aktas, B., *Influence of α-Al_2O_3 addition on sintering and grain growth behaviour of 8 mol% Y_2O_3-stabilised cubic zirconia (c-ZrO_2)*, Ceram. Int., **2004**, 30: p. 2203-2209.

Tsai, T., Barnett, S.A., *Effect of LSM-YSZ cathode on thin-electrolyte solid oxide fuel cell performance*, Solid State Ionics, **1997**, 93: p. 207-217.

Traversa, E., *Toward the Miniaturization of Solid Oxide Fuel Cells*, Interface, **2009**, 18(3): 49-52.

Tseng, W.J., and Chen, C.-N. *Effect of polymeric dispersant on rheological behavior of nickel-terpineol suspensions*, Mater. Sci. Eng. A, **2003**, 347: p. 145-153.

Tseng, W.J., Liu, D.-M., and Hsu, C.-K., *Influence of stearic acid on suspension structure and green microstructure of injection-molded zirconia ceramics*. Ceram. Int., **1999**, 25: p. 191-195.

van Heuveln, F. H., and Bouwmeester, H. J. M., *Electrode Properties of Sr-Doped $LaMnO_3$ on Yttria-Stabilized Zirconia: II. Electrode Kinetics*, J. Electrochemic. Soc., **1997**, 144(1): p. 134-140.

Verkerk, M.J., Middelhuis, B.J., and Burggraaf, A.J., *Effect of Grain Boundaries on the Conductivity of High-Purity ZrO_2-Y_2O_3 Ceramics*, Solid State Ionics, **1982**, 6: p. 159-170.

Voegtlin, C., *Toxicity of Certain Heavy Metal Carbonyls-Ni(Co)$_4$, Mo(Co)$_6$, W(Co)$_6$, Cr(Co)$_6$*, Official Document, **1947**: p.1-3.

Wang, W., and Jiang, S.P., *Effect of polarization on the electrode behavior and microstructure of (La,Sr)MnO3 electrodes of solid oxide fuel cells*, J. Solid State Electrochem., **2004**, 8: p. 914-922.

Wang, X., and Guo, L., *Effect of preparation methods on rheological properties of Al2O$_3$/ZrO$_2$ suspensions*. Colloids and Surfaces A: Physicochem. Eng. Aspects, **2006**, 281: p. 171-176.

Wang, X., and Guo, L., *Effect of temperature on the stability of aqueous ZrO_2 suspensions*. Colloids and Surfaces A: Physicochem. Eng. Aspects, **2007**, 304: p. 1-6.

Weller, M., Herzog, R., Kilo, M., Borchardt, G., Weber, S., and Scherrer, S., *Oxygen mobility in yttria-doped zirconia studied by internal friction, electrical conductivity and tracer diffusion experiments*, Solid State Ionics, **2004**, 175: 409-413.

Will, J., Mitterdorfer, A.,Kleinlogel, C., Perednis, D., and Gauckle, L.J., *Fabrication of thin electrolytes for second-generation solid oxide fuel cells*, Solid State Ionics, **2000**, 131: p. 79-96.

White, J., Reimains, I.E., Menzer, S., and Coors, G., *The Enhanced Stabilization of the Cubic Phase in Yttria-Stabilized Zirconia with the Addition of Nickel Oxide*, J. Am. Ceram. Soc., **2011**, 94(7): p. 2030-2036.

Xia, C.-M., Jin, G.-J., Shi, X.-D., and Ma, Y.-Q., *Entropy-driven phase transition in binary mixtures*, Phys. Rev. E, **2001**, 64: p. 0011402-1-0011402-5.

Xia, Y., Byron, G., Yin, Y., Lu, Y., *Monodispersed Colloidal Spheres: Old Materials with New Applications*, Adv. Mater. **2000**, 12(10), p: 693-713.

Yamahara, K., Jacobson, C.P., Visco, S.J., and De Jonghe, L.J., *Catalyst-infiltrated supporting cathode for thin-film SOFCs*, Solid State Ionics, **2005**, 176: p. 451-456.

Yang, C., Jin, C., and Chen, F., *Performances of micro-tubular solid oxide cell with novel asymmetric porous hydrogen electrode*, Electrochim. Acta, **2010**, 56: p. 80-84.

Yu, H.J., Park, G.W., Lee, S., and Woo, S.K., *Microstructural effects on the electrical and mechanical properties of Ni-YSZ cermet for SOFC anode*, J. Power Sources, **2007**, 163: p. 926-932.

Zhang, L., He, H.Q., Kwek, W.R., Ma, J., Tang, E.H., and Jiang, S.P., *Fabrication and Characterization of Anode-Supported Tubular Solid-Oxide Fuel Cells by Slip Casting and Dip Coating Techniques*, J. Am. Ceram. Soc., **2009**, 92(2): p. 302-310.

Zhang, T.S., Chan, S.H., Kong, L.B., Sheng, P.T., and Ma, *Synergetic effect of NiO and SiO2 on the sintering and properties of 8 mol% yttria-stabilized zirconia electrolytes*, Electrochim. Acta, **2009**, 54: p. 927-934.

Zhang, T.S., Du, Z.H., Li, S., Kong, L.B., Song, X.C., Lu, J., and Ma, J., *Transitional metal-doped 8 mol% yttria-stabilized zirconia electrolytes*, Solid State Ionics, **2009**, 180: 1311-1317.

Zhou, J., and Lucas J.P., *Hygrothermal effects of epoxy resin. Part II: variations of glass transition temperature*. Polymer, **1999**, 40: p. 5513-5522.

Zhou, X.-D., Simmer, S.P., Templeton, J., Nie, Z., Stevenson, J.W., and Gorman, B.P., *Electrochemical Performance and Stability of the Cathode for Solid Oxide Fuel Cells, II. Role of Ni Diffusion on LSM Performance*, J. Electrochem. Soc., **2010**, 157(5): p. B643-B649.

Zhu, W.Z., and Deevi, S.C., *A review on the status of anode materials for solid oxide fuel cells*, Mater. Sci. Eng. A, **2003**, 362: p. 228-239.

Scientific Production

M. Casarin, R. Ceccato and V.M. Sglavo, "*Tailoring the Anode Microstructure in Micro Tubular SOFCs by the Optimization of the Slurry*" in Advances in Solid Oxide Fuel Cells VIII: Ceramic Engineering and Science Proceedings, Volume 33, 36th International Conference on Advanced Ceramics and Composites, Daytona Beach, FL, USA, January 22-27, **2012**.

R. De La Torre, M. Casarin and V.M. Sglavo, "*Production Of Current Collector-Supported Micro-Tubular Solid Oxide Fuel Cells With Sacrificial Inner Core*", in Advances in Solid Oxide Fuel Cells VII: Ceramic Engineering and Science Proceedings, Volume 32, 35th International Conference on Advanced Ceramics and Composites, Daytona Beach, FL, USA, January, 23-28, **2011**.

R. De La Torre, M. Casarin and V.M. Sglavo, "*Production of Compliant Current Collector-Supported Micro-Tubular Solid Oxide Fuel Cells*", ECS Transactions, 35(1), **2011**, 747-55.

Congresses, Schools and Workshops

ICACC, (International Conference on Advanced Ceramics and Composites), 22-27 Jan., **2012**, Daytona Beach, Florida, USA.

TICME, (Trento Innovation Conferences on Materials Engineering), 12-14 Dec., **2011**, Trento, Italy.

EUROMAT, (European Congress on Advanced Materials and Processes), 12-15 Sept., **2011**, Montpellier, France.

SOFC Summer School, 28 Aug. to 2 Sept., **2010**, Saloniki, Greece.